Synthesis and characterization of metal doped BiVO4 nanostructured materials for photocatalytic applications

Victor Ishrayelu Merupo

UNIVERSITE BRETAGNE LOIRE

Université du Maine

Thèse de Doctorat

Cinvestav – IPN Mexico D.F.

Victor Ishrayelu MERUPO

Mémoire présenté en vue de l'obtention du
grade de Docteur de l'Université du Maine
sous le sous le sceau de l'Université Bretagne Loire

École doctorale : *3MPL-Le Mans*

Discipline : *Physique*
Spécialité : *Physique des matériaux*
Unité de recherche : *IMMM-UMR 6283*

Soutenue le *18/03/2016*
Thèse N° : *(10)*

Synthèse et caractérisation de matériaux nanostructurés $BiVO_4$ dopés par des métaux pour des applications en Photocatalyse

JURY

Rapporteurs: Prof. Benoit Guiffard, IETR, Université de Nantes, France
Prof. José Álvaro Chávez Carvayar, IIM-UNAM, D.F. Mexico

Examinateurs : Prof. Jean-Paul Salvestrini, Université de Lorraine et Centrale Supélec
Prof. Mauricio Ortega López, SEES-IE, Cinvestav – IPN, D.F. Mexico
Prof. Ramón Pena Sierra, SEES-IE, Cinvestav – IPN, D.F. Mexico

Directeurs de Thèse : Prof. Abdel Hadi Kassiba, IMMM, Université du Maine, Le Mans, France
Prof. Velumani Subramaniam, SEES-IE, Cinvestav – IPN, D.F. Mexico

UNIVERSITE BRETAGNE LOIRE

Université du Maine

Thèse de Doctorat

Victor Ishrayelu MERUPO

Cinvestav – IPN
Mexico D.F.

Synthèse et caractérisation de matériaux nanostructurés $BiVO_4$ dopés par des métaux pour des applications en photocatalyse

Résumé

Le travail de thèse est consacré à la synthèse, l'élaboration et à l'étude des propriétés physiques d'une famille d'oxydes semi-conducteurs $BiVO_4$ sous formes de nanostructures et de films minces incluant un dopage métallique (Metal = Cu, Mo et Ag) dans le but de réaliser des photocatalyseurs efficaces sous irradiation en lumière visible. La synthèse de de nanopoudres dopées a ainsi été effectuée par la technique de broyage planétaire à haute énergie ainsi que par la méthode sol-gel. Les matériaux obtenus et les effets de dopage ont été étudiés sur les caractéristiques structurales, électroniques et optiques. En conjuguant des études par XPS, Raman et RPE, nous avons montré que le dopage substitutionnel est effectivement réalisé pour les ions (Cu, Mo) localisés dans les sites cristallins des ions vanadium alors que le dopage par l'élément Ag contribue à former des clusters métalliques localisés à la surface de nanoparticules de BiVO4 formant ainsi des nanocomposites. Les réactions photocatalytiques ont été étudiées par la dégradation de colorants organiques (Acide bleu 113, méthyle orange (MO)) dans des solutions faiblement concentrées. Parmi les ions dopants substitués dans les matrices hôtes, le dopage au cuivre (Cu^{2+}) a montré de meilleures performances en raison d'une augmentation de la densité de charges photo-générées et de la conductivité électrique par rapport au cas du dopage au molybdène. Pour le dopage à l'argent, la formation de clusters métalliques donnent lieu à des effets de résonances plasmoniques qui améliorent l'efficacité photocatlytique à un niveau équivalent à celui du dopage substitutionnel au cuivre. La deuxième contribution de ce travail a porté sur la réalisation par pulvérisation cathodique rf-magnétron de films minces $BiVO_4$ dopés par des éléments Mo et Cu dans des conditions définies par l'atmosphère de dépôt à base de pressions partielles d'un gaz Ar ou d'un mélange Ar / O_2 et des températures de substrats variables jusqu'à 450 ° C. Les paramètres optimaux de dépôt ont été identifiés pour réaliser des films cristallins à faible rugosité de surfaces ou à morphologies en nano-îlots. Des études photocatalytiques utilisant des films minces dopés ont été effectuées par la dégradation des colorants organiques (MO) sous rayonnement visible. Ces études montrent que la morphologie des films avec des surfaces spécifiques importante est aussi un facteur d'amplification des performances photocatalytiques des films minces dopés Me-$BiVO_4$.

Mots clés : Dopage métallique, $BiVO_4$, Oxydes semiconducteurs, Photocatalyse, Nanopoudres, films minces, sol-gel, broyage planétaire haute énergie, pulvérisation cathodique, colorants organiques, RPE, DRX, Raman, XPS, MET, FE-SEM.

Abstract

The thesis work is devoted to the synthesis and investigations of the physical properties of a family of semiconducting oxides based on $BiVO_4$ as nanostructures or thin films including a metal doping (Metal = Cu, Mo and Ag) in order to achieve effective photocatalysts under visible light irradiation. The synthesis of doped nanopowders was carried out by the techniques of high-energy ball milling and sol-gel. The resulting materials and doping effects were characterized on the structural, electronic and optical properties. By combining XPS, Raman and EPR studies, it was shown that the substitutional doping is achieved for the doping ions (Cu, Mo) being located in the lattice sites of the vanadium ions. Oppositely, Ag doping contributes to form Ag metal clusters located on the surface of nanoparticles of BiVO4 thereby forming nanocomposites. Photocatalytic reactions were studied by the degradation of organic dyes (Acid Blue 113, methyl orange (MO)) in low concentrated solutions. Among the doping ions substituted in the host matrices, Cu^{2+} showed better photocatalytic performances because of an increase in the density of photo-generated charges and similar effect on the electrical conductivity compared to the case of Mo doping. In the Ag based nanocomposites, the formation of metal clusters seems to induce surface resonance plasmonic effects that improve the efficiency of photocatalytic reactions with respect to the activity demonstrated for substitutional doping. The second contribution of the thesis work was devoted to $BiVO_4$ thin films deposition by rf sputtering process with Mo and Cu doping under defined synthesis conditions such as the partial pressures of Ar gas or an Ar / O2 mixture and varying the substrate temperatures up to 450 ° C. The optimal deposition parameters have been identified to achieve crystalline films with low roughness surface or alternatively with nano-islands morphologies. Photocatalytic studies using doped thin films were carried out through the degradation of organic dyes (MO) under visible light irradiation. The performed measurements show that the film morphology with high specific surface is also a key factor in the amplification of photocatalytic reactions in metal doped thin films.

Key Words: Metal doping, $BiVO_4$, Semiconducting oxides, Photocatalyst, Nanopowders, Thin films, Solgel, High energy ball mill, rf-sputtering, Organic dyes, EPR, XRD, Raman, XPS, FE-SEM, TEM

L'Université Bretagne Loire

ABSTRACT

The thesis work is devoted to the synthesis and investigations of the physical properties of a family of semiconducting oxides based on $BiVO_4$ as nanostructures or thin films including a metal doping (Metal = Cu, Mo and Ag) in order to achieve effective photocatalysts under visible light irradiation. The synthesis of doped nanopowders was carried out by the techniques of high-energy ball milling and sol-gel. The resulting materials and doping effects were characterized on the structural, electronic and optical properties. By combining XPS, Raman and EPR studies, it was shown that the substitutional doping is achieved for the doping ions (Cu, Mo) being located in the lattice sites of the vanadium ions. Oppositely, Ag doping contributes to form Ag metal clusters located on the surface of nanoparticles of $BiVO_4$ thereby forming nanocomposites. Photocatalytic reactions were studied by the degradation of organic dyes (Acid Blue 113, methyl orange (MO)) in low concentrated solutions. Among the doping ions substituted in the host matrices, Cu^{2+} showed better photocatalytic performances because of an increase in the density of photo-generated charges and similar effect on the electrical conductivity compared to the case of Mo doping. In the Ag based nanocomposites, the formation of metal clusters seems to induce surface resonance plasmonic effect that improve the efficiency of photocatalytic reactions with respect to the activity demonstrated for substitutional doping. The second contribution of the thesis work was devoted to $BiVO_4$ thin films deposition by rf sputtering process with Mo and Cu doping under defined synthesis conditions such as the partial pressures of Ar gas or an Ar / O_2 mixture and varying the substrate temperatures up to 450 °C. The optimal deposition parameters have been identified to achieve crystalline films with low thickness and roughness surface or alternatively with nano-islands morphologies. Photocatalytic studies using doped thin films were carried out through the degradation of organic dyes (MO) under visible light irradiation. The performed measurements show that the film morphology with high specific surface is also a key factor in the amplification of photocatalytic reactions in metal doped thin films.

Key Words: Metal doping, $BiVO_4$, Semiconducting oxides, Photocatalyst, Nanopowders, Thin films, Solgel, High energy ball mill, rf-sputtering, Organic dyes, EPR, XRD, Raman, XPS, FE-SEM, TEM.

ACKNOWLEDGEMENT

This work has been performed in the section of solid state electronics, electrical engineering department (SEES-IE), Cinvestav-IPN, Mexico and Institute of molecules and materials (IMMM), University of Maine, Le Mans, France during Jan 2012-Dec 2015. I express my deepest gratitude for financial support from CONACYT for four years doctoral scholarship and as well as 3MPL doctoral school for one year financial support. I should also express my gratitude to number of people in Mexico and France, without whom it wouldn't have been possible for me to undertake this rigorous academic programme. During these 4 years, I have learned great things not only about science and academics, but also about the life, the truth, and the faith. It was a quite tough lesson especially in the beginning, but I have to say that I have truly enjoyed every moment of learning and I am so grateful to have these kinds of experience in my life.

This is indeed a great opportunity to thank my research supervisor **Prof. Velumani Subramanian**, who gave me co-title PhD opportunity and more challenges in various academic and research exposures and enhanced my receptivity through constant encouragements in whole lot of academic and research events. On other hand, with great pleasure and gratitude, I express my sincere thanks to my co-graduation research co-supervisor **Prof. Abdel Hadi Kassiba** from France for his continuous guidance and encouragement throughout my research work. His words on life, ideas on research and views on academics would always reside with me in all my endeavours in my life.

I extend my sincere thanks and gratitude to my committee members, Prof. María de la Luz Olvera, Prof. Mauricio López Ortega, Prof. Ramón Pena and Prof. Hasihiro Mashumoto from Cinvestav-IPN, Mexico for their valuable time spent for meetings and scientific discussions. Especially Prof. María de la Luz and Prof. Maldonado for their generosity to help me in providing required equipment for this project which is greatly appreciated. I will extend my gratitude to few more knowledgeable committee Prof. Alain Bulou, Prof. Jens Dittmer and Prof. Alain Gibaud who helped me by scientific advices and support in France.

Appreciation would be an essential factor to motivate people to break their present boundaries and take them to the higher possibilities. In that sense, I express my sincere thanks to my friend and supporter Dr. Goldie Oza for his continuous support and valuable scientific as well as philosophical conversations, made me feel confident in my research career and life.

Thanks to all secretaries in Cinvestav-IPN, Mexico and University of Maine for their hearty smile and care, that made me comfortable to work in these research institutes. Appreciation will be essential for auxiliary people help. I would like to thank Eng. Mathieu Edely, for his guidance on handling the experiments and RF sputtering equipment. I extent my thanks to Dr. Nicolas Errien for handling characterization techniques. I express many thanks to Eng. Cyrille Galven, Anne-Marie for

powder XRD analysis and Dr. Marie-Pierre Crosnier-Lopez and Dr. Nadia Haneche for HRTEM analysis in Universite du Maine. I am also indebted to Alvaro Pascual Angeles for HRTEM, Prof. Sergio Tomas for XPS analysis, Miguel Luna, Miguel Galvan Arellano, Adolfo Tavira Fuentes, Marcela Guerrero and Alejandra Garcia Sotelo for their technical assistance without whom it would have not been possible for me to complete my research.

I express my cheerful thanks to my friends Karthik, Fernando Pena, Eswar, Vinoth, Ateet, Angelica, Gayathri, Tauqeer, Archana, Juan, Ophelie, Romain, Mariusz, Dan and Alla for their chitchat and encouragement throughout my PhD. I sincerely extent my thanks to my friends and colleagues Ravichandran, Rohini, Latha, Aruna and my co-title colleagues Pablo Reyes, Marco, Jesus, Carlos, Karolina and Mina.

At last but not least, I would like to pay high regards to my beloved parents for sincere encouragement and unconditional support to take over these vigorous academic studies in abroad, without them it would be impossible to achieve. My special thanks to my siblings especially my sister Prema Santhi; I can't even imagine this without their support towards my academic journey. With their consistent love, support, and prayers, I could be able to go through all the hardships.

CONTENT

LIST OF TABLES

LIST OF FIGURES

Abbreviations:

μm: Micrometre

s: Work function of semiconductor

m: Work function of metal

α: Absorption coefficient

λ: Wavelength of light

υ: Frequency

ε': Real part of dielectric function

ε": Imaginary part of dielectric function

σ_{dc}: DC conductively

τ_{max}: Relaxation time

°C: Degree Celsius

AC113: Acid blue 113 dye

AOP: Advanced oxidation process

Ag: Silver

Ar: Argon

BET: Brunauer-Emmett –Teller

BF: Bright field

Bi: Bismuth

Bi_2O_3: Bismuth oxide

$Bi(NO_3)_3.5H_2O$: Bismuth nitrate penta hydrate

$BiVO_4$: Bismuth vanadate

BPR: Ball per powder ratio

C: Concentration

CB: Conduction band

CO_2: Carbon dioxide

CS: Case study

Cu: Copper

CuO: Copper oxide

D: Crystallite size

DC: Direct current

DE: Degradation efficiency

DFT:	Density functional theory
DRS:	Diffuse Reflectance spectroscopy
E_f:	Fermi energy
E_g:	Band gap energy
EDAX:	Energy dispersive analysis of X-rays
EPR:	Electron paramagnetron spectroscopy
eV:	Electron volt
FE-SEM:	Field emission scanning electron microscopy
FFT:	Fast Fourier Transform
FT-IT:	Fourier transform infrared
FWHM:	Full-width at half- maximum
g:	Lande g-factor
h:	Hours
h^+:	Hole
H_2O:	Water
H_2O_2:	Hydrogen peroxide
HN:	Havriliak-Negami
HNO_3:	Nitric acid
HRTEM:	High resolution transmission electron microscopy
Hz:	Hertz
JCPDS:	Joint committee on powder diffraction standards
k:	Degradation rate constant
K:	Kelvin
L:	Litre
LSPR:	Localized surface plasmon resonance
M:	Mol per Litre
MB:	Methylene blue
mbar:	Milli bar
min:	Minute
mL:	Millilitre
mol:	Mole
Mo:	Molybdenum
MO:	Methyl orange
N:	Nitrogen

O:	Oxygen
O^-_2:	Superoxide anions
OH:	Hydroxyl group
PC:	Photocatalyst
Pd:	Palladium
PL:	Photoluminescence
Pt:	Platinum
R:	Reflectance
rf :	Radio frequency
RhB:	Rhodamine B
s:	Second
SAED:	Selected area electron diffraction
Si:	Silicon
STEM:	Scanning transmission electron
T:	Temperature
t:	Time
T_c :	Critical temperature
TEM:	Transmission electron microscopy
Ti:	Titanium
TiO_2:	Titanium dioxide
UV:	Ultra-violet
V:	Vanadium
V_2O_5:	Vanadium oxide
Vis:	Visible
VB:	Valence band
VBM:	Valence band maximum
WO_3:	Tungsten trioxide
XPS:	X-ray photoelectron spectroscopy microscopy
XRD:	X-ray diffraction
ZnO:	Zinc oxide

Chapter-1

Introduction

1.1 General context

Water is the most basic natural resource in this world embracing over 70 % of the earth's surface. In spite of this, the accessibility of safe drinking water is crucial for the survival of mankind as well as animals. To date, water crisis is the most important concern of a modern society. According to World Economic Forum 2015, water crisis is the major global risk causing a big impact to a society as shown in Fig.1.1. Continuous developments or evolution of mankind or globalization pollutes the water by dumping of toxic wastes, radioactive materials, etc. Moreover, drinking water is rapidly decreasing by detrimentally affecting the quality and quantity of water. Currently, 760 million people i.e. one in nine people, in Africa and South America have a least access to a safe drinking water [1]. This water scarcity impact/problem will increase to 43.3% in next 10 years. The continuous growth of population in the world and intern diminishing water resources consequently leads to inadequate sanitation, inevitably increasing the levels of pathogens in water. More than 840,000 people per year are dying due to water related diseases caused by inadequate drinking water, sanitation etc. In short, water quality and human existence are closely colligated. Targeting these tremendous environmental problems related to the remediation of hazardous wastes, toxic heavy metals and materials, and contaminated ground waters is most essential for human existence. Considering the above cases, it is necessary to have the proper measures to protect our water resources and to achieve drinking water quality. This can be achieved by effectively enforcing various sustainable water treatments to meet the urgent global need for clean water.

In order to address these significant problems such as hazardous waste, toxic heavy metals and organic pollutants, an extensive research is underway to develop and produce enormous functional materials combined with advanced analytical, biochemical and physicochemical methods for detection and elimination of hazardous chemical compounds from water as well as from air and soil also. One of the physicochemical processes includes photocatalytic reactions by employing various photoactive semiconducting oxides for the destruction or transformation of hazardous chemical wastes from the natural resources. The above process is extremely promising especially in water purification and treatment.

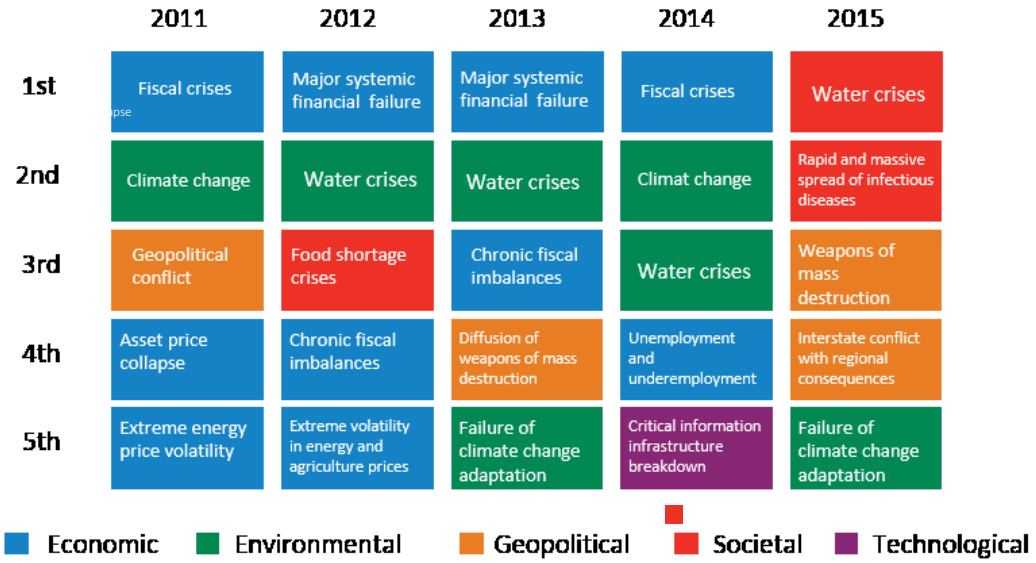

Fig.1.1. Top 5 global risks in the terms of impact on societal and environmental areas from last 2011-2015. Source: Global risks reports on 2011-2015, World Economic Forum.

1.2 Photocatalysis

The *photocatalysis* can be defined as the acceleration of a chemical reaction by the presence of a catalyst under photo irradiation. From last two decades, heterogeneous photocatalysis with photoactive semiconducting oxide catalysts has pulled great attention on its efficacy in the area of applications. As far as the current scenario of energy and environment stipulation is concerned, the need for the development of efficient photocatalytic materials is crucial. Accordingly, the distinct features of a photocatalyst can be divided into two major applications as illustrated in Fig.1.2.

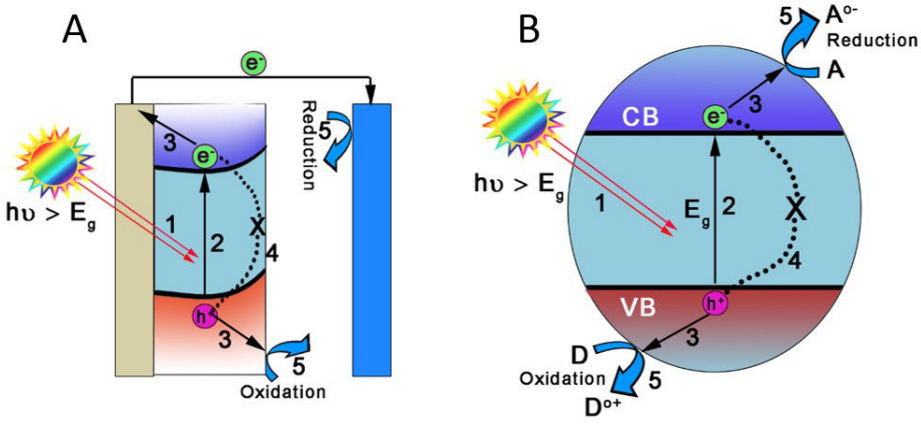

Fig.1.2: Scheme illustration of (A) a particulate photocatalyst, (B) a photoelectrochemical (PEC) cell with an n-type photoelectrode

The first strategy concerns the renewable energy source known as water splitting or photo electrochemical (PEC) applications. In this process, a photocatalyst can split water into oxygen and hydrogen molecules, which is an excellent environment friendly method of generating hydrogen fuels without any residual chemical pollutants (CO_2 etc.) One of the earlier pioneering work on PEC studies were reported by Honda and A. Fijushima in 1972 with analogy of natural photosynthesis by using TiO_2 thin films [2].

The second approach is devoted to environmental remediation applications known as photodegradation. In this frame, a photocatalyst can decompose the organic pollutants in waste splitting into H_2O and CO_2. Such process is also known as Advance Oxidation Processes (AOPs), which can be effectively utilized to clean the environment such as water, air or soil. One of the first references for AOPs was done by Glaze in 1987 which involve the generation of hydroxyl radicals in sufficient quantity for water purification [3].

The photocatalysis process is based on following steps: (1) light absorption, (2) charge separation, (3) charge migration, (4) charge recombination and (5) redox reactions as shown in Fig.1.2. The mechanism of photocatalysis will be exhaustively explained in the upcoming section. In photodecomposition system, the freestanding photocatalyst in the form of either powders or thin films are used in a solution with organic pollutants. Whereas in PEC system, photocatalyst can be either in pellet or film form which will be fixed at reactor bed as an electrode and considering water as an electrolyte.

Therefore, understanding the photocatalytic behaviour for the effective utilization of semiconducting material and exploiting its properties would be interesting to develop potential materials for the photocatalytic applications.

1.3. Mechanism of Photocatalysis

The compound semiconducting materials (e.g., TiO_2, ZnO, $BiVO_4$, Fe_2O_3, CdS and ZnS etc.) act as a key elements for light-induced redox processes as shown in Fig. 1.3. In case of semiconductor photocatalysts upon light irradiation, absorption of photons with energy greater than the bandgap energy, induce the formation of electron (e^-) – hole (h^+) pairs, where e^- are promoted into the conduction band (CB) while h^+ remain into the valence band (VB). These electron–hole pairs reach the catalyst surface and contribute to redox reactions with sorbed species. The positively charged holes react either with electron donors in the solution or with hydroxide (OH^-) ions to produce highly oxidizing species like hydroxyl ion (OH*). And the

electrons (e^-) in the conduction band, which interact with adsorbed oxygen molecules and contribute to generate superoxide radicals (O_2^{*-}).

In fact, a portion of the photogenerated charge carriers is subjected to the recombination in the bulk and on the surface, dissipating the excess of energy in radiative or non-radiative processes. Charge recombination is believed to be a major loss of the excited charge carriers and a critical factor that limits the solar-to-chemical energy conversion efficiency for semiconductor photocatalysts. The charge carriers have a recombination time in the order of 10^{-9} s, while the chemical interaction with adsorbed species has a longer time scale between 10^{-8} and 10^{-3} s. Therefore, charge recombination can reach up to 90% within a period of 10 ns after generation.

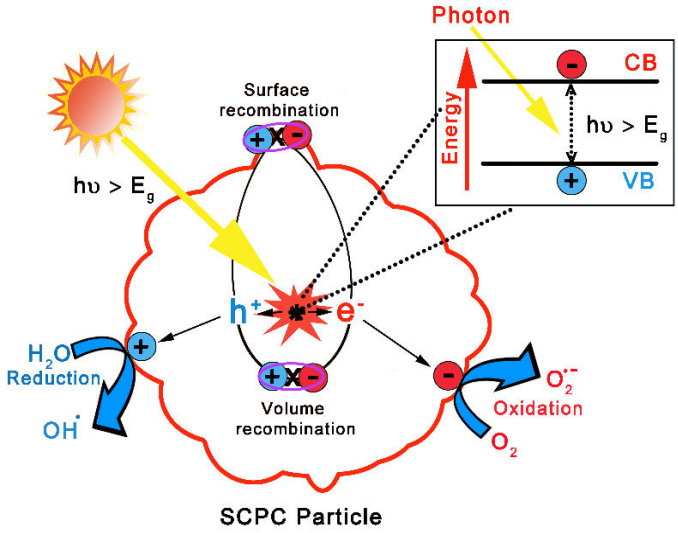

Fig.1.3. Photocatalytic process in a typical semiconductor photocatalyst (SCPC).

1.3.1 Photocatalysis reactions

When the photocatalytic process is applied to the decomposition of organic system, several reactions occur as outlined. First, the absorption/absorbed photons with required energies by semiconductor photocatalyst (SCPC) creates photogenerated carriers such as electron e_{CB}^- in CB whereas hole h_{VB}^+ in VB:

$$SCPC + h\upsilon \rightarrow \ h_{VB}^+ + \ e_{CB}^- \qquad \rightarrow (1.1)$$

In the (CB), the excited electrons induce the formation of superoxide radical anion:

$$O_2 \ + \ e_{CB}^- \ \rightarrow \ O_2^{*-} \qquad \rightarrow (1.2)$$

In the VB, the holes contribute to the neutralization of OH- group into hydroxyl ion ($OH^{\bullet}$) according to the below reaction:

$$H_2O + h_{VB}^{+} \rightarrow OH^{-} + H^{+} \quad \Rightarrow h_{VB}^{+} + OH^{-} \rightarrow OH^{*} \qquad \rightarrow (1.3)$$

The hydroxyl radical (OH^{*}) and superoxide radical anions (O_2^{*-}) are the primary oxidizing species in the photocatalytic reactions processes (Fig.1.4). These oxidative reactions cause the degradation of organic pollutants (R) via successive attack by $OH^{\bullet}$ radicals:

$$R + OH^{*} \rightarrow R^{*} + H_2O \qquad \rightarrow (1.4)$$

Or by direct reaction with holes given by products degradation:

$$R + h_{VB}^{+} \rightarrow R^{*+} \rightarrow \text{Degradation products} \qquad \rightarrow (1.5)$$

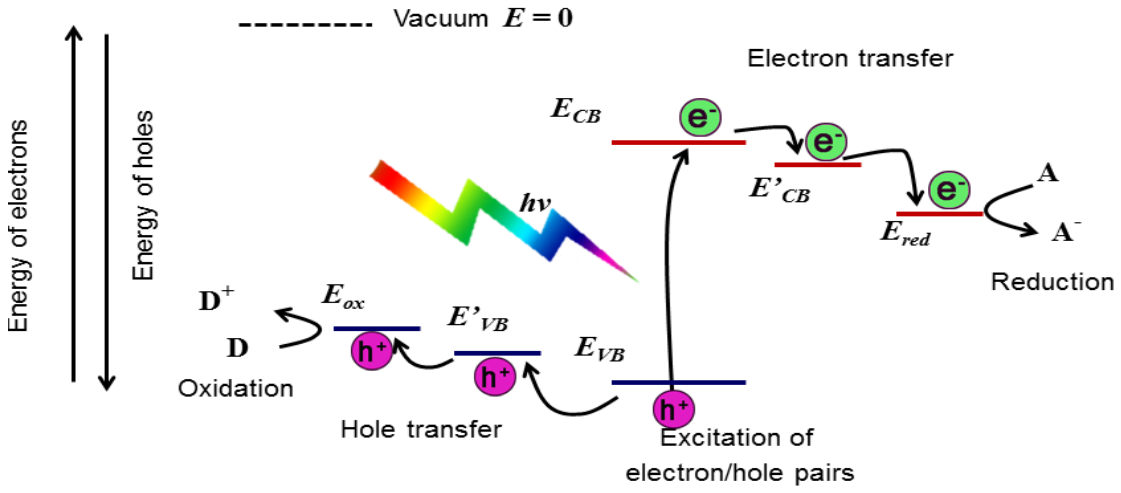

Fig.1.4. Generation and transfer of photo-induced charge carrier's redox reaction in typical photocatalysis process.

1.4. Photocatalytic process in the prospective of semiconductor properties

Many factors affect the photoreactions and their efficiencies, such as material type, crystal structure, particle size, morphology, optical properties, metal doping/loading, pH value, temperature etc.

1.4.1. Energy bandgap (E_g) and edge positions (LUMO and HOMO)

The dominant factors for an efficient photocatalysts for water splitting or contaminants degradation mainly depends on the bandgap which defines the spectral range of the absorbed radiations and energy band edge positions of the materials compared to the redox reaction potentials of water. Fig.1.5 shows the relationship between band structure of semiconductor and band edge positions with respect to the vacuum level and the normal hydrogen electrode (NHE) level for selected semiconductors at zero pH for metal oxides, sulphates, carbides chalcogenides and silicon.

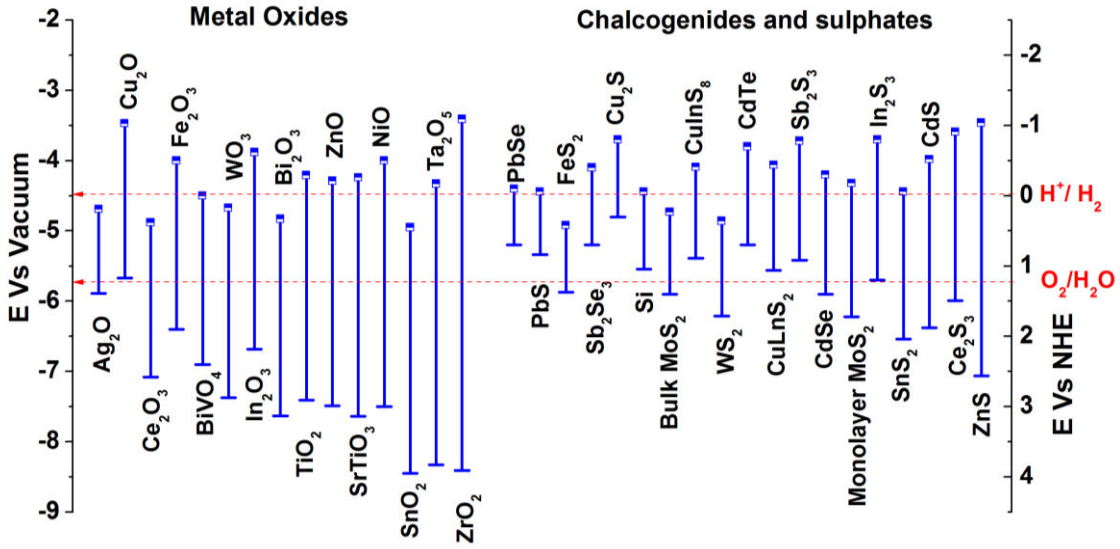

Fig.1.5. Relationship between band structure of semiconductor and band edge positions with respect to the vacuum level and the NHE for selected semiconductors at zero pH (a) oxides (b) sulphates and carbides chalcogenides and silicon. The top line cap ■ represents the conduction band edges; the bottom line cap – present the valence band edges. The top names indicate the semiconductor material and length of each vertical line indicates bandgap value correspondingly. The two dashed lines indicate the water redox reaction potentials for H^+/H_2 and O_2/H_2O respectively.

The energy band positions of the photocatalyst determine its spectral absorption wavelength and also determines efficiency of specific reduction or oxidation reactions. Moreover, the electronic band edge position determines the aqueous stability of photocatalyst by statistically determining the vulnerability towards photocorrosion during solar fuel generation [4]. Generally smaller bandgap leads to higher vulnerability of photocorrosion. Although some narrow bandgap semiconductors such as Si, Cu_2O, CdSe, $CuInSe_2$ and GaAs have an advantage of wide light absorption spectral range, they are subjected to photocorrosion when acting as the photoelectrodes during water splitting by photocatalytic reactions. Basically, in the view of thermodynamics, if the electrochemical potential of anodic

decomposition is lower with respect to the valence band maximum (VBM) of a semiconductor and if the electrochemical potential of cathodic decomposition is higher with respect to the conduction band minimum (CBM) level of semiconductor photocatalyst, the chances of photocorrosion is almost null [5,6].

Furthermore, the electronic band structure determines the spectral range of light absorption of semiconductor and the theoretical maximum solar-to-hydrogen (STH) efficiency as shown in Fig.1.6. For example, the theoretical maximum STH efficiency is only 0.22% for $SrTiO_3$ (E_g = 3.7 eV), 1.3% for anatase TiO_2 (E_g = 3.2 eV), 9.1% for (s-m) $BiVO_4$ and 12.9% for Fe_2O_3. The most effective approach to increase the conversion efficiency is to reduce the bandgap to extend the light absorption spectral range into the visible-light region (~43% of total solar radiation) and even near-infrared light region (~80% of total solar radiation). However, the bandgap must be large enough to meet the thermodynamics and kinetics requirements for water splitting where minimum energy is required to overcome the standard Gibbs free energy change (1.23 eV) for water splitting plus the thermodynamic losses (0.3–0.5 eV) [7]. In the viewpoint of kinetics, a potential of 0.4–0.6 eV is required to enable a fast reaction [8]. Therefore, an ideal and optimal bandgap must be around 1.9–2.3 eV for solar water splitting [6]. TiO_2 is a benchmark semiconductor for photocatalysis, but it has a wide bandgap (3.2 eV for anatase). Hence, it can only absorb UV light, which is less than 4-6% of total solar radiation. Whereas, monoclinic $BiVO_4$ and Fe_2O_3 has energy bandgaps of 2.2, 2.4 eV respectively, which is near to the optimal bandgap. Fe_2O_3 has a major drawback as compared to $BiVO_4$, i.e. its low conduction band level for H^+/H_2 reduction potential of water[9]. Moreover it's not very stable in acidic solutions as well. Therefore, monoclinic $BiVO_4$ has optimal bandgap with the redox potential is exactly just above H_2/H^+ and enough below O_2/O^{-2} levels.

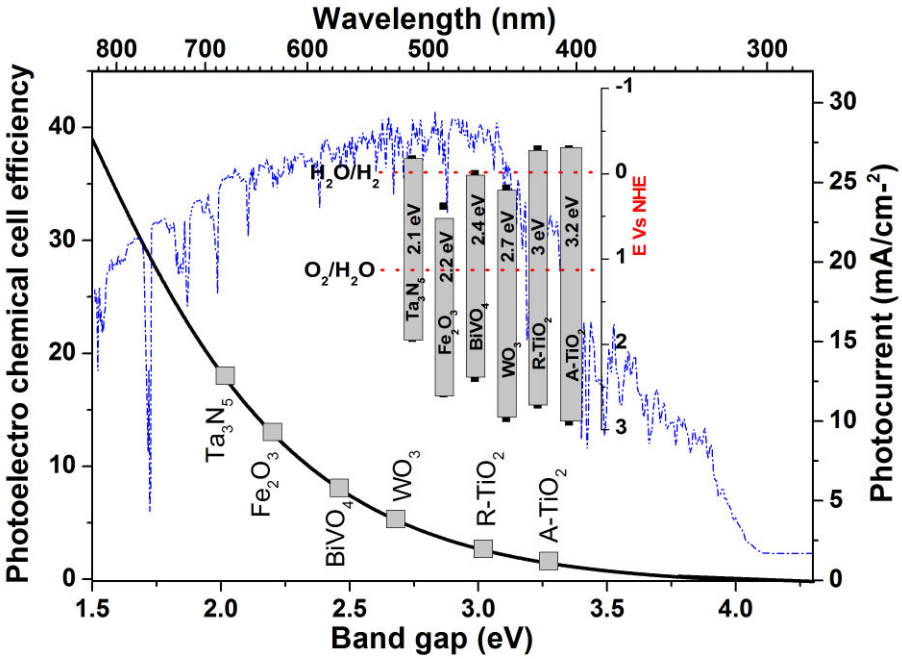

Fig.1.6. Dependence of the theoretical maximum solar-to-hydrogen (STH) efficiency and the photocurrent density of photoelectrodes on bandgap of semiconductor materials under AM 1.5 G irradiation (100 mW cm^{-2}) and blue line on background indicates solar spectrum of with respect to wavelength. Inset shows energy bandgap and band edges locations correspondingly [6].

1.4.2. Crystal structure and atomic positions

Crystal structure determines the electronic band structure and physicochemical properties of semiconductor. For instance $BiVO_4$ adopts commonly scheelite monoclinic (s-m) and scheelite tetragonal (s-t) phases. (s–m), (s-t) $BiVO_4$ are used for photocatalysis which has energy bandgaps of 2.4 and 2.9 eV respectively. Monoclinic scheelite absorbs more range of light as compared to tetragonal and more suitable for PC applications. In fact, not only (s-m) $BiVO_4$ possesses narrow bandgap to harvest visible light driven photocatalysis, but also shows distorted Bi-O polyhedron with $6s^2$ lone pairs of Bi^{3+} which induces Bi-O shorter bonds in BiO_8 dodecahedron structure as compared to (s-t) $BiVO_4$. On other instance, TiO_2 anatase and rutile phases are commonly used as photocatalysts with bandgaps of 3.2 eV and 3.0 eV, respectively. Although rutile TiO_2 can capture more light due to a narrower bandgap E_g, exhibiting lower photocatalytic activity than anatase phase. Both of them are composed of TiO_6 octahedra with each Ti^{4+} ion surrounded by six O^{2-} ions. However, rutile octahedra share two edges, while anatase octahedra share four edges [10]. This possess a reduced symmetry with changes in longer Ti–Ti distance and shorter Ti–O distance in anatase TiO_2, that benefits in terms of the charge dynamics such as better charge carrier mobility and longer charge carrier

lifetime [11]. Thus, significant influence on the photocatalytic/photoelectrochemical performance of semiconductor lies in its crystal structure and the peculiarities of molecular bonding.

1.4.3. Size effect on photocatalytic activity

The PC performance of semiconductor is strongly dependent upon the specific surface which is defined by nanoscale grain sizes or nanostructures. It has been demonstrated that a large surface area is a basic requirement for an effective photocatalyst. When the size of materials falls into the nanoscale range, quantum effects comes to play, so that nanomaterials may exhibit completely different properties as compared to bulk materials. As the sizes of particles are reduced down, the percentage of atoms or ions exposed on the surface is massively increased, leading to an increase in the surface-to-volume ratio,thus increasing the number of active sites for catalytic reactions. As a result, the bandgap increases and the band edges shift to yield larger redox potentials, which increases larger driving forces for charge carriers with high mobility. Therefore, nanoscale materials exhibit a high surface and photocatalytic activity that does not exist in the bulk.

Indeed, the charge carriers which can be efficiently photogenerated within the bulk materials migrate at the surface of the catalyst during the process of heterogeneous catalysis leading to the chemical degradation of pollutants. Generally, in bulk semiconductor catalyst, only one charge type, either the holes or electrons are available for photoactivated reactions due to band bending [12,13]. However, in very small semiconducting particle, both species are present on the surface and activate efficiently the PC process. Therefore, careful consideration of both oxidative and reductive paths is required.

H. Golmojdeh et al. demonstrated that synthesis of nanoparticles with precipitation method and in presence of ETDA creates specific surface as high as 115 m^2/g which provoke better degradation of MB dye solution [14]. Sun et al. reported that synthesized (s-m) $BiVO_4$ nanoparticles with the help of EDTA as a chelating agent by hydrothermal technique has shown better photocatalytic performance for photochemical degradation of phenol solution under visible light illumination as compared to the bulk $BiVO_4$ synthesized by the conventional un-modified hydrothermal process [15]. Similarly for another PC material such as molybdenum disulfide (MoS_2) is a nontoxic and earth-abundant semiconductor with a potential to replace precious metal catalysts. However, bulk MoS_2 has a poor catalytic activity toward hydrogen evolution reaction (HER) while nanosized or monolayer MoS_2 is very active for the same process [16]. Therefore, both the size and the surface effects are of great importance in

photocatalysis. For nanostructured semiconductors, however, the volume or bulk recombinations of a material is reduced as the size is reduced, but the surface and interfacial charge recombination may increase considerably.

1.4.4. Morphology effect

As compared to zero dimensional (0D) nano-objects, 1D nanomaterials possess better efficiency in PC process. Nanowires, nanorods, nanotubes, nanofibers and nanobelts are typical 1D architecture and the longitudinal mean free path favours the charge transport along the longitudinal direction in a 1D single-crystalline nanomaterial [17]. The charge separation in (0D) nanoparticles is not as effective as that in bulk because of the confined space in the nanostructure [18]. This can be alleviated in 1D nanostructures where the charge carriers are less localized compared to 0D nanoparticles [19]. So that 1D nanostructured semiconductors are of particular interest in solar energy conversion devices. The (s-m) $BiVO_4$ nanorods with diameters of 15–20 nm possess a large specific surface area up to 28.2 m^2/g leading to visible light driven PC of $BiVO_4$ nanorods better than the commercial Degussa (P25) in the degradation of rhodamine B and phenol [20]. Several techniques such as microemulsions method [21], hydrothermal [20] and solvothermal techniques [22] have been developed for the synthesis of (s-m) $BiVO_4$ as 1D nanorods or nanoplates. Self-assembled nanotubes synthesised by solvothermal technique have shown more than two times higher photoactivity for O_2 evolution than demonstrated by bulk $BiVO_4$ [22]. Similarly $BiVO_4$ nanobelts [23] and nanofibers [24] shows quite efficient PC activity. Such behaviour was also shown for 0D nanosphere counterparts [17]. Another advantage of 1D nanomaterials is favoured by the light trapping and scattering between nanowires. Thus, Y. Pihose et al. obtain high photocurrent of 3.2 mA cm^{-2} at 1.23 V_{RHE} for $WO_3/BiVO_4$ heterojunction photoanode based on WO_3 nanorods (NRs) fabricated by Glancing Angle Deposition (GLAD) technique[25]. Similarly, $BiVO_4$ decorated by nano-coating of Co-Pt co-catalyst as shown in Fig.1.7(a), dramatically increases the path length of the incident light, which is different from the large outward reflection as seen in a planar electrode. For other morphologies, 2D nanomaterials refer to materials such as freestanding nanosheets or planar films deposited on a substrate as shown in Fig.1.7(b). In most cases, the freestanding nanosheets as photocatalysts act in the same way as 1D nanostructures discussed above. Compared to 1D nanostructures, the two large-area dominant surfaces of 2D single-crystalline nanosheets can be engineered to a highly reactive facet for photocatalysis. The nanoplate (2D) morphology of $BiVO_4$ synthesized by green route solvothermal method with ethanol and water mixture has shown higher photodegradation for RhB dyes under visible

light irradiation as compared to 3D flower like and bulk particles of $BiVO_4$ with low surface area 11.35m^2/g [26]. On the other hand, 20-40 nm thick (m-s) $BiVO_4$ nanosheets prepared by hydrothermal technique, where Bi $(NO_3)_3 \cdot 5H_2O$ and NH_4VO_3 used as precursors, sodium dodecyl benzene sulfonate (SDBS) was used as the morphology-directing agent [27]. For 3D template with highly ordered porous structures, interesting PC efficiency occurs from their larger surface area (Fig.1.7(C)). Moreover, negligible bulk charges recombinations, hole interface transfer and multiple light scattering, enables more light to be harvested and also possess continuous pore channels that facilitate the transfer of reactant molecules. Generally, these structures are fabricated by using ordered spheres replica templates by nanocasting method. However; achieving such 3D opal or porous structures are too complicated. However, Guisheng Li et al. fabricated ordered mesoporous $BiVO_4$ which shows a superior photocatalytic performance in the photochemical degradation of methylene blue and photocatalytic oxidation of NO gas in air under visible light irradiation [28]. Similarly, 2 at% of Mo doped $BiVO_4$ with the shape of 3D ordered porous architecture with pore sizes in the range 30-50 nm has demonstrated 40% IPEC efficiency with 2 mA/cm^2 photocurrent [29]. M. Zhou also reported comparative studies of the effect of porous sizes in 3D ordered marcoporous structure of $BiVO_4$ with 200 nm to 1 μm[30]. As a matter of fact, smaller porous size architectures show higher photocurrent and gradual reduction occurs with increment of porous size. Such effects are due to high surface charge migration, suppression of surface recombination and easy interface charge transfer.

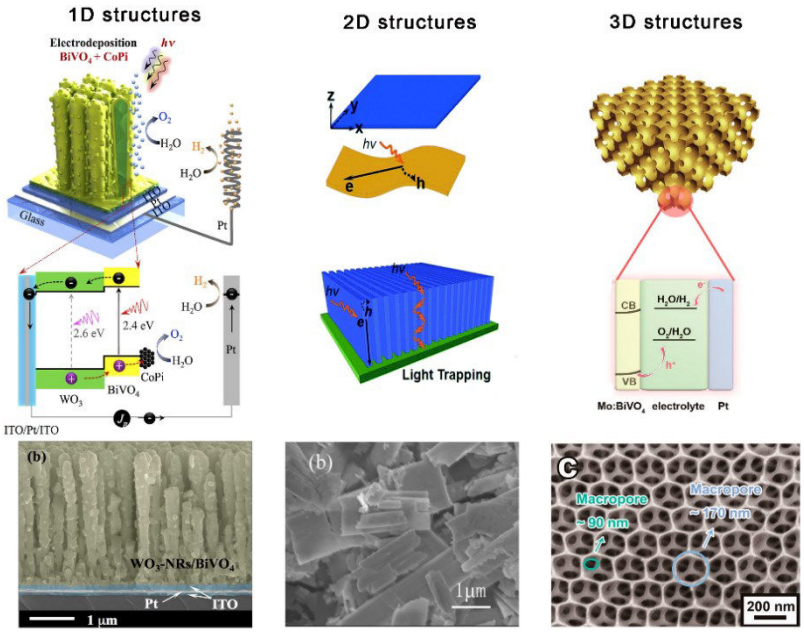

Fig.1.7. Light scattering/trapping and charge transport in nanoscale architectures for single material as the photoelectrode or the suspension photocatalyst. (a) 1D nanostructures[25], (b) 2D nanosheets and films[26], (c) 3D opal or ordered porous structures[30].

1.4.5. pH value

pH values of the precursor solution tend to have the greater influence on the phase and morphology of photocatalytic materials. G. Tan et al [31] studied the effect of pH on morphologies of $BiVO_4$ powders prepared via a microwave hydrothermal method. Under strong acidic conditions (pH $\leqslant$0.59), it was found that (m-s)-$BiVO_4$ crystals with high crystallinity, later (t-z) $BiVO_4$ started appearing and strengthen until pH 2.55. After that (m-s) $BiVO_4$ appeared again, So that the mixed phases of (m-s) $BiVO_4$ and (t-z) $BiVO_4$ appeared and continued for the pH range of 0.70 to 4.26. Later in the wide range of pH region from 4.26 to 9.76, only pure (m-s) $BiVO_4$ phase could be obtained with different morphologies. He reported that the nucleation rate and the growth rate reached the balance at pH 6.47 where high crystallinity and complete crystal growth was obtained. It possess smaller particles with spherical shape have strong absorption in the visible-light regions. They have also reported that PC performance based on the degradation rate of Rhodamine B dye (RhB) solution within 5h under simulated sunlight irradiation, where the catalytic activity order of the various catalyst samples are $BiVO_4$ (pH 0.59, 4.26 to 9.76, monoclinic phase) > $BiVO_4$ (pH 0.70 to 4.26 and 10.44, mixed phase) > BiVO4 (pH 2.55, tetragonal phase). Similarly, A. Zhang et al [32] has also reported the effect of pH on hydrothermally synthesised $BiVO_4$ powders. For pH less than 5.3, he has observed a mixed phases of monoclinic and tetragonal with whereas only monoclinic phase in both neutral and alkaline pH. Even morphologies were varied from small particle with smooth surface (1.7 pH) to aggregation of small crystals (3.2 pH) to slice like flower shapes (5.3 pH) to rod like with small portion of slices shape (pH 6.9) to spherical particle with agglomeration at pH 8.8 and larger agglomeration at pH at 11.5. The photocatalytic studies for the degradation of methyl orange dye solution, where neutral pH 6.9 has shown highest degradation 98.5% for 60 min under visible light irradiation.

1.4.6. Oxygen vacancies

Qin et al. [33] demonstrated the improvement of photocurrent of electrochemically synthesized (m-s) $BiVO_4$ treated by using $NaBH_4$ in PEC applications leading to reduced $BiVO_4$ with high donor density due to reduction of V^{5+} to V^{4+}. This oxygen deficiency improves the separation of electron hole pairs and enhances the photocurrent efficiently. These oxygen

vacancies can be created by several approaches such as electrochemical reduction, hydrogenation, surface charge defects etc. However, oxygen vacancy has both positive and negative aspects, because from one side, it is beneficial to the adsorption of reactants and then enhances electron–hole separation. But on the other side, vanadium reduction as V^{4+} is similar to conventional doping. Such V^{4+} ions with larger radius provoke lattice distortions, reducing the effective diffusion length of holes. Hence, an excess of V^{4+} is detrimental to the photocatalytic performance of (m-s) $BiVO_4$. Also, suitable m-$BiVO_4$ with both excellent absorbability and photocatalytic property can be achieved by adjusting the content of V^{4+}. Nevertheless, it remains difficult to prepare m-$BiVO_4$ with abundant V^{4+} directly by using chemical methods as compared to physical methods, where high energy ball milling technique creates large amount of V^{4+} ions leading to surface charge defects on typical 50 nm sized spherical particles [34,35]

1.5. Concept of plasmon enhanced photocatalytic process

The chemical modification of a photocatalyst towards enhancing performances includes another interesting approach known as plasmonic sensitization. Plasmonic effects require the incorporation or decoration of a semiconductor with metal nanostructures such as noble metals Ag, Au, Pt etc. The recent and rapid development of noble metal nanoparticles (NMNPs) or plasmonic photocatalysts offered a new opportunity to overcome the limited efficiency of photocatalysts and photovoltaic devices. It has been reported that incorporating plasmonic nanostructures with semiconductors increases the efficiency of the photocatalytic activity toward water splitting or organic compound decomposition [36]. The phenomenon in which the conducting electrons on the NPs undergo collective oscillations (excitation) induced by the oscillating electric fields on the metallic clusters surfaces under suitable irradiation. When the frequency of the incident light satisfies the resonance conditions of the NMNPs, the

surface plasmon resonance (SPR) occurs with the associated light absorption. Such effect is essentially driven by the phenomenon known as localized surface plasmon resonance (LSPR).

The unique capacity of plasmonic nanostructures to concentrate electromagnetic fields, scatter electromagnetic radiation or convert the energy of photons into heat makes them

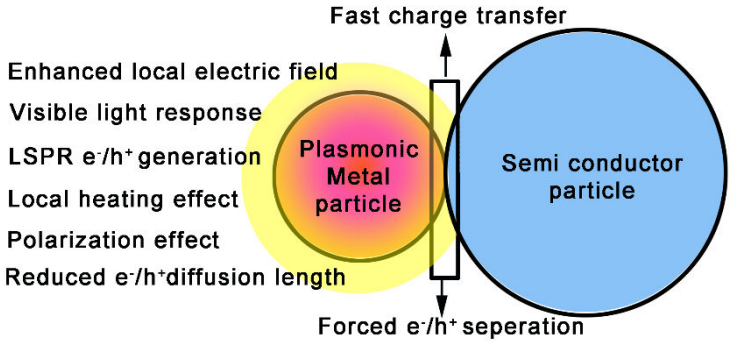

Fig.1.8. Major mechanism involved in plasmonic photocatalysis.

suitable for various applications as illustrated in Fig.1.8. It offers an alternative solution to harvest the broad range of solar irradiation. The resonant photon wavelength is function of the nature of the metal. For example, gold, silver and copper nanostructures exhibit resonant behaviour when interacting with ultraviolet (UV) and visible (Vis) photons. The resonant wavelength and SPR intensity depend not only on the nature of the metal, but also on the size and shape of metallic nanostructures [33,34]. By manipulating the composition, shape and size of plasmonic nanoparticles, it is possible to design nanostructures that interact with the entire solar spectrum [39].

The benefits of plasmon enhanced metal/semiconductor photocatalysis are depicted in Fig.1.8. For metal/ semiconductor, direct contact lead to formation of the Schottky junction which provoke fast charge transportation and suppression of the charge carrier recombination. As major advantages from plasmonic metal/semiconductor system, are outlined:

(1) LSPR enhances drastically the broad spectral range of visible light absorption

(2) LSPR based on oscillating charges on the metal cluster surfaces excite e-/h+ pairs in space charge region [40].

(3) Local heating effect occurring from the electric field at metallic cluster increase the redox reaction rate and as well the mass transfer [41].

(4) As most of light absorbed on outermost surface (~10 nm) of NMNPs, short diffusion lengths are required for photogenerated e-h pairs to participate to redox reaction [42].

(5) LSPR electric field around the metal nanoparticle will polarize the nonpolar molecule for better absorption. Moreover it further enhances the polarization of molecules for better absorption [43].

The role of the noble metal co-catalyst lies in providing chemically active sites where relevant chemical transformations can take place with lower activation barriers than for bare semiconductor. Furthermore, co-catalyst nanoparticles act to extend the lifetime of energetic charge carriers that reach the surface of the semiconductor by enhancing the rates of electron–hole separation at the co-catalyst/semiconductor interface. Moreover, the presence of NMNPs in contact with the semiconductor surface can also accelerate the redox reaction between the semiconductor and H_2O, CO_2 [44]. The LSPR based photocatalysis contribute to better efficiency compared to other configurations including several forms of doping.

Nevertheless, the role of plasmonic effect associated with semiconductor is of prime interest as it is the driving material in the photocatalytic process where the plasmonic NPs are supportive materials. Another context, the photocatalytic efficiency of plasmonic photocatalyst was essentially attributed to the transfer of hot electrons from the semiconductor to plasmonic NPs rather than NPs to semiconductor.

Moreover the doping rates of plasmonic NPs are critical in effective PC performance, sometimes, it should be noted that the photocatalytic efficiency of plasmonic photocatalyst hybrids is found to decrease with increasing concentration of NPs. This may be due to the following reasons.

(1) The increasing concentration of NPs may cover the surface of semiconductor largely so that it may screen the surface to be exposed to the medium and even to the applied light energy.
(2) The excess NPs may themselves act as recombination centres for the excited carriers in the host photocatalyst.
(3) It is possible for these excess NPs to form as separate particles rather than getting deposited on the surface of host
(4) The presence of inhomogeneous size distribution of metal NPs may also affect the photocatalytic process.

The relevant semiconductors for photocatalysis require high charge mobility and long charge carrier diffusion length which will be chemically, electrochemically and photo-electrochemically stable in the electrolyte. Last but not least, to meet the global sustainable

development, the materials employed should be inexpensive, earth abundant, environmentally friendly and are desirable to be synthesized *via* green process.

1.6. Introduction to $BiVO_4$ photocatalyst

The investigations on various types of photocatalytic materials have been the subject of intensive developments. Among all semiconducting photocatalyst, titanium dioxide (TiO_2) is definitely the most popular. It is known for its low cost, non-toxic, chemically stable and offering highly efficient photocatalytic activity for decomposition of organic media or for water splitting for hydrogen production. However, one drawback of such photocatalyst consists in selective reaction to only UV radiation due to the wide bandgap (3.2 eV) limiting the photoactivity to less than 4-6% of solar spectrum. Therefore, it is highly essential to materialize an efficient photocatalyst capable of being driven by visible light which is >43% of solar spectrum, especially under sunlight, with controlled recombination lifetime for the photogenerated charge carriers and also oxidizing agents.

The wide range of heterogeneous photocatalyst materials with reasonable activities under sunlight irradiation can be classified into two major groups. The metal based oxides, especially those with involved composition from phosphides, sulphides, chalcogenides and silicon. Generally, a wide range of well-known metal oxides such as TiO_2, ZnO, $SrTiO_3$, WO_3, and Bi_2O_3 exhibit wide band gaps with their VB usually composed of O 2p orbitals, which lead to photoactivity only under near UV light region ($\lambda < 400$ nm) [45].

Generally, other classes of materials like sulphides such as PbS, WS_2, PbSe, FeS_2, CdS and MoS_2 possess relatively narrow bandgaps with their VB usually composed from S 3p orbitals, which can efficiently absorb broad range of sun radiation. Thus, they show good efficiency in producing H_2 from aqueous solutions including sacrificial reagents with assistance of co-catalysts. However, most of them show limited stability through photo-corrosive phenomena which overcame their photoactivity over long periods. Additionally, toxic and harmful nature [46] limit their use in critical problems as water or environment purification.

The search and development of new visible-light-driven photocatalysts have been directed to $BiVO_4$ due to its optimal electronic and optical properties with narrow bandgap of 2.4 eV and electronic structure for water redox processes under visible radiation. The following arguments point out $BiVO_4$ as a suitable candidate for efficient visible light driven photocatalysis:

1. A narrow bandgap energy (~2.4 eV) with suitable positions of CB and VB energy levels compared to redox potentials of water required in photocatalysis.
2. Low environmental toxicity and high aqueous stability.
3. Low cost compared to other photocatalysts as well as easy processing in nanostructured powders, thin films or as bulk.

1.6.1. Historical background

Bismuth vanadate ($BiVO_4$) is an inorganic compound and belongs to ABO_4 family. In earth crust, bismuth is almost twice as abundant as gold. It was first reported in a medical patent in 1924 and first time synthesized by mixed oxides V_2O_5 and Bi_2O_3 by R.S Roth et al. as a solid substance in 1963 [47] and improved by S.H Chou [48]. In 1975 J.D. Bierlien et al. reported the first studies related to ferroelectric properties [49]. Monilikas et al. found that $BiVO_4$ is promising material for acousto-optical properties in 1980 [50]. Later on, $BiVO_4$ attracts the interest of researchers due to Ferroelastic [47,48] acousto-optical properties [53,54] as well as ion conductivity [55], nontoxic pigment for "brilliant primrose yellow" and numerous pigment combinations based on $BiVO_4$ [56]. Bismuth Vanadates pigments are a relatively new pigment class that has gained importance steadily over the last two decades. Today it is manufactured across the world for pigment use. Suppliers include Heubach Color, Heucotech, DCC, BASF, Caterpillar (Mexico) and Cappelle. Such characteristics of $BiVO_4$ have motivated its wide applications inspite of nontoxic yellow pigment for high performance lead-free paints, there are several applications such as gas sensors, posistors (It's a thermal resistor like thermistor, but with positive resistance temperature factor), solid-state electrolytes, positive electrode materials for lithium rechargeable batteries, etc.

Since 1986, A. Kudo et al. investigated extensively new materials for photocatalytic applications, such as potassium niobate ($K_4Nb_6O_{17}$) [57] and further improvement studies on metal based oxides such as TiO_2, $SrTiO_3$, NiO, etc. On that trails, he reported for the first time, $BiVO_4$ has excellent photocatalytic efficiency for O_2 evolution from water splitting in an aqueous $AgNO_3$ solution and also for pollutant decomposition under visible light [58]. Later in 1999, several synthesis techniques were developed for the preparation of highly crystalline $BiVO_4$ microparticles [59]. Oshikiri et al. have reported theoretical and numerical simulation studies on the electronic structure of $BiVO_4$ and pointed out the photo induced carrier mobility [60].

1.6.2. Structural properties

$BiVO_4$ properties are strongly depended on the crystal polytype which consist in the scheelite or the zircon-type structure. The scheelite structure can have either tetragonal crystal system (space group: $I4_1/a$ with a = b = 5.1470 Å, c = 11.7216 Å) or a monoclinic crystal system (space group: I2/b with a = 5.1935 Å, b = 5.0898 Å, c = 11.6972 Å, and β = 90.3871), also known as clinobisvanite. The zircon-type is a tetragonal crystal structure with the space group: $I4_1/a$ with a = b = 7.303 Å and c = 6.584 Å.

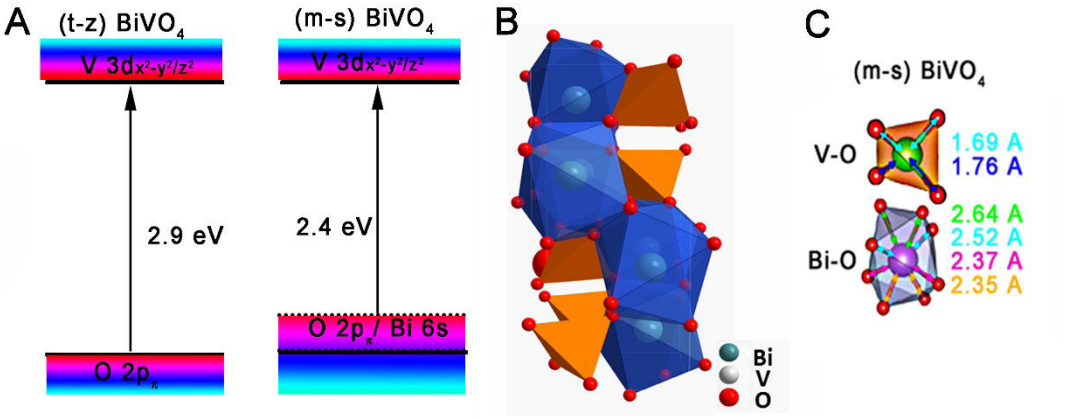

Fig.1.9. A) Energy band diagram for (t-z) $BiVO_4$ and (m-s) $BiVO_4$; B) The crystal structure of monoclinic clinobisvanite $BiVO_4$. The corresponding polyhedron structure is represented in (B) where, VO_4 tetrahedron in orange, and BiO_8 dodecahedron in blue and C) V-O and Bi-O bonds with corresponding lengths for (m-s) $BiVO_4$.

Among crystalline forms of $BiVO_4$, (m-s) $BiVO_4$ has been considered as the more popular and efficient photocatalyst due to its narrow band gap (c.a. 2.4 eV) with distorted Bi-O polyhedron structure. The optical band gaps for (t-s) $BiVO_4$ and (t-z) $BiVO_4$ are 2.35 and 2.9 eV respectively. The crystal structure of (m-s) $BiVO_4$ is similar to (t-s) $BiVO_4$ because they possess same scheelite basic structure which consists in combinations of VO_4 tetrahedrons and BiO_8 dodecahedrons (Fig.1.9 (B)). The four-coordinated V ions and the eight coordinated Bi ions alternate along the [001] direction. Each oxygen atom in this structure is coordinated to two Bi atoms and one V to form a three dimensional structure. The only difference between the tetragonal and monoclinic scheelite structure is that the local environments of V and Bi ions are more significantly distorted in the monoclinic structure suppressing the four-fold symmetry which is involved in a tetragonal structure. On the other hand, (m-s) $BiVO_4$ is characterized mainly by a layered structure containing cations with formal oxidation states of Bi^{3+} ($6s^2$) and V^{5+} ($3d^0$) in coordination with O^{2-} ($2p^6$). The VB is primarily built by O $2p^6$ orbitals having a distorted trigonal planar geometry with un-hybridized $2p_\pi$ and hybridized sp^2 orbitals. At the VBM, orbital mixing occurs between a major contributions from O $2p_\pi$, together

with minor contribution from Bi 6s orbitals. The CB is primarily composed by antibonding V 3d states, with a significant contribution from antibonding O sp^{2*}. The lower region of the CB (CBM) includes contribution from a ligand orbital splitting of V d orbitals, Such as V d_{z2} and V d_{x2-y2} along with small contribution of d_{zx} states, which are mixed with the d_{z2} orbitals (Fig.1.9(A)) [61–64].

The Bi coordination environment is a distorted oxygen dodecahedron, with nearest neighbour distances ranging from 2.35 to 2.64 Å, while V is at the centre of a distorted tetrahedron with 2 × 1.69 Å and 2 × 1.76 Å bond lengths. O1 is coordinated to one Bi and V, while O2 is coordinated to two Bi and a single V atom as shown in Fig.1.9 (C).

1.7. Limitations of pure $BiVO_4$ photocatalyst

Recently, monoclinic phase of Bismuth vanadate ($BiVO_4$) has attracted lot of scientists attention due to its most promising photocatalytic reactions in oxidation of water. As main criterion, its proper VB edge located at ca. 2.4 eV vs. reversible hydrogen electrode (RHE), with near to optimal energy bandgap 2.3-2.4 eV. In addition, such compound possess a large natural abundance of its chemical elements with low cost and good stability. The corresponding theoretical solar-to-hydrogen (STH) conversion efficiency (η) approaches 9.2% with a maximum photocurrent of 7.5 $mA.cm^{-2}$ under standard AM 1.5 solar light irradiation (Fig.1.6) However to date, the actual conversion efficiency achieved with $BiVO_4$-based materials is far below what is expected, because it suffers from some limitations:

1. Slow photogenerated bulk charge mobility leads to approximately 60%–80% of the electron–hole pairs recombination before they reach the interfaces [65]. The localization of photo-induced electrons, together with the polar nature of $BiVO_4$ suggests that self-trapping and small electron polaron formation delay the charge separation and reduce the carrier diffusion length (L_d) down to 70 nm.
2. The kinetics for oxygen evolution is very slow relative to sulphite oxidation. It takes place with extremely fast oxidation process; therefore, the surface recombination is negligible.
3. The location of conduction band (CB) edge is little lower to the reversible hydrogen electrode (RHE) level.
4. Weak surface absorption property limits drastically the efficiency of the reactions at the interfaces [66].

Numerous attempts and different methods have been developed to improve the photocatalytic performances, such as shallow level doping, novel nanostructures, loading co-catalysts, surface modification with electrocatalysts or morphology control. Generally, ion doping modifies in large extent because of the electrical properties of a semiconductor. For example, doping an oxide semiconductor with metal ions possessing higher valence states can significantly increase the carrier concentration and then the conductivity. Doping $BiVO_4$ by transition metal ions induce intermediate energy levels within the bandgap when an effective incorporations of metal ions in the lattice of host matrix occurs. Electron can be excited from the defect state to the $BiVO_4$ conduction band with lower photon energy requirement as compared to undoped material. Additional benefit from transition metal doping is an improved trapping of electrons to inhibit electron-hole recombination during irradiation leading to an enhanced photoactivity.

1.8. Photocatalytic process in the perspective of metal doped $BiVO_4$

The electronic band structure governs the physical properties of semiconductors such as light absorption, charge separation, migration and recombination as well as the thermodynamic drive force for photocatalytic chemical reactions [67]. This in turn has a significant influence on the photocatalytic/photoelectrochemical performance of semiconductors.

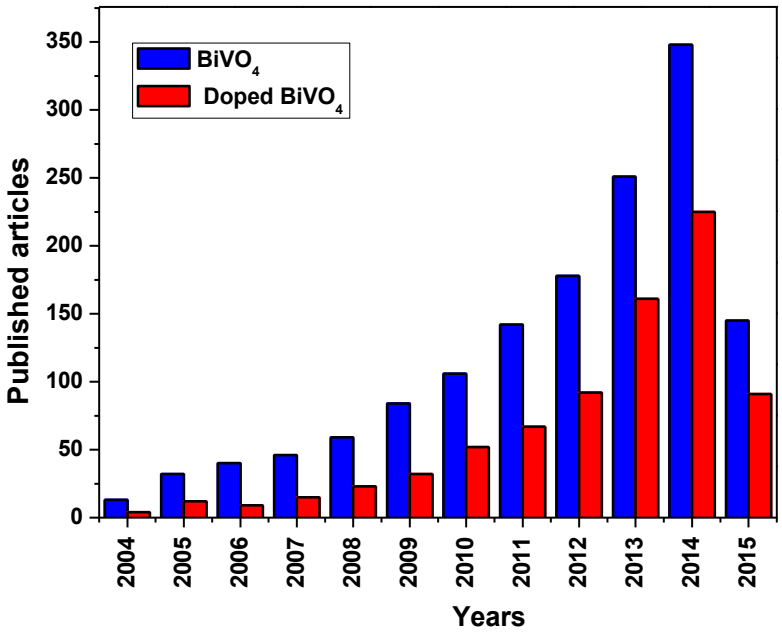

Fig.1.10. Number of publications concerning preparation and properties of photocatalyst $BiVO_4$ and doped $BiVO_4$ nanostructured materials over the years 2004–2015 (till January), based on database of the Science Direct, with search keywords on $BiVO_4$.

To enhance the photoactivity of $BiVO_4$, metal doping is an efficient approach whereas some features like, hole mobility increment which led the formation of hydroxyl oxide radicals, improving the photo-induced separation of electron-hole pairs(reduces charge recombination) and efficiently extending visible light absorption by supressing optical bandgaps. Theoretical studies were developed in this frame by first principle DFT calculations [68–70]. From the last decade, important contributions and encouraging breakthroughs have been made on pure $BiVO_4$ and doped $BiVO_4$ materials as shown in Fig.1.10.

Thus, $BiVO_4$ has been extensively doped with Non-metals (B, C, F, N, S, P) [71–76] , transition metal ions (Mo, W, Cr, Ta, Zr, Si, Ti, Zr, Hf, Sn, Fe, Sr, and Zn), rare earth metals (La, Ce, Eu, Er, Y, Ho, Yb, Sm, Nd and Gd) [77–81] and noble metals(Ag, Au, Pd, Pt) [82–86]. Generally, doping leads to great changes in the electronic band structures that may contribute efficiently to photocatalytic activity. However, the degree of improvement depends on dopant valence state and its atomic size with respect to the substituted ions from the host structures. So far, $BiVO_4$ has been doped with several elements as highlighted with color according to their categories in below periodic table Fig.1.11.

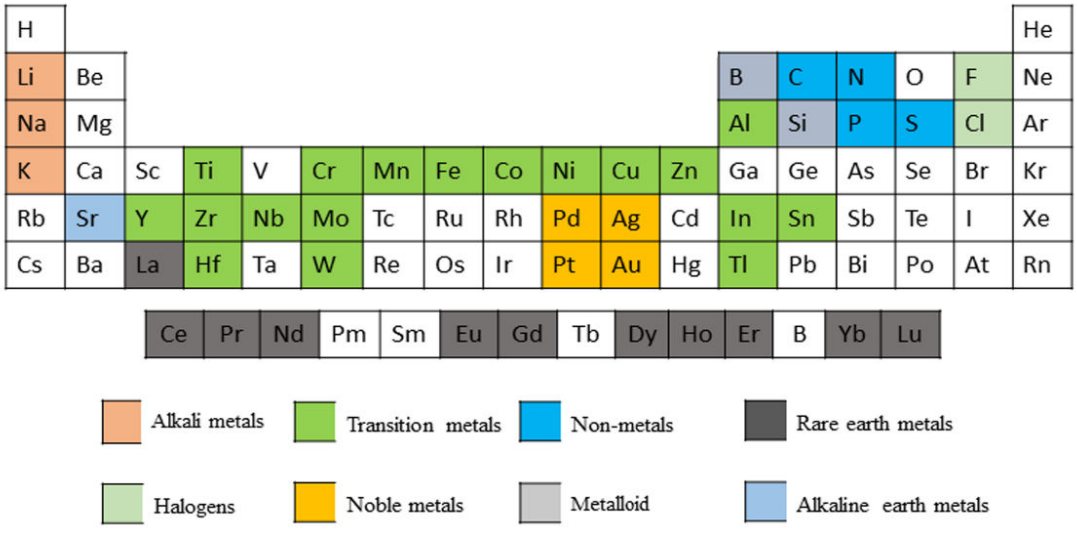

Fig.1.11. Periodic table of elements used for doping $BiVO_4$ semiconductor for PC applications.

The method of photocatalyst semiconductor doping can be categories into two major groups, such as substitutional/ interstitial doping and cluster loading.

1.8.1. Substitutional/ interstitial doping

The doping atoms are indeed inserted in the host crystalline sites of the samples by replacing one of its original atoms i.e. effective doping by atom incorporation. Whereas introducing a foreign atom into interstitial space or into the lattice of host matrix without replacing existing atom is called interstitial doping. Both doping will come into the same category of degeneracy doping with little differences. Basically impurities can be of the same features as substituted atoms or with different valence states generating stoichiometric departure, resulting in excess of electrons or holes.

It is worth noting that substitutional doping has obvious advantages in electrical and optical properties over interstitial doping.

For instance, Jared Lynch et al [87] have shown clear difference between the nitrogen substitutional and interstitial doping in TiO_2. In UV−Vis absorption spectra of $N_{int\text{-}rich}$-TiO_2 where with 10% ratio (N_{int}/N_{tot}) of interstitial doping, they observed a shoulder in the visible region between 400 and 500 nm. However, the absorption tail of $N_{sub\text{-}rich}-TiO_2$ with 74% ratio (N_{sub}/N_{tot}) of substitutional doping exhibited longer extension in the visible range with red shift in absorption edge while optical band gaps can be reduced down to 2.7 and 2.5 eV for the $N_{int\text{-}rich}$ and $N_{sub\text{-}rich}$ samples, respectively compared to the 2.9 eV indirect band gap measured for pure rutile TiO_2.

Anyhow, several studies have been devoted to the influence of different metal ion doping (Mo $^{6+}$, W^{6+}, Cr $^{6+}$, Ta^{5+}, Zr^{5+}, Si^{4+}, Ti^{4+}, Zr^{4+}, Hf^{4+}, Sn^{4+}, La^{3+}, Fe^{3+},Sr^{3+}, Cu^{2+}, Zn^{2+} and Ag^{+}) as well as non-metals as anionic dopants such as (C, N, F, P and S) on the PEC as well as PC applications. In contrast to single metal oxide materials, $BiVO_4$ structures possess two metal doping sites Bi^{3+} and V^{5+}. Z. Zhao et al investigated the doping effect at Bi^{3+} and V^{5+} with higher and lower valence metal ions from DFT theory [88]. Thus, for V^{5+} sites, Mo^{6+} and W^{6+}, Cr $^{6+}$ are chosen as substitutional elements whereas, for Bi^{3+} sites, the four valence ions as Ti^{4+}, Zr^{4+}, Hf^{4+} and Sn^{4+} were considered. The substitution of Vanadium by Mo or W atoms in $BiV_{1-x}M_xO_4$ (M = Mo, W) or for substitution of Bismuth by a Sn atoms as in $Bi_{1\_x}Sn_xVO_4$, intermediate energy levels were created inside the band-gap of $BiVO_4$. Obviously Mo, W and Sn possess relatively similar ionic radius as compared to V^{5+} and Bi^{3}, respectively. Experimentally, it was shown that only Mo [89], [66] and W [90] has significant enhancement in photocurrent as compared to other doping elements particularly for ion doping with higher valence states enhancing the photocurrent of an n-type oxide semiconductor. This is the case Mo^{6+} and/or W^{6+} doping which increase drastically the photocurrent of a $BiVO_4$ photoelectrode due to the donor density which is expected to shift the Fermi level of $BiVO_4$ toward the

conduction band and accelerate the charge separation by increasing the band bending. It can also be attributed to the increment of effective charge carrier mobility as well as their diffusion lengths.

Coming to doping with non-metals (B, C, N, F, P and S), three different major debates were addressed regarding modification mechanism of $BiVO_4$ by (1) bandgap narrowing; (2) impurity energy levels and (3) Oxygen vacancies.

1. Band gap narrowing: M.Wang et al. found that N 1s state hybrids with O 2p states in monoclinic $BiVO_4$ doped with nitrogen because their energies are very close, and thus the band gap of N-$BiVO_4$ is narrowed up to 2.23 eV and able to absorb visible light until 600 nm [73]. Similarly, Y. Li et al reported the B substituted in V sites in VO_4 tetrahedron and form localized defect levels just above 0.17eV to VB of $BiVO_4$ [71].
2. Impurity energy levels: in $BiVO_4$, Z. Zhao et al. suggested that the Sulphur impurity decreased the bandgap energy by the mixing of the Bi 6*s* VB with S 3*p* as well as the mixing states of S 3*s* and O 2*p* located in the band structure [75]. As a consequence, narrowing band gap may occurs due to impurity levels above the valence band.
3. Oxygen vacancies: M.Wang et al. point out that nitrogen is substituted in the place of oxygen. Additional oxygen vacancies and V^{4+} sites would become the active sites for $BiVO_4$, which are advantageous for the enhancement of photocatalytic performance of N-doped $BiVO_4$ [73].

Substitutional/interstitial doping does not change the bandgap dramatically, but it introduces the shallow- or deep-level states, as shown in Fig. 1.12. Such intermediate levels are able to extend the light absorption spectral range to longer wavelengths. Compared to the pure semiconductor, a shallow-level doped semiconductor shows an add-on shoulder on the edge of the absorbance curve. The optical absorption cross section of these defects is quite small. Although the mid-gap deep-level states can extend the light absorption spectral range of wide band gap semiconductors from the UV light to the visible-light range, they make little or no contribution to the visible-light photocatalytic activity because the charge carrier mobility in these states is very low and these states act as the charge recombination centers [91]. The shallow-level states could improve the charge carrier mobility and increase the minority carrier diffusion length. For example, doping $BiVO_4$ with Mo greatly improves the conductivity as Mo^{6+} replaces the V^{5+} in VO_4 tetrahedron positions and contributes by its one excess electron/site to photocatalytic reactions [89], [66]. Similarly, doping Fe_2O_3 with Ti enhances

the conductivity. However, the shallow-level state may still serve as the charge recombination centers [92].

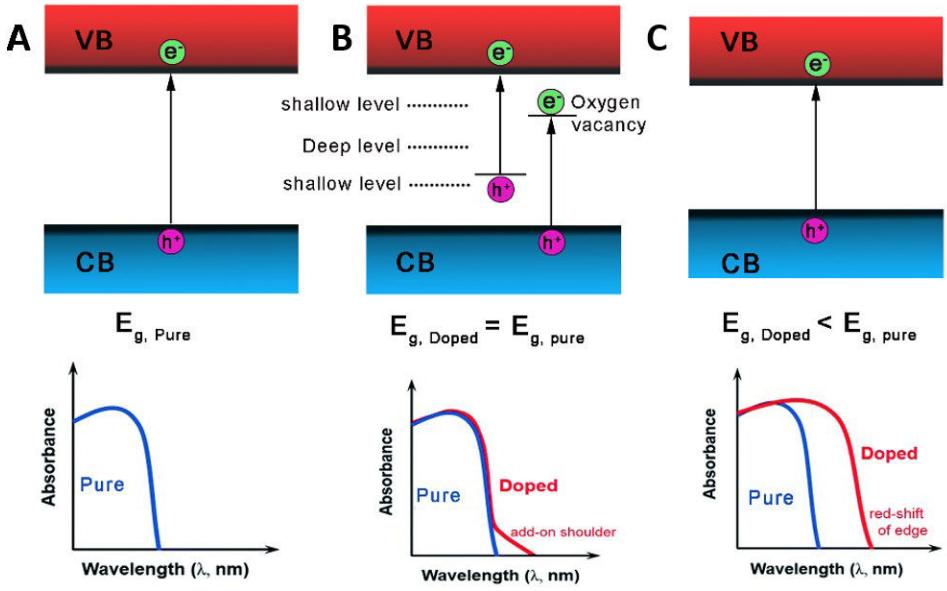

Fig.1.12. Scheme for engineering the electronic band structure of semiconductors. The band structure and optical absorption curves of (a) pure semiconductor, (b) doping-induced shallow-level and deep-level states and (c) doping-induced band gap narrowing.

1.8.2. Metal loading or grafting

Another category of doping is based on adding impurities in the form of metal nanoparticles or cluster onto the surface of host materials. This is known as metal loading technique to realize semiconductor composite structures with enhanced photocatalytic performances. So far $BiVO_4$ has been investigated by loading several transition metals such as Cu, Co, Ni, Fe and Mn [77-81]. Noble metals Au, Pt, Pd and Ag and rare earth metals (La, Ce, Ho, Yb, Eu, Sm, Nd and Gd) were also considered. Coming to the mechanism, the loaded metal nanoparticles would collect photogenerated electrons generated from the host semiconductor under light irradiation so that they liberate holes in VB of SC for effective redox reaction as shown in Fig.1.13. These metal nanoparticles will act as electron acceptors or electron trapping agents.

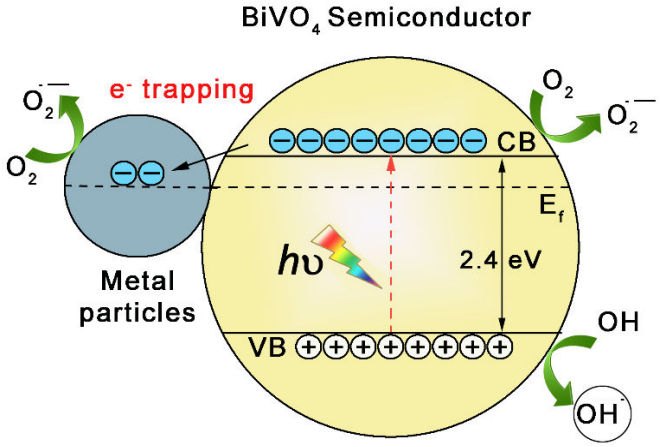

Fig.1.13. Schematic mechanism of metal nanoparticle loaded in BiVO4 semiconductor particle for PC process.

1.8.3. Heterojunction Photocatalysts

Metal oxides based composites were also exploited in order to absorb the visible light, grafting smaller band gap materials or visible light active materials with larger band gap materials in order to enhance the PC performance. However, these heterojunction structures come into the category of metal oxide composites. For instance, several metal oxides were associated with $BiVO_4$ as tabulated in Table 1.1. The main aim lies in harvesting the broad spectral range of sun light as well as elongating the photo induced charge carrier life times and improving the charge carrier separation and their transfer.

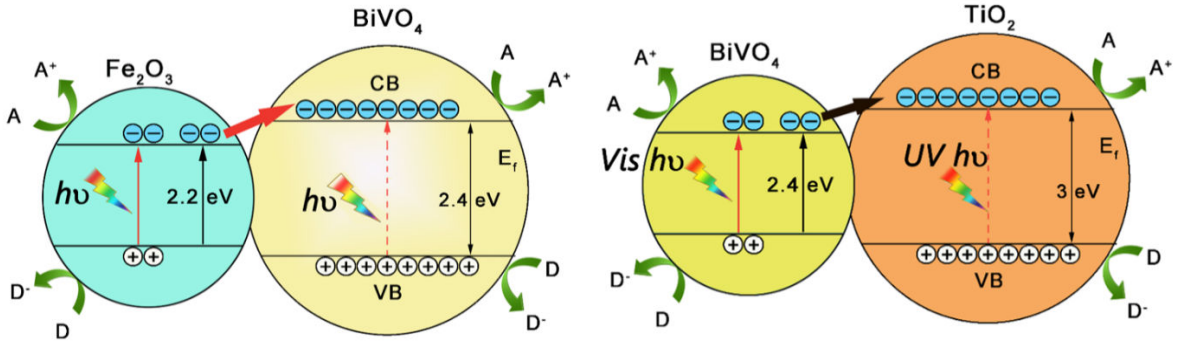

Fig.1.14. A.schematic of transfer and separation of Fe_2O_3 and $BiVO_4$ heterojunction photocatalyst under visible light irradiation, B shows the same mechanism for $TiO_2/BiVO_4$ composite under UV-Vis light irradiation. A- Acceptor and D- Donor for reduction and oxidation processes respectively.

M. Xie et al. explained the heterojunction role in PC system made from $TiO_2/BiVO_4$ composite [107]. By photo-activating $BiVO_4$ under Visible light irradiations, photoexcited high energy electrons transfers to CB of TiO_2, which would elongate the life time of charge carriers and improve the charge separation by limiting the recombination rates as depicted in Fig.1.14.

This mechanism remarkably enhances the PC performance as compared to bare semiconductors PC performances.

To sum up, the advantages of heterojunction PC systems may be as follows:

- Suppression of charge recombinations in lower bandgap SCs
- Improvement of the charge separation and transfer
- Elongation of the life time of high energy excited electrons
- Utilization of wide range from sun radiation

Table 1.1. Several nanocompsites with $BiVO_4$ in form of powders or thin films for photocatalysiss applications.

Name of Composites	**Synthesis technique**	**Organic pollutant used**	**Source of light irradiation**	**Degradation efficiency**	**References**
$TiO_2/BiVO_4$	Sol-gel	Methyl orange (6mg/L)	Visible light irradation	99.8% (140 min)	[94]
$TiO_2/BiVO_4$	Sol-gel	C_6H_6 conversion (gas phase)	500W Xe lamp with >450 nm cutoff filter	~80% (8 h)	[95]
$TiO_2/BiVO_4$	Solgel cum hydrothermal	Methylene blue	50W halogen lamp with 185mW cm^{-2}	~84% (2h)	[96]
$AgO/BiVO_4$	Hydrothermal	PAHs	Visible light (>400nm, 300 mW cm^{-2})	Almost 95% (after 8 h)	[97]
$CuO/BiVO_4$	Impregnation method	Methylene blue	2- 125 W mercury lamps (λ_{max}-365 nm)	95%(2 h)	[98]
CeO_2/ $BiVO_4$	Hydrothermal	Methylene blue	Visible light(>400nm, 185 mW cm^{-2})	80% (30 min)	[99]
WO_3/ $BiVO_4$ (thin films)	Polymer assisted deposition	Water oxidation	Solar simulator lamp (AM 1.5G)	7.3 times compared to BiVO4	[65]
Fe_2O_3/ $BiVO_4$	Facile Hydrothermal route	Rhodamine B and Phenol	500 W Xe light with 400 nm cutoff filter	27 and 31 times to $BiVO_4$	[100]

V_2O_5/ $BiVO_4$	Hydrothermal	Methylene blue	Visible light irradiation with cutoff filter (>420 nm)	92% (after 3 h)	[101]
Bi_2O_3/ $BiVO_4$	Precipitation method	Rhodamin B	Tungsten halogen lamp (500 W, cutoff fliter λ>380 nm)	Complete degrade after 2 h.	[102]
Bi_2O_3/ $BiVO_4$	Solvothermal method	Methylene blue	350 W Xe Solar simulator lamp	Complete degrade after 40-80 min.	[103]
$CuCr_2O_4$/ $BiVO_4$	Wet chemical method	Methylene blue	Visible light source Philips 65W.	~90% for 3 h	[104]
MWCNT/ $BiVO_4$	Hydrothermal	Methylene blue	1KW Xe lamp with cutoff filter 420 nm	~86% for 100 min	[105]
Graphene/ $BiVO_4$	Hydrothermal	Rhodamin B	450W mercury lamp	~87% after 20h	[106]

Similarly, plasmon enhanced metal/semiconductor photocatalysis are explained in section 1.5. Table 1.2 shows the some reports regarding plasmonic photocatalysts of $BiVO_4$

Table 1.2**.** Several noble metal doped/loaded $BiVO_4$ in form of powders for photocatalysiss applications.

Sample	**Synthesis technique**	**Organic pollutant**	**Light source**	**Degradation efficiency**	**Reference**
Ag/$BiVO_4$	Hydrothermal and modified precipitation method	Rhodamin B	300 W Xe lamp with cutoff filter >420 nm	Complete degradation in 24 min	[108]
Au/$BiVO_4$	Modified Hydrothermal	Methyl Orange	300 W Xe lamp with cutoff filter >420 nm	Complete degradation in 50 min	[109]

$Au/BiVO_4$	Hydrothermal method	Rhodamine 6G	Visible light irradiation >400 nm	Complete degradation	[110]
$Au/ BiVO_4$	Deposition and precipitation method	Phenol	500 Watt Xe lamp with >400 nm cutoff filter	99% in 150 min	[111]

Regarding rare earth elements doping, H. Xu et al. [80] have studied $BiVO_4$ doped with 3rd valence state ions such as (La, Ce, Ho, Yb, Eu, Sm, Nd and Gd). The synthesis was realized by impregnation method and with regard to the atomic radius of these metals compared to Bi or V, they did not affect the lattice and form oxide arrangements on the surface of $BiVO_4$. PC performance for degradation of methylene blue (MB) dye under visible light irradiation were then reported for Gd^{3+}-$BiVO_4$ > $BiVO_4$ > Eu^{3+}-$BiVO_4$ > Nd^{3+}-$BiVO_4$ > Yb^{3+}- $BiVO_4$ > Ho^{3+}-$BiVO_4$ > Sm^{3+}-$BiVO_4$ > Ce^{3+}-$BiVO_4$ > La^{3+}-$BiVO_4$. It was also shown that the Gd^{3+}-$BiVO_4$ possesses higher photocatalytic activity than the P25 (commercial TiO_2) under visible light irradiation. On the other hand, S. Usai et al. reported an interesting feature of yttrium(Y) doped $BiVO_4$ by hydrothermal technique. Structural change occurs through the transition from monoclinic- to tetragonal phase, with increment of Y doping rates. An explanation was proposed by considering that Y^{3+} ions with low concentrations <3at% are located in interstitial sites of monoclinic $BiVO_4$ and slowly replace Bi^{3+} sites to convert the structure to tetragonal-$BiVO_4$ polymorph. For 3 at% of Y-$BiVO_4$, heterojunction of half tetragonal and half monoclinic phase are involved and lead to higher O_2 evolution as compared to other Y doping rates.

1.9. Promising photocatalytic properties of $BiVO_4$

In general, ideal photocatalyst should possess the following properties: Photoactivity, biological and chemical inertness, stability toward photo-corrosion, suitability for visible and near UV light energy harnessing, low cost and lack of toxicity[112], and $BiVO_4$ satisfies all aforementioned characteristics and has high potential be a suitable candidate for ideal photocatalyst /efficient visible light driven photocatalyst. In detail, refer previous section 1.6.

A variety of synthesis methods as physical route (top down approach) or chemical route (bottom up approach) [113] were used to obtain $BiVO_4$ and to modulate several features including:

a) Chemical composition of the surface and bulk

b) Crystallinity

c) Morphology (1D, 2D, micro, bulk, porous etc)

d) Surface area, ensuring number of reactive sites

e) Intrinsic or extrinsic defect contents (doping, oxygen vacancies, other defects etc.)

There is a need for an efficient technique that able to impart all the above criteria in a photocatalyst. Moreover, the main criterion for an efficient photocatalysis depends on effective formation of photogenerated electron-hole pairs with longer lifetimes. This favours the interaction of the charge carriers with the surrounding media contributing then to the production of radical ions such as hydroxyl ions and superoxide anions required for heterogeneous catalysis. These radical ions interact with organic molecules for their degradation [114]. The recombination delay is necessary to sustain the charge carriers to form radical ions for redox process. The delay in the charge recombination could be directly proportional to the production rate of radical ions in the reaction medium. The recombination delay or resistance can be introduced in an ideal photocatalytic material through band gap engineering and changing the surface reactivity. Band gap engineering in a photocatalyst also supports the selectivity of light to activate the material under required energies as discussed in chapter 1. It is also known that the photocatalytic process is a surface phenomenon where the surface manipulation of a photoactive media is a potential factor to enhance the photocatalytic properties. Several strategies were then developed to enhance the properties of a photocatalyst by suitable design of the material surface features. These essentially include the surface energy enhancement through particle size reduction, creating high surface roughness with active surface sites.

Investigation on photocatalysts irrespective material structure dimensions, are encouraged and motivated by the facts that using either powder form or thin films of immobilized photocatalyst are most preferable in photocatalytic applications such as water splitting, purification and air cleaning etc. Schematic representation of Powder and thin film photocatalyts can be seen in Fig.1.15.

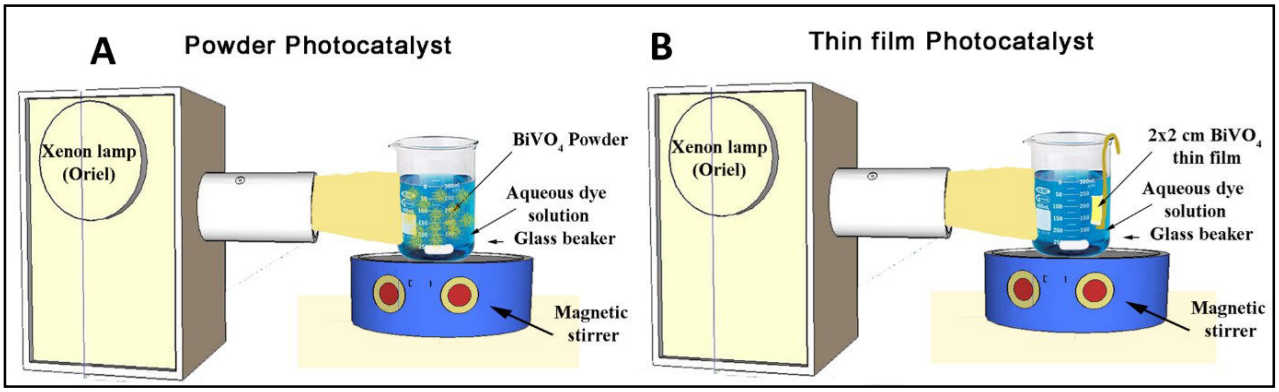

Fig.1.15: Schematic representation of photocatalytic setup for (A) Powder photocatalyst and (B) Thin film photocatalyst.

The few comparisons between usage of powder form of photocatalyst and thin film photocatalyst.

1. **Additional filtration system:** Effective filtration system is very essential for powdered photocatalystic reaction. After the photocatalytic reaction, cascade filtration will eliminates the powder catalyst, along with hazardous pollutants. Whereas, thin films with immobilized catalyst, filtration system is not as essential as for powder system.
2. **Specific surface area:** Nanoparticle have more surface to volume ratio as compared to bulk. Similarly, powdered photocatalysts with nano-sized particles have more specific surface area. Moreover it can be improved with various morphologies such as, quantum dots, nano-spheres, nano-rods, nano-belts, nano-flakes, etc. In the case of thin films, its obvious that specific surface area is less as compared to powders. However, it can be improved with various morphologies on the surface of the thin film. In short, powder catalysts are more efficient in degradation of pollutants as compared to thin films due to its high specific surface area, which directly lead to higher absorption of light, consequently led to better/faster photocatalytic performances.
3. **Position of light source:** Position of light source is critical for static thin films, higher photocatalytic efficiency can be achieved only when the position of light source is exactly opposite to surface plane of thin film. In case of powders, position of light source has flexibility as compared to thin films, which is obvious due to mobile catalyst along with the pollutant.

The only discouraging point about using photocatalytic powders, though they offer high absorption of light with easy screening of the pollutant around catalyst surface, but due to the

difficulty of separation of the powder catalyst from water, they are not encouraged in water treatment and water splitting application. However, this problem could be avoided by using the photocatalyst in the form of thin films[115]. With regard to the interest in technological applications, the realization of thin films is worthy of interest.

1.10. Objective of the thesis work

Development of doped bismuth vanadate photocatalysts using several doping agents such as Cu, Mo, Ag and their photocatalytic applications to the photodegradation of organic pollutants

Specific objectives are:

- Understanding structural and optical properties of doped $BiVO_4$ nanostructures prepared by mechano-chemical (HEM) synthesis technique using different dopants such as Copper (Cu), Silver (Ag) and Molybdenum (Mo).
- Investigating electric and dielectric properties as well as electronic active centers by EPR analysis for all doped $BiVO_4$ nanopowders.
- Synthesis of doped $BiVO_4$ nanostructures with Cu, Ag, and Mo by Sol-gel technique for effective doping.
- Deposition of metal doped $BiVO_4$ thin films by R.F sputtering technique.
- Evaluating the photocatalytic activity through the degradation of organic pollutants by doped $BiVO_4$ and to exploring their performance respectively.

The synthesis of nanosized- innovative structures are achieved by using both physical and chemical route such as mechano-chemical synthesis/ High energy ball milling (HEM) and sol-gel technique, incorporating different doping ions such as Cu, Mo and Ag. Such methods are most reliable for synthesis of pristine $BiVO_4$ [34]. Therefore, Ball mill was identified as potential techniques to synthesize pristine and doped $BiVO_4$ nanostructures with nano-sized with high surface active sites and various morphology for the effective utilization for the photocatalytic applications.

One of the peculiar features of doping, it often inhibits the particle growth rate resulting in smaller particles. This is highly beneficial for photocatalysis, where smaller particles have larger specific surface area as compared to large particles. So the increased surface area

accommodate more dye for degradation and leading to higher light absorption and charge transportation.

In conclusion, Doping with suitable metal elements will enhances photocatalysis reaction in various manners, which is seen in upcoming chapters. $BiVO_4$ semiconducting materials in the form of powders doped with Cu, Mo and Ag dopants with defined doping rates are achieved by both physical route and chemical route, such as high energy ball milling technique and sol-gel technique. Well crystalline Mo and Cu doped $BiVO_4$ in the form of thin films under three different conditions, are achieved by rf sputtering technique.

References:

[1] http://apps.who.int/iris/bitstream/10665/112727/1/9789241507240_eng.pdf.

[2] A. Fujishima, K. Honda, Electrochemical photolysis of water at a semiconductor electrode., Nature. 238 (1972) 37–38.

[3] W.H. Glaze, J.-W. Kang, D.H. Chapin, The Chemistry of Water Treatment Processes Involving Ozone, Hydrogen Peroxide and Ultraviolet Radiation, Ozone Sci. Eng. 9 (1987) 335–352.

[4] T. Bak, J. Nowotny, M. Rekas, C.C. Sorrell, Photo-electrochemical hydrogen generation from water using solar energy. Materials-related aspects, Int. J. Hydrogen Energy. 27 (2002) 991–1022.

[5] S. Chen, L.W. Wang, Thermodynamic oxidation and reduction potentials of photocatalytic semiconductors in aqueous solution, Chem. Mater. 24 (2012) 3659–3666.

[6] J. Li, N. Wu, Semiconductor-based photocatalysts and photoelectrochemical cells for solar fuel generation: a review, Catal. Sci. Technol. 5 (2015) 1360–1384.

[7] M. WEBER, M. DIGNAM, Splitting water with semiconducting photoelectrodes—Efficiency considerations, Int. J. Hydrogen Energy. 11 (1986) 225–232.

[8] J.R. Bolton, S.J. Strickler, J.S. Connolly, Limiting and realizable efficiencies of solar photolysis of water, Nature. 316 (1985) 495–500.

[9] J.C. Colmenares, R. Luque, J.M. Campelo, F. Colmenares, Z. Karpiński, A.A. Romero, Nanostructured Photocatalysts and Their Applications in the Photocatalytic Transformation of Lignocellulosic Biomass: An Overview, Materials (Basel). 2 (2009) 2228–2258.

[10] S.N. Habisreutinger, L. Schmidt-Mende, J.K. Stolarczyk, Photocatalytic reduction of CO_2 on TiO_2 and other semiconductors, Angew. Chemie - Int. Ed. 52 (2013) 7372–7408.

[11] G. Li, K.A. Gray, The solid-solid interface: Explaining the high and unique photocatalytic reactivity of TiO_2-based nanocomposite materials, Chem. Phys. 339 (2007) 173–187.

[12] B. Atomsa Gonfa, H. Zhao, J. Li, J. Qiu, M. Saidani, S. Zhang, et al., Air-processed depleted bulk heterojunction solar cells based on PbS/CdS core–shell quantum dots and TiO_2 nanorod arrays, Sol. Energy Mater. Sol. Cells. 124 (2014) 67–74.

[13] J. Li, M.W.G. Hoffmann, H. Shen, C. Fabrega, J.D. Prades, T. Andreu, et al., Enhanced photoelectrochemical activity of an excitonic staircase in CdS@TiO_2 and CdS@anatase@rutile TiO_2 heterostructures, J. Mater. Chem. 22 (2012) 20472.

[14] H. Golmojdeh, M.A. Zanjanchi, A facile approach for synthesis of $BiVO_4$ nano-particles possessing high surface area and various morphologies, Cryst. Res. Technol. 47 (2012) 1014–1025.

[15] W. Sun, M. Xie, L. Jing, Y. Luan, H. Fu, Synthesis of large surface area nano-sized $BiVO_4$ by an EDTA-modified hydrothermal process and its enhanced visible photocatalytic activity, J. Solid State Chem. 184 (2011) 3050–3054.

[16] T.F. Jaramillo, K.P. Jørgensen, J. Bonde, J.H. Nielsen, S. Horch, I. Chorkendorff, Identification of active edge sites for electrochemical H_2 evolution from MoS2 nanocatalysts., Science. 317 (2007) 100–102.

[17] N. Wu, J. Wang, D.N. Tafen, H. Wang, J.G. Zheng, J.P. Lewis, et al., Shape-enhanced photocatalytic activity of single-crystalline anatase TiO_2 (101) nanobelts, J. Am. Chem. Soc. 132 (2010) 6679–6685.

[18] N. Murakami, Y. Kurihara, T. Tsubota, T. Ohno, Shape-Controlled Anatase Titanium(IV) Oxide Particles Prepared by Hydrothermal Treatment of Peroxo Titanic Acid in the Presence of Polyvinyl Alcohol, J. Phys. Chem. C. 113 (2009) 3062–3069.

[19] G.K. Mor, K. Shankar, M. Paulose, O.K. Varghese, C.A. Grimes, Enhanced photocleavage of water using titania nanotube arrays, Nano Lett. 5 (2005) 191–195.

[20] Y. Zhang, Y. Guo, H. Duan, H. Li, C. Sun, H. Liu, Facile synthesis of V^{4+} self-doped, [010] oriented $BiVO_4$ nanorods with highly efficient visible light-induced photocatalytic activity, Phys. Chem. Chem. Phys. 16 (2014) 24519–24526.

[21] H. Li, G. Liu, S. Chen, Q. Liu, W. Lu, Synthesis and characterization of monoclinic $BiVO_4$ nanorods and nanoplates via microemulsion-mediated hydrothermal method, Phys. E Low-Dimensional Syst. Nanostructures. 43 (2011) 1323–1328.

[22] L. Ren, L. Jin, J.-B. Wang, F. Yang, M.-Q. Qiu, Y. Yu, Template-free synthesis of $BiVO_4$ nanostructures: I. Nanotubes with hexagonal cross sections by oriented attachment and their photocatalytic property for water splitting under visible light., Nanotechnology. 20 (2009) 115603.

[23] S. Xie, T. Zhai, Y. Zhu, W. Li, R. Qiu, Y. Tong, et al., NiO decorated Mo:$BiVO_4$ photoanode with enhanced visible-light photoelectrochemical activity, Int. J. Hydrogen Energy. 39 (2014) 4820–4827.

[24] M.J. Nalbandian, M. Zhang, J. Sanchez, Y.-H. Choa, D.M. Cwiertny, N. V. Myung, Synthesis and optimization of $BiVO_4$ and co-catalyzed $BiVO_4$ nanofibers for visible light-activated photocatalytic degradation of aquatic micropollutants, J. Mol. Catal. A Chem. 404-405 (2015) 18–26.

[25] Y. Pihosh, I. Turkevych, K. Mawatari, J. Uemura, Y. Kazoe, S. Kosar, et al., Photocatalytic generation of hydrogen by core-shell WO_3/$BiVO_4$ nanorods with ultimate water splitting efficiency, Sci. Rep. 5 (2015) 11141.

[26] L. Ren, L. Ma, L. Jin, J.-B. Wang, M. Qiu, Y. Yu, Template-free synthesis of $BiVO_4$ nanostructures: II. Relationship between various microstructures for monoclinic $BiVO_4$ and their photocatalytic activity for the degradation of rhodamine B under visible light., Nanotechnology. 20 (2009) 405602.

[27] L. Zhang, D. Chen, X. Jiao, Monoclinic structured $BiVO_4$ nanosheets: Hydrothermal preparation, formation mechanism, and coloristic and photocatalytic properties, J. Phys. Chem. B. 110 (2006) 2668–2673.

[28] G. Li, D. Zhang, J.C. Yu, Ordered mesoporous $BiVO_4$ through nanocasting: A superior visible light-driven photocatalyst, Chem. Mater. 20 (2008) 3983–3992.

[29] M. Zhou, J. Bao, Y. Xu, J. Zhang, J. Xie, M. Guan, et al., Photoelectrodes Based upon Mo:$BiVO_4$ Inverse Opals for Photoelectrochemical Water Splitting., ACS Nano. (2014).

[30] M. Zhou, H. Bin Wu, J. Bao, L. Liang, X.W.D. Lou, Y. Xie, Ordered Macroporous $BiVO_4$ Architectures with Controllable Dual Porosity for Efficient Solar Water Splitting, Angew. Chemie Int. Ed. 52 (2013) 8579–8583.

[31] G. Tan, L. Zhang, H. Ren, S. Wei, J. Huang, A. Xia, Effects of pH on the Hierarchical Structures and Photocatalytic Performance of $BiVO_4$ Powders Prepared via the Microwave Hydrothermal Method, ACS Appl. Mater. Interfaces. 5 (2013) 5186–5193.

[32] A. Zhang, J. Zhang, N. Cui, X. Tie, Y. An, L. Li, Effects of pH on hydrothermal synthesis and characterization of visible-light-driven $BiVO_4$ photocatalyst, J. Mol. Catal. A Chem. 304 (2009) 28–32.

[33] D.-D. Qin, T. Wang, Y.-M. Song, C.-L. Tao, Reduced monoclinic $BiVO_4$ for improved photoelectrochemical oxidation of water under visible light, Dalt. Trans. 43 (2014) 7691.

[34] R. Venkatesan, S. Velumani, a. Kassiba, Mechanochemical synthesis of nanostructured $BiVO_4$ and investigations of related features, Mater. Chem. Phys. 135 (2012) 842–848.

[35] W. Liu, L. Cao, G. Su, H. Liu, X. Wang, L. Zhang, Ultrasound assisted synthesis of monoclinic structured spindle $BiVO_4$ particles with hollow structure and its photocatalytic property., Ultrason. Sonochem. 17 (2010) 669–74.

[36] S. Linic, P. Christopher, D.B. Ingram, Plasmonic-metal nanostructures for efficient conversion of solar to chemical energy, Nat. Mater. 10 (2011) 911–921.

[37] M.A. El-Sayed, Some interesting properties of metals confined in time and nanometer space of different shapes, Acc. Chem. Res. 34 (2001) 257–264.

[38] C. Burda, X. Chen, R. Narayanan, M.A. El-Sayed, Chemistry and properties of nanocrystals of different shapes, Chem. Rev. 105 (2005) 1025–1102.

[39] M. Rycenga, C.M. Cobley, J. Zeng, W. Li, C.H. Moran, Q. Zhang, et al., Controlling the synthesis and assembly of silver nanostructures for plasmonic applications, Chem. Rev. 111 (2011) 3669–3712.

[40] C. Langhammer, Z. Yuan, I. Zorić, B. Kasemo, Plasmonic properties of supported Pt and Pd nanostructures, Nano Lett. 6 (2006) 833–838.

[41] P. Christopher, H. Xin, S. Linic, Visible-light-enhanced catalytic oxidation reactions on plasmonic silver nanostructures., Nat. Chem. 3 (2011) 467–472.

[42] I. Thomann, B.A. Pinaud, Z. Chen, B.M. Clemens, T.F. Jaramillo, M.L. Brongersma, Plasmon enhanced solar-to-fuel energy conversion, Nano Lett. 11 (2011) 3440–3446.

[43] S. Sun, W. Wang, L. Zhang, M. Shang, L. Wang, Ag@C core/shell nanocomposite as a highly efficient plasmonic photocatalyst, Catal. Commun. 11 (2009) 290–293.

[44] X.F. Wu, H.Y. Song, J.M. Yoon, Y.T. Yu, Y.F. Chen, Synthesis of core-shell $Au@TiO_2$ nanopartides with truncated wedge-shaped morphology and their photocatalytic properties, Langmuir. 25 (2009) 6438–6447.

[45] J.R. Darwent, A. Mills, Photo-oxidation of water sensitized by WO_3 powder, J. Chem. Soc. Faraday Trans. 2. 78 (1982) 359.

[46] Sakata T, N.S. and E.P., Photocatalysis, Wiley. (1989) p. 311.

[47] Roth. R.S and J.L. Waring, Amerrican Mineral. 48 (1963) 1348–1357.

[48] S.H. Choh, Y.J. Park, H.K. Kim, Effects of Domain and Electric Field on 14 N NQR in $NaNO_2$, Jpn. J. Appl. Phys. 24 (1985) 634.

[49] J.D. Bierlein, A.W. Sleight, Ferroelasticity in $BiVO_4$, Solid State Commun. 16 (1975) 69–70.

[50] A.S. Manolakis C, Phys. Sfam Solidi a. 60 (1980) 167.

[51] W.I.F. David, I.G. Wood, : VI. Some comments on the relationship between spontaneous deformation and domain walls in ferroelastics, J. Phys. C Solid State Phys. 16 (2000) 5149–5166.

[52] A.R. Lim, S.H. Choh, M.S. Jang, Prominent ferroelastic domain walls in $BiVO_4$ crystal, J. Phys. Condens. Matter. 7 (1995) 7309.

[53] C. Manolikas, S. Amelinckx, Ferroelastic domains in $BiVO_4$, Phys. Status Solidi. 60 (1980) 167–172.

[54] K. Hirota, G. Komatsu, M. Yamashita, H. Takemura, O. Yamaguchi, Formation, characterization and sintering of alkoxy-derived bismuth vanadate, Mater. Res. Bull. 27 (1992) 823–830.

[55] T. Lu, Electrical conductivity of polycrystalline $BiVO_4$ samples having the scheelite structure, Solid State Ionics. 21 (1986) 339–342.

[56] E.B. Faulkner, R.J. Schwartz, High Performance Pigments, 9 WILEY-VC, WILEY-VCH Verlag GmbH & Co. KGaA, 2009.

[57] K. Domen, A. Kudo, M. Shibata, A. Tanaka, K.-I. Maruya, T. Onishi, Novel photocatalysts, ion-exchanged $K_4Nb_6O_{17}$, with a layer structure, J. Chem. Soc. Chem. Commun. (1986) 1706.

[58] A. Kudo, K. Ueda, H. Kato, I. Mikami, Photocatalytic O^{-2} evolution under visible light irradiation on $BiVO_4$ in aqueous $AgNO_3$ solution, Catal. Letters. 53 (1998) 229–230.

[59] A. Kudo, K. Omori, H. Kato, A novel aqueous process for preparation of crystal form-controlled and highly crystalline $BiVO_4$ powder from layered vanadates at room temperature and its photocatalytic and photophysical properties, J. Am. Chem. Soc. 121

(1999) 11459–11467.

[60] M. Oshikiri, M. Boero, J. Ye, Z. Zou, G. Kido, Electronic structures of promising photocatalysts $InMO_4$ (M=V, Nb, Ta) and $BiVO_4$ for water decomposition in the visible wavelength region, J. Chem. Phys. 117 (2002) 7313.

[61] J.K. Cooper, S. Gul, F.M. Toma, L. Chen, P.-A. Glans, J. Guo, et al., Electronic Structure of Monoclinic $BiVO_4$, Chem. Mater. 26 (2014) 5365–5373.

[62] A. Kudo, K. Omori, H. Kato, A Novel Aqueous Process for Preparation of Crystal Form-Controlled and Highly Crystalline $BiVO_4$ Powder from Layered Vanadates at Room Temperature and Its Photocatalytic and Photophysical Properties, (1999) 11459–11467.

[63] A. Walsh, Y. Yan, M.N. Huda, M.M. Al-Jassim, S.H. Wei, Band edge electronic structure of $BiVO_4$: Elucidating the role of the Bi s and V d orbitals, Chem. Mater. 21 (2009) 547–551.

[64] Z. Zhao, Z. Li, Z. Zou, Electronic structure and optical properties of monoclinic clinobisvanite $BiVO_4$., Phys. Chem. Chem. Phys. 13 (2011) 4746–4753.

[65] S.J. Hong, S. Lee, J.S. Jang, J.S. Lee, Heterojunction $BiVO_4/WO_3$ electrodes for enhanced photoactivity of water oxidation, Energy Environ. Sci. 4 (2011) 1781.

[66] W. Yao, H. Iwai, J. Ye, Effects of molybdenum substitution on the photocatalytic behavior of BiVO4., Dalton Trans. (2008) 1426–30.

[67] M.R. Hoffmann, S.T. Martin, W. Choi, et al., Environmental Applications of Semiconductor Photocatalysis, Chem. Rev. 95 (1995) 69–96.

[68] H.S. Park, K.E. Kweon, H. Ye, E. Paek, G.S. Hwang, A.J. Bard, J. Phys. Chem. C. 115 (2011) 17870–17879.

[69] Z. Zhao, Z. Li, Z. Zou, Electronic structure and optical properties of monoclinic clinobisvanite $BiVO_4$., Phys. Chem. Chem. Phys. 13 (2011) 4746–53.

[70] G. Mestl, N.F.D. Verbruggen, E. Bosch, H. Kno, Mechanically Activated $MoO_{3.5}$. Redox Behavior, 7463 (1996) 2961–2968.

[71] Y. Li, T. Jing, Y. Liu, B. Huang, Y. Dai, X. Zhang, et al., Enhancing the Efficiency of Water Oxidation by Boron-Doped $BiVO_4$ under Visible Light: Hole Trapping by BO_4 Tetrahedra, Chempluschem. (2015).

[72] G.P. Nagabhushana, G. Nagaraju, G.T. Chandrappa, Synthesis of bismuth vanadate: its application in H_2 evolution and sunlight-driven photodegradation, J. Mater. Chem. A. 1 (2013) 388.

[73] M. Wang, Q. Liu, Y. Che, L. Zhang, D. Zhang, Characterization and photocatalytic properties of N-doped $BiVO_4$ synthesized via a sol-gel method, J. Alloys Compd. 548 (2013) 70–76.

[74] H. Jiang, H. Dai, J. Deng, Y. Liu, L. Zhang, K. Ji, Porous F-doped $BiVO_4$: Synthesis and enhanced photocatalytic performance for the degradation of phenol under visible-light illumination, Solid State Sci. 17 (2013) 21–27.

[75] Z. Zhao, H. Dai, J. Deng, Y. Liu, C.T. Au, Effect of sulfur doping on the photocatalytic performance of $BiVO_4$ under visible light illumination, Chinese J. Catal. 34 (2013) 1617–1626.

[76] W.J. Jo, J.-W. Jang, K. Kong, H.J. Kang, J.Y. Kim, H. Jun, et al., Phosphate Doping into Monoclinic $BiVO_4$ for Enhanced Photoelectrochemical Water Oxidation Activity, Angew. Chemie Int. Ed. 51 (2012) 3147–3151.

[77] A.P. Zhang, J.Z. Zhang, Synthesis and activities of ln-doped $BiVO_4$ (Ln=Eu, Gd and Er) photocatalysts, Chinese J. Inorg. Chem. 25 (2009) 2040–2047.

[78] C. Karunakaran, S. Kalaivani, P. Vinayagamoorthy, S. Dash, Optical, electrical and visible light-photocatalytic properties of yttrium-substituted $BiVO_4$ nanoparticles, Mater. Sci. Eng. B Solid-State Mater. Adv. Technol. 187 (2014) 53–60.

[79] A. Zhang, J. Zhang, Effects of europium doping on the photocatalytic behavior of $BiVO_4$, J. Hazard. Mater. 173 (2010) 265–272.

[80] S. Usai, S. Obrego, A.I. Becerro, G. Colo, Monoclinic − Tetragonal Heterostructured $BiVO_4$ by Yttrium Doping with Improved Photocatalytic Activity, 3 (2013).

[81] H. Xu, C. Wu, H. Li, J. Chu, G. Sun, Y. Xu, et al., Synthesis, characterization and photocatalytic activities of rare earth-loaded $BiVO_4$ catalysts, Appl. Surf. Sci. 256 (2009) 597–602.

[82] L. Chen, R. Huang, Y.-J. Ma, S.-L. Luo, C.-T. Au, S.-F. Yin, Controllable synthesis of hollow and porous Ag/$BiVO_4$ composites with enhanced visible-light photocatalytic performance, RSC Adv. 3 (2013) 24354.

[83] A. Zhang, J. Zhang, Characterization and photocatalytic properties of Au/$BiVO_4$ composites, J. Alloys Compd. 491 (2010) 631–635.

[84] L. Ge, Novel visible-light-driven Pt/$BiVO_4$ photocatalyst for efficient degradation of methyl orange, J. Mol. Catal. A Chem. 282 (2008) 62–66.

[85] L. Ge, Synthesis and characterization of novel visible-light-driven Pd/$BiVO_4$ composite photocatalysts, Mater. Lett. 62 (2008) 926–928.

[86] X. Zhang, Y. Zhang, X. Quan, S. Chen, Preparation of Ag doped $BiVO_4$ film and its enhanced photoelectrocatalytic (PEC) ability of phenol degradation under visible light., J. Hazard. Mater. 167 (2009) 911–4.

[87] J. Lynch, C. Giannini, J.K. Cooper, A. Loiudice, I.D. Sharp, R. Buonsanti, Substitutional or Interstitial Site-Selective Nitrogen Doping in TiO 2 Nanostructures, J. Phys. Chem. C. 119 (2015) 7443–7452.

[88] Z. Zhao, W. Luo, Z. Li, Z. Zou, Density functional theory study of doping effects in monoclinic clinobisvanite $BiVO_4$, Phys. Lett. Sect. A Gen. At. Solid State Phys. 374 (2010) 4919–4927.

[89] K. Ding, B. Chen, Z. Fang, Y. Zhang, Z. Chen, Why the photocatalytic activity of Mo-doped $BiVO_4$ is enhanced: a comprehensive density functional study., Phys. Chem. Chem. Phys. 16 (2014) 13465–76.

[90] S.P. Berglund, A.J.E. Rettie, S. Hoang, C.B. Mullins, Incorporation of Mo and W into nanostructured $BiVO_4$ films for efficient photoelectrochemical water oxidation, Phys. Chem. Chem. Phys. 14 (2012) 7065.

[91] J. Wang, D.N. Tafen, J.P. Lewis, Z. Hong, A. Manivannan, M. Zhi, et al., Origin of photocatalytic activity of Nitrogen-doped TiO_2 nanobelts, J. Am. Chem. Soc. 131 (2009) 12290–12297.

[92] M.A. Henderson, J.M. White, H. Uetsuka, H. Onishi, Photochemical Charge Transfer and Trapping at the Interface between an Organic Adlayer and an Oxide Semiconductor, J. Am. Chem. Soc. 125 (2003) 14974–14975.

[93] H. Xu, H. Li, C. Wu, J. Chu, Y. Yan, H. Shu, Preparation, characterization and photocatalytic activity of transition metal-loaded $BiVO_4$, Mater. Sci. Eng. B Solid-State Mater. Adv. Technol. 147 (2008) 52–56.

[94] R. Rahimi, S. Zargari, M.M. Moghaddas, $BiVO_4$-TiO_2 Nanocomposite: Synthesis and Photocatalytic Investigation, Adv. Mater. Res. 702 (2013) 172–175.

[95] Y. Hu, D. Li, Y. Zheng, W. Chen, Y. He, Y. Shao, et al., $BiVO_4$/TiO_2 nanocrystalline heterostructure: A wide spectrum responsive photocatalyst towards the highly efficient decomposition of gaseous benzene, Appl. Catal. B Environ. 104 (2011) 30–36.

[96] N. Wetchakun, S. Chainet, S. Phanichphant, K. Wetchakun, Efficient photocatalytic degradation of methylene blue over $BiVO_4$/TiO_2 nanocomposites, Ceram. Int. 41 (2015) 5999–6004.

[97] S. Kohtani, M. Tomohiro, K. Tokumura, R. Nakagaki, Photooxidation reactions of polycyclic aromatic hydrocarbons over pure and Ag-loaded $BiVO_4$ photocatalysts, Appl. Catal. B Environ. 58 (2005) 265–272.

[98] H. Xu, H. Li, C. Wu, J. Chu, Y. Yan, H. Shu, et al., Preparation, characterization and photocatalytic properties of Cu-loaded BiVO4, J. Hazard. Mater. 153 (2008) 877–884.

[99] N. Wetchakun, S. Chaiwichain, B. Inceesungvorn, K. Pingmuang, S. Phanichphant, A.I. Minett, et al., $BiVO_4$ /CeO_2 Nanocomposites with High Visible-Light-Induced Photocatalytic Activity, ACS Appl. Mater. Interfaces. 4 (2012) 3718–3723.

[100] P. Cai, S.-M. Zhou, D.-K. Ma, S.-N. Liu, W. Chen, S.-M. Huang, Fe_2O_3-Modified Porous $BiVO_4$ Nanoplates with Enhanced Photocatalytic Activity, Nano-Micro Lett. 7 (2015) 183–193.

[101] J. Su, X. Zou, G. Li, X. Wei, C. Yan, Y. Wang, et al., Macroporous V_2O_5 À $BiVO_4$ Composites : Effect of Heterojunction on the Behavior of Photogenerated Charges, (2011) 8064–8071.

[102] L. Li, B. Yan, BiVO4/Bi2O3 submicrometer sphere composite: Microstructure and photocatalytic activity under visible-light irradiation, J. Alloys Compd. 476 (2009) 624–628.

[103] L. Chen, Q. Zhang, R. Huang, S.-F. Yin, S.-L. Luo, C.-T. Au, Porous peanut-like Bi_2O_3–$BiVO_4$ composites with heterojunctions: one-step synthesis and their photocatalytic properties, Dalt. Trans. 41 (2012) 9513.

[104] R. Bajaj, M. Sharma, D. Bahadur, Visible light-driven novel nanocomposite ($BiVO_4$/$CuCr_2O_4$) for efficient degradation of organic dye., Dalton Trans. 42 (2013)

6736–44.

[105] B. Liu, Z. Li, S. Xu, X. Ren, D. Han, D. Lu, Facile in situ hydrothermal synthesis of $BiVO_4$/MWCNT nanocomposites as high performance visible-light driven photocatalysts, J. Phys. Chem. Solids. 75 (2014) 977–983.

[106] X. Xu, Q. Zou, Y. Yuan, F. Ji, Z. Fan, B. Zhou, Preparation of $BiVO_4$-Graphene Nanocomposites and Their Photocatalytic Activity, J. Nanomater. 2014 (2014) 1–6.

[107] M. Xie, X. Fu, L. Jing, P. Luan, Y. Feng, H. Fu, Long-Lived, Visible-Light-Excited Charge Carriers of TiO_2 /$BiVO_4$ Nanocomposites and their Unexpected Photoactivity for Water Splitting, Adv. Energy Mater. 4 (2014).

[108] Y. Sang, Y. Huang, W. Wang, Z. Fang, B. Geng, Low cost visible light driven plasmonic Ag–AgBr/$BiVO_4$ system: fabrication and application as an efficient photocatalyst, RSC Adv. 5 (2015) 39651–39656.

[109] S.-W. Cao, Z. Yin, J. Barber, F.Y.C. Boey, S.C.J. Loo, C. Xue, Preparation of Au-$BiVO_4$ Heterogeneous Nanostructures as Highly Efficient Visible-Light Photocatalysts, ACS Appl. Mater. Interfaces. 4 (2012) 418–423.

[110] L. Chen, Y. Yu, M. Wu, J. Huang, Y. Liu, X. Liu, et al., Synthesis of Hollow $BiVO_4$ /Ag Composite Microspheres and Their Photocatalytic and Surface-Enhanced Raman Scattering Properties, Chempluschem. 80 (2015) 871–877.

[111] M. Long, J. Jiang, Y. Li, R. Cao, L. Zhang, W. Cai, Effect of Gold Nanoparticles on the Photocatalytic and Photoelectrochemical Performance of Au Modified $BiVO_4$, Nano-Micro Lett. 3 (2011) 171–177.

[112] A. Ibhadon, P. Fitzpatrick, Heterogeneous Photocatalysis: Recent Advances and Applications, Catalysts. 3 (2013) 189–218.

[113] J.A. Schwarz, C. Contescu, A. Contescu, Methods for Preparation of Catalytic Materials, Chem. Rev. 95 (1995) 477–510.

[114] D.B. and M.M. Malik Mohibbul Haque, Organic Pollutants Ten Years After the Stockholm Convention - Environmental and Analytical Update, InTech, 2012.

[115] R.. Sonawane, S.. Hegde, M.. Dongare, Preparation of titanium(IV) oxide thin film photocatalyst by sol–gel dip coating, Mater. Chem. Phys. 77 (2003) 744–750.

Chapter 2

Synthesis and characterization techniques

Doped $BiVO_4$ nanoparticles were synthesized by using mechano-chemical technique-high energy ball milling technique and Sol gel technique. All the materials are essentially characterized for their structural, morphological, electronic, optical, and photocatalytic properties. The X-ray diffraction (XRD), Field emission scanning electron microscopy (FESEM), High resolution transmission electron microscopy (HRTEM), Electron paramagnetic resonance (EPR), Atomic Forced Microscopy (AFM) and UV-Visible diffuse reflectance/absorption spectrophotometer techniques were employed for the systemic data collection and analysis. The principle, working mechanism and other associated experimental details are discussed in this chapter

2.1. Mechano-chemical synthesis technique

Milling is one of the well-practised techniques to realize several chemical compositions and structures. High energy ball milling is established as a mature and industrial technique, especially used for the size reduction of solid particles to nanometer scale [1]. Technical terms used to refer milling technique are mechano-chemistry or mechanical alloying or mechanochemical synthesis and its potential advantages of mechanochemical synthesis technique over conventional solvent-based chemical synthesis technique as outlined below:

- Increased reaction rates,
- Lower reaction temperatures,
- Simple execution
- Inexpensive [2]

- **Working principle**

The high energy ball milling (HEM) is a familiar technique and suitable for producing large scale, micro- and nano-sized materials for several applications. In the process of HEM, balls are made from hard phase materials like carbides or ceramics confined in a closed container together with sample powders such as metals and alloys. Products are obtained by high energy mechanical collisions with balls inside jar chamber with defined number of balls, rotation speed and time of reactions. Kinetic energy is transferred to powders trapped between colliding balls or between the inner surface of the container and a moving ball. During the

HEM process, repeated fracturing and welding ensures that the milling operations will lead to the solid state reaction of the individual materials resulting in the formation of the final composite materials. By this means, doping or alloying chemical elements can form micro or nanostructured powders with defined stoichiometry and crystalline order. Fig.2.1 illustrates the main steps involved in HEM synthesis. During mechanical milling such as repeated fracturing and welding process, continual stresses applied to ground powders may produce different kinds of defects. These defects would depend upon the dynamic milling conditions and to the mechanical, chemical properties of the ground materials. Especially ball-to-powder weight ratio, the milling atmosphere, the nature of the milling media (dry or wet), the nature of precursor and the type of mill [2, 3].

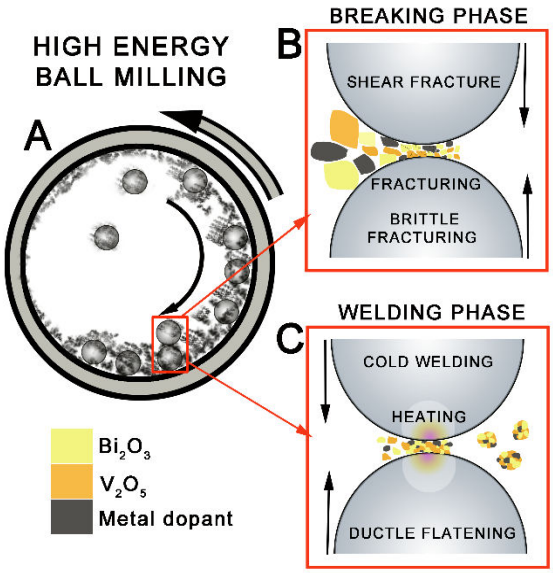

Fig.2.1. Schematic representation of high energy ball milling synthesis mechanism for metal ion doped $BiVO_4$ nanoparticle: (A) shows the content of the rotating (rpm) reaction chamber with hard balls and mixture of the initial reactants at defined stoichiometric ratios which define the final product. (B) illustrates the breaking phase, where repeated fracturing of bulk reactants cause formation of composite particles with desired composition. (C) Shows welding phase, where small agglomeration of particles forms the final morphology of the powder.

In our synthesis process, pristine and doped $BiVO_4$ samples were prepared by HEM technique. The starting materials were Bismuth oxide (99.999 %) and Vanadium oxide (99.99 %) and doping metal grains such as Cu (99.9%), Ag (99.9%) and Mo (99.9%) powders purchased from Sigma Aldrich with analytical grade. The reactants were used at different atomic percentages (*x)* in a stoichiometric ratio as given below in detail for each dopant. Initially the mixture was blended homogenously using agate mortar for the total mixture weight

of 7.7 grams which is equal to the weight of one tungsten carbide (WC) ball (9 mm diameter) and loaded inside 80 ml WC made jar. Retsch-planetary high energy ball mill PM 400 was used and the milling was performed for 6 hours at 400 rpm with 10:1 BPR ratio.

For Copper doping, Cu grains (<1mm, 99.9%) was used at different atomic percentages (x) along with Bi_2O_3 and V_2O_5 in a stoichiometric ratio of *[1: (1-x): x]* where Cu (1, 5 and 10 at.%). The as-prepared doped Cu-$BiVO_4$ samples were annealed at 450°C for 2 hours under air atmosphere to improve the crystallinity.

For Molybdenum doping, Molybdenum micro sized particle (99.9%) was added at different atomic percentages along with Bi_2O_3 and V_2O_5 in a stoichiometric ratio of *[1: (1-x): x]* where Mo (2, 6 and 10 at.%). Synthesis strategy was divided into three stages, In first stage Mo-$BiVO_4$ samples was annealed at 450°C for 2 hours, second step was to anneal these samples again at 700°C for 1 hour to improve the crystallinity of same samples. Finally these samples again were re-milled with milling parameters of 25:1 BPR, 400 rpm and 2 hours duration to obtain the nanoparticles.

For Ag/$BiVO_4$ synthesis, Bi_2O_3 , V_2O_5 and Ag micro particles (< 99.9% purity, 10μm diameter) were added in 1 : 1 : *x* stoichiometric molar ratio, where Ag (1, 3 and 5 at.%). After that as-prepared samples were annealed at 450°C for 2 hours under air atmosphere to improve the crystallinity.

Schematic illustration of steps followed in the mechano-chemical synthesis is depicted in Fig.2.2.

Fig.1.2. Schematic illustration of steps followed in the mechano-chemical synthesis of doped $BiVO_4$ nanoparticles with several dopants.

2.2. Sol gel synthesis technique

Solgel technique involves the generation of colloidal suspension (sol) which then subsequently converted to viscous gels and then to solid materials. This controlled method has many advantages [4] such as:

1. Low temperatures in all the stages, except during the densification stage. It is mostly (<100^{o}C) and often near room temperatures.
2. High purity and stoichiometry is achievable.
3. Organometallic precursors involving metal ions are miscible and homogeneous doping can be realized easily.
4. Chemical conditions are mild, strong acid or basic conditions are not required.
5. Highly porous and nanocrystalline materials can be prepared; through controlled rates of hydrolysis, condensation, aging and drying process, reliable control on particle size, porosity, porous size, pore wall etc can be achieved easily.
6. Since liquid precursors are used, it is possible to cast ceramic materials in various shapes to produce thin films without any requirement of melting and machining.

Generally sol-gel precursors consist of metal ions and other elements surrounded by various reactive species called ligands. The properties of sol–gel network that consists of hydrolysis and condensation reactions are affected by a number of factors, such as pH, temperature, time of reaction, reagent concentration, nature and concentration of the catalyst, aging temperature, time, and drying process. The sol–gel process generally involves four stages [5] as discussed below:

1. Hydrolysis

2. Condensation and polymerization of monomers for particle formation,

3. Nucleation of particles,

4. Coalescence of particles.

These stages are followed by the formation of materials that extend throughout the liquid medium, which results in the formation of the gel. During the sol–gel process, the most obvious precursors for oxides are molecules having metal-oxygen bonds, namely metal alkoxides $M(OR)_n$ where OR group is called as ligands. Similarly Bismuth nitrate penta hydrate and ammonium metavanadate has metal-oxygen bonds. Bismuth nitrate pentahydrate is dissolved in HNO_3, whereas ammonium metavanadate dissolves in water, which undergo hydrolysis and form transparent bismuth nitrate salt solution ‘A’ and yellowish vanadium nitrate salt solution ‘B’. The schematic work flow is shown in **Fig.2.3.** Hydrolysis and condensation can be represented by following simplest equations:

$$M\text{-}OR + H_2O \rightarrow M\text{-}OH + ROH$$

$$M\text{-}OR + HO\text{-}M \rightarrow M\text{-}O\text{-}M + ROH$$

$$M\text{-}OH + HO\text{-}M \rightarrow M\text{-}O\text{-}M + H_2O$$

Where M-metal and OR ligand groups. At the end of the hydrolysis and condensation, metal ions coordinate with oxygen and nitrogen atoms. Later chelating agent citric acid will be added slowly into metal salt solutions A and B respectively which acts as a stabilizing agent to control the rate of hydrolysis and condensation process. It lowers the reactivity of metal alkoxides with water. So that it forms a complex coordination with metal ions with ligands groups which consists of oxygen and nitrogen atoms.

Sol A + Sol B → Sol C.

At this stage, dissolved dopants can be added into the sol C under continuous stirring for at least one hour in order to achieve homogeneous consistency. Later, the pH value was adjusted at around 6.5 or 7 using NH_4OH solution and the solution is stirred on hot plate at 80 ^oC in order to initiate the reaction between them. The growth process then occurs in the supersaturated solution until the saturation concentration of the solid is attained. After nucleation and growth, the average particle size and size distribution can be changed by aging.

In a typical sol gel process, 0.01 mol $Bi(NO_3)_3 \cdot 5H_2O$ was first dissolved in 50 mL of 10% (w/w) HNO_3. The appropriate amount of citric acid was added until the molar ratio of citric acid and bismuth nitrate was 2:1 lablled as Solution A. NH_4VO_3 was dissolved in 80°C distilled water and the solution was magnetically stirred until the dissolution was complete. The appropriate amount of citric acid was then added until the molar ratio of citric acid and NH_4VO_3 was 2:1. The mixture was completely stirred to dissolve the solid, generating solution B. Solution A was then added drop-wise into solution B with continual magnetic stirring until the two solutions were mixed at a 1:1 M ratio to obtain solution C which can be seen in Fig.2.3.

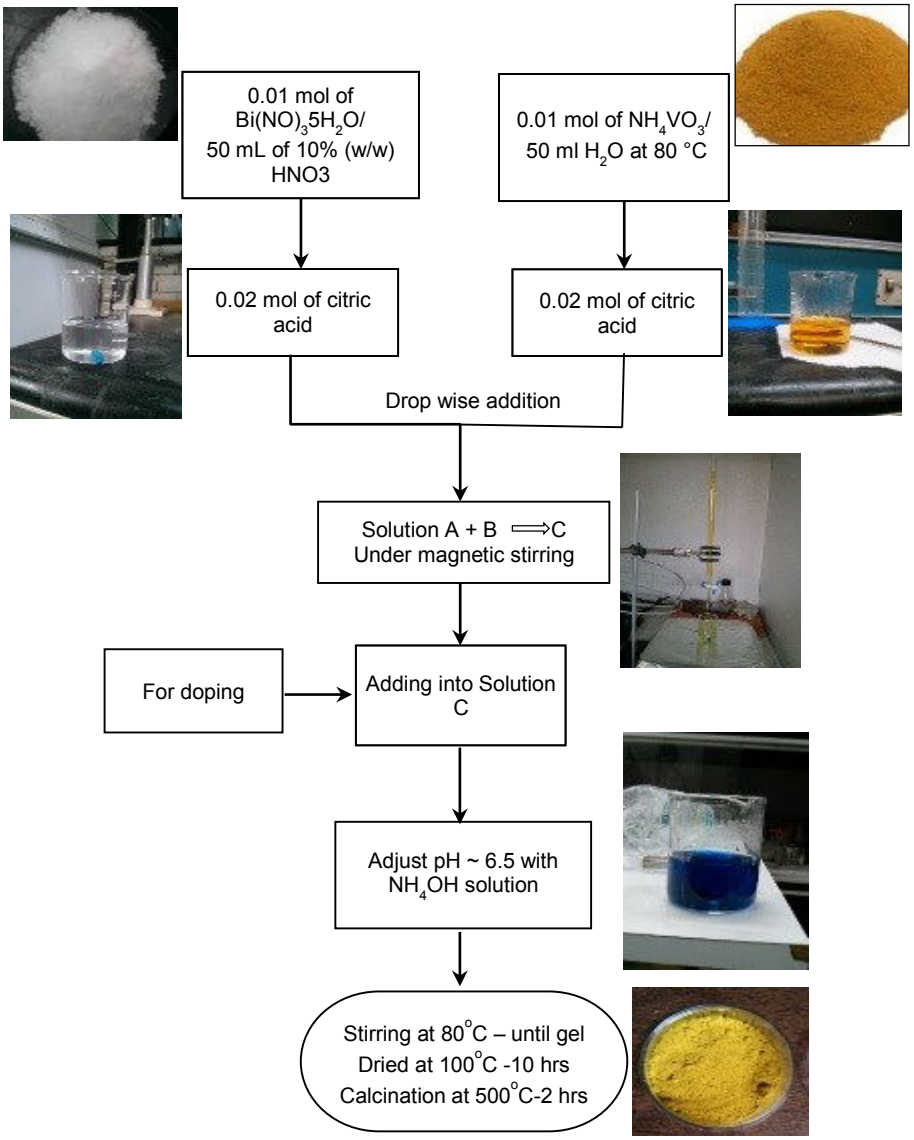

Fig.2.3. Schematic flow chart of sol gel synthesis techniques for preparation of doped $BiVO_4$ powders.

As dopants, Cu $(NO_3)_2$ $3H_2O$ and $AgNO_3$ were used 2 at.% molar ratio for Cu and Ag dopants, 2 at.% molar ratio of MoO_3 was dissolved in NH_4OH for Mo dopant, which were added into solution C and then stirred until it dissolves completely. In summary, we have 4 solutions which are undoped and doped by 2 at.% Cu, 2 at.% Ag and 2 at.% Mo-$BiVO_4$. Under vigorous stirring, the pH of the mixture was adjusted to approximately 6.5 using ammonia solution. The mixture was stirred at 80°C until the dark blue $BiVO_4$ sol–gel was obtained and then dried at 80°C in a drying chamber for 10 h to produce the $BiVO_4$ precursor. The resulting powder was collected and calcinated in air at 450 °C for 2 h with increment of 5°C per min, cooled to room temperature and then crushed to obtain a fine powder [6].

2.3. Preparation of $BiVO_4$ thin film by RF – Sputtering

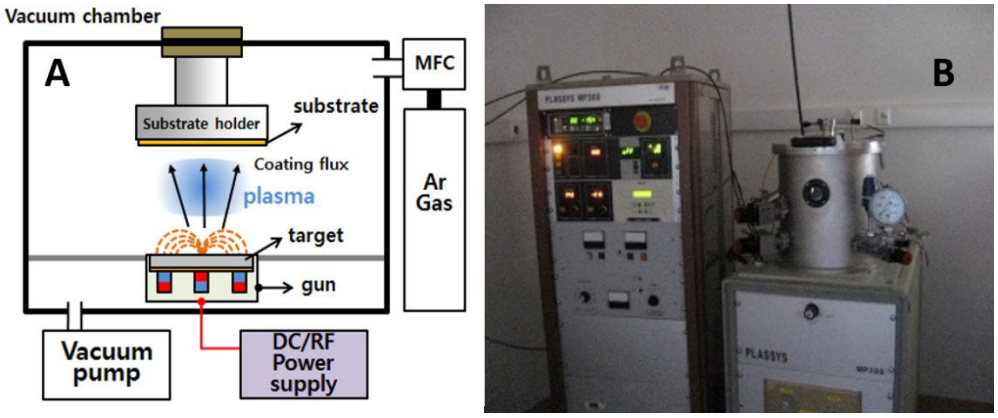

Fig.2.4. (A) schematic representation of rf-sputtering working mechanism; (B) rf-sputtering instrument used for doped $BiVO_4$ thin film depositions.

Thin film deposition by sputtering is considered as the most reliable technique, involving atom-by-atom deposition process. It is capable of depositing metals and compounds onto cooled and heated substrates at specific rates. It also ensures sputtering of non-conductive materials at enhanced rates. RF-sputtering has gained an excellent reputation for providing uniform and homogeneous preparation of different kinds of single or mixed oxides and can be used at both laboratory and industrial scales [7].

A schematic diagram is shown in Fig.2.4 (a), the equipment possesses a cryogenic vacuum pump which achieves almost $1x10^{-3}$ mbar. A RF power supply (50 Watt, 13.5MHz) is applied to cathode (35 mm diameter) planner target holder. The substrate is placed at the top of the deposition chamber. It has Argon (Ar) and Oxygen (O_2) as inlet gases for designing atmosphere in deposition chamber to a pressure between 10^{-3} to 10^{-2} mbar. A high negative voltage is applied to the target (cathode), while substrate holder (anode) is connected to chamber which is held at fixed potential. Under high voltage, gas is ionized and plasma is created between cathode and anode. Positive ions are accelerated from plasma into the target which is a negative potential with respect to the plasma. The energetic ions bombard the target surface with an energy given by the potential difference between the target and the other electrode. The bombardment process causes the removal, i.e., sputtering of target atoms, which may then collected onto the substrate as a thin film, where the target surface is considered as the source material. In this process, secondary electrons are also emitted from the target surface as a result of the ion bombardment and these electrons play an important role in maintaining

the plasma. Schematic representation of rf-sputtering technique, working mechanism and Plassys (MP 300) commercial rf-sputtering system used in this study are shown in Fig.2.4b.

Fig.2.5. Schematic representation (work flow) for the preparation of doped $BiVO_4$ powders by HEM and pellet preparation and to thin films deposition by rf-sputtering technique.

Cu and Mo doped $BiVO_4$ thin films were deposited by rf-sputtering system and the schematic representation was shown in Fig.2.5. Cu and Mo doped $BiVO_4$ targets were prepared using $BiVO_4$ doped powders with 5 at.% of respective dopants synthesized by HEM route. These powders were made as pellets made by 35 mm diameter stainless steel moulder and applied uniaxial hydraulic pressure near 8 ton for 30 seconds. This pressed pellet was annealed at optimized temperature of 700^oC for 10 hours. Metal doped $BiVO_4$ thin films were deposited on silicon substrates which were pre-cleaned, degreased ultrasonically and blown with double filtered N_2 gas before their introduction into chamber. The rf-sputtering deposition has been carried out under different ratio of atmosphere gas Ar (argon) and reactive gas O_2 (oxygen). Doped $BiVO_4$ thin films were deposited at three different conditions as tabulated below table 2.1. RF power is about 50 W and deposition time of 15 min are fixed in our experiments and these parameters are optimized by our group. Before deposition into the substrate, the target was pre-sputtered for 10 min, closing the substrate by stainless steel shutter. After this step, the deposition is realized onto the substrate with duration of 15 min.

Table 2.1. Rf sputtering deposition conditions used for depositing doped $BiVO_4$ thin films.

Case study	RFpower (Watts)	Gas flow (sccm)	Pressure (mbar)	Time (min)	Temperature (^oC)	Substrate
1	50	75	$5.2*10^{-2}$	15	RT	Si
2	50	60:12	$5.2*10^{-2}$	15	RT	Si
3	50	60:12	$5.2*10^{-2}$	15	450	Si

2.4. Characterization techniques carried out in our studies

2.4.1. X-ray diffraction spectroscopy

X-ray diffraction is a key technique to determine the phase and crystalline structure of materials whichever form they present such as bulk, thin films, nanoparticles etc.

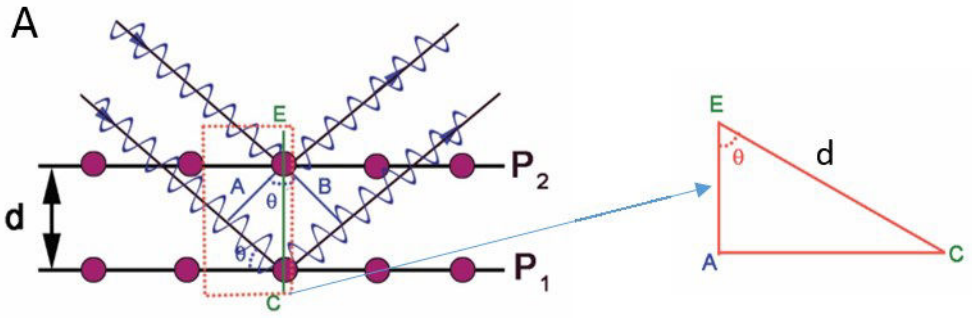

Fig.2.6. Diffraction of X-ray with constructive interference, d is the distance between the diffraction planes.

In XRD experiments, X-rays impinge upon the atomic planes involved in crystals and are scattered constructively to build patterns which account for the symmetry and the lattice dimensions. We can view the interaction of X-rays with a crystal due to reflection from the atomic planes as shown in Fig.2.6.

Scattered X-rays 1 and 2 will be completely in phase if the Bragg relation is satisfied i.e.

$$n\lambda = 2d \sin\theta \qquad \rightarrow(2.1)$$

From X-ray diffraction pattern we can obtain the following information:

1. Unit cell structure, lattice parameters and Miller indices,
2. Types of crystalline phases present in the materials,
3. Estimation of crystalline/amorphous contents in the sample,
4. Evaluation of the average crystalline size from the width of the peaks with higher intensity in a particular phase pattern by appropriate use of Scherrer relation [13]. In this frame, large crystal size gives rise to sharp peaks while the peak width increases with decreasing crystal size.

5. An analysis of structural distortion arising as a result of variation in *d*-spacing caused by the strain and thermal distortion.

Fig 2.7. PANanalytical system in IMMM lab.

In our studies, X-ray diffraction (XRD) patterns of all the powder samples were recorded on X-ray powder diffractometer (PANanalytical system) which operating at 40 kV and 30 mA using Cu *K*α radiation (λ=1.5418Å) (Fig.2.7). The 2θ range used for the measurements was from 10 to 70° with step size 0.033° with 20 sec per step with divergence slit (¼") and anti-scatter slit (½"). Crystal domain sizes were estimated from the diffraction peak widths (FWHM) using Scherrer's formula:

$$\tau = \frac{K\lambda}{\beta \cos\theta} \qquad \rightarrow (2.2)$$

Where, $'\tau'$ is the mean size of the ordered domains (crystallite size); $'K'$ is a dimensionless shape factor, with a value close to unity. The shape factor has a typical value of about 0.9 but varies with the shape of the crystallite; λ is the X-ray wavelength Cu Kα=0.154 nm; β is FWHM of peak at particular plane in radians. $'\theta'$ is the Bragg's angle.

The line broadening was measured by using a standard diffraction pattern of LaB_6 (Lanthanum Hexaboride powder). Instrumental broadening measured as 0.046 degrees (2θ) was subtracted from the FWHM observed diffracted patterns using equation (3).

$$FWHM_{2\theta} = \sqrt{(FWHM)^2_{observed} - (FWHM)^2_{LaB_6}} \qquad \rightarrow (2.3)$$

2.4.2. Raman spectroscopy

Theory and mechanism

Raman spectroscopy technique is based on inelastic scattering of monochromatic laser radiation. Raman effect is the change in the wavelength of light that occurs when the absorbed photons is deflected by the molecules in the sample. And then scattered with shifts of the frequencies due to photons involved in the structure. This shift provides information about vibrational, rotational and other low frequency transitions in molecules. Raman spectroscopy can be used to study solid, liquid and gaseous samples. Fig.2.8. illustrates the transitions involved during the Raman process.

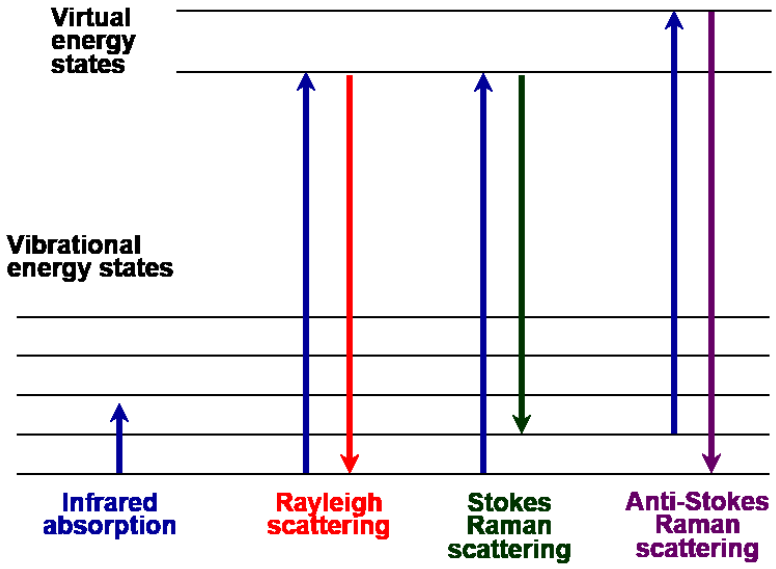

Fig.2.8. Energy-level diagram with states involved in Raman process.

After excitation of molecules by laser radiation with frequency υ_0, several features are involved:

1. The excited molecule returns back to its fundamental vibrational state and emits light with the same frequency υ_o as the excitation source. This interaction is called an elastic Rayleigh scattering.

2. When the final state is higher than the fundamental state by photon energy, the resulting frequency of scattered light is reduced to $\upsilon_0 - \upsilon_m$ (υ_m – molecular vibration frequency) and this is called Stokes scattering process.

3. A photon with frequency υ_0 is absorbed by a Raman-active molecule, an excess energy of excited Raman active mode is released, molecule returns to the basic vibrational state and the

resulting frequency of scattered light goes up to $\upsilon_0 + \upsilon_m$ (υ_m – molecular vibration frequency) and is called Anti Stokes frequency, or Anti-Stokes.

About 99.999% of all incident laser light in Raman undergoes elastic Rayleigh scattering which is useless for molecular characterization. Only about 0.001% of the incident light produces inelastic Raman signal with frequencies $\upsilon_0 \pm \upsilon_m$. The corresponding signals are very weak and should be distinguished from the dominant Rayleigh scattering. Generally, the Stokes-Raman bands on the low-energy side are stronger than the anti-Stokes-Raman bands on the high-energy side located symmetrically to Stokes bands with respect to the Rayleigh line [8].

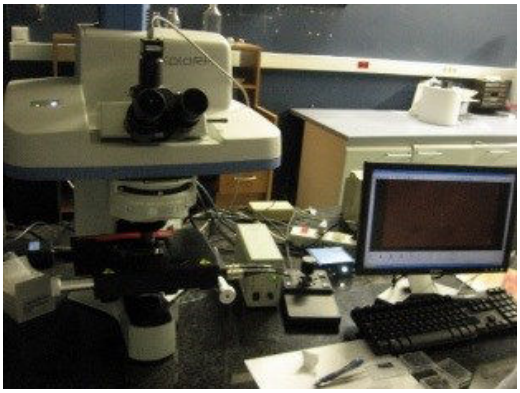

Fig.2.9. LabRAM Jobin Yvon Raman spectrometer.

Raman analysis were carried out on metal doped $BiVO_4$ samples using Micro-Raman LabRAM Jobin Yvon scientific X'plora with 638 nm wavelength red emission laser at 50X objective lens (Fig.2.9). Powder samples or thin films were exposed to laser light with 10% filter in order to avoid the samples overheating. The Raman spectra were recorded between 100 and 1200 cm^{-1} due to the main active modes being involved within that wavenumber range.

2.4.3. FE-SEM electron microscopy

FE-SEM technique analyses the surface characteristics such as morphology and chemical composition of the sample thanks to a high-energy beam of electrons. The electrons interact with the atoms which make up the sample giving rise to informative signals (Fig.2.10) on the sample's topographical information, elemental composition and homogeneity etc. A FE-SEM differs from usual SEM technique by the use of field-emission cathode as electron gun providing narrow probing beams at low currents as well as high electron energy beam under

high vacuums (10^{-1} Torr). With such instrumental parameters, analyses are realized by improved spatial resolution and minimized sample charging as well as less damage.

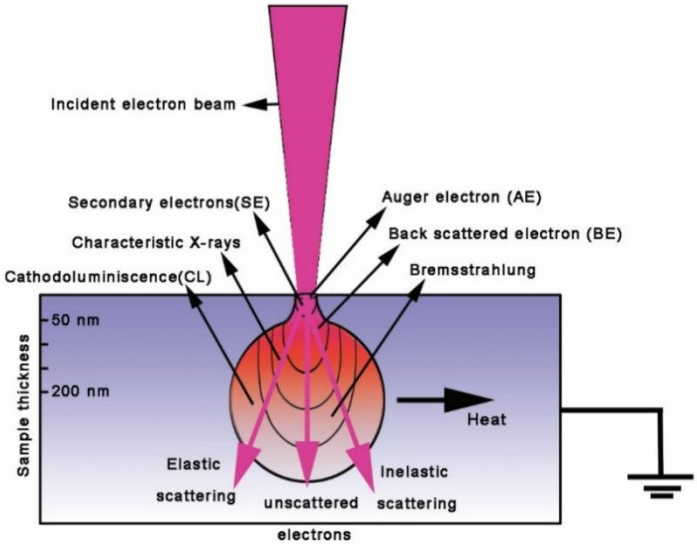

Fig.2.10. Types of emission from a specimen surface excited by the primary incident.

In our studies, morphology and composition studies for metal doped $BiVO_4$ powders and thin films were performed by using two instruments as shown in Fig.2.11. They are related FE-SEM from Carl Zeiss Auriga 60 available in LANE, Cinvestav-IPN, Mexico and JEOL, JSM 6510 LV Scanning electron microscopy available in IMMM, Universite du Maine, France. Accelerating voltage and variable slit sizes were adjusted for proper focus on samples, with manual corrected astigmatism and beam shape. Chemical composition analyses were measured by OXFROD-EDS detector with supported Aztec software for Jeol SEM, whereas, Bruker, PB-ZAF method, Sensor 5010, 129 eV resolution was used along with FE-SEM Carl Zeisis equipment.

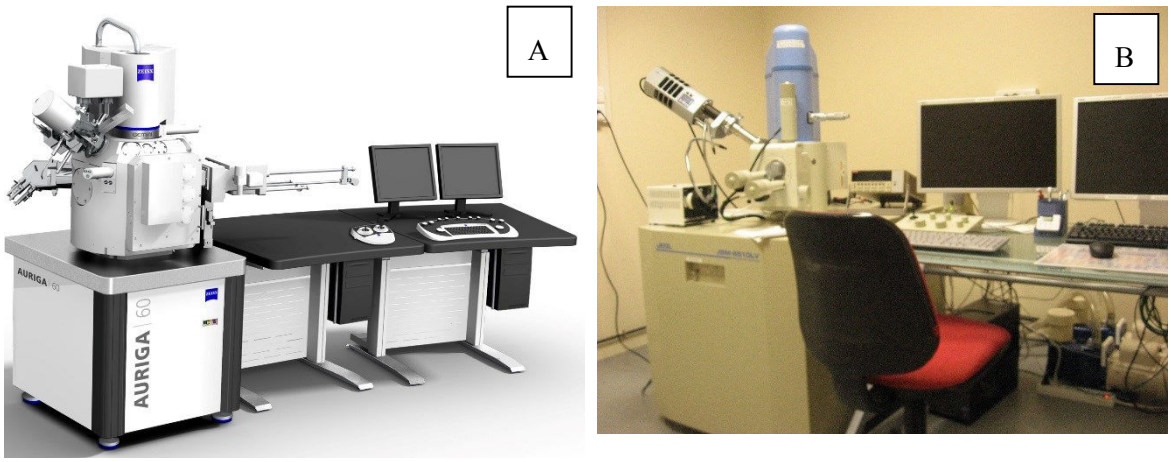

Fig.2.11. Carl Zeiss Auriga 60 and JEOL, JSM 6510.

2.4.4. High resolution transmission electron microscopy

High resolution transmission electron microscopy (HR-TEM) is particularly powerful technique to probe the matter at its ultimate atomic level and nanoscale resolutions. Moreover, the technique associates also electron diffraction tool able to probe the crystallography such space group of the involved structure. Also HR-TEM investigations provide explicit images of the system organization in nanoparticles, clusters, thin films etc.

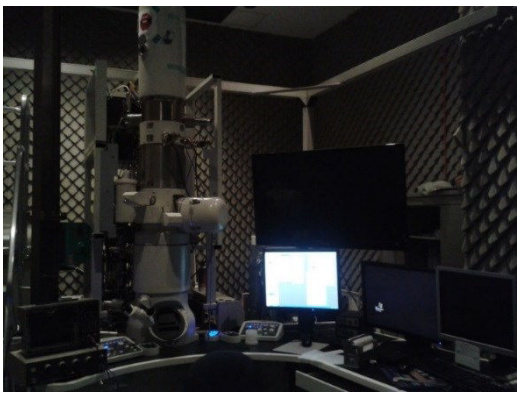

Fig.2.12. JEOL ARM200F in Cinvestav-IPN, Mexico.

The transmission electron microscope uses high energy electrons (typically 100 keV to 300 k eV), generated by an electron gun through either heating (thermionic emission) or the application of an electric field (field emission) followed by acceleration through the applied accelerating voltage. HR-TEM observations were obtained using JEOL-ARM200F as shown in Fig.2.12. It incorporated with a spherical aberration corrector for electron optic system as standard, has achieved a scanning transmission image (STEM-HAADF) resolution of 0.08 nm, the highest in the world among the commercial transmission electron microscopies.

2.4.5. X – Ray Photoelectron Spectroscopy (XPS)

X –ray photoelectron spectroscopy (XPS), or electron spectroscopy for chemical applications (ESCA), is a non-destructive spectroscopic technique for studying the surface of solids. Thus, this technique probes the composition of the samples on few nanometers close to the surface and possesses very high resolution to detect the involved elements even with very low concentrations (~ at 0.1 atomic percent abundance) except hydrogen.

In XPS experiments, when a sample is placed in the path of X-rays beam with defined energy, all the electrons of atomic species with binding energies less than the energy of the X-rays are ejected, with a kinetic energy dependent on the incident X- ray and the binding energy of the atomic orbitals. The kinetic energies of these photoelectrons are measured by an energy analyser in a high resolution electron spectrometer to determine the concentrations of the elements present as shown in Fig.2.13. The binding energy is indicative of a specific element and a particular structural feature of electron distribution. The electron binding energy of each of the emitted electrons can be determined by using an equation that is based on the work of Ernest Rutherford.

$$E_{BE} = h\upsilon - E_{kinetic} - \phi \qquad \rightarrow (2.4)$$

The relation between the binding energy and the kinetic energy is given by the equation (4) with E_b the binding energy of the electron, E_k its kinetic energy, $h\upsilon$ is the X-ray photon energy and ϕ the spectrometer work function (constant for a given analyzer) [9].

The obtained information from XPS investigations are the following:

- Elemental composition of the surface (top 0–10 nm usually)
- Eventual surface contaminant elements
- Chemical bonding and electronic states of the surface atoms
- Homogeneity of elemental composition across the top surface (or line profiling or mapping)
- Homogeneity of elemental composition as a function of ion beam etching (or depth profiling)

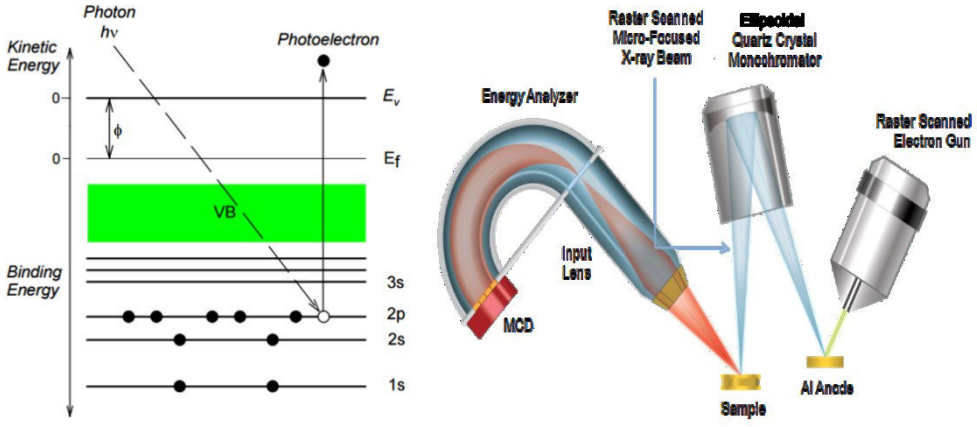

Fig.2.13. Scheme showing the principles of x-ray photoelectron spectroscopy (XPS).

The ability of this technique is used to study the enabled surfaces for bulk systems, thin films and nanostructures.

2.4.6. Ultraviolet-Visible (UV-Vis) Spectroscopy

Ultraviolet-Visible spectroscopy (UV-Vis) probes the optical absorption of different classes of materials in the UV-Vis-NIR region. For semiconducting compounds, the optical absorption curves can be used to evaluate the electronic band gap of the materials. In the case of doped materials, characteristic bands of doping elements may be detected and inform on occupied sites in the host matrices. In the case of organic compounds, the molecules with conjugated bonds with delocalized π-electrons or those with non-bonding electrons (n-electrons) possesses specific absorption bands reflecting the HUMO-LUMO energy difference. On the other hand, in the frame of photocatalytic degradation of organic dyes in solutions based on semiconducting photocatalysts. The method is most often used in a quantitative way to determine concentrations of the absorbing dyes in solution by using the Beer-Lambert law [10]

$$A = -\log_{10}\left(\frac{I}{I_o}\right) = \epsilon * c * L \qquad \rightarrow (2.5)$$

Where, A is the measured absorbance, I_0 is the intensity of the incident light at a given wavelength, I is the transmitted intensity, L the path length through the sample, and c the concentration of the absorbing species. For each species and wavelength, ε is a constant known as the molar absorptivity or extinction coefficient. This constant is a fundamental molecular property in a given solvent, at a particular temperature and pressure. This procedure was applied in the photocatalysis reactions performed and discussed below section 2.7.

In our studies, optical absorbance and energy band gap studies for metal doped $BiVO_4$ powders were investigated by using Varian Cary 500 UV-Vis- NIR spectrometer in a wavelength range from 350 nm to 800 nm.

2.4.7. Diffuse Reflectance Spectroscopy (DRS)

Diffuse reflectance is similar to UV-Vis spectroscopy applied to powdered or crystalline materials. It can also be used for analysis of intractable solid samples. Diffuse reflectance relies upon the focused projection of the spectrometer beam into the sample where it is reflected, scattered and transmitted through the sample material as shown in Fig.2.14. The back reflected, diffusely scattered light (with partial absorption by the sample) is then collected

by the accessory and directed to the detector optics. Only the part of the beam that is scattered within a sample and returned to the surface is considered to be related to diffuse reflection.

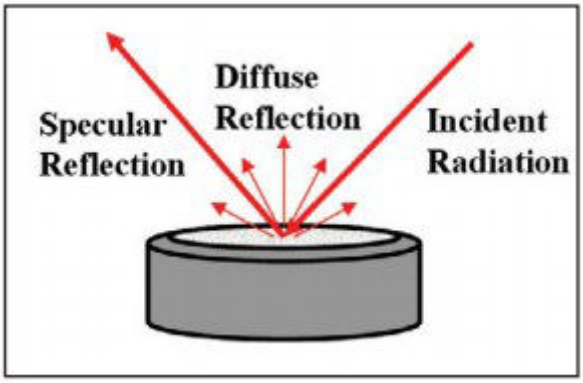

Fig.2.14. DRS Spectrometer working principle, where UV-Vis-NIR beam incident into the sample, where it is reflected, scattered and transmitted through the sample material.

Usually, the sample must be grinded properly, it can be also mixed with a non-absorbing matrix such as KBr. Proper grinding or dilution ensures a deeper penetration of the incident beam into the sample which increases the contribution of the scattered component in the spectrum and minimizes the specular reflection component. A Kubelka-Munk conversion can be applied to a diffuse reflectance spectrum to compensate these differences. The Kubelka-Munk equation (6) creates a linear relationship for the spectral intensity relative to the sample concentration (it assumes infinite sample dilution in a non-absorbing matrix, a constant scattering coefficient and an "infinitely thick" sample layer). For semiconductors, the absorption coefficient and band gap values can be estimated using DFR spectroscopy measurements. The band gap energies (E_g) for the various samples were calculated by plotting the values of $(\alpha h\upsilon)^n$ vs the photon energy ($h\upsilon$)[11].

In our studies, the UV-visible diffuse reflectance spectra were recorded on undoped and doped $BiVO_4$ powder samples in the range of 400-900 nm at room temperature with a UV-Visible spectrometer (UV-2500, SHIMADZU) and converted to an absorbance spectrum by the Kubelka–Munk method. From the absorption spectra, the optical band gap measurements were determined by using approximate formulae derived from Kubelka-Munk model (eq.6):

$$F(R) = \frac{(1-R)^2}{2R} = \frac{k}{s} = \frac{Ac}{s} \quad \rightarrow (2.6)$$

Where R is the absolute reflectance of the sample, k is the molar absorption coefficient, s is the scattering coefficient, c is the concentration of the absorbing species and A is the absorbance.

2.4.8. Atomic Force Microscopy

Atomic force microscopy (AFM) is a powerful technique for probing the topographical features of the material surface with a resolution at the nanoscale. AFM works by scanning a very sharp (end radius ca. 10 nm) probe along the sample surface, carefully maintaining the force between the probe and surface at a low level set. Usually, the probe is formed by a silicon or silicon nitride cantilever with a sharp integrated tip. The vertical bending (deflection) of the cantilever due to forces acting on the tip is detected by a laser focussed on the back of the cantilever as seen in schematic representation in Fig.2.15. The laser is reflected by the cantilever onto a distant photodetector. The movement of the laser spot on the photodetector gives a measurement of the movement of the probe. We have performed AFM analysis under non-contact mode, where the probe is moved over the sample in a little distant by a scanner, typically a piezoelectric element, which can make extremely precise movements. The NC AFM works via the principle "amplitude modulation" detection. The corresponding detection scheme exploits the change in the amplitude. The combination of the sharp tip, the very sensitive optical lever, and the highly precise movements by the scanner, combined with the careful control of probe-sample forces allow the extremely high resolution of observations made by AFM [12]

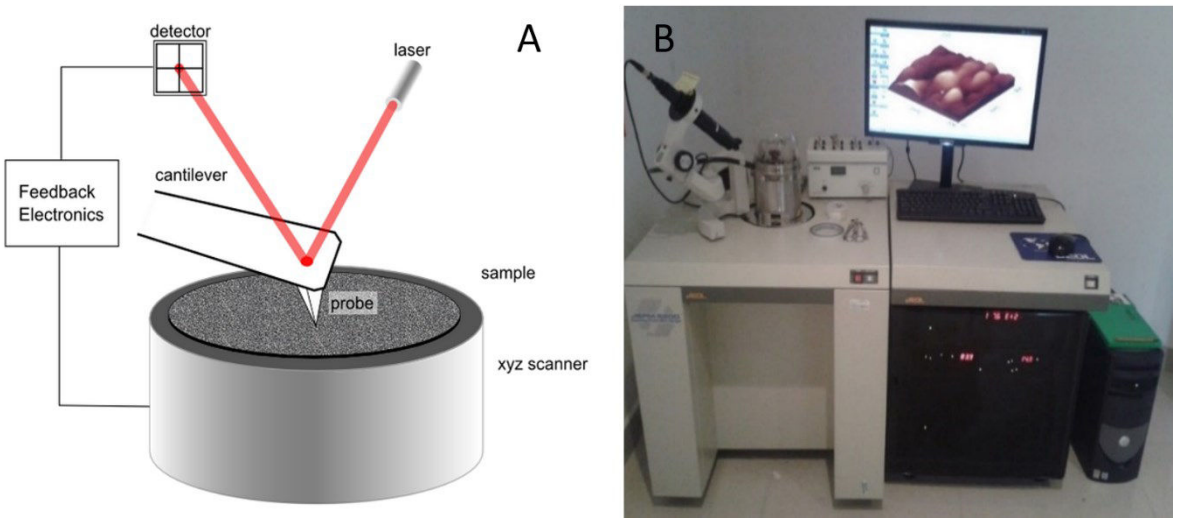

Fig.2.15. A) Schematic representation and B) Joel JSPM 5200 setup of AFM.

2.4.9. Electron Paramagnetic Resonance (EPR):

Electron Paramagnetic Resonance (EPR) spectroscopy, is also known as ESR (electron spin resonance) is a method which probe paramagnetic species present in investigated materials. The examples of applications are related to different classes of active elements such as free radicals such as hydroxyl ions, superoxide anions present in organic media, doping ions with particular electronic configuration in defined host sites of crystalline or amorphous materials, charged vacancies due to non-stoichiometry as in oxygen semiconductors. Despite of the nature of the paramagnetic centres and their concentration, the analysis of EPR spectra by specific numerical tools gives the spectral parameters that reflect the interactions between the paramagnetic species and their environments.

Theoretical background:

The theoretical background of EPR is based on the unpaired spins located on ions or molecules and giving rise to net magnetic moment on each paramagnetic centre. When a static magnetic field is applied on the host material with paramagnetic species, magnetic interactions occur and give rise to splitting of the spin energy levels. The local interactions of the paramagnetic centre with its surrounding ions modify also the energy levels for high spin values (spin>$^1/_2$). Additional interaction occurs when electronic spins are situated close to nuclei with nuclear spins leading to hyperfine interaction. The magnetic and environment interactions lead to defined energetic diagram of spin states with additional splitting in the case of hyperfine coupling. When the material is submitted to electromagnetic radiation in the X-band of microwave frequency 9.5 GHz, transitions between spin energy levels occurs and gives rise to EPR signal. The numerical simulations by suitable theoretical models determine the EPR spectral parameters which gives information about the paramagnetic centres.

From theoretical point of view and within the frame of (x. y, z) coordinates, the interactions of unpaired spin (S=1/2) is a consequence of coupling between electronic spin and external magnetic field (Zeeman interaction) as well as between electronic and nuclear spin I (hyperfine interaction). The interactions define the spin Hamiltonian as:

$$\hat{H} = \beta\left(B_x g_x \hat{S}_x + B_y g_y \hat{S}_y + B_z g_z \hat{S}_z\right) + \left(A_x \hat{S}_x \hat{I}_x + A_y \hat{S}_y \hat{I}_y + A_z \hat{S}_z \hat{I}_z\right) \quad \rightarrow (2.7)$$

In this expression, β represents Bohr magneton and the frame (x,y,z) refers to principal axes of g-tensor with the components $g_{x,y,z}$. The components $B_{x,y,z}$ are related to applied static

magnetic field and $A_{x,y,z}$ represent the hyperfine tensor (A-tensor) parameters which characterize the strength of hyperfine coupling [13].

Particularly, the g-tensor components exhibit departures ($\Delta g_{x,y,z}$) with respect to the Landé g-factor of free electron (g=2.0023). These shifts depend on the spin-orbit coupling and on the energies of fundamental and excited orbitals occupied by unpaired electrons. Interpretation of the parameters gives information about the environments of free radical ions and their electronic properties contributing to better understanding of conductivity of materials and also their relevance in catalytic processes.

EPR experiments were performed on EMX - Bruker spectrometer working in X-Band (9.5 GHz). The EPR signal is related to Vanadium ions (V^{4+}), Copper ions (Cu^{2+}) Molybdenum ions (Mo^{5+}) which occur in samples due to the stoichiometry departure as oxygen vacancies within $BiVO_4$ structures or from nanoparticle surfaces. The measurements were made at different temperatures by using Oxford cryostat in the range of 70 K-300 K. The resonance positions of EPR lines were accurately evaluated by using a characteristic EPR line of dry DPPH sample associated to g-factor about 2.0036. Experimental parameters such as microwave power, modulation field and detection frequency were chosen to avoid any resonant line distortion. A typical modulation field of about 1-5 Gauss and frequency modulation of about 100 kHz were used. The recorded EPR spectra were adjusted by using Bruker commercial software Winsinfonia.

2.4.10. Dielectric Relaxation Spectroscopy (DRS) analysis

Dielectric relaxation spectroscopy (DRS) represents a powerful method for the measurements of dielectric functions, electrical conductivity and characteristic relaxation times of dipolar or charge carriers motions in wide frequency and temperature ranges. The reorientation of dipoles and the translational diffusion of charged particles in an oscillating electric field provide the basis of the analysis based on alternating-current (AC) dielectric methods which principally measures of the complex permittivity (ε^*) in the frequency or time domain and at constant or varying temperature.

Theoretical background:

Polar molecules possess dipole moments which are oriented in a random manner in the absence of an electric field so that no macroscopic polarization exists. Under an electrical field the dipoles rotate to align along the electric field causing the occurrence of a polarization on the whole sample as shown in Fig.2.16. A material may have several dielectric mechanisms or

polarization effects that contribute to its overall permittivity. Dipole orientation and ionic conduction interact strongly at microwave frequencies.

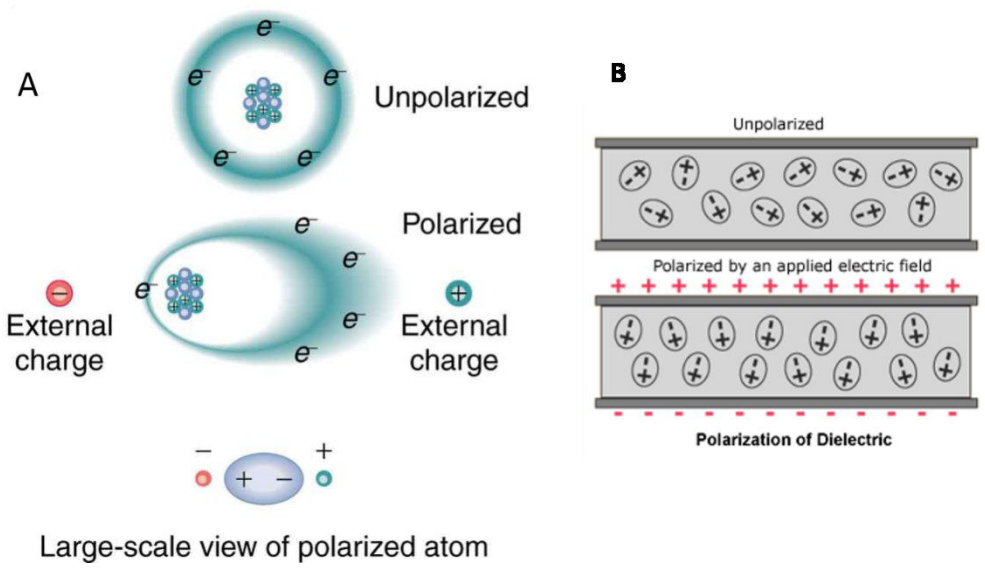

Fig.2.16. Net dipole moment per ion in the material without and with an externally applied field.

A complex dielectric permittivity consists of a real part and an imaginary part. The real part of the complex permittivity, also known as dielectric constant (at fixed frequency) is a measure

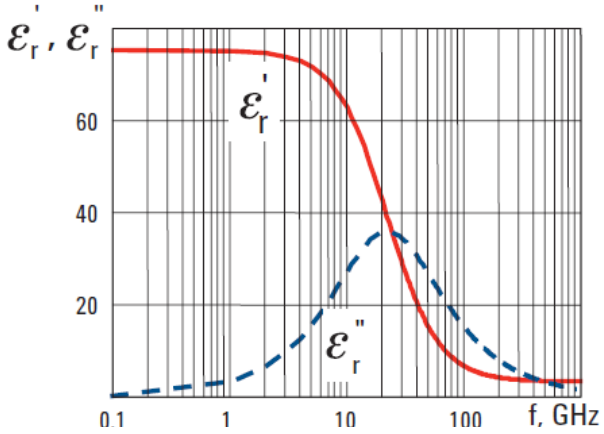

Fig.2.17. Schematic representation of the signal ascribed to a single-relaxation-time

of the amount of energy from an external electrical field stored in the material. The imaginary part is zero for lossless dielectric materials and is also known as loss factor. It is a measure of the amount of energy loss from the material due to an external electric field. Materials that exhibit a single relaxation time constant can be modelled by the Debye relation [14], which appears as a characteristic response in permittivity as a function of frequency (Fig.2.17). $\varepsilon'(\omega, T)$ is constant above and below the relaxation with the transition occurring near the relaxation frequency. Additionally, $\varepsilon''(\omega, T)$ is small above and below relaxation and peaks in the transition region at the relaxation frequency.

DRS determines the relative complex permittivity $\varepsilon^*(\omega,T) = \varepsilon'(\omega,T) + i\varepsilon''(\omega,T)$ with respect to applied alternative voltage with frequency $(\omega/2\pi)$ and at different temperatures from 213 K to 473 K. The analytical model usually applied to account for the frequency dependence of complex dielectric function $\varepsilon^*(\omega)$ is given by the Havriliak–Negami (HN) model [15]

$$\varepsilon^*(\omega) = \varepsilon'(\omega) - i\varepsilon''(\omega) = \frac{\sigma_{dc}}{i\omega\varepsilon_0} + \varepsilon_\infty + \frac{\Delta\varepsilon}{((1+i\omega\tau)^\alpha)^\beta} \quad \rightarrow(2.8)$$

In this expression, dielectric strength Δε represents the difference between the quasi-static dielectric permittivity ε_s and the high frequency referred to as ε_∞. The coefficient τ corresponds to a characteristic time related to the dielectric relaxation phenomena which is also closely related to the conductivity process as discussed below. The phenomenological parameters α and β, in the range $0 < \alpha, \beta < 1$, are related to the distribution of relaxation times due to some inhomogeneous processes. The coefficients α and β can be estimated only by tuning the experimental curves according to equation (1). For the frequency dependence (ac) and steady state (dc) conductivities, they are determined from the relation between the complex conductivity and dielectric function; i.e.

$$\sigma^*(\omega) = I\,\omega.\,\varepsilon_o\,\varepsilon^*(\omega) \quad \rightarrow(2.9)$$

From this relation, we can determine the static conductivity versus the temperature $\sigma_{dc}(T)$, as well as the frequency dependant part of the conductivity. By plotting $\sigma_{dc}(T)$ versus (1/T), we can estimate the thermal activation energy of the conductivity as function of the temperature ranges.

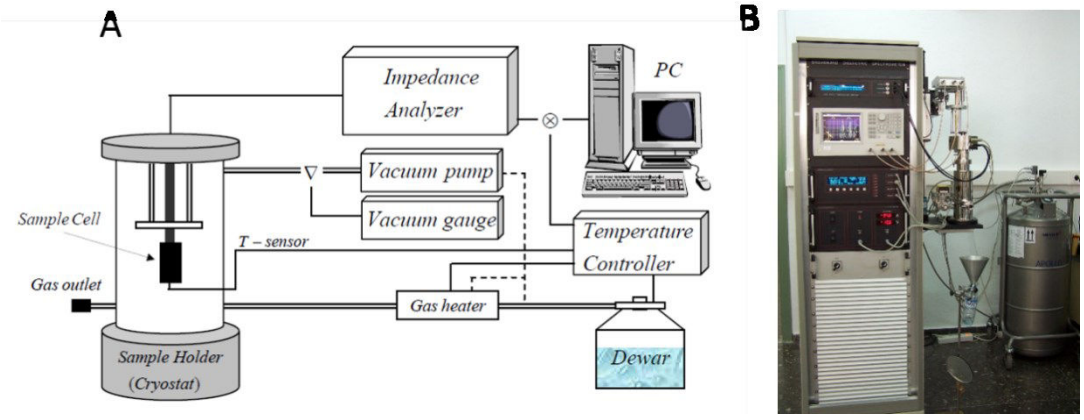

Fig.2.18. Schematic representation of dielectric measurement setup and Novocontrol set up in IMMM lab, Le Mans France.

Dielectric relaxation spectroscopy (DRS) measurements were performed by using Novocontrol broadband dielectric spectrometer (Fig.2.18). To cover the experiments in a wide frequency range (10 Hz to 100 KHz), an automated setup Solartron Sl-1260 combined with a broadband dielectric converter (BDC) were used to obtain impedance measurements. The sample temperature was varied between 273 K and 473 K with 20 K difference by using a stream of nitrogen gas and resistance with a controlled temperature close to sample within the accuracy of ± 0.1 K.

2.4.11. Photocatalytic set – up

Homebuilt photocatalytic reactor setup was used for photocatalytic studies. Photocatalytic activities of the samples were determined by the decolourization of organic dyes solution under exposure of simulated sunlight Hg (Xe) arc lamp-illuminator (Newport-67005) (50-500 Watts, λ= 200 – 2500 nm) used as a light source. The organic dye solution taken into a cylindrical flask and stirred continuously with a magnetic stirrer at moderate speed. The total photocatalysis system can be seen as schematic view in Fig.2.19(A) and experimental setup in Fig2.19(B).

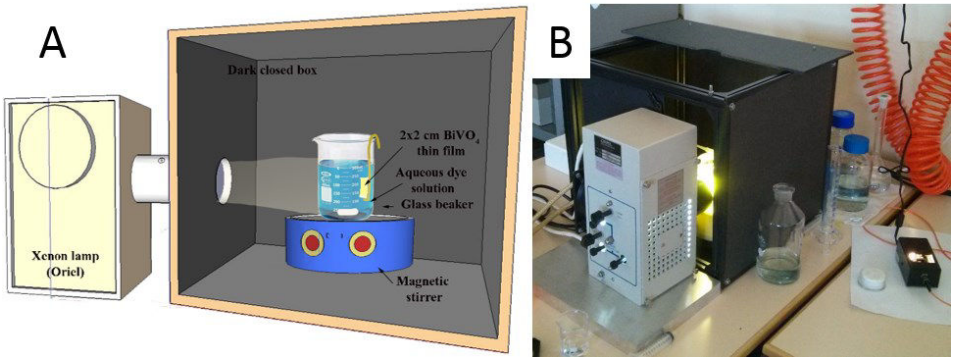

Fig.2.19. A) Schematic representation and B) experimental set up of photocatalytic reactor.

2.4.12. Photocatalytic experiments

Organic pollutants show continuous increase of their concentration in the environment due to several factors including human activities. As an example, the textile industries are the most contributor to such pollution problems through the use of hazardous dyes and colorants in high concentrations. Recently advance oxidation processes (AOPs) have got attention in destruction of organic and inorganic pollutants compared to conventional physicochemical and biological treatment methods. AOPs rely on in situ generation of highly reactive radical species, mainly hydroxyl (HO^*) radicals by using solar or chemical energy [16]. Azo dyes are considered as

harmful compounds due to their mutagenic and carcinogenic characteristics. Azo dyes chemical structure contains azo group (–N=N–) and aromatic groups. Therefore, removal of these species is crucial for saving the environment such as water sources.

The power of the lamp (75 W) was used without UV-cut off filter (cylindrical glass flask acted as filter for UV radiation). The photocatalytic activities of as-prepared $BiVO_4$ catalysts were evaluated by the degradation of organic dyes consist in methylene blue (MB), Acid blue 113 (AB 113) and Methyl orange as shown in Fig.2.20 with molecular structure in inset. Experiments were carried out at room temperature with the photocatalyst immerged in solution charged with organic dyes in defined molar concentration and with pH of the solution. Under irradiation, the optical absorption of the solution is measured at defined time slots. The decolourization of the remnant dye solution was measured by UV-Vis spectroscopy (UV-1800, SHIMADZU).

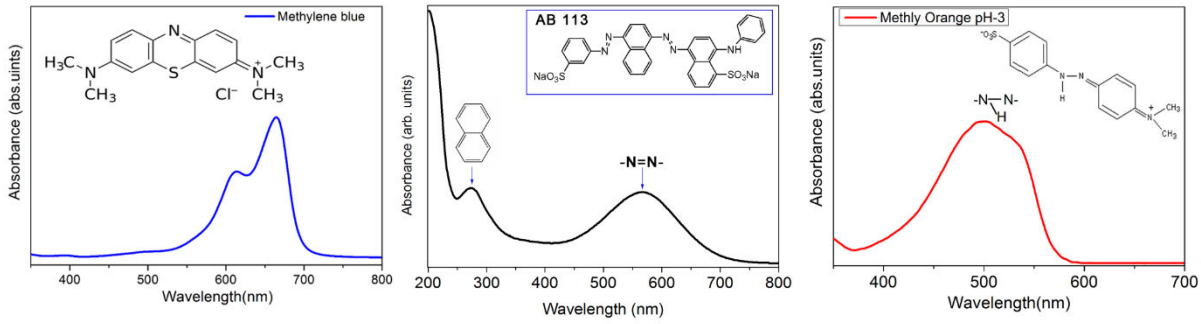

Fig.2.20. The optical absorbance of dyes Methylene blue (MB), Acid blue 113 (AB113) and Methyl orange (MO), along with its chemical structure in inset.

The kinetics involved in the degradation of dye with respect to photo-irradiation time were derived by using Pseudo first order kinetics equation as following relation:

$$[Abs]_t = [Abs]_0 \, e^{-tk} \qquad \rightarrow (2.10)$$

Where $[Abs]_0$ represents the initial absorbance, $[Abs]_t$ is the measured absorbance versus irradiation time t and k the degradation rate constant or pseudo-first-order rate constant, which is obtained as the slope (absolute value) of a linear relation from the plot.

In summary, Doped $BiVO_4$ nanoparticles were synthesized by using mechano-chemical technique-high energy ball milling technique (HEM) and sol-gel technique. Structural, morphological and optical properties are studied by using XRD, micro-Raman, FESEM, HRTEM, EPR, AFM and UV-Visible diffuse reflectance/absorption spectrophotometer techniques. The photocatalytic studies were performed by using homemade photocatalytic reactor setup with xenon lamp as visible light source.

References:

[1] V. Šepelák, S. Bégin-Colin, G. Le Caër, Transformations in oxides induced by high-energy ball-milling, Dalt. Trans. 41 (2012) 11927.

[2] K. Ralphs, C. Hardacre, S.L. James, Application of heterogeneous catalysts prepared by mechanochemical synthesis, Chem. Soc. Rev. 42 (2013) 7701.

[3] D.W. Kwon, K.H. Park, S.C. Hong, The influence on SCR activity of the atomic structure of V_2O_5/TiO_2 catalysts prepared by a mechanochemical method, Appl. Catal. A Gen. 451 (2013) 227–235.

[4] S.S. Alias, A.A. Mohamad, Synthesis of Zinc Oxide by Sol–Gel Method for Photoelectrochemical Cells, Springer Singapore, Singapore, 2014.

[5] F. Branda, The Sol-Gel Route to Nanocomposites, in: Adv. Nanocomposites - Synth. Charact. Ind. Appl., InTech, 2011.

[6] M. Wang, Y. Che, C. Niu, M. Dang, D. Dong, Effective visible light-active boron and europium co-doped $BiVO_4$ synthesized by sol-gel method for photodegradion of methyl orange., J. Hazard. Mater. 262 (2013) 447–55.

[7] P.. Kelly, R.. Arnell, Magnetron sputtering: a review of recent developments and applications, Vacuum. 56 (2000) 159–172.

[8] J.R. Ferraro, K. Nakamoto, C.W. Brown, Introductory Raman Spectroscopy, 2003.

[9] D. Briggs, Handbook of X-ray Photoelectron Spectroscopy C. D. Wanger, W. M. Riggs, L. E. Davis, J. F. Moulder and G. E.Muilenberg Perkin-Elmer Corp., Physical Electronics Division, Eden Prairie, Minnesota, USA, 1979. 190 pp. Surf. Interface Anal. 3 (1981)

[10] R. Sturgeon, Spectrochemical analysis, Spectrochim. Acta Part A Mol. Spectrosc. 44 (1988) 1229–1230.

[11] J.H. Nobbs, Kubelka-Munk Theory and the Prediction of Reflectance, Rev. Prog. Color. Relat. Top. 15 (2008) 66–75.

[12] D. Johnson, N. Hilal, W.R. Bowen, Basic principles of atomic force microscopy, in: At. Force Microsc. Process Eng., 2009: pp. 1–30.

[13] A. Kassiba, R. Hrabanski, D. Bonhomme, A. Hader, Electron paramagnetic resonance investigations of $MgSiF_6.6H_2O:Mn^{2+}$ single crystals, J. Phys. Condens. Matter. 7 (1995)

3339–3353.

[14] J. Macutkevic, J. Banys, A. Matulis, Determination of the Distribution of the Relaxation Times from Dielectric Spectra, Nonlinear Anal. Model. Control. 9 (2004) 75–88.

[15] S. Havriliak, S. Negami, A complex plane analysis of α-dispersions in some polymer systems, J. Polym. Sci. Part C Polym. Symp. 14 (2007) 99–117.

[16] T. Kudo, Y. Nakamura, A. Ruike, Development of rectangular column structured titanium oxide photocatalysts anchored on silica sheets by a wet process, Res. Chem. Intermed. 29 (2003) 631–639.

Chapter 3

Mechano-chemical synthesis and characterization of doped $BiVO_4$ powders for photocatalytic applications

The high energy ball milling synthesis method was demonstrated as an appropriate technique to obtain high purity $BiVO_4$ powders with homogeneous composition with single crystalline phase. The challenge in this present work is to use this technique to obtain metal doped $BiVO_4$ with stabilized monoclinic scheelite phase and substitutional doping elements within the crystal sites. Thus, this chapter is devoted to the mechano-chemical synthesis and characterization of $BiVO_4$ nanoparticle doped with several metal ion such as Copper (Cu), Molybdenum (Mo) and Silver (Ag) with different atomic percentages. The selection of the doping elements was made in such a manner induce changes into the electronic band structure of $BiVO_4$ and to improve the photo-induced charge transfer required in photocatalytic reactions. The parameters of this synthesis will be tuned to obtain the relevant features of the doped powders. This include organisation of nanostructured powders offering larger specific surface area, pure crystalline phase and location of doping metal ions in defined crystal sites that modifies coherently electronic structure of the materials. The characterization methods will be used in the way to make complementary analyses of all relevant features (structural, electronic and optical) for the applications of heterogeneous photocatalysis for water purification by degradation of organic compounds.

This chapter is divided into three sections that are dedicated to three doping metal species Cu, Mo and Ag used for modifying $BiVO_4$ catalyst. Synthesis of metal doped $BiVO_4$ will be described with the search of optimized conditions leading to specific morphologies of the samples, crystal structure and crystalline sites of host for doping ions. The investigations of physical features were analysed by complementary techniques and discussed as a function of electronic modifications induced by doping elements. The photocatalytic reactions were performed in aqueous solutions with several organic dyes. Photocatalytic degradation and efficiencies will be discussed as following as peculiarities of the representative metal doped $BiVO_4$ photocatalysts.

3.1. Mechano-chemical synthesis of copper doped $BiVO_4$ powders

3.1.1. Importance of Cu doped $BiVO_4$ in the prospect of photocatalysis

Nowadays, transition metal ions doped semiconductor nanocrystals are coming forth as a new alternative to conventional single metal oxide materials with tunable, intense and stable emission in visible as well as in near-IR spectral window for various photocatalytic and optoelectronic applications. Recently, the study of Cu doping for photocatalytic has attracted more attention, through Cu p-type doping of semiconductor materials which increases the density of "holes" as well as the lifetimes of photogenerated excitons required for a high performances [1]. The process is based on the presence of Cu cations with energies of d states located near to the semiconductor valence band [2]. Cu ions act as an electron traps reducing effectively the photogenerated electron-hole recombination rate in photocatalytic reactions [3]. Moreover, Cu doped nanophotocatalysts show spectral broadening of the absorption bands in the visible spectrum with a dependence on the composition and the local environment of Cu ions in the host materials [4]. Xu et al. synthesized Fe, Co and Cu loaded $BiVO_4$ by wet impregnation method and found that the Cu-loaded $BiVO_4$ has shown highest photocatalytic activity compared to other transition metals [5]. Park et al analyzed the effect of metal ions Co^{2+}, Ni^{2+}, Cu^{2+} and Zn^{2+} doped TiO_2 nanofibers were fabricated by a sol-gel method and electro-spinning technique. The Zn and Cu doped $BiVO_4$ has shown promising photocatalytic efficiency in the degradation of methylene blue dye solution. Similarly, Yang et al investigated the effect of doping Cu-TiO_2 mesoporous structure on the degradation rate of methyl orange as compared to pristine mesoporous structure [6].

The forthcoming sections are dedicated to ball milled $BiVO_4$ with Cu-doping to understand suitable doped structures and compare their photocatalytic reactions. Detail discussion on characterizations techniques applied and in depth analyses were realized such as pure monoclinic crystalline phase and substitutional location of Cu ions inside the crystal sites of $BiVO_4$ on the Cu doped samples.

3.1.2. Results and discussion

This part reports the characterizations of Cu-$BiVO_4$ X-ray powder diffraction (XRD) and micro-Raman for structural studies, Field Emission Scanning electron microscopy (FE-SEM) and High resolution transmission microscopy (HR-TEM) for the morphology, particle size and homogeneity of the materials. These studies were also supported by X-ray

photoelectron spectroscopy (XPS) which probes the involved chemical bonding. As Cu^{2+} are paramagnetic ions, electron paramagnetic spectroscopy (EPR) studies were performed on several doped samples to evaluate the degree of substitution and to study about the distribution of doped species inside the host matrices. The evolution of the optical band gap was investigated and correlated with the structural and electronic changes induced by Cu doping.

3.1.2.1. X-ray powder diffraction

Diffraction patterns of Cu–$BiVO_4$ powders at different Cu concentrations exhibit monoclinic scheelite phase according to the standard JCPDS data (014-0688) depicted in Fig.3.1 along with Cu-$BiVO_4$ refined pattern. It has been noticed that the high intense diffraction peak (-121) corresponding to Cu-$BiVO_4$ samples shifts towards a higher angle (2θ) compared to pure $BiVO_4$ as shown in inset of Fig.3.1. This shift occurs from structural distortions are due to compressive strains due to the incorporation of copper into the crystal sites of $BiVO_4$ structure. The diffraction angle lines N {denoted by $N= h^2 + k^2 + l^2$} such as 2 (110, 011), 4 (200, 002), 6 (211, -112), 14 (231, 132), 20 (240, 042) doublet peaks were merging for highly doped Cu-$BiVO_4$ samples (Fig. 3.1 C, D). The intensity of the lines completely depend on the arrangement of atoms in the unit cell. The decrease in the intensity and an increase in the FWHM of the diffraction lines can be attributed to disorder in the location of Cu inside the lattice or by distortions, due to size differences between substituted ions. It is worth noting that all the as-prepared samples were annealed at the same temperature i.e. 450°C, which is defined as an optimal temperature for monoclinic polymorph phase formation for pristine form [7]. However, this temperature cannot be optimized to reproduce the good crystalline structure in Cu doped $BiVO_4$ for higher doping rates. Crystal domain sizes of $BiVO_4$ and Cu-$BiVO_4$ were calculated from Scherrer's formula and given in Table 3.1. The XRD line broadening FWHM values subtracted from the standard FWHM of the used reference LaB_6 fixed at $\Delta(2\theta)=0.046°$(for further details Chapter 2. Section 2.4.1). The average size of crystalline domains in Cu-$BiVO_4$ is situated in the range 33 – 40 nm with the lowest size in the heavily doped sample.

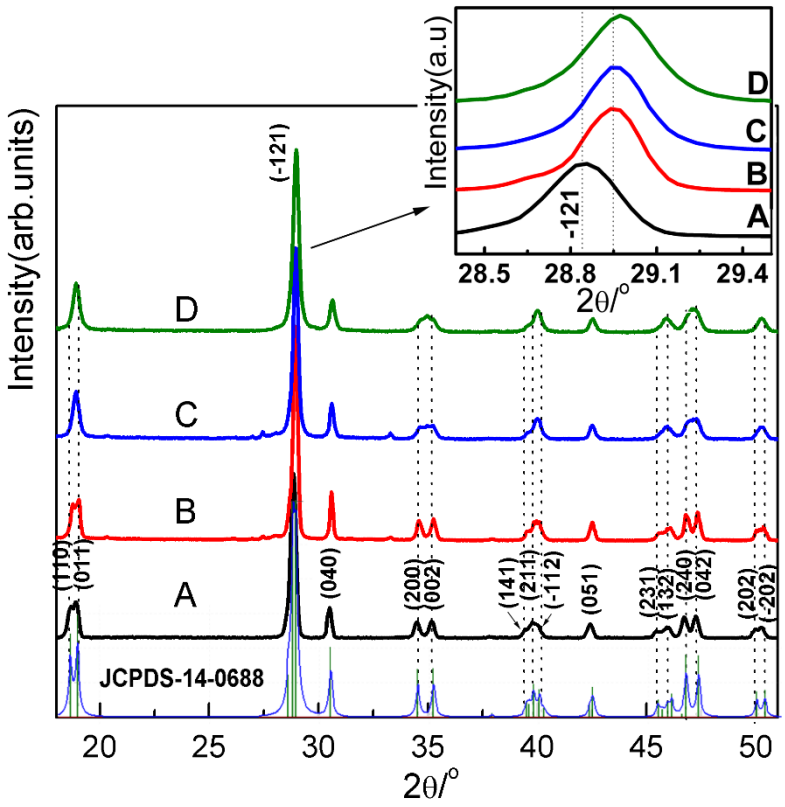

Fig.3.1. X-ray diffraction patterns of copper doped $BiVO_4$ nanopowders with different Cu doping ratios with reference to standard (JCPDS-14-0688) monoclinic scheelite $BiVO_4$ data. Samples labelled as A, B, C and D for pure, 1at.%, 5at.% and 10at.% respectively.

Table 3.1. Calculated coherent diffracting domains from Scherrer's formula and optical band gap values of Cu-$BiVO_4$ samples.

Labels	Samples	FWHM	2θ position (-121)	Crystallite size(nm)	Band gap E_g(eV)
A	**$BiVO_4$**	0.220	28.86	37.78	2.41
B	**1at.% Cu-$BiVO_4$**	0.206	28.946	40.49	2.40
C	**5at.% Cu-$BiVO_4$**	0.231	28.958	35.9	2.37
D	**10at.% Cu-$BiVO_4$**	0.2505	28.973	33.03	2.34

The distribution of the copper ions in the lattice are the reasons for a shift in diffraction lines and increased FWHM with respect to the doping rates. The doping process alters the crystallographic lattice parameters as illustrated below for 10 at.% doped sample (Table 3.1.2a). Indeed, crystal unit cell dimensions were refined by Rietveld method using MAUD software as shown in Fig.3.2. The diffraction patterns for doped and undoped samples were adjusted to standard monoclinic system with space group I2/c. The refined data such as lattice parameters and characteristic 2θ shifts are summarized in table 3.1.2a and depicted in Fig.3.3

for various Cu doping rates. The refined crystallographic data reveals a reduction of lattice parameters with the amount of Cu-doping. The atomic positions of Bi, V, O1 and O2 summarized in table 3.2(B) indicate lattice compression in the direction of crystallographic axes 'a' and 'c' and also a compression in V-O covalent bonds of the VO_4 tetrahedron [8]. Since the atomic radius of Cu (1.45 Å) is less than V (1.71 Å), the incorporation of Cu ions in $BiVO_4$ matrix will be as a substitution to V ions leading to a reduction of the lattice parameters. Structural distortions in VO_4 tetrahedron are expected to induce an internal electric field that contributes to the separation of electron-hole pairs. Hence, metals doped $BiVO_4$ materials are of particular interest for the photocatalytic processes [9].

Table 3.2(A) Phase composition and crystallographic lattice parameters of monoclinic Cu doped $BiVO_4$ nanopowders, refined by Rietveld method from X- ray powder diffraction patterns.

X	**Phase fraction**				**Crystal lattice parameters**			
Sample name	$BiVO_4$	Bi_2O_3	V_2O_5	Crystal size(nm)	a(Å)	b(Å)	c(Å)	γ(°)
1at%Cu-$BiVO_4$	98.6 (±0.02)	1.3 (±0.008)	0 (±0)	43	5.189 ($\pm3.2e^{-4}$)	5.100 ($3.2e^{-4}$)	11.707 ($6.4e^{-4}$)	90.297
5at%Cu-$BiVO_4$	97.6 (±0.02)	2.3 (±0.004)	0 (±0)	40	5.161 ($\pm4.2e^{-4}$)	5.097 ($4.1e^{-4}$)	11.675 ($8.4e^{-4}$)	90.1806
10at%Cu-$BiVO_4$	100 (±0.03)	0 (±0)	0 (±0)	31	5.156 ($\pm4.5e^{-4}$)	5.097 ($4.3e^{-4}$)	11.607 ($9.1e^{-4}$)	90.1406

Table 3.2(B) Atomic positions of monoclinic phase in Cu doped $BiVO_4$ nanopowders refined by Rietveld method for different Cu doping rates.

Sample name	**Bi**			**V**			**O1**			**O2**		
1at.%Cu-$BiVO_4$	0	0.249	0.632	0	0.25	0.128	0.144	0.472	0.2019	0.325	0.353	0.429
	(±0.002-0.003)			(±0.002-0.003)			(±0.002-0.003)			(±0.002-0.003)		
5at.%Cu-$BiVO_4$	4.7e-4	0.25	0.63	0.01	0.315	0.111	0.137	0.55	0.22	0.278	0.384	0.428
	(±0.002-0.003)			(±0.002-0.003)			(±0.002-0.003)			(±0.002-0.003)		
10at.%Cu-$BiVO_4$	2.5e-4	0.249	0.635	0.012	0.31	0.116	0.132	0.55	0.216	0.28	0.383	0.435
	(±0.002-0.003)			(±0.002-0.003)			(±0.002-0.003)			(±0.002-0.003)		

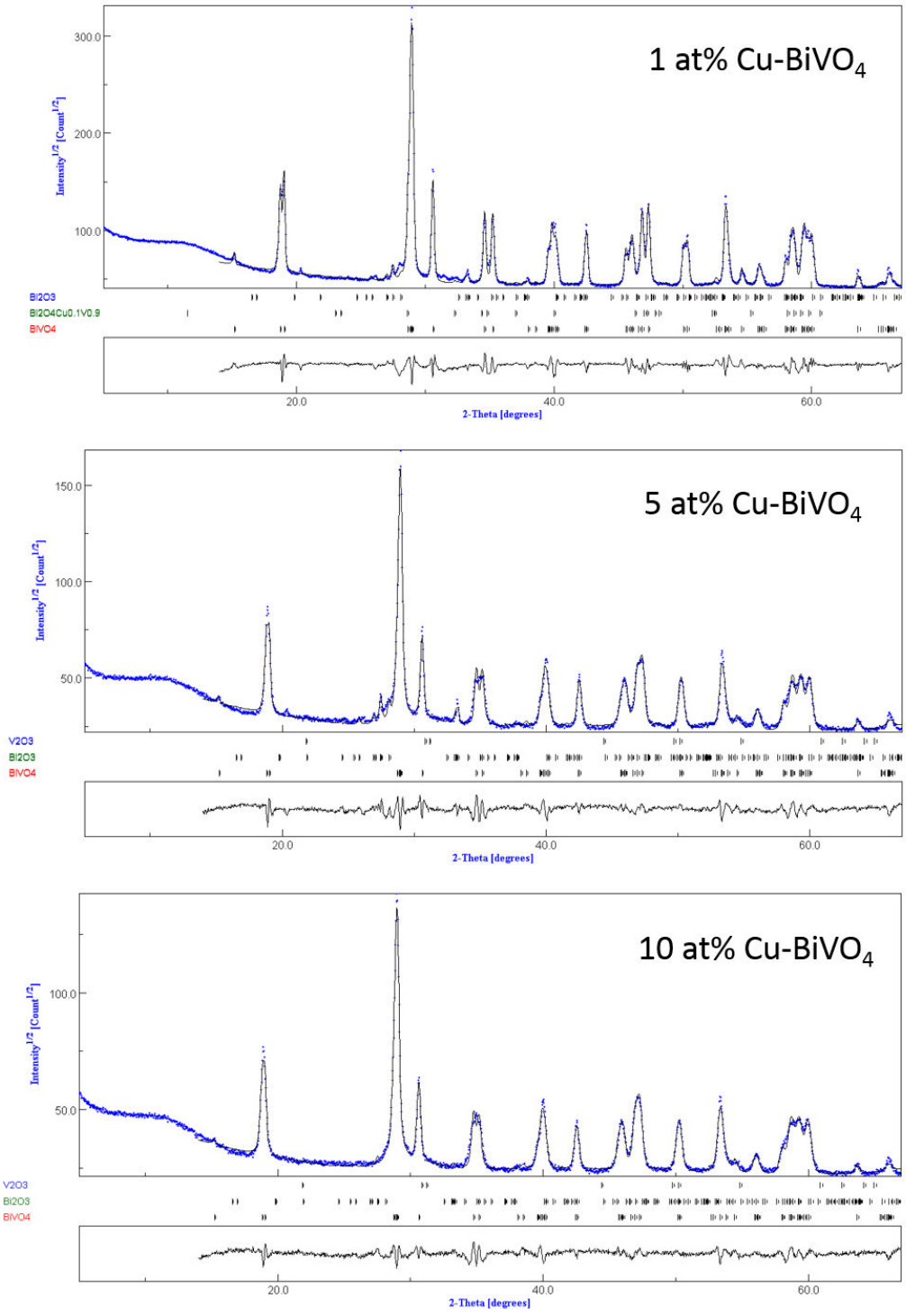

Fig.3.2. Refinement of Cu-doped $BiVO_4$ powders by using MAUD software.

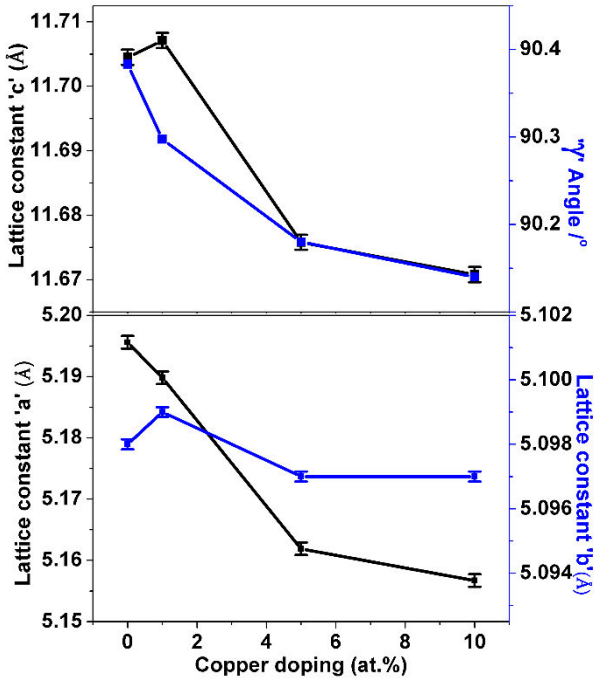

Fig.3.3. Crystallographic lattice parameters obtained from refined XRD patterns by Rietveld method for Cu-$BiVO_4$ samples.

3.1.2.2. Raman analysis

Raman spectroscopy is an efficient tool for probing the structure and bonding in metal–oxide species through their vibrational characteristics. In the monoclinic phase of $BiVO_4$, the Raman spectra (Fig.3.4) exhibits six noticeable vibrational bands at 210, 327, 367, 637, 702 and 826 cm^{-1} which are related to the vibrational features of VO_4 tetrahedron [10]. The intense band at 826 cm^{-1} was attributed to the shorter symmetric V–O stretching mode (A_g) and the weak bands at 702 and 637 cm^{-1} were assigned to the long (Ag) and short (Bg) asymmetric V–O stretching modes respectively. The asymmetric and symmetric bending vibrations of the VO_4 tetrahedron were detected at 327 and 367 cm^{-1} respectively accordance with the report by Sandhya Kumari et al [11]. By using higher doping rates as 5 at.% and 10 at.%, the V–O stretching modes (819, 821 cm^{-1}) of the Cu-$BiVO_4$ are shifted to a lower wavenumber as compared to the pure sample or for low doping rate (i.e. 1 at.%). Such results are consistent with elongation of bond length of V–O for highly Cu doped $BiVO_4$ samples. Similar effects were reported in $BiVO_4$ grown by wet chemistry under different conditions where the shift of Raman bands is attributed to structural distortions which are induced by modified electronic band structures of $BiVO_4$ [12]. In addition to the behaviour of the Raman band intensities, the FWHM of the major Raman band associated to symmetric stretching mode at 826 cm^{-1} little

broaden with Cu content as illustrated in Fig.3.4. This behaviour correlates with the degree of crystallinity or defects including oxygen vacancies. Similar effects were reported previously with other doping element of cobalt leading to shifts and overlap of the Raman bands of VO_4 tetrahedrons [13]. The analysis of the Raman spectra affirms the conclusions inferred from XRD investigations and gives consistent support to the structural evolution induced by Cu-doping in monoclinic scheelite phase of $BiVO_4$.

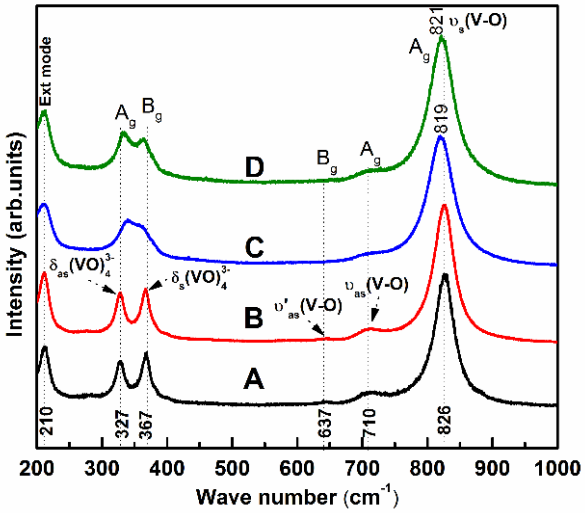

Fig.3.4. Raman spectra of copper doped Cu-$BiVO_4$ samples with the assignment of stretching and bending modes with their respective notations. Samples are referred as A, B, C and D for undoped $BiVO_4$, 1 at.%, 5 at.% and 10 at.% in Cu-$BiVO_4$ respectively.

3.1.2.3. FESEM analysis

FE-SEM microscopy images of Cu-$BiVO_4$ nanoparticles show a spherical shape and sizes ranging from 40-160 nm (Fig.3.5). The particles are found to be composed by small and nanosized grains. The "image J 1.48v" software was used for the quantitative evaluation of the particle size distribution. Noticeable reduction in the particles sizes was clearly seen for higher Cu doped samples as depicted by particle size distribution plots given in the inset of Fig.3.5. The main reason lies in the effect of Cu incorporation on the thermodynamic properties of the ball milled powders as previously attributed to the fact that Cu-doping of $BiVO_4$ inhibits the particle growth [14]. The elemental composition analysis was performed by EDAX for Cu-$BiVO_4$ nanoparticles and their atomic (at.) % values are summarized in Table 3.3. Chemical element distribution mappings were also carried out for Bi, O, V and doping ions Cu as illustrated in the Fig.3.6. Within the uncertainty of the EDAX, homogenous distributions of elements were inferred, testifying the absence of agglomeration or some phase segregations.

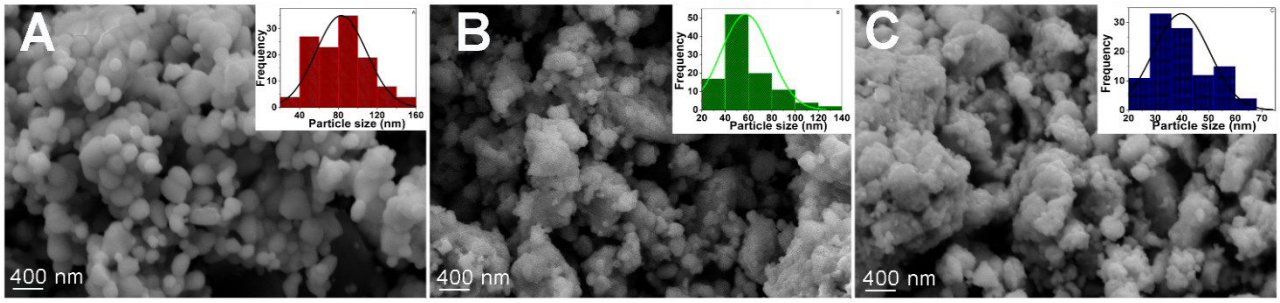

Fig.3.5. FE-SEM images for copper doped $BiVO_4$ nanopowders for (A): 1 at.%, (B:) 5 at.%, (C): 10 at.% with particle size distributions as inset.

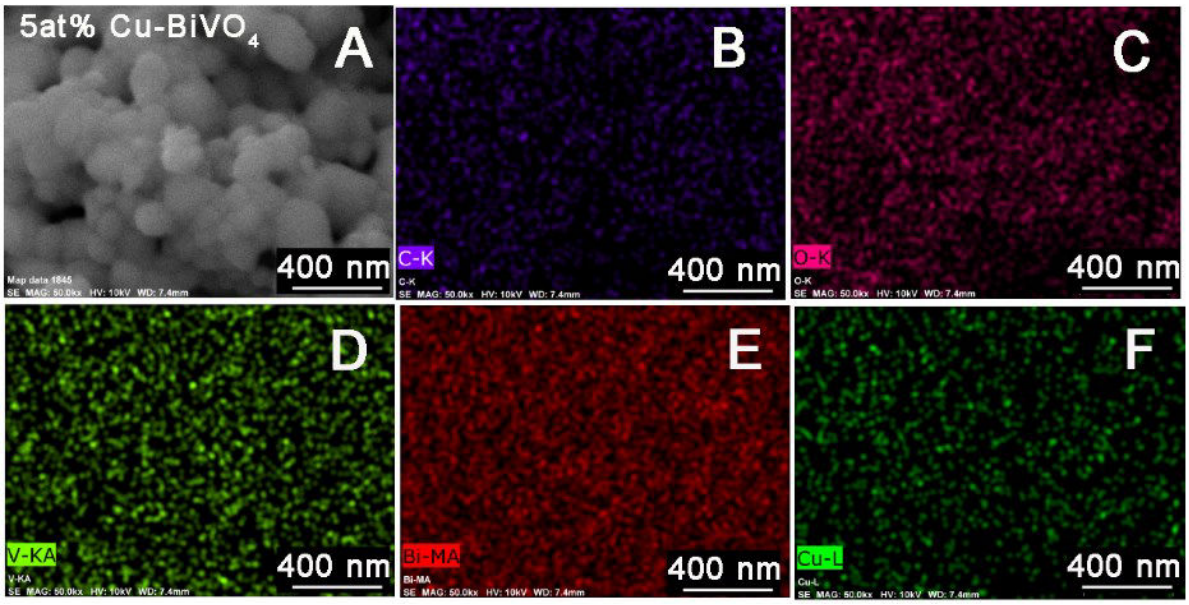

Fig.3.6. Elemental mapping from EDAX composition profile for 5 at.% in Cu-$BiVO_4$ sample (A). (B): Carbon K-line from substrate, (C): Oxygen K-line, (D): Vanadium K-alpha line, (E): Bismuth M-alpha line and (F): Copper L-line.

Table 3.3. Energy dispersive X-ray spectroscopy showing chemical compositions for Cu-$BiVO_4$ samples.

Labelled in the plot	Cu (at. %) Experimental	Bismuth (at. %)	Vanadium (at. %)	Oxygen (at. %)	Cu (at. %) (EDAX)
	0	16.46	17.54	66.0	-
A	**1**	15.36	15.66	67.99	0.99
B	**5**	18.88	19.36	59.94	1.82
C	**10**	19.09	18.87	59.28	2.76

3.1.2.4 HRTEM analysis

HR-TEM analysis of Cu-$BiVO_4$ particles reveals well crystalline domains (Fig.3.7B

inset) through the resolved crystal lattice fringes for the considered samples (A, B, C, and D) with corresponding FFT crystallographic planes (Fig.3.7). The inter-reticular distances d_{hkl}, in the crystalline monoclinic phase, were calculated for all the samples and the obtained values are associated to d_{110} = 0.474 nm, d_{011} = 0.467 nm, d_{040} = 0.312 nm and d_{220} = 0.237 nm. Although distortions of the lattice parameters were demonstrated with increased rates of Cu-doping, HR-TEM observations show good crystalline quality of doped samples.

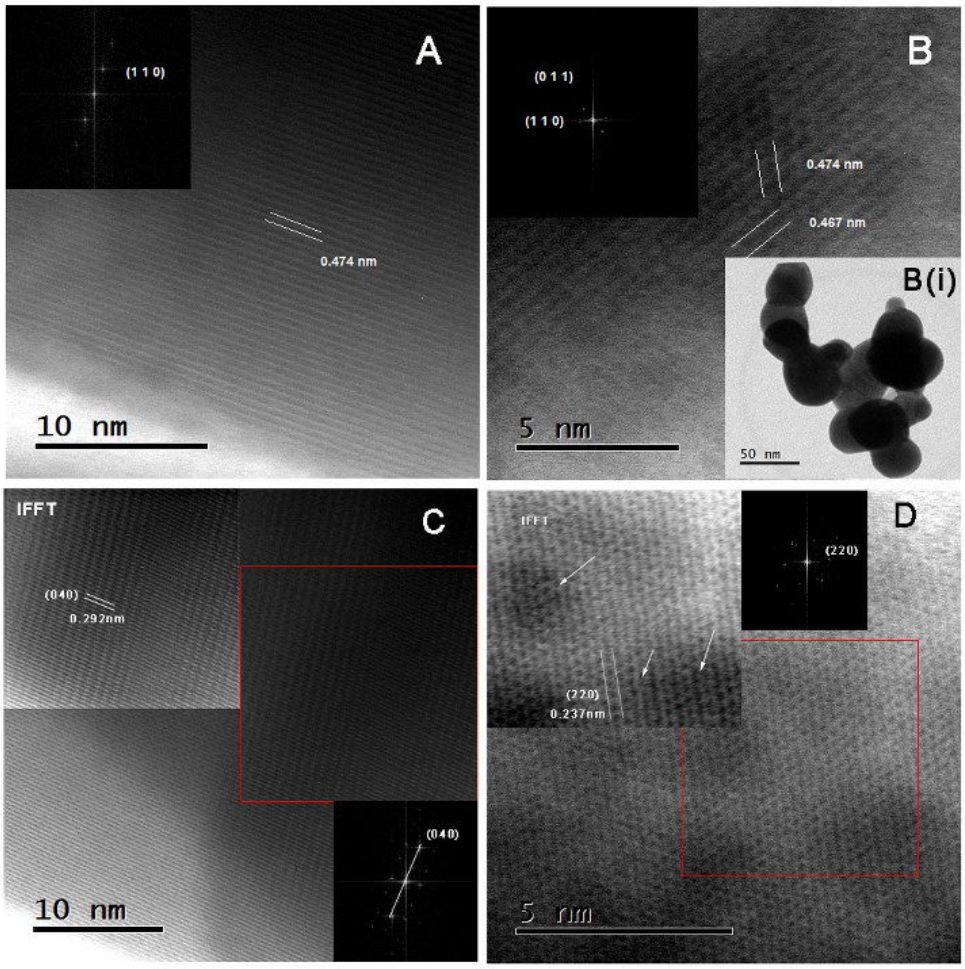

Fig.3.7. HR-TEM images with corresponding FFT in inset for copper doped Cu-$BiVO_4$ samples. (A): undoped, (B): 1 at.% with inset (i) of particle size around 50nm, (C): 5 at.% with inset of IFFT image and (D): 10 at.% with inset of IFFT image showing distorted lattice indicated by arrows.

3.1.2.5. XPS investigations

As far as the chemical bonding with Cu ions is concerned, XPS analysis is an appropriate method to probe the molecular bonding. XPS patterns were recorded on representative samples of Cu–$BiVO_4$. As shown in Fig.3.8a, XPS spectra reveal the binding

energy levels of Bi 4f, V 2p, O 1s and Cu 2p. The binding energies (E_b) of Cu species taking into account the spin orbital splitting of 2p core level were found at E_b =933 eV and 953 eV associated to doublet peaks Cu-$2p_{1/2}$ and Cu-$2p_{3/2}$ respectively as illustrated in Fig. 3.8b. It can be seen from the XPS curves, the Cu-$BiVO_4$ sample possesses binding energies suggesting the presence of copper in oxidized form. In Fig.3.8c, the XPS spectra related to Bi-4f, consist in two intense and symmetrical peaks at E_b = 159.8 and 165.1 eV, corresponding to the Bi-$4f_{7/2}$ and Bi - $4f_{5/2}$ terms, respectively in accordance with Bi ions in their trivalent oxidation state. The XPS spectrum of V $2p_{3/2}$ depicted in Fig.3.8d can be de-convoluted into two peaks with energies E_b = 515.5 and 516.4 eV attributed to the surface V^{4+} and V^{5+} species respectively. Also, the stable oxidation state V^{5+} can be converted to V^{4+} due to surface effect (nanoparticles) or when oxygen vacancies are involved [15].

For oxygen, O1s XPS spectra in Cu-$BiVO_4$ samples are shown in Fig. 3.8e**.** The asymmetric peak centred at 530 eV was deconvoluted into two components. Different bonding states of the oxygen content coexist and associated to the binding energies E_b = 529.4 and 531.2 eV. Such values are assigned to lattice oxygen (O_{latt}) and adsorbed oxygen (O_{ads}) species respectively [16]. However, the O_{ads}/O_{latt} molar ratios are relatively high for all the samples irrespective of the powders morphologies and the doping rates. XPS results which are more sensitive to surface compositions, are complimented by EPR experiments which probes precisely the Cu^{2+} and V^{4+} ions for their absolute concentrations as well as their local environments in the samples.

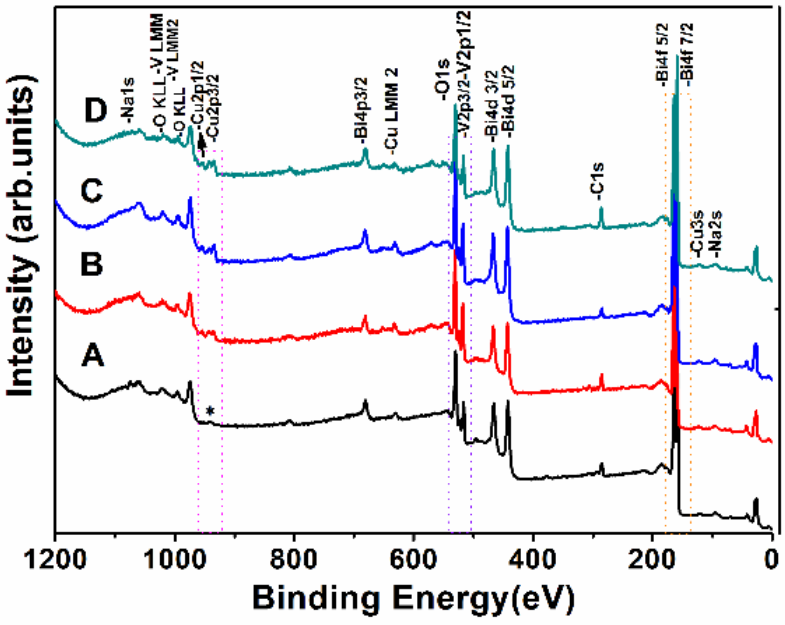

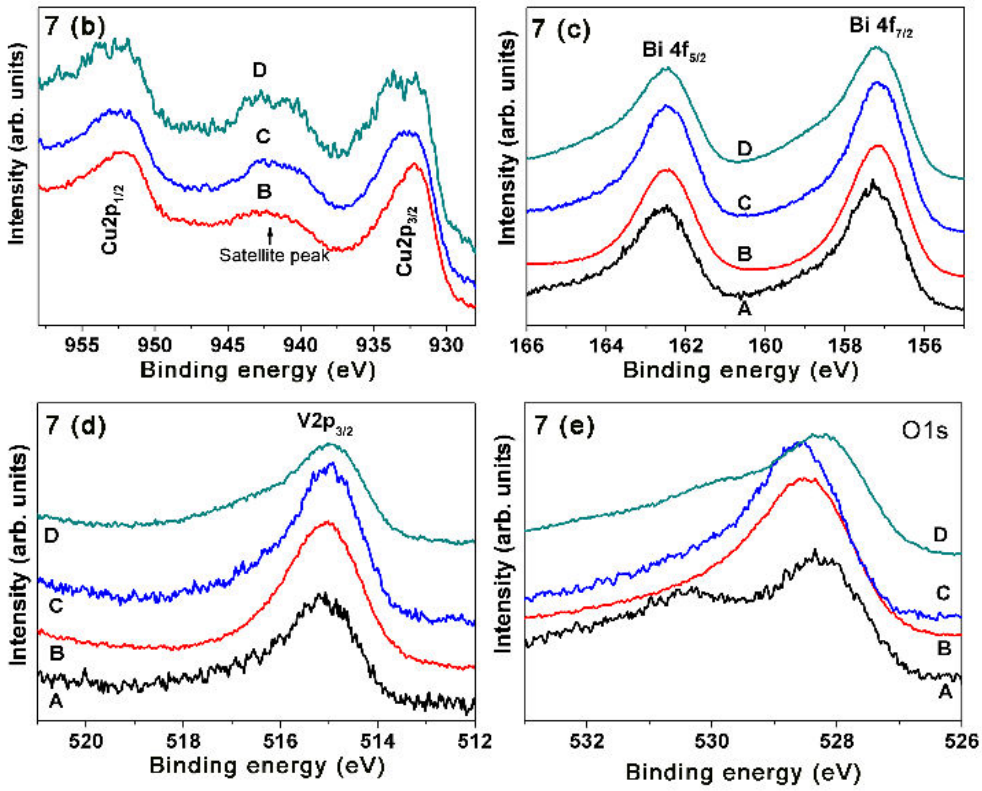

Fig.3.8. XPS spectra for undoped and Cu doped $BiVO_4$ samples where A, B, C and D are associated to undoped $BiVO_4$, 1 at.%, 5 at.% and 10 at.% Cu-$BiVO_4$ respectively; (b, c, d & e) illustrate the binding energies of Cu 2p, Bi 4f, V 2p and O 1s orbitals.

3.1.2.6. EPR studies

EPR spectroscopy is a sensitive tool to probe the doping process or surface effects, where the oxidation state of particular ion leads to electronic configurations with unpaired spins. The situation of monoclinic $BiVO_4$ structure doped by copper ions is worthy of interest. Indeed, in perfect crystalline structure, vanadium ions possess the valence state V^{5+} state leading to spinless ions. However, due to oxygen vacancies induced notably in nanosized particles with high specific surfaces, the departure of vanadium to its normal valence state leads to reduced species as V^{4+} which are paramagnetic ions. The electronic configuration of V^{4+} ($3d^1$) possesses an effective electronic spin (S=1/2) giving rise to an EPR signal. For copper doping of $BiVO_4$, oxygen environment stabilizes the oxidation state Cu^{2+} with an electronic configuration ($3d^9$) giving rise to an EPR signal with an electronic spin S=1/2. The EPR spectra of Cu-$BiVO_4$, are summarized in Fig.3.9 (A) for different doping ratios. Each EPR spectrum is composed of two central isotropic sharp lines superimposed to broad and structured resonance band. The experimental EPR spectra were fitted by using Bruker-Winsinfonia

software and the procedure of fitting determines the magnetic fields (B_{ir}) related to both electronic and nuclear spin states. By using derivative of Lorentzian lines centred at different B_{ir} and using suitable line width we can reproduce precisely all features of the experimental spectra. This allows extracting g_x, g_y, g_z components and the other parameters summarized in table 6. Thus, the single EPR line is associated to V^{4+} ($3d^1$) with regard to the magnetic interaction marked by an isotropic g-Landé tensor with diagonal components $g_x = g_y = g_z = 1.97$. The EPR signal associated to Cu^{2+} ions is accounted by an anisotropic magnetic Landé tensor $g_x = 2.15$, $g_y = 2.07$ and $g_z = 2.35$ as given in the table 3.5. The Cu^{2+} EPR line width (100-200 Gauss) and also V^{4+} (100 Gauss) as well as the unresolved hyperfine structures for both ions are accounted by dipolar or exchange interactions between copper and vanadium ions situated at relatively short distances. In other words, this effect can be due to agglomeration paramagnetic species such as Cu^{2+} and V^{4+}. On the other hand, the rate V^{4+} /V^{5+} is more important for low copper doping rates and drastically decreases with increased copper concentrations in the samples.

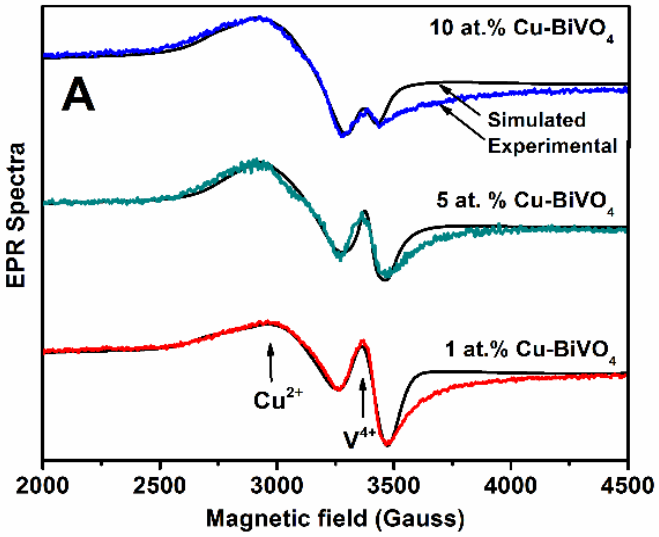

Fig.3.9(A). EPR spectra of copper doped $BiVO_4$ samples with different copper doping rates.

Meanwhile, the evolution of the EPR spectrum intensity related to copper ions didn't follow the initial doping rate. Such behaviour is plausibly due to the occurrence of efficient charge transfer between Cu^{2+} and V^{4+} as well as the suppression of oxygen vacancies which contributes to the creation of reduced vanadium. Quantitatively, the absolute concentrations of these ions were obtained from the double integration of the EPR spectra related to each paramagnetic ion and using a reference sample ($CuSO_4$) with calibrated spin concentration. The results summarized in Fig.3.9(B) give a quantitative evaluation of Cu^{2+} content in the

investigated samples as well as active electronic centres as V^{4+}. Concentrations of Cu^{2+} were found to increase with the doping rate from 0.8 $X10^{17}$ (initial doping 1at.%) up to 2 $X10^{17}$ ion/gram (initial 10 at.%).

For vanadium ions V^{4+}, a decrease of its concentration from 1.2 $X10^{17}$ to 0.3 $X10^{16}$ spin/gram

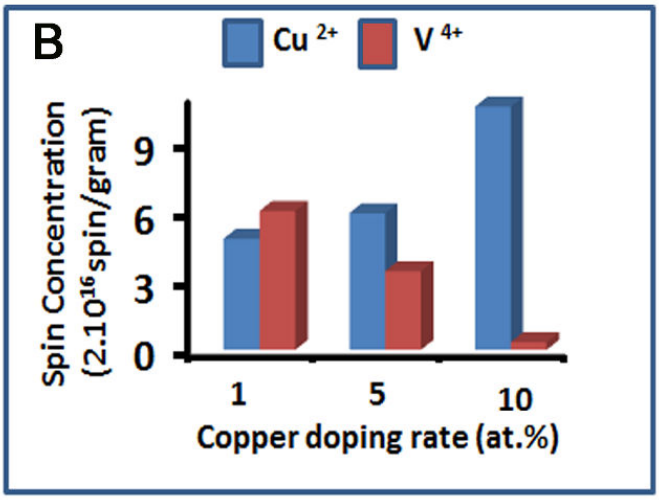

Fig.3.9 (B). Absolute concentrations of Cu^{2+} and V^{4+} ions and their evolution with copper doping rate.

occurs with increasing the doping from 1 at% to 10 at.%.

Table 3.5. EPR spectral parameters of V^{4+} ions and Cu^{2+} ions for Cu-$BiVO_4$ nanocrystalites obtained by mechano-chemical synthesis.

	Cu^{2+}							V^{4+}					
Cu at%	A∥	A_x⊥	A_y⊥	g∥	g_x	g_y	ΔH	A∥	A⊥	g∥	g_x	g_y	ΔH
1	120	80	40	2.345	2.14	2.05	120	0	0	1.975	1.975	1.975	120
5	100	100	50	2.32	2.17	2.05	100	5	0	1.95	2.00	1.98	30
10	140	100	50	2.305	2.165	2.09	140	0	0	1.985	2.005	1.995	60

To sum up, the EPR experiments show the existence of reduced valence states of vanadium ions (V^{4+}) along with oxidized environments of copper ions (Cu^{2+}). The effective concentration of Cu^{2+} in the samples is evaluated with good accuracy. Dipolar or exchange interactions are involved between copper and vanadium ions as well as charge transfer between these species. This process contributes to the photocatalytic activity of Cu-$BiVO_4$ materials.

3.1.2.7. Optical analysis

The optical absorption spectrum of a semiconducting material depicts by its electronic structure which defines the threshold and the concerned spectral range. The doping process is dedicated to extend the optical absorption to a larger visible range leading to visible light driven photocatalysis. In the case of undoped $BiVO_4$, the main absorption band is observed in the wavelength range 350-530 nm. In doped Cu-$BiVO_4$ powders, broad shoulder and extended absorption background appear on the main band over the range of 530 - 800 nm and their importance correlate with the Cu content as depicted in Fig.3.10A. By using the Tauc plot based on the absorbance and incident photon energy hν, the following relation (equation 3.1) serves to evaluate the direct band gap value:

$$\alpha = A(h\nu - E_g)^{n/2}/h\nu \qquad \rightarrow (3.1)$$

α, A, n and E_g represent the absorption coefficient, a constant of proportionality, index with different values (1, 3, 4, 6) depends on nature of optical transition and the direct band gap energy respectively. The threshold absorption edges were evaluated by an asymptotic extrapolation (Fig. 3.10B) for the pure sample and for Cu-doped $BiVO_4$ with the doping rates about 1, 5 and 10 at.%. The obtained values were respectively 2.41, 2.40, 2.37 and 2.34 eV for the "pseudo-direct" band gap of $BiVO_4$. The term "pseudo" is used due to a favourable direct transition between (VB) and (CB) which occurs outside the Brillouin zone center [2]. Indeed, the minimum of conduction band (CBM) is located at the Z point which corresponds to (0.000, -0.500, 0.500) direction in the Brillouin zone. The involved atomic orbitals in (VB) are constituted by Bi (6s) and O (2p) while they are composed by V (3d) states for (CB). The optical band gap is then defined by transitions between (VB) and (CB) with finite probability at the Z point. In the doped samples, copper ions contribute in one hand to lower the band gap by introducing allowed states within the band gap. On the other hand, the Cu-O environments demonstrated by EPR and XPS favours the occurrence of transitions between O (2p) and Cu (3d). The broad shoulder on the main absorption band can be accounted by the copper doping in agreement with large effect with increasing the doping rate. This effect correlates well with the colour of Cu doped $BiVO_4$ samples being changing from bright yellow (pure $BiVO_4$) to dark brown as shown in Fig.3.10A inset. The colour change is a feature of a semiconductor material, which is dependent on its electronic structure and considered as an important factor for photocatalytic activity [17]. The broad background absorption can be accounted by intermediate electronic levels induced in the band gap by Cu substitution in the host crystal

sites. This effect enhances the photocatalytic efficiency compared to undoped materials as reported below.

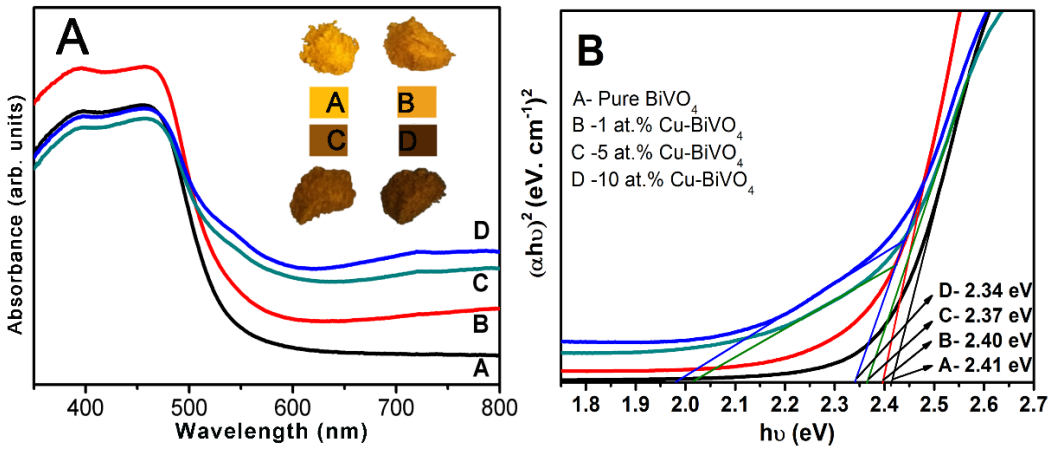

Fig.3.10. UV-Vis diffuse absorption spectra of $BiVO_4$ samples; (A): undoped $BiVO_4$ (B): 1 at.%, (C): 5 at.% and D: 10 at.% in Cu-$BiVO_4$ respectively. The inset (A) shows the color of Cu doped $BiVO_4$ powders with different Cu concentrations and (B) reports the band gap energy values for Cu doped $BiVO_4$ obtained from Tauc plot.

3.1.3. Photocatalytic studies

The photocatalytic activity of Cu doped $BiVO_4$ powders prepared by high energy ball mill (HEM) technique was investigated on the degradation of methylene blue (MB) dyes. The experiments were carried out in a glass beaker with circulating water jacket. It contains 50 ml of an aqueous solution of MB dyes (10^{-5} M) and 50 mg of Cu doped $BiVO_4$ catalyst powders. The photocatalytic reactions were induced with a simulated sunlight based on Hg (Xe) arc lamp (Newport-67005) with 40 W/cm^2 as the illumination power received on the reaction glass beaker. Before illumination, the mixture solution was stirred for 20 min under dark in order to reach the adsorption–desorption equilibrium between catalyst and dye molecules.

During the photocatalytic reactions under illumination, 5 mL solution was collected at an interval of 20 or 30 minutes and then centrifuged to separate the catalyst powder from the MB dyes. The UV-Vis optical absorption of the centrifuged solution was then recorded and used to monitor the degradation of MB dyes by the photocatalytic process. The optical absorption of the dye solution with catalyst vs irradiation time is reported in the Fig.3.11, associated respectively to the use of pure, 5 at.% and 10 at.% Cu doped $BiVO_4$. A net effect of the Cu doping is clearly observed through the evolution of the intensity of the absorption spectra during the photocatalytic process where the characteristic λ_{max} shift is attributed to N-demethylation derivatives of MB dyes [18].

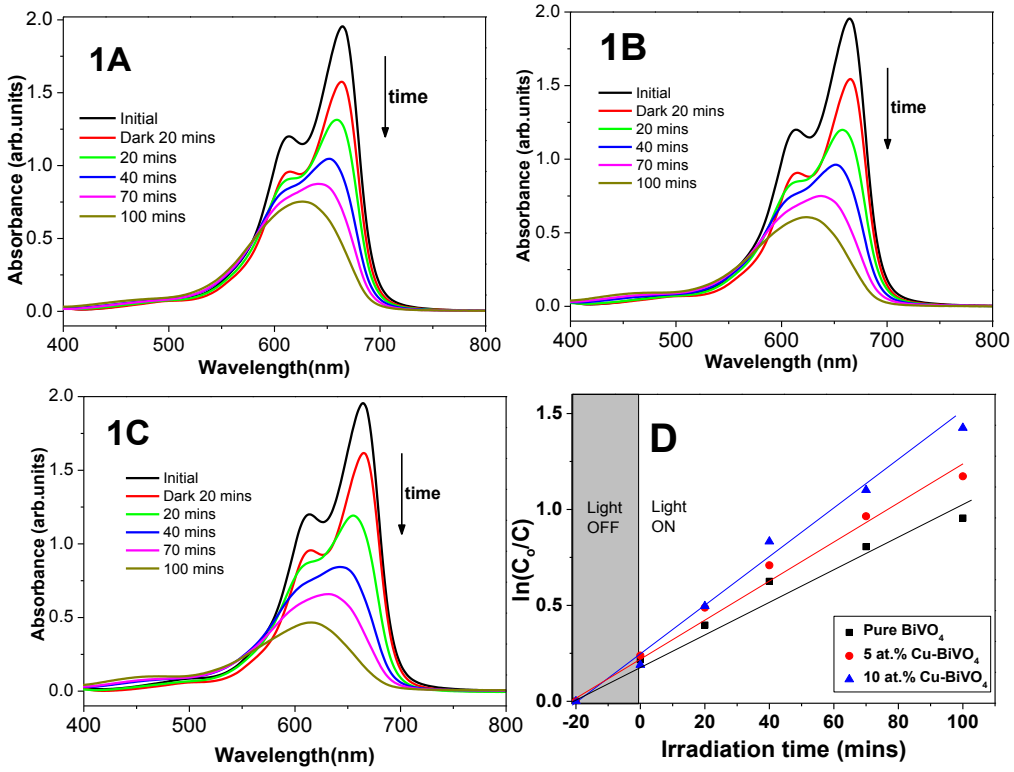

Fig.3.11. Evolution of the optical absorption of MB dye solutions versus irradiation time following the Cu doping rates (1A, 1B and 1C are related to pure, 5 at.% and 10 at.% Cu doped $BiVO_4$ samples respectively). Fig.3.11D shows kinetic reaction rates of photodegradation of MB dyes.

Table 3.6**.** Final photodegradation rate (%) of MB dyes by pure and Cu doped $BiVO_4$ photocatalysts with the corresponding kinetic reaction rates.

Cu doping rates (at.%)	MB degradation rate (%) after 100 min illumination	Kinetic reaction rate 'k' (min^{-1})
0	61.5	0.0074 ± 7.1e-4
5	69.1	0.0092 ± 6.38e-4
10	75.9	0.0121 ± 8.7e-4

The kinetic reaction rates were calculated from the slope of ln (C_0/C_t) plot shown in the Fig.3.11D (where C_0 is initial concentration of the MB dyes in solution and C_t is the concentration of the MB dye solution at a given time 't' during the photocatalytic reactions). Indeed, the time evolution of the C_t parameter follows a pseudo-first-order reaction as $C_t =$

$C_0\, e^{-tk}$ where k represents the kinetic reaction rate. The final degradation rate (%) derived from $[C_0 - C_t/C_0]\, X\, 100$ and 'k' values are summarized in Table 3.6. as function of Cu doping rates.

3.1.7. Summary of the study

Cu doped $BiVO_4$ nanoparticles were synthesized by mechano-chemical technique with and applied post-synthesis treatments to optimize the crystal structure. Monoclinic scheelite structure was obtained for Cu doped $BiVO_4$ samples with different Cu doping rates. Structural distortions were analysed by XRD and micro-Raman investigations with quantitative estimation of the lattice parameters and the lattice compression as function of the Cu doping rates. Spherical nanoparticles are in the range 40 - 160 nm were estimated from FE-SEM images with the tendency to decrease their sizes for higher Cu doped samples. XPS analysis determined the chemical bonding involved between the constitutive elements and including the Cu location in the host lattice. Mixed oxidation states of V^{4+}/V^{5+} with variable concentrations were shown from XPS spectra also supported by EPR experiments and correlate with the Cu doping ratios. The effective concentrations of copper ions in the valance state Cu^{2+} as well as that of the reduced form of vanadium ions V^{4+} were quantitatively determined by EPR. The features of the EPR spectra and the evolution of these concentrations with the copper doping rate indicates the occurrence of interactions and charge transfer between these electronic active species. These results suggest that the mechanism of charge transfer required for photocatalysis reactions would be affected by Cu doping. Similarly UV-Vis optical absorption bands show an extension in the spectral range 530-800 nm by Cu doping. This evolution of optical features is of particular interest for visible light driven photocatalysis based on stabilized scheelite monoclinic structure in Cu-$BiVO_4$. Photocatalysis studies on degradation of Methylene blue dye solution in presences of solar simulator lamp has proved that Cu doping would enhances reaction with doping rates, due to broad range of visible light absorption as well as interaction and charge transfer between Cu^{2+} and V^{4+} ions. According to the objectives of this study mentioned in section 3.1.2, where mechano-chemical synthesis of doped $BiVO_4$ with copper metal ions and their detail study on structural, morphological and optical properties were achieved. Furthermore Cu doped $BiVO_4$ nanoparticle were proved as enhancement of photocatalytic efficiency in degradation of organic dye solution as compared to pristine $BiVO_4$ nanoparticles.

3.2. Synthesis and Investigations of Molybdenum doped $BiVO_4$ Powders

3.2.1 Importance of Molybdenum doping with $BiVO_4$ in the prospect of photocatalysis

The incorporation of Mo ions with small percentage in the crystal sites of $BiVO_4$ semiconductors, as in V^{5+} centred tetrahedra, is expected to modify the bulk electronic and structural properties. The main reasons are related to versatility of the oxidation degrees of Mo ions and the departure of ionic radii to that of V ions. The lattice distortions are not obvious after introducing the Mo atoms substitute on V sites, which may be owing to the low impurity concentration and their similar radii [19].

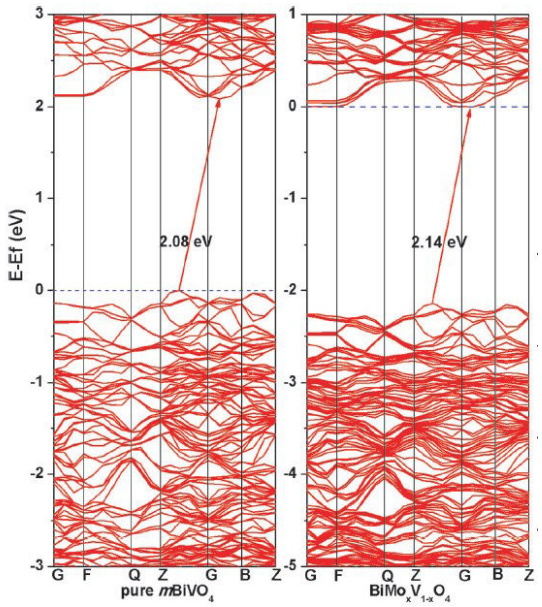

Fig.3.12. The electronic band structures for the bulk supercells of pure and Mo-doped mBiVO4. Spin contributions were shown in red color. The red arrows highlight the photoexcited transition in minimum energies. The blue dashed lines symbolize the Fermi levels which are set as 0 eV[19].

However, Mo atoms are fully 6-fold coordinated in MoO_3, while V atoms are 4-fold coordinated in pure $BiVO_4$. Thus, when Mo atoms substitute on V sites, all Mo–O bonds are slightly expanded but Mo atoms still keep the 4-fold coordination of V atoms due to steric hindrance.

For the electronic structure, former numerical simulation report [19] illustrated in Fig.3.12. Depicts the features of pure $BiVO_4$ as an indirect band gap semiconductor, and the

calculated band gap (2.08 eV) is smaller to the experimental value (2.40 eV). The discrepancy is well-known from the underestimated values from DFT calculations based on the GGA functional [20]. This theoretical model underlines that doping Mo atoms into the host lattice of $BiVO_4$ provides extra electrons, leading to the raising of the Fermi level as in the case of impurity energy levels acting as donor levels. For the case of Mo substitution in the V sites, the electronic band structure is nearly the same as that of the pure $BiVO_4$. The slight change in the energy gap (2.14 eV) of $BiMo_xV_{1-x}O_4$ traduces the limited effect of Mo doping on the electronic structure of $BiVO_4$. This result is consistent with experimental observations [62,87] where the Mo 4d states are mainly distributed in the bottom of VB and CB and these regions are attributed to the bonding features and anti-bonding features for Mo–O respectively. Besides, the distribution of Mo 4d states slightly broadens the VB by 0.2 eV, which is in agreement with the study of Zhao et al. [23].

The forthcoming section reports experimental investigations of Mo doping effects in the ball milled $BiVO_4$. The optimized synthesis parameters were defined to obtain the relevant crystalline structure, precise insights on the electronic and optical features as function of doping rates. The characterizations were realized by X-ray diffraction, field emission scanning electron microscopy FE-SEM and high resolution transmission electron microscopy HR-TEM. EPR and UV-Vis absorption experiments were analysed to shed light on the location of Mo doping ions in the host structures and the ability to harvest better the visible light. The main aim lies in the improvement of photocatalytic efficiency of Mo-$BiVO_4$ compared to undoped material or other doping elements.

3.2.2. Results and discussion

3.2.2.1. X-ray powder diffraction analysis

X-ray diffraction of Mo-$BiVO_4$ samples obtained in as-formed and annealed samples were shown in Fig.3.13. The diffraction peaks observed for all the samples are related to monoclinic scheelite phase (JCPDS No.14-0688) without further secondary phases. Moreover, there is no change in the 2θ position of characteristic peaks at 28.8211 corresponding to (hkl) plane (-121) as compared to un-doped $BiVO_4$ shown in inset Fig.3.13. In the as-formed powders (Fig.3.13 (A)), the diffraction doublet peaks corresponding to crystallographic plans such as (110, 011), (200, 002), (211, -112), (231, 132), (240, 042) were moved close to each other and merging with an increase of Mo concentrations. A similar behaviour was observed by Park et al for 2 at.% W doping and 6 at.% Mo doped $BiVO_4$ suggesting that, phase

distortions are caused by the substitution of W^{6+} and Mo^{6+} ions in crystal sites of V^{5+}. Thus, for Mo doped-$BiVO_4$ samples, lattice distortions with increment of Mo concentration indicate substitutional doping in V sites within VO_4 tetrahedra. This is supported by the size differences between ionic radii of Mo^{6+} (0.055 nm) and even higher for Mo^{5+} with V^{5+} (0.050 nm) ions.

To improve the crystalline structure by limiting the lattice distortions caused by doping $BiVO_4$ powder samples, annealing treatments were performed up to 700°C for 1 h. The resultant diffraction patterns of Fig.3.13 (B), show highly resolved diffraction lines indicative of high crystallinity in Mo-doped $BiVO_4$ powders accompanied by grain size increasing as discussed in next paragraph.

However, the role of specific surfaces is crucial in photocatalysis and the need to realize nanosized powders is of primary importance. Also, second stage of ball milling process was performed to limit the particle sizes. The X-ray diffraction patterns after second milling are shown in Fig.3.13(C). Particle size's reduction can be clearly observed from the FWHM of the characteristic plane (-121) locate at 2θ = 28.82. The crystallite domain sizes were calculated by using Scherrer's formula and compared to SEM observations discussed below.

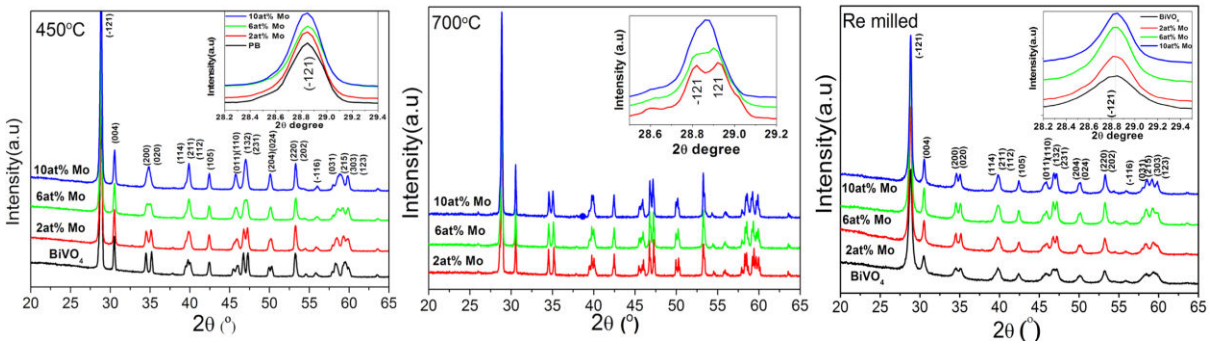

Fig.3.13. X-ray powder diffraction patterns of Mo-$BiVO_4$ nanoparticle prepared by ball milling technique for three stages: (A-450°C) Annealed at 450°C (B-700°C) Annealed at 700°C and (C-Re-milled) Re- milled powders.

3.2.2.2 Micro-Raman analysis

Monoclinic scheelite-$BiVO_4$ structure gives rise to five distinct internal Raman modes. Those located at 326, 366, 708 and 826 cm^{-1} are associated to vibrations of V-O bonds in tetrahedral group VO_4 as shown in Fig.3.14. The external mode at 210 cm^{-1} is less informative on the quality of the crystalline structure and can be associated to some rotational motions of VO_4 groups. Among internal modes, 326 and 366 cm^{-1} are assigned to the asymmetrical and symmetrical bending vibrations V-O bonds. The major Raman modes A_g at 826 and the shoulder at 708 cm^{-1} are assigned to the symmetric and asymmetric stretching modes of V–O

bonds in VO_4 tetrahedron respectively [11]. For Mo doped $BiVO_4$ samples, distortions in V-O bending modes of VO_4 tetrahedra can be suggested from the shift of Raman bands. This infers the substitution of doping Mo ions in crystal sites of V ions in $BiVO_4$ structure. This is traduced by V-O stretching mode being shifted to a lower frequency (822 cm^{-1}) as compared to undoped $BiVO_4$. A slight increment in V-O bond length can be due to Mo replacing V atoms with higher ionic radii. Moreover, all Mo doped $BiVO_4$ samples has shown Mo-O-Mo stretching mode at 871cm^{-1}.

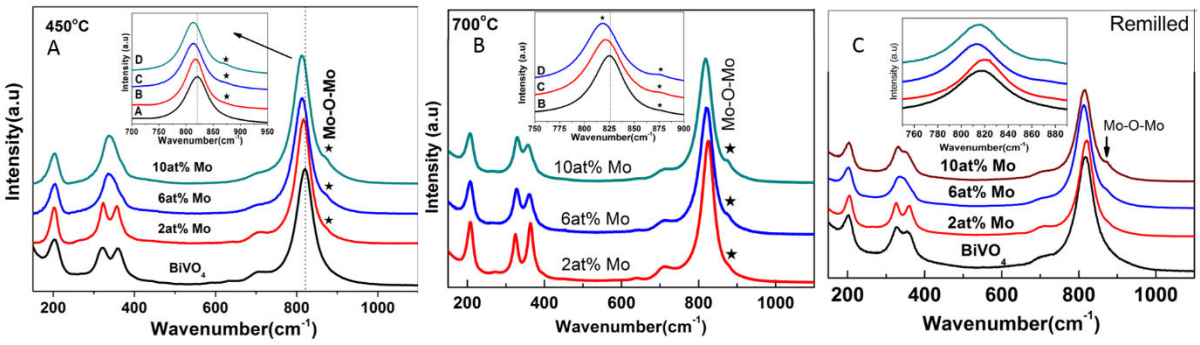

Fig.3.14. Micro-Raman analysis of Mo- $BiVO_4$ nanoparticle prepared by ball milling technique for three stages. (A-450°C) Annealed at 450°C (B-700°C) Annealed at 700°C and (C-Re-milled) Re-milled powders.

3.2.2.3. FE SEM analysis:

FE SEM technique is used to visualize the morphologies of Mo doped $BiVO_4$ powders prepared by ball milling process and submitted to different annealing treatments (Fig.3.15). For annealing at 450°C, un-doped $BiVO_4$ particles exhibit spherical shape with a size range from 400 - 500 nm whereas Mo doped $BiVO_4$ shows limited particle sizes as depicted in Fig.3.15. This observation is in-agreement with Wang et al who showed similar effect for Eu doped $BiVO_4$ [24,25]. Analyses of the chemical composition of Mo-doped $BiVO_4$ powders by EDX were summarized in Table 3.7. The analyses were carried out by averaging on different area of the samples and by using the energy about 10 kV for the performed elemental scans.

For annealing at 700°C during 1 hour, the particle sizes of Mo- doped sample increase dramatically to the micron level with better improved crystalline order. Additionally, the low level detection of Mo doping ions can be explained by phase segregation with the possible formation of Mo-rich clusters. The appearance of vibrational features of Mo-O-Mo bonds for high doping rates is in-agreement with such diagnostic. The mechanism can be explained by the high temperature annealing which causes migration of doping elements to segregated Mo

clusters from $BiVO_4$ particles. The inhomogeneous distribution of Mo in the powders can overcome precise estimation of Mo concentrations from EDX analyses.

The final stage based on re-milling the annealed powders is performed to reduce particle sizes to nanosized particles. However, after just 2 hours milling time, we have achieved 5-10 nm size particles with heavy agglomeration, as shown in Fig.3.15. EDAX composition results for re-mill samples has shown similar to first stage samples, where Mo was identified bit higher amounts that's due to presence of smaller sized nanoparticles 5-10 nm.

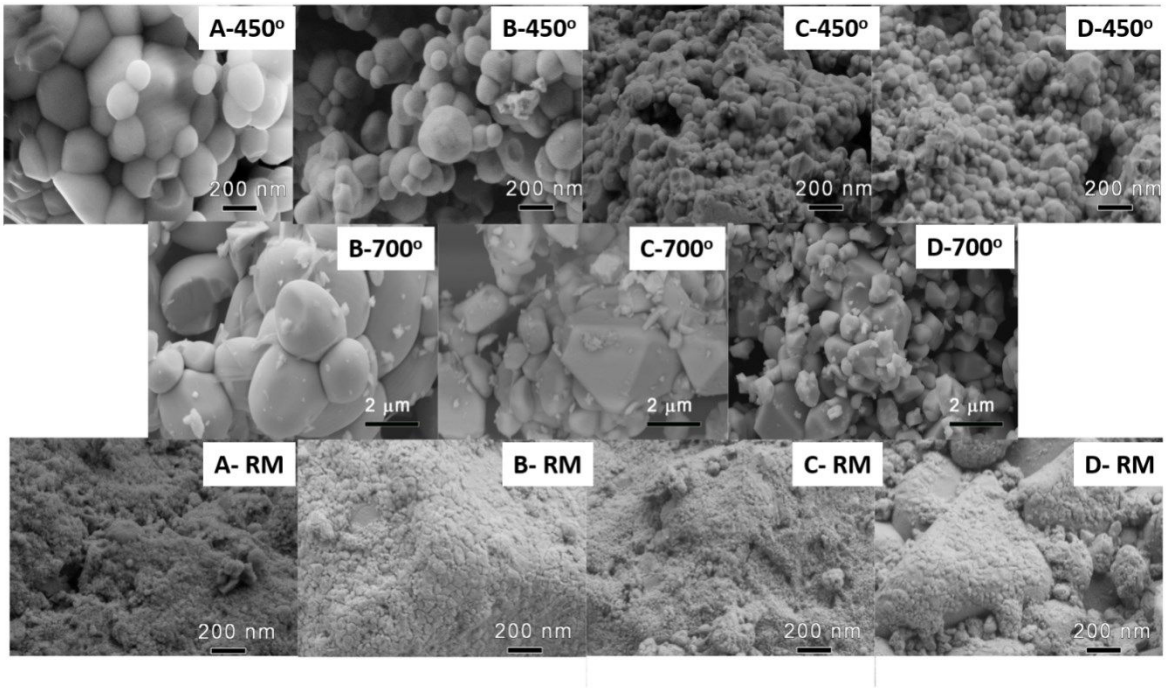

Fig.3.15. FESEM images of morphologies of Mo-$BiVO_4$ nanoparticle prepared by ball milling technique for three stages. where 450°C, 700°C and RM are related to three stages and where A, B, C and D are 0, 2, 6 and 10 at.% doped molybdenum concentrations.

Table 3.7. Chemical compositions data for Mo-$BiVO_4$ nanoparticles analysed by EDAX for the three stages.

	450°C (at.%)				**700°C (at.%)**				**Re-milled (at.%)**			
Samples	**Bi**	**V**	**O**	**Mo**	**Bi**	**V**	**O**	**Mo**	**Bi**	**V**	**O**	**Mo**
$BiVO_4$	22.26	32.63	45.11	-					24.26	30.63	45.11	
2at.%Mo	27.34	38.68	31.42	2.56	23.90	39.71	36.12	0.27	23.88	37.73	36.12	2.27
6at.%Mo	23.17	41.15	32.4	3.27	25.10	37.54	36.46	0.91	24.10	34.54	37.65	3.71
10at.%Mo	21.56	31.83	42.6	4.01	28.01	35.76	35.42	0.80	29.01	32.76	34.13	4.10

3.2.2.4: HRTEM Analysis

HR-TEM analyses was performed for first and final stages of Mo-$BiVO_4$ samples. The Fig.3.16 shows 6at.% Mo-$BiVO_4$ sample annealed at 450°C for 2 hrs. It is clearly seen the formation of powders by particles with spherical shape and an average diameter in the range of 50-80 nm as shown in Fig.3.16 A, B. These particles possess well crystalline domains (Fig.3.16B inset) through the resolved crystal-lattice fringes for the consider samples. The lattice fringes give d-spacing of 0.58 nm which is closely related to (020) crystallographic plane. STEM-EDAX reveals elemental composition of 6at.% Mo doped $BiVO_4$ samples as shown in Table 3.8.below.

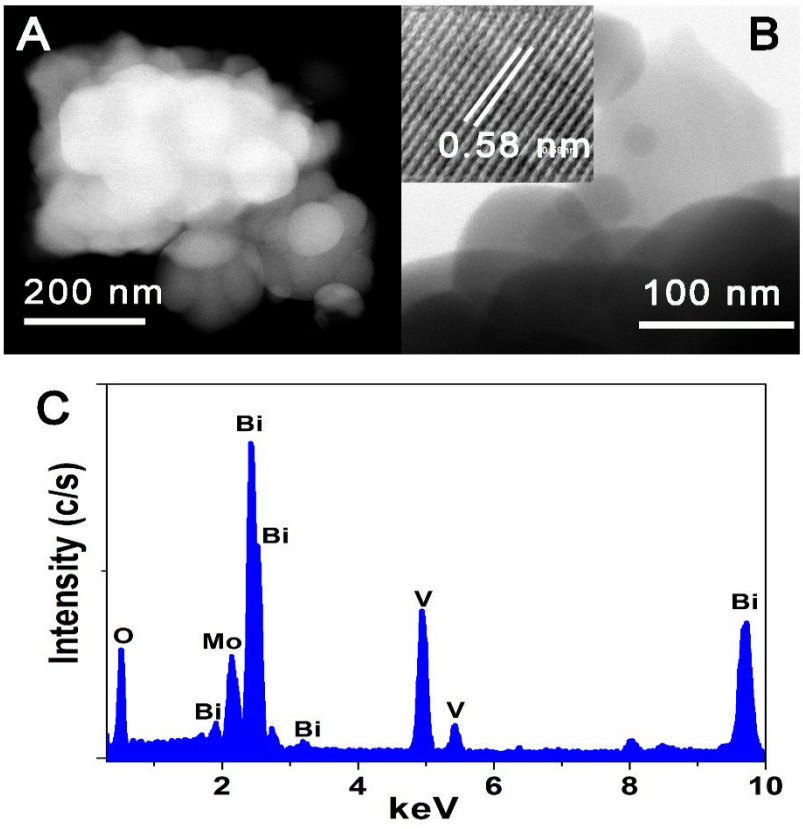

Fig.3.16**.** HRTEM images of 6at.% Mo-$BiVO_4$ nanoparticles for the first stage of annealing at 450°C for 2 hrs. A) and B) images show two different area. The inset of B shows the lattice inter-planar distances for the plane (020). C) Graph shows the EDS analysis from the STEM mode for the same sample.

For the samples made from final treatment stage (annealing and re-milling), the particle sizes are tremendously reduced to 5 to 10 nm without altering the crystalline quality. At low resolutions, these samples show agglomerated particles as shown in Fig.3.17A.with improved resolutions from A to B, B to C and C to D, we can observe high crystallinity through crystallographic lattice planes.

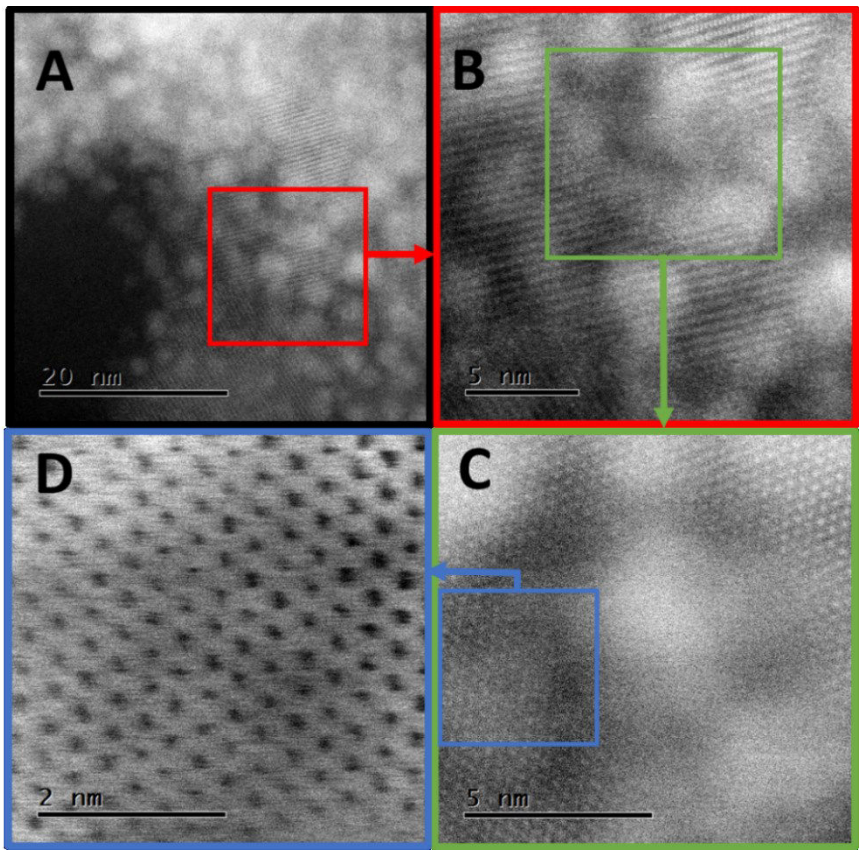

Fig.3.17. HR-STEM images of 2at.% Mo-$BiVO_4$ prepared by ball milling technique for the remilled sample with increment of magnifications from A to D.

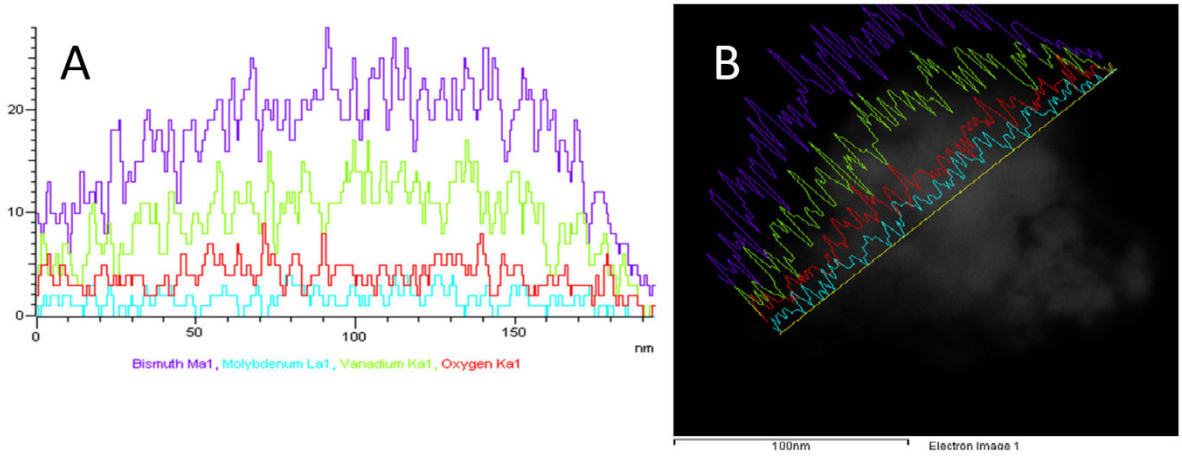

Fig.3.18. Chemical line mapping of 2at% Mo-$BiVO_4$ prepared by ball milling technique for the remilled sample in STEM mode. A. line profile elemental mapping in STEM mode. B. Shows similar on the particle site.

In order to visualize the presence of molybdenum doping, high angle annular dark-field (HAADF) experiments along with EDS line mapping were carried out in scanning transmission electron microscope (STEM). The STEM image with corresponding EDS mapping can be seen

in Fig.3.18, where it can be seen clearly that Bi, V and O along with Mo homogenously observed along particle with line profile mapping.

3.2.2.5. Optical studies

UV–Vis absorption spectroscopy was used to characterize the modifications of the optical properties induced by Mo doping of $BiVO_4$ powders obtained by ball milling technique and submitted to annealing (450°C, 700°C) and re-milling. Fig.3.19. shows the optical absorption curves for the considered samples and highlight the major difference in optical features. Particularly, an additional broad background curve develops with the increase of Mo concentration. This emergence of such additional band denotes the formation of the charge transfer states between doping Mo ions and the host structure $BiVO_4$ [143,144]. In order to define the band gap of the doped structures, the relationship of absorbance and incident photon energy hν can be described as reported in Eq. (3.1) for direct band gap estimation. The threshold absorption edges were calculated for 0, 2, 6 and 10 at.% Mo doped $BiVO_4$ samples under the different treatments. The bandgap values were shown in Table.3.2.2.

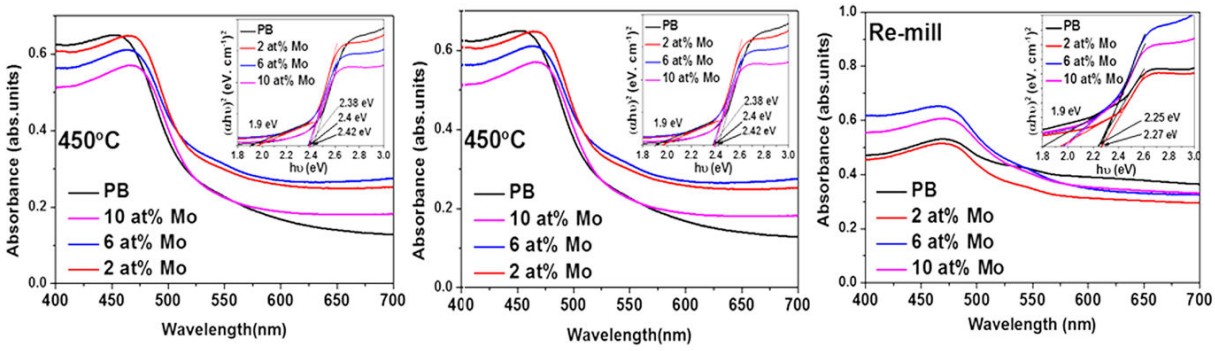

Fig.3.19. Absorption spectra of Mo doped $BiVO_4$ nanoparticle prepared by ball milling technique for the stages. (A-450°C) Annealed at 450°C (B-700°C) Annealed at 700°C and (C-Re-milled) Re-milled powders.

Table 3.8. Energy bandgap calculations for the Mo doped $BiVO_4$ nanoparticles for the three stages.

Mo -$BiVO_4$ Mo: at.%	Band-gap (eV) Stage 1: 450°C	Band-gap (eV) Stage 2: 700°C	Band-gap (eV) Stage 3: Re- milled
0	2.42		2.27
2	2.38	2.32	2.27
6	2.38	2.3	2.25
10	2.4	2.3	2.25

3.2.3. Photocatalytic studies

Photocatalytic tests were realized by using Mo-$BiVO_4$ as photocatalyst to degrade Acid blue 113 dye in solutions. Initially, 10 mg of Mo-$BiVO_4$ powders were added to 10 ml of AB 113 dye solution with initial concentration 10^{-5}M. These solutions were stirred for 20 min under dark to reach absorption/desorption equilibrium and to dissolve the excess of oxygen in solution. For the degradation of di-azo groups in AB113 dye, Mo-$BiVO_4$ powders with 0, 2, 6 and 10at.% doping rates, were tested in the same conditions under the presence of visible light (OSRAM-fluorescent lamp-13 watt) irradiation. The following schematic representation illustrates the experimental setup in Fig.3.20.

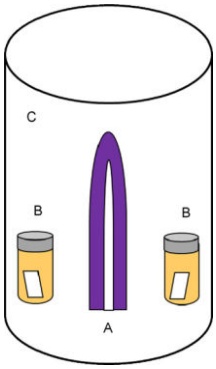

Fig.3.20. A schematic representation of the photocatalytic reactor. (A) Visible light lamp of 13 W, (B) vials containing Mo-$BiVO_4$. (B) Powder catalyst with AB 133 dye solution.(C) dark casing.

Initially, we have performed photocatalysis tests for the different stages of treatment (450°C, 700°C and re-milled) of the powders. The 2 at% of Mo doped $BiVO_4$ and remilled powder shows the best performance in the degradation of organic dyes compared to the other samples. The whole comparative activities are depicted in Fig.3.21.for all the considered samples with different doping rates and different treatments.

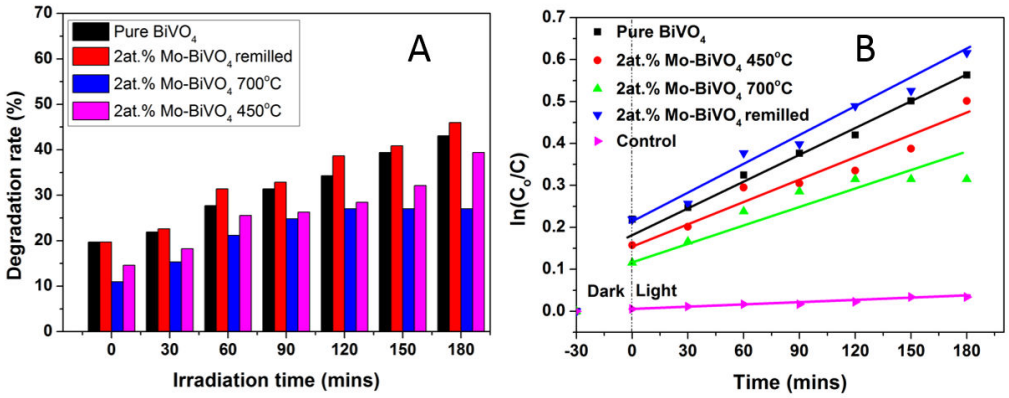

Fig.3.21. Degradation rate of Acid113 vs irradiation time for the powder 2 at.% Mo doped $BiVO_4$ samples at the three treatment stages. B. shows the pseudo-first-order kinetics of degradation of AB 113 di-azo in solution.

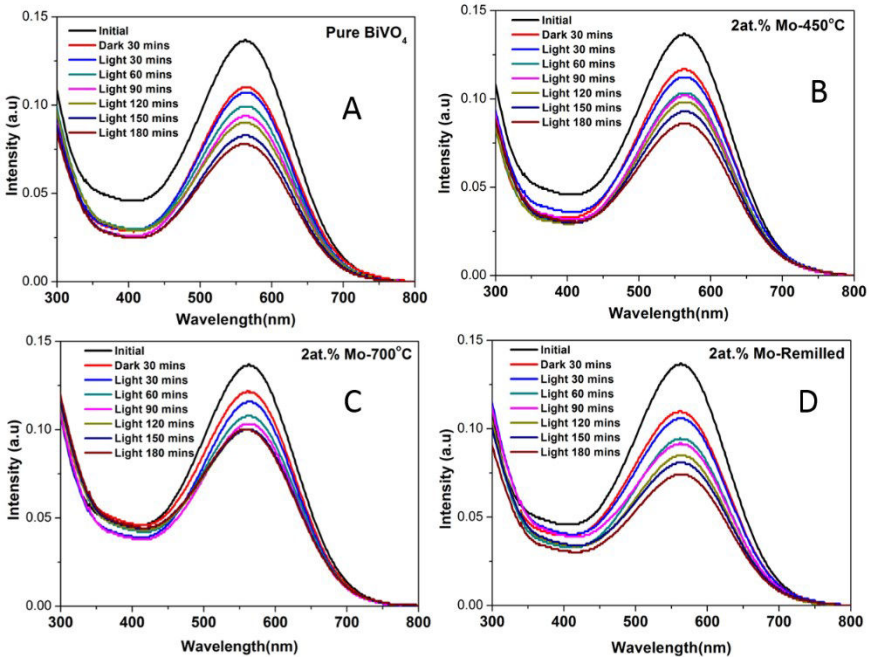

Fig.3.22. Evolution of the optical absorption of Acid blue 113 dye solutions versus irradiation time following the 2at% Mo doped $BiVO_4$ for the three treatment stages. (B, C and D are related to three stages, 450°C, 700°C and remilled samples respectively).

For all remilled samples with all considered Mo concentrations, we have performed the photocatalytic tests at the same conditions and the results are summarized in Fig.3.23. Photocatalytic efficiencies of remilled samples were classified as follows: 2at.% Mo doped $BiVO_4$ > 6at.% Mo-doped $BiVO_4$ remilled> 10at.% Mo- $BiVO_4$ remilled > pure $BiVO_4$.

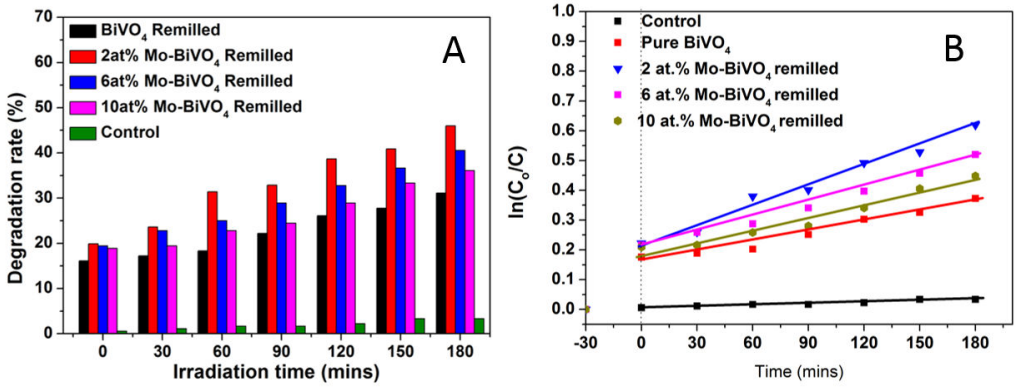

Fig.3.23. Degradation rate of Acid-113 versus irradiation time with respect to the concentration of Mo doped $BiVO_4$ re-milled samples. B. shows the pseudo-first-order kinetics of degradation of AB 113 di-azo dye solutions.

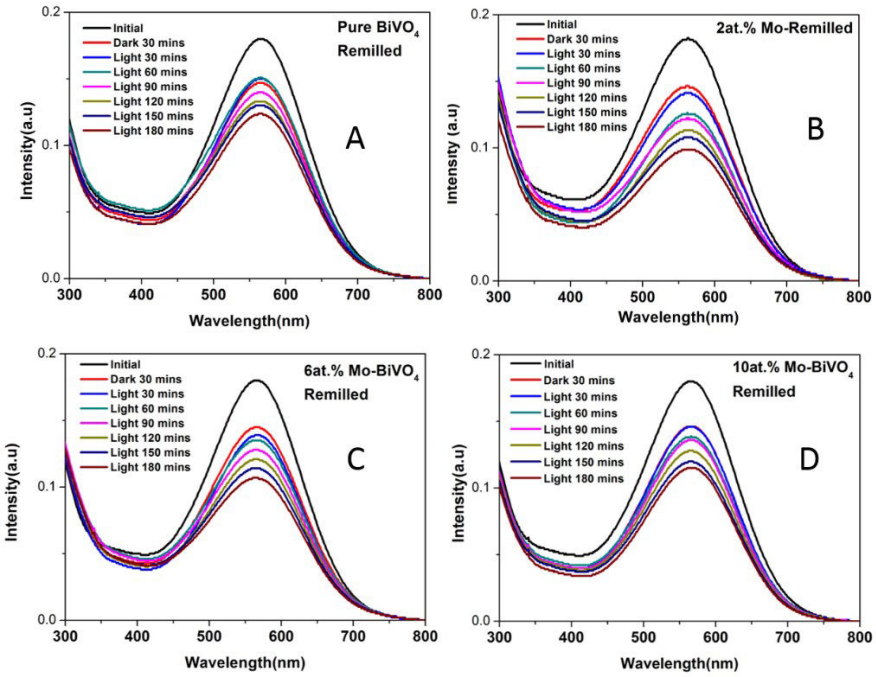

Fig.3.24. Evolution of the optical absorption of Acid blue 113 dye solutions versus irradiation time for the re-milled samples with different doping concentrations. (A, B, C and D are related to 0, 2, 6 and 10 at.% Mo rates).

Higher concentration of Mo doped $BiVO_4$ powders have shown lower degradation rates probably due to inhomogeneous distribution of Mo ions in the host matrices. The possibility of phase segregation with the formation of Mo clusters can acts as electron traps preventing the oxidation process required in heterogeneous catalysis.

3.2.4. Summary of the study

Mo doped $BiVO_4$ nanoparticles were synthesized by mechano-chemical method with different Mo doping rates and submitted to different treatments (annealing 450°C, 700°C, annealed and re-milled powder) in order to optimize the crystal structure with limited particle sizes. Thus, by XRD and micro-Raman investigations, monoclinic scheelite structure with good crystalline features was obtained for representative samples. Spherical shapes of nanoparticles with sizes in the range 50-100 nm for annealing at 450°C, whereas average 2 μm as diameter was obtained for annealing at 700°C and finally, after re-milling, the powders are formed by agglomerated smaller nanoparticles with nanosized diameters 8-10 nm. Optimal crystalline quality was confirmed by using HRTEM analysis and from FE-SEM images, it was shown the tendency of decreasing the particle size with rising the concentration of Mo doping. For the optical behaviour, UV-Vis optical absorption bands show a net decrease of the band gap for the doped and re-milled powders irrespective to the doping rates. This evolution of

optical features is of particular interest for visible light driven photocatalysis based on stabilized scheelite monoclinic structure in Mo-$BiVO_4$. Additionally, the doping rates manifests by additional shoulder which develops as function of the doping rates and tend to increase the absorption in the visible range. Photocatalysis studies were carried out through the degradation of acid blue 113 dyes in solution under visible light irradiation. The comparative photocatalysis efficiency indicates that the annealed and re-milled powder with doping rate at 2at.% Mo possesses the highest performance. It seems that the small particle sizes favour the photocatalysis which proceeds at the outermost particle surfaces. The good compromise between doping rate, particle size and crystalline quality seems achieved in the 2 at.% Mo doping of $BiVO_4$ offering the highest efficiency in heterogeneous photocatalysis based on dyes degradation.

3.3. Mechano-chemical synthesis of Silver doped $BiVO_4$ powders

3.3.1 Importance of Silver doping $BiVO_4$ in the prospect of photocatalysis

Plasmonic sensitization considerably enhances photocatalytic efficiencies, which is due to the separation of the photo-excited electrons and holes which suppresses their recombination [27]. Plasmonic sensitization involves the incorporation or decoration of a semiconductor with noble metal nanoparticles (NMNPs) such as Au, Ag, Pt and Cu etc. Moreover, insertion of Ag would extend the absorption in visible light due to phenomena of Local Surface Plasmon Resonance (LSPR). The LSPR excitation will aid photocatalytic performance by transfer localized photon energy nearby semiconductors to drive the distant chemistry[28][29][30]. In LSPR of NMNPs refers to the phenomenon in which the conducting electrons on the NPs undergo a collective oscillation (excitation) induced by the oscillating electric field of the impinging light. The oscillating charges increase an electrical field near the surface. When the frequency of the incident light satisfies the resonance conditions of the NMNPs, the SPR occurs with the associated light absorption. The unique capacity of plasmonic nanostructures to concentrate electromagnetic fields, scatter electromagnetic radiation, or convert the energy of photons into heat makes them suitable for various applications. By manipulating the composition, shape and size of Ag nanoparticles, it is possible to design nanostructures that interact with the entire solar spectrum and beyond [31]. Apart from the LSPR effect, silver metal can trap the excited electrons from $BiVO_4$ and leave the holes for the degradation reaction of organic species. The Ag^+ might act as hole trapping sites, reducing electron-hole recombination and promoting interfacial charge transfer should be optimized in order to improve the efficiency of the photocatalysts [32, 33, 34]. Doping with silver has been of considerable interest, due to its strong LSPR effect under near visible light irradiation [35, 36, 37], strong electron trapping ability [38]. An important feature of the electric fields is that they are spatially non-homogenous, with the highest field strength in the proximity of the nanostructures. This suggests that SP-induced e-/h+ pair formation should be greatest in the part of the semiconductor that is the closest to Ag particle.

In this context, we report the photochemical reactivity of plasmonic $Ag/BiVO_4$ nanocomposites prepared by industrial favour technique, high energy ball milling (HEM). Complementary characterization methods were conjugated to shed light on all relevant features and investigations of structural, electronic and optical properties of $Ag/BiVO_4$ powder samples.

The forthcoming section reports experimental investigations of Ag/$BiVO_4$ nanocomposite formation in the ball milled $BiVO_4$. The optimized synthesis parameters were defined to obtain the relevant crystalline structure, precise insights on the electronic and optical features as function of doping rates. The characterizations were realized by X-ray diffraction, field emission scanning electron microscopy FE-SEM and high resolution transmission electron microscopy HR-TEM. Dielectric relaxation measurements and UV-Vis absorption experiments were analyzed to shed light on the plasmonic effect of Ag embedded with the host structures $BiVO_4$ and the ability to harvest better the visible light. The main aim lies in the improvement of photocatalytic efficiency of Ag-$BiVO_4$ nanocomposites compared to un-doped material.

3.3.2. Results and discussion

3.3.2.1. X- ray diffraction analysis

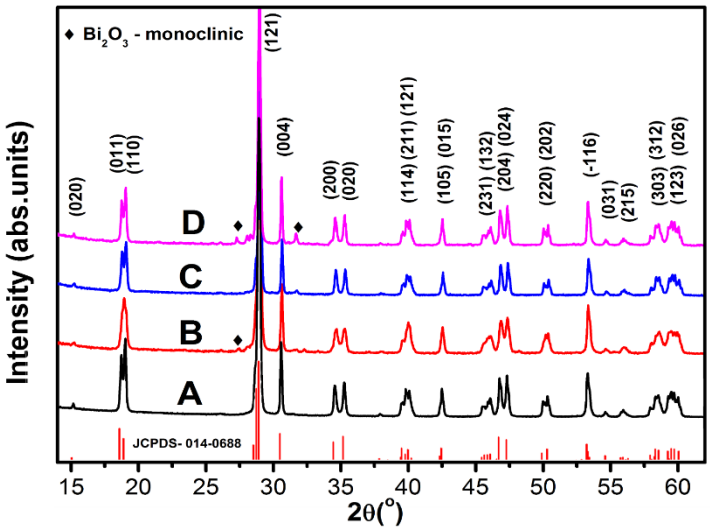

Fig.3.25. X-ray powder diffraction patterns of Ag: $BiVO_4$ nanoparticle prepared by ball milling technique. The bottom red lines represent the reference positions of the powder diffraction peaks of monoclinic $BiVO_4$ (pattern 14-0688).

The crystal structure of the Ag/$BiVO_4$ nanoparticles synthesized by ball milling techniques was studied by XRD and micro Raman techniques. All the powder samples have shown monoclinic scheelite phase with characteristic peaks in agreement with JCPDS data card (No: 14-0688) depicted in Fig.3.25. However, there is no distortion in monoclinic scheelite phase as well as no obvious diffraction peaks of the silver based compound. Thus, silver incorporation did not affect the crystal structure of $BiVO_4$ [39, 37] and seems to indicate smaller sized silver clusters homogeneously distributed in the host semiconductor (see below

HR-TEM). Crystalline domain sizes of $BiVO_4$ and $Ag/BiVO_4$ were estimated from Scherrer's formula and reported in table 3.3.1. The calculations consider the XRD line broadening FWHM values subtracted from the standard FWHM of the used reference LaB_6 fixed at $\Delta(2\theta)=0.046°$. The average size of the crystalline domains for $Ag/BiVO_4$ nanocomposites were situated in the range of 35 – 50 nm.

Table 3.9. Calculated crystal domains sizes from Scherrer's formula and optical band gap values of $Ag/BiVO_4$ nanocomposites.

samples	Crystallite size(nm)	Band gap E_g(eV)
$BiVO_4$	45.78	2.51
1at.% $Ag/BiVO_4$	37.07	2.47
3at.% $Ag/BiVO_4$	43.93	2.46
5at.% $Ag/BiVO_4$	48.29	2.45

3.3.2.2 micro-Raman analysis

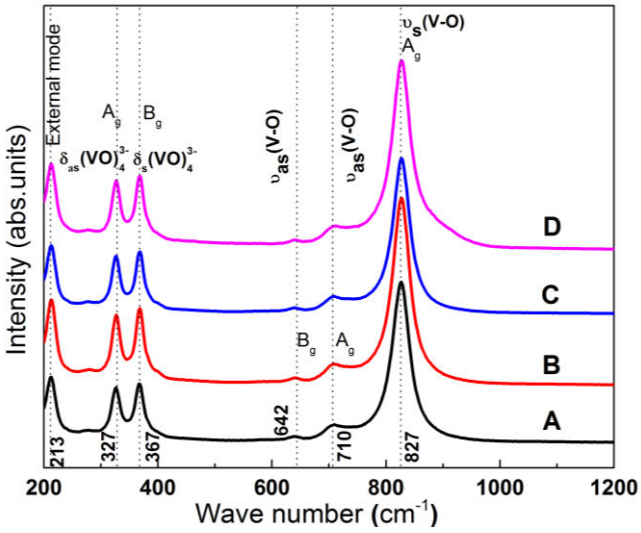

Fig.3.26. Raman spectra of Ag: $BiVO_4$ nanoparticles prepared ball milling technique, where A, B, C and D are 0, 1, 3 and 5 at.% silver concentrations.

The Raman spectra of monoclinic $BiVO_4$ has five distinguishable vibrational bands around 210, 326, 366, 710 and 826 cm^{-1} as shown in Fig.3.26. The vibrational mode at 210 cm^{-1} is the external mode of monoclinic $BiVO_4$. Remaining modes are inferred from VO_4 tetrahedron subject to two sets of stretching mode V–O bonds such as shorter symmetric A_g at

831 and longer asymmetric A_g -710 cm^{-1} respectively. The symmetric (A_g) and anti-symmetric (B_g) bending modes occur at 366 and 326 cm^{-1} respectively. All the spectra of Ag-$BiVO_4$ have shown the features according to monoclinic phase for the host structure. This suggests that the crystalline quality of samples didn't change significantly with Ag loading rates as was also reported in some metal loaded semiconductor materials [40, 41].

3.3.2.3. FE-SEM analysis

FE-SEM images of Ag/$BiVO_4$ nanocomposites (**Fig.3.27)** show highly agglomerated spherical particles with sizes around 50 nm**.** Agglomeration may due to the high surface energy and inter-particles forces which is obvious due to strong collusions between reactants and hard phase balls in HEM process. Quantitative chemical composition by EDAX analysis of Ag/$BiVO_4$ nanoparticle are summarized in **Table 3.10**.

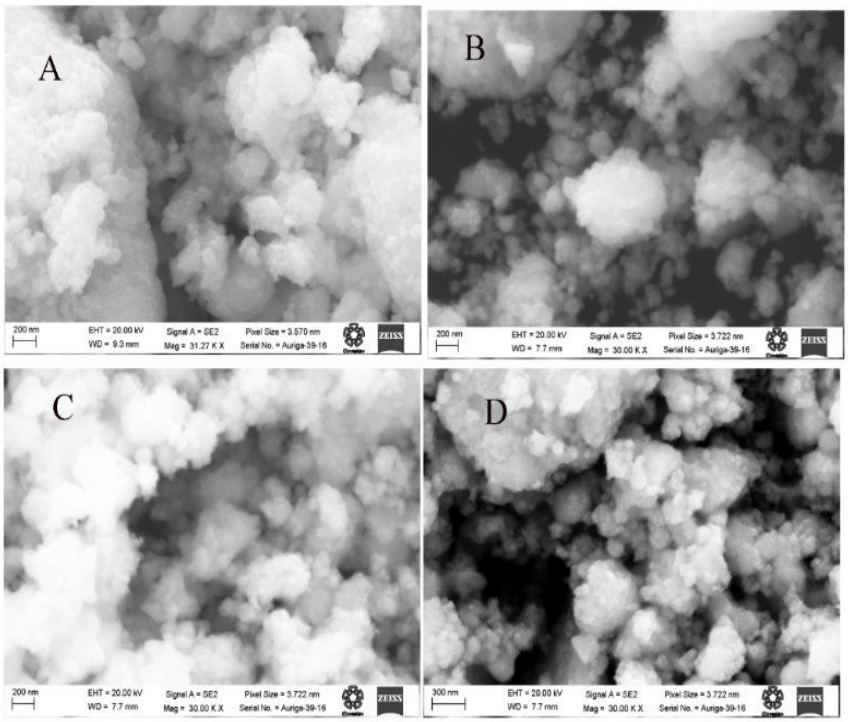

Fig.3.27. Morphologies of Ag/$BiVO_4$ nanoparticle from SEM. where A, B, C and D are 0, 1, 3 and 5 at.% silver concentrations.

Table 3.10. Compositional data of Ag: $BiVO_4$ nanoparticles from EDAX.

Ag (at.%) Experimental	Ag (at.%) (EDS)	Bismuth (at.%)	Vanadium (at.%)	Oxygen (at.%)
0	0	19.05	20.20	60.75
1	0.40	20.42	20.48	58.68
3	0.78	19.49	20.17	59.55
5	1.30	19.30	18.99	60.41

3.3.3.4. HR-TEM analysis:

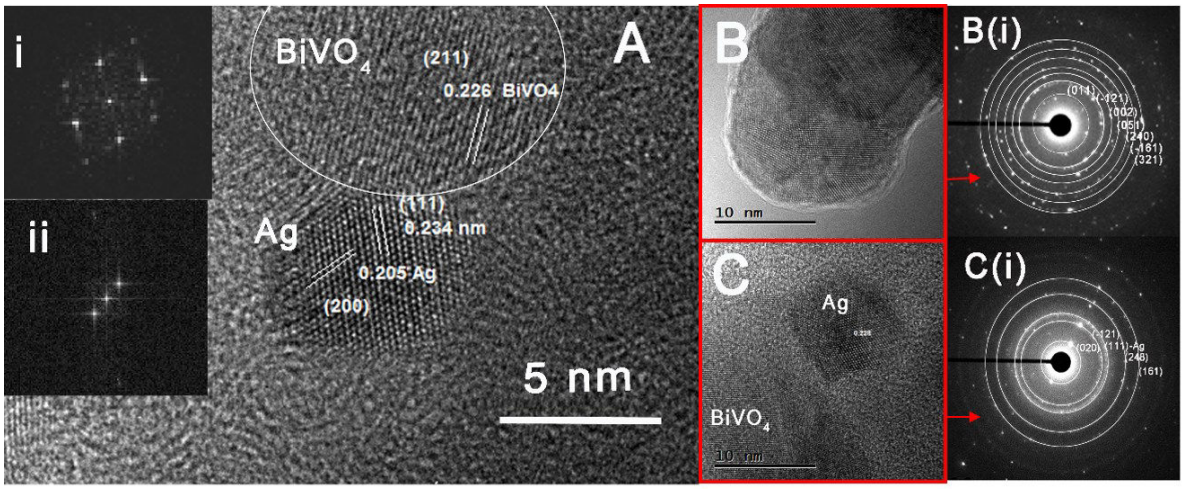

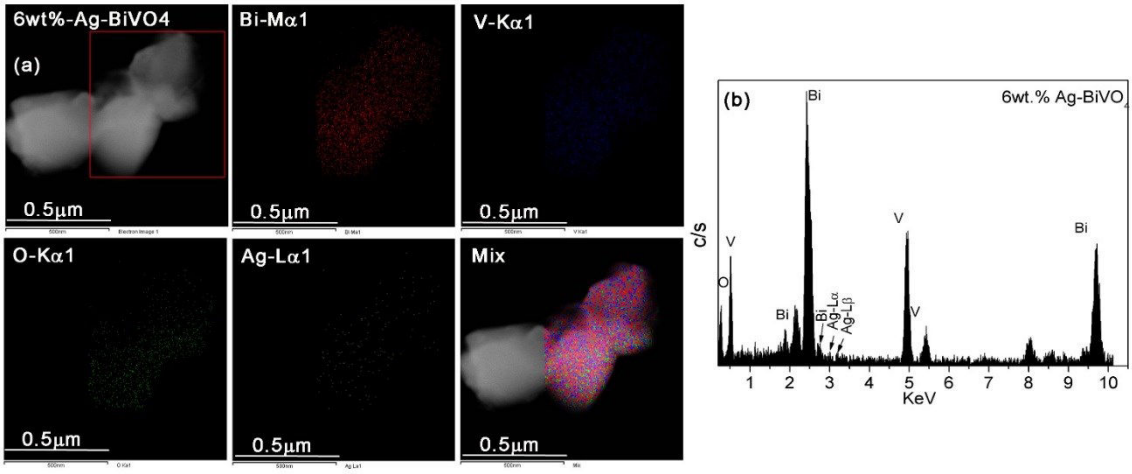

Fig. 3.28. High resolution TEM images of 5 at.% Ag/$BiVO_4$ nanoparticles. A) An enlarged HRTEM image of $BiVO_4$ and Ag as a composite from the area marked under black circles. Inset (i) and (ii) shows fast FFT patterns of Ag and $BiVO_4$ parts from A. B and C of undoped $BiVO_4$ and Ag/$BiVO_4$ composites with corresponding SAED patterns in Fig B(i) and C(i) respectively. Shows the EDS analysis from the STEM mode for the same sample.

High-resolution transmission electron microscopy (HRTEM) images reveal well crystallized domains through resolved crystalline lattice fringes as illustrated in Fig.3.28 for 5at.% Ag/$BiVO_4$ nanocomposites. The observed lattice fringes with reticular spacing of 0.226 nm are consistent with (211) reticular planes of monoclinic $BiVO_4$. In addition, separate lattice fringes with spacing about 0.205 nm and 0.224 nm are clearly observed in Fig.3.28A, in agreement with the (200) and (111) lattice planes of crystalline silver lattice superimposed to $BiVO_4$ structure. Selected area were probed by electron diffraction (SAED) performed on pure $BiVO_4$ (Fig.3.28B) and 5at.% Ag/$BiVO_4$ (Fig.3.28C) and the obtained patterns are shown in the Fig.3.28B(i) and 3.28C(ii) for un-doped and 5at.% silver loaded $BiVO_4$ samples respectively [10].

3.3.2.5. UV-Vis spectroscopy analysis

The electronic structure of semiconductors monitors their interaction with defined radiation. By acting on the crystalline structure, morphology and doping by suitable elements, the electronic and optical features can be fine-tuned to harvest defined spectral range of light. Beyond such approaches, the exploitation of plasmonic effect is worthy of interest to act efficiently on the optical features of the concerned systems [31] as we propose to point out on Ag/$BiVO_4$ nanocomposites. Thus, diffuse reflectance UV Vis spectra of Ag/$BiVO_4$ plasmonic photocatalysts for the different silver loading rates were recorded and summarized in Fig.3.29. In plasmonic photocatalyst systems, the metal clusters with oscillating electrons possess dipole nature, which in turn enhances local electric field and radiates energy to neighbour semiconducting particles. This effect enlarges the absorption band in the visible range in such plasmonic photocatalysts compared to the conventional heterogeneous photocatalysts. Similarly, as compared to pristine $BiVO_4$, a broad absorption occurs in the range of 400-800 nm for Ag/$BiVO_4$ nanocomposites. Gradual increment on spectral absorption at 520 nm with Ag loading rates correlates with LSPR effect originating from Ag nanoparticle. Furthermore, it is also demonstrated that compared to pure $BiVO_4$, the absorption edge of Ag/$BiVO_4$ nanocomposites undergoes red shift with increment of Ag loading and correlates also with the increase of silver particle size [42]. Since most of composite particles possess high interface area, the plasmonic effect can act efficiently on the optical field enhancing its intensity in the vicinity of semiconducting oxide nanoparticles. We have then proceeded to optical absorption measurements as function of the composite features and Ag loading. The relationship of absorbance and incident photon energy $h\nu$ can be described as Eq. (3.1) for direct VB to CB transitions. The threshold absorption edges were calculated for 0, 1, 3 and 5 at.% Ag loaded

$BiVO_4$ samples and are 2.51, 2.47, 2.46 and 2.45 eV respectively as summarized in Fig.3.29. After annealing treatment at 450°C, the change of the sample colour from greenish yellow to dark green was observed with Ag increment [43] (Fig.3.29).

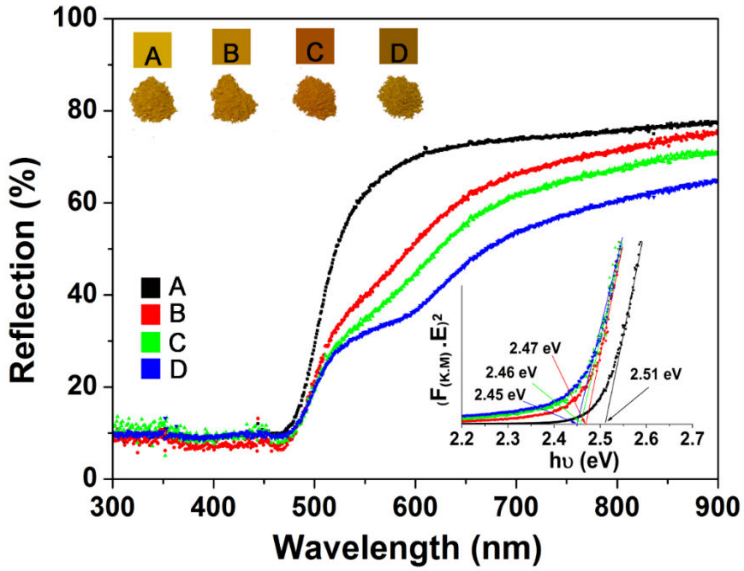

Fig. 3.29**.** Diffuse reflective spectra with inset tauc plot of Ag/BiVO4along with Colour of nanocomposites after annealing at 450°C. where A, B, C and D are 0, 1, 3 and 5 at.% silver concentrations.

The role of interfaces made by metal clusters (NMNPs) and semiconductor on the photocatalysis process can be understood based on key features of such as components and LSPR involved in metal clusters. In this context, the schematic representations of electronic band structures related to Ag particle embedded in host $BiVO_4$ SC is depicted in Fig.3.30A. For $BiVO_4$ with the features of n-type semiconductor, its Fermi level E_f is close to the conduction band energy level E_{CB}, the valence band energy E_{VB} is far below. Similarly, the Ag noble metal has a work function ϕ_m of 4.7 eV. Before their contact or embedded form, the fermi energy levels of semiconductor photocatalyst E_{fsc} and that of the noble metal E_{fM} *are* different as shown in Fig.3.30B. Once they come in-contact, schottky junction build-ups and the electrons and holes flow and forms a new equilibrium state, in which E_{fSC} and E_{fM} are equilibrated as shown in energy band diagram in Fig.3.30C. In this process, the electrons diffuse from the $BiVO_4$ side to the Ag side and create a positively charged region with no free carriers in the $BiVO_4$ nanoparticle. This forms a depleted region, or called as space-charge region. In the equilibrium state, an equal amount of electrons are trapped in the adjacent Ag surface. This builds up an internal electrical field from the $BiVO_4$ side toward the Ag part preventing further movement of the carriers. When an electron–hole pair is excited in or near

the space-charge region by an incident light, the internal electrical field E forces the electrons to move to the Ag region and the hole to the $BiVO_4$ region, preventing their recombination. The electrons and holes are then captured by the acceptors and donors in the solution, respectively, and initiate further redox reactions and improved photocatalytic efficiency.

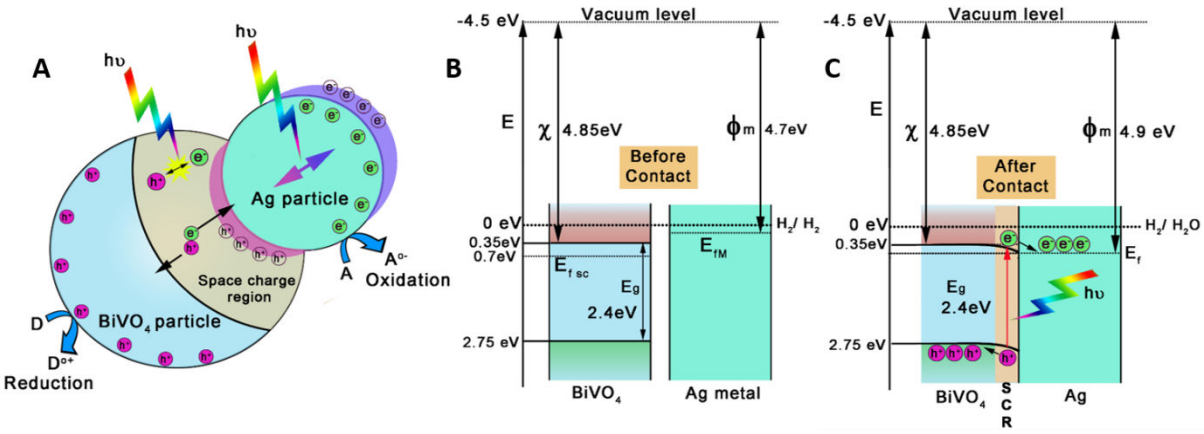

Fig.3.30A. Schematic representation of photocatalysis mechanism of Ag/$BiVO_4$ metal- semiconductor nanocomposites: A) the presence of plasmonic nanoparticle induces a space charge region in the $BiVO_4$ particle towards to Ag metal; B) before contact of $BiVO_4$ with Ag metal and corresponding their fermi energy levels $E_{f\,sc}$ and E_{fM} ; C) after contact of $BiVO_4$ with Ag metal and corresponding movement of charge transfer.

3.3.2.6. Dielectric relaxation Spectroscopy (DRS) analysis

DRS determines the relative complex permittivity $\varepsilon^*(\omega,T) = \varepsilon'(\omega,T) + i\varepsilon''(\omega,T)$ with respect to applied alternative voltage with frequency $(\omega/2\pi)$ at different temperature values varied from 273 K to 473 K. Phenomenological model was used for the adjustment of the complex permittivity $\varepsilon^*(\omega,T)$ and consist in the using Havriliak–Negami (HN) relaxation model [44].

$$\varepsilon^*(\omega,T) = \frac{\sigma_{dc}}{i\omega\varepsilon_0} + \varepsilon_\infty + \frac{\Delta\varepsilon}{((1+i\omega\tau)^\alpha)^\beta} \qquad \rightarrow(3.2)$$

In this expression, dielectric strength Δε represents the difference between the quasi-static dielectric permittivity ε_s and the high frequency one referred as ε_∞. The coefficient τ corresponds to a characteristic time related to the dielectric relaxation phenomena which are also closely related to the conductivity process as will be discussed below. The phenomenological parameters α and β, in the range $0 < \alpha, \beta < 1$, traduce the distribution of relaxation times due to some inhomogeneous processes which may be induced by nanocrystallite sizes or surface effects on $BiVO_4$ nanoparticles. In the simple case of Arrhenius process, the dielectric relaxation is characterized by a unique relaxation time τ_0 leading to α =

1 and β = 1. For a general case, we may only give asymptotic behaviour of $\varepsilon''(\omega)$ in the low and high frequency range with respect to the characteristic relaxation times. The tendencies are expressed in terms of α and β such as $\varepsilon'' \propto \omega^{\alpha}$ when ωτ << 1 and $\varepsilon'' \propto \omega^{\alpha\beta}$ for ωτ >> 1. From the plot of dielectric functions, the characteristic time τ correlates with the frequency where the maximum of dielectric loss peak is located. The coefficients α and β are evaluated by an adjustment of experimental curves according to Eq. (1). In HN simulation fit, the same set of fitting parameters were used for both real and imaginary parts of dielectric function as well as for the frequency dependant conductivity. This procedure allows to obtain more precise values and made confident in evaluated parameters using HN model.

Fig.3.31 summarizes the experimental results for real and imaginary parts of the relative complex dielectric permittivity related to Ag/$BiVO_4$ with different silver concentrations 0, 1, 3 and 5at.% denoted by A, B, C, and D respectively. The frequency dependence of the dielectric function reflects dynamic processes with thermally dependant relaxation phenomena. The dielectric behaviour at low frequencies manifests through the divergence of $\varepsilon'(\omega)$ is related to electrodes polarization induced by ionic conductivity being thermally activated with rise of temperature. Excluding this LF divergent contribution, the adjustment of dielectric data is well accounted by HN model depicted as continuous lines in Fig. 3.31 & Fig.3.32. The calculated asymptotic behaviour of $\varepsilon'(\omega)$ in the quasi-static regime is assigned to the dielectric constant which is indicative of large interfacial polarizations. Indeed, the quasi-static values of $\varepsilon'(\omega)$ are approximately around 80, 110, 140 and 100 for Ag loading concentrations such as 0, 1, 3 and 5at.% respectively. Compared to solo pristine $BiVO_4$, Ag/$BiVO_4$ composite structures got higher dielectric constant values, which is due to interfacial polarization induced by metal-semiconductor interface. Among Ag/$BiVO_4$ composites, 3at.% Ag has shown higher value i.e.140 as compared other doping rates, which means it has related to size of particle and higher charge carrier density and for longer times, it obviously benefits their higher plasmonic induced charge transfer of on the surface of composites, which effectively participate to further redox process.

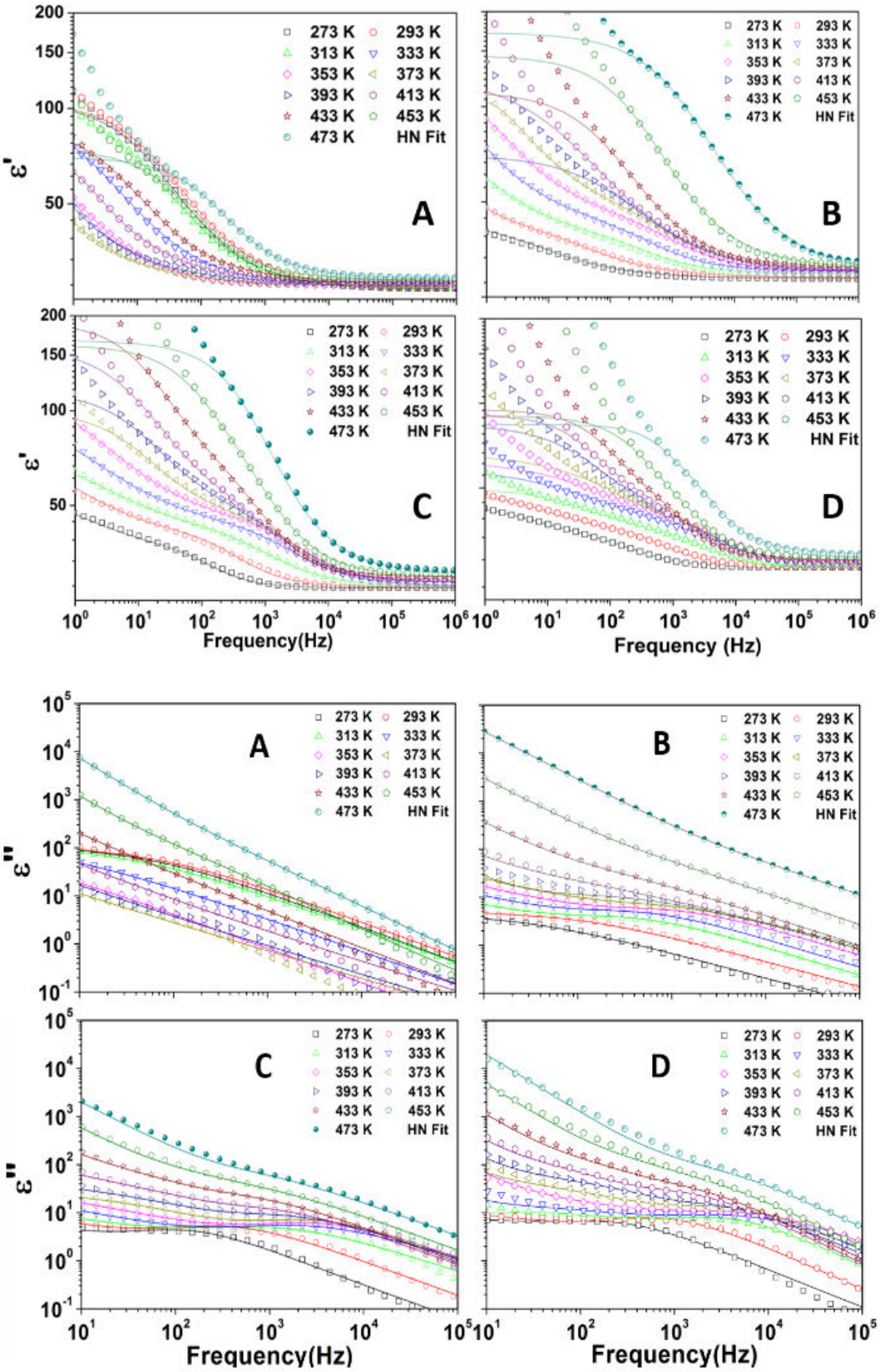

Fig.3.31. Temperature and frequency dependencies of real and imaginary dielectric permittivity of Ag/ BiVO4 samples where A, B, C and D are 0, 1, 3 and 5 at.% of Silver concentration. The continuous lines are fits obtained by Havriliak–Negami model.

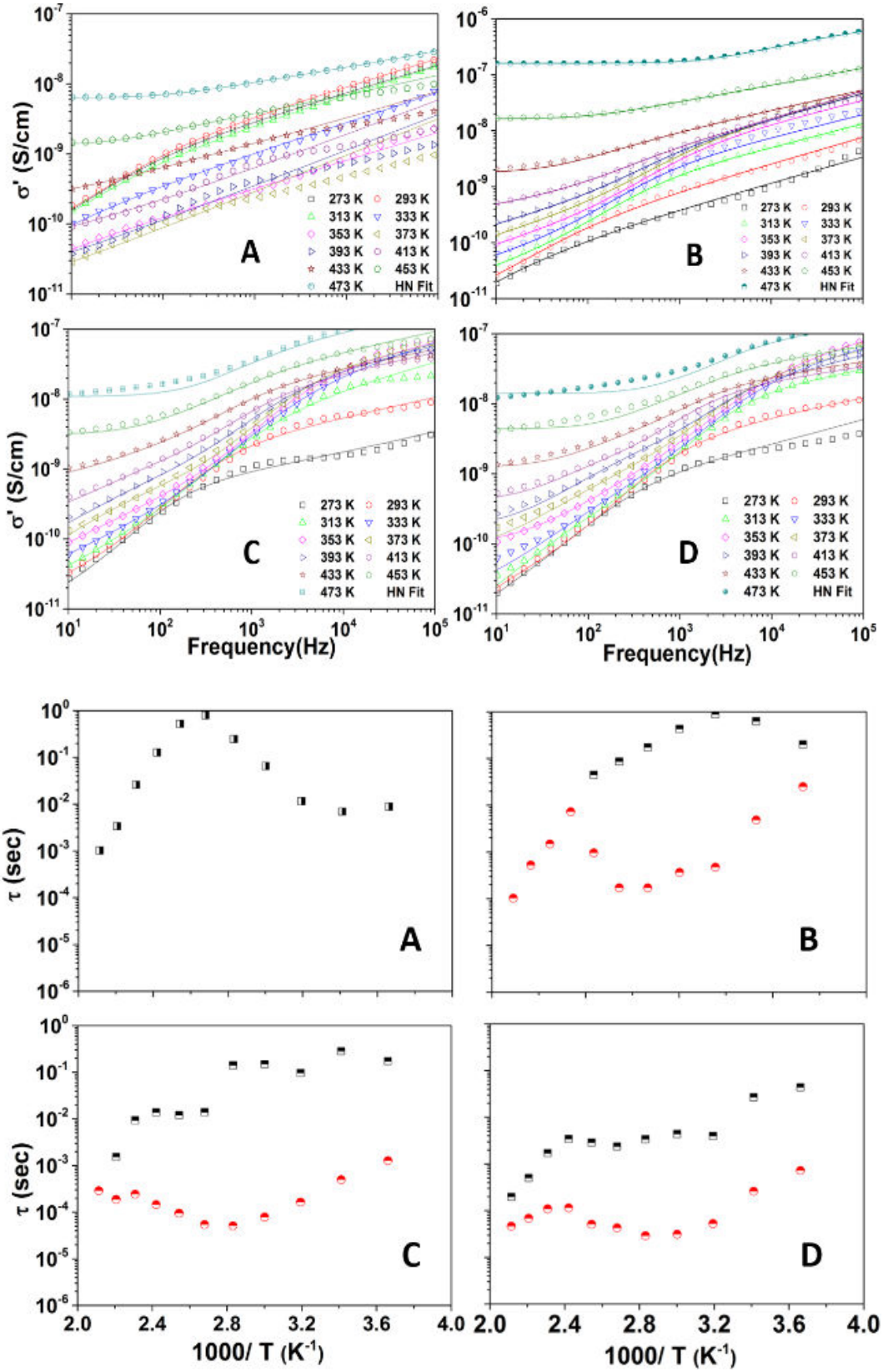

Fig.3.32. Frequency dependent (ac) of real part of conductivity σ_{dc} for different temperatures and continues lines are fits by HN model and Variation of the relaxation times for different temperatures for Ag/ $BiVO_4$ samples where A, B, C and D are 0, 1, 3 and 5 at.% of silver concentrations.

The relaxation times characterize the dynamics of processes induced in the samples by dipolar relaxation or charge carriers mobility under alternative voltages. A distribution of relaxation times (DRT) is more relevant and may be accounted for by the well-known Havriliak–Negami phenomenological model. In this case, the parameters define the shape of the dielectric functions and inform on the occurrence of DRT. For pure $BiVO_4$ single regime is shown with one relaxation model, whereas Ag loaded $BiVO_4$ as shown two relaxation regimes. The dielectric behaviour of $BiVO_4$ semiconductor particles is marked by a unique relaxation mechanism with defined relaxation time. The situation is different in Ag loaded $BiVO_4$ samples were dielectric functions show two relaxation processes with different relaxation times. The incorporation of Ag in the composites is expected to contribute on both interfacial polarization and charge transfer mechanism as well and modify the dynamic of such phenomena. In addition to the relaxation peculiarities, the thermal evolution of the dc conductivities is also modified as function of silver loading as shown in Fig.3.32 and particularly the activation energies of charge carriers analysed below. Indeed, the semi-log plot of $\sigma_{dc}^{i}(T)$ versus the inverse of temperature 1000/T(K) is reported in Fig.3.33 and exhibits quite complex behaviour depending on the temperature range and the composition of the sample.

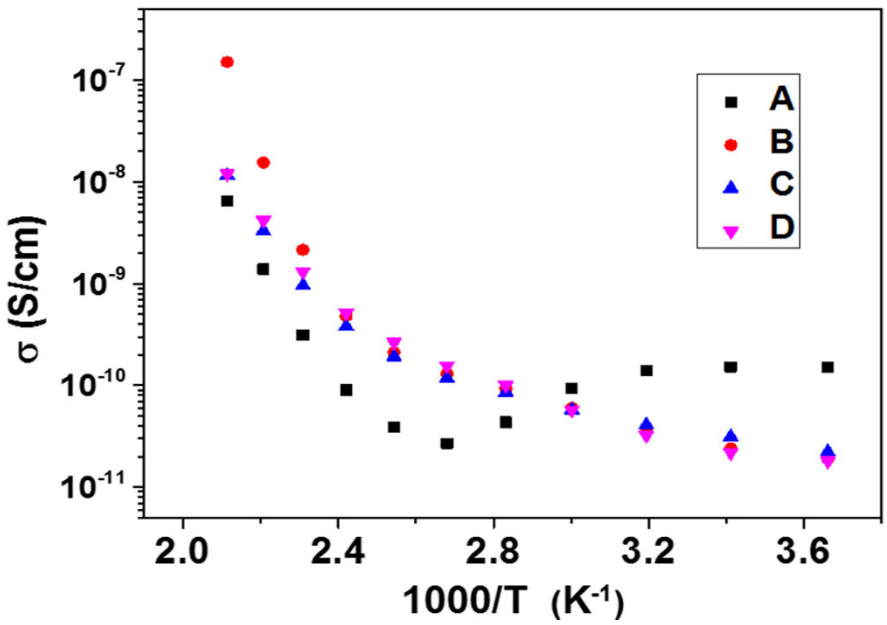

Fig.3.33. DC-conductivity versus inverse temperature plots for Ag/ $BiVO_4$ samples where A, B, C and D are 0, 1, 3 and 5 at.% of silver concentrations.

The variation regime of the conductivity depends on the sample composition (Ag loading) and on the temperature range. Thus, for temperature in the range 373-473K, the conductivity is thermally activated as $\sigma_{dc}^{i}(T) = \sigma_{dc}^{i0}.e^{-\frac{E_a^i}{kT}}$ with the activation energy estimated by adjustment of the experimental data and summarized in table 1 as function of the Ag content. The energy value is similar for all samples even if a tendency of slight decrease is noticed for higher Ag loading. The most striking behaviour is observed for pure sample in the low temperature regime (273K-373K) where a slight increase of the conductivity occurs with decreasing the temperature. This contrast with Ag/$BiVO_4$ which show a decrease of the conductivity with the temperature in the range 373-473K. The low temperature regime is marked by change in the activation energy as summarized in Table 3.11.

The activation energies are about 10 times higher in the temperature range 373–473 K as compared to the temperature range 273–373 K. Low activation energies indicate low barrier heights on the conduction channels which depend on the microstructure of the samples. Indeed, 3at.% Ag loaded sample has larger size particles as compared to others and then possesses low density of interfaces. This lead to low activation energies for the charge carrier motions in the order of 0.06 eV. An expectation might be formulated also for this sample for applications in photocatalysis because efficient process of photo-induced charge carriers enhances the redox reactions as compared to other samples. On the other hand, the silver clusters involved at the interfaces facilitate the electron transport in one hand and enhance the intensity of radiation fields through plasmonic effect (SPR) as will be discussed in forthcoming section.

Table 3.11. Activation energies for Ag/$BiVO_4$ nanocomposites prepared by ball milling technique.

Samples	E_a^i (eV) (273 K - 373 K)	E_a^i (eV) (373 K- 473 K)
Pure $BiVO_4$	/	0.36
1at.% Ag/$BiVO_4$	0.07	0.46
3at.% Ag/$BiVO_4$	0.06	0.30
5at.% Ag/$BiVO_4$	0.08	0.28

To sum up, the thermally activated conductivity of two representative nanocomposites $Ag/BiVO_4$ samples is in the order of 7 x 10^{-9} S/cm, 1.7 x 10^{-7} S/cm, 1.5 x 10^{-8} S/cm and 1.5 x 10^{-8} S/cm at T (K) 473 K. Two main thermal evolution regimes were demonstrated with cross-over at critical temperature about 353 K. The activation energies depend on the considered temperature ranges, on the microstructure and crystalline order of the samples which modulate the height of barriers acting on the conduction channels. The charge carrier mobility is expected to be optimal in 3% Ag loaded BiVO4 and combined with plasmonic effect from Ag clusters can offer contribute to the creation of efficient plasmonic photocatalysts.

3.3.3. Photocatalytic studies

The photocatalytic activity of the $Ag/BiVO_4$ samples were analysed from the degradation of AB 113 with in particle diffusion method under water. Photocatalytic tests for $Ag/ BiVO_4$ were carried out by adding powders to a solution with a defined molar concentration of dyes. Stirring during 20 min under dark leads absorption/ desorption equilibrium. At this stage, the charged solutions of AB113 dyes dissolved in pure, 1at.% , 3at.% and 5at.% doping rates of Ag in $BiVO_4$, show, respectively, total degradation rate of 22%, 33% 38 % and 24%. Under irradiation with Xe-lamp (1.5 W/cm^2) the photoactive solution charged by 1at.% and 3at.% $Ag/BiVO_4$ powders show the most efficient photocatalytic process illustrated by the rapid decrease in intensity of the absorption band at 566 nm, suggesting a rapid degradation of the azo groups. Such process of degradation of AB113 dyes seems to create as a product small aromatic molecules leading to the absorption band located in the UV range (280 nm wavelength). The photocatalytic activity is compared between the different Ag loaded (Fig.3.34(A)) and indicates that the 3at.% $Ag/BiVO_4$ sample exhibits the best efficiency to degrade AB113 groups. For higher Ag loading (5at.%) the degradation rate remain quite low and almost at the same level as pure $BiVO_4$. Several reasons may be invoked such as non-homogeneous distribution of Ag nanoparticles in the host media. The increase of silver loading may create also stoichiometry departure and the deficit in oxygen may create traps centres for the photoactivated charge carriers. Similar trend has been already observed for hydrothermal synthesized Ag doped $BiVO_4$ where the rate of doping of 1at.% constitutes an optimal concentration for the highest degradation rate of methyl orange aqueous dye solution [39].

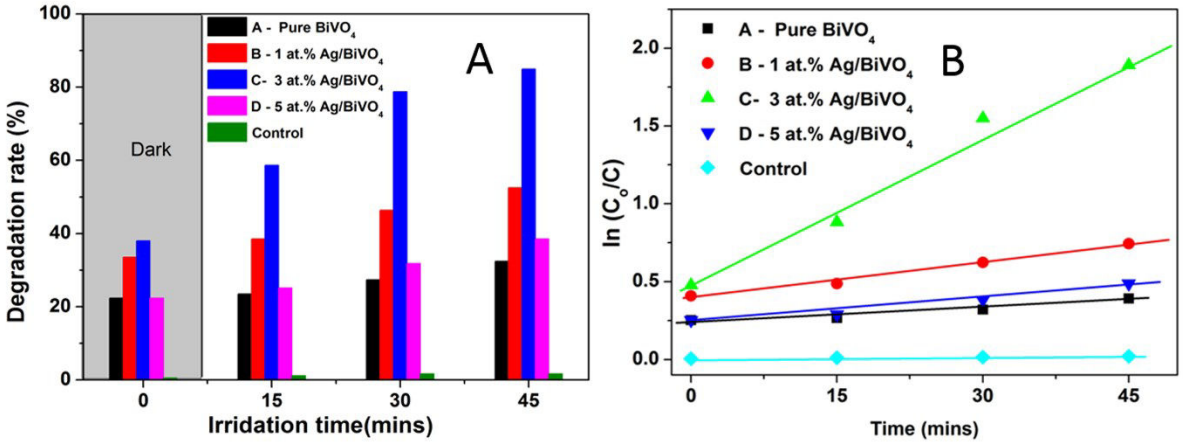

Fig.3.34. A) Kinetic analysis of degradation of Acid113 measured by absorbance at room temperature with showing the effect of increasing concentration of Ag with $BiVO_4$; B) shows the pseudo-first-order kinetics of degradation of AB 113 diazo in solution at absorbance peak 556 nm.

The analysis of the kinetics of degradation of AB113 dyes by $Ag/BiVO_4$ as shown in Fig.3.34(B) is made by using the following relation:

$$[Abs]_t = [Abs]_0 \, e^{-tk}$$

where, $[Abs]_0$ represents the initial absorbance, $[Abs]_t$ is the measured absorbance versus irradiation time t and k the degradation rate constant or pseudo-first-order rate constant. For degradation of azo groups in AB113, k is found in the order of 3.2×10^{-2} min^{-1} for the sample 3 at.% $Ag/ BiVO_4$. For all samples, the rates of degradation constant values are tabulated below (Table 3.12).

Table 3.12. Pseudo first-order degradation rate constant of AB113 dye in the presence of $Ag/BiVO_4$ with different loading content of silver.

Doping rates of $Ag/BiVO_4$ (at.%)	**Degradation rate constant, k (min^{-1}) ± error**	**Remaining percent of AB113 after radiation for 45 min (%)**
0	0.004 ± 2.6e-4	67.6
1	0.008 ± 1.7e-4	47.5
3	0.032 ± 0.0028	15.1
5	0.0055 ± 3.4e-4	61.5

3.3.4. Summary of the study

Ag/$BiVO_4$ nanocomposites were synthesized by high energy ball milling technique with different loading rates of Ag from 1-5 at.%. Structural properties were investigated by usual XRD technique demonstrating the occurrence of single phase of monoclinic sheelite symmetry. The composition and morphology of the synthesized powders were clarified by FE-SEM, EDX and HR-TEM techniques and point out the existence of agglomerated particles of $BiVO_4$ with the involvement of Ag clusters. Electronic, dielectric and optical behaviours were studied and the main features characterized by complementary techniques. The electrical conductivity is marked by thermally activated values without net changes as function of the incorporation of Ag in the composites. However, the interfacial polarization and the dynamic of charge transfer mechanism reflect the effect of Ag loading. Plasmonic effect created by Ag clusters associated to $BiVO_4$ particles seems relevant to enhance the photocatalytic process based on the photo degradation of Acid blue 113 dye in solution. In this process, optimal concentration of Ag at 3at.% Ag-$BiVO_4$ was found through the high degradation rate constant with more than 90% of dyes supressed within 45 min under solar mimic lamp. Higher rates of doping overcame the efficiency of the photocatalytic reactions probably because of inhomogeneous distribution of Ag clusters in the host media.

3.4. Conclusions

M doped $BiVO_4$ (M- Cu, Mo and Ag) nanoparticles were synthesized by mechano-chemical technique with improved processing parameters as mentioned in chapter 2.2. High energy ball milled Cu, Mo and Ag doped $BiVO_4$ nanoparticles with defined doping rates were investigated by using XRD, micro-Raman HRTEM and EPR in order to probe the structural, morphology and doping features in these systems. The structural features were characterized with quantitative estimation of the lattice parameters and the lattice compression as function of the metal ion doping rates. Monoclinic scheelite structure was obtained for all the metal doped $BiVO_4$ samples with different doping ratios. For the doping process, we have demonstrated that the Cu^{2+} (0.054 nm) and Mo^{6+} (0.055 nm) ions were indeed substituted inside $BiVO_4$ crystalline sites of V^{5+} (0.050 nm) whereas metallic Ag (0.102 nm) is segregated on the surface of the $BiVO_4$ and formed nanocomposites. The substitutional doping (Cu, Mo) justified by EPR analysis, acts on the sample morphologies and electronic features through the particle size reduction, the slight lowering of the electronic band gap and extension of the absorption band

tail to red wavelengths. The photocatalytic studies performed on powder samples through the degradation of organic dyes have shown an enhancement of photocatlysis efficiency with increasing Cu doping rates. This effect is also correlated with the reduction of oxygen vacancies by doping which contributes to increase the photogenerated charges concentration and lifetimes. For Mo doped $BiVO_4$ powders, different treatments of the samples (annealed at 450°C, at 700°C and re-milled) were realized in order to optimize the crystal structure with limited particle sizes. The morphology of the particles seems to follow similar behaviour with Mo content as in the case of Cu doping. Additional optical shoulder manifests and tends to increase the absorption in the visible range with the expected improvement on the photocatalytic activity. The good compromise between doping rate, particle size and crystalline quality seems achieved in the 2 at.% Mo doped $BiVO_4$ remilled offering the higher efficiency as compared to pristine.

For Ag doped $BiVO_4$ samples case, a single phase with well crystalline monoclinic scheelite symmetry was obtained. The composition and morphology of the synthesized powders were addressed by FE-SEM, EDX and HR-TEM techniques. Thus it was shown that agglomerated particles of $BiVO_4$ associated with Ag clusters form Ag-$BiVO_4$ nanocomposites. Electronic, dielectric and optical behaviours were studied and the main features characterized by complementary techniques. However, the interfacial polarization and the dynamic of charge transfer mechanism reflect the effect of Ag loading. Plasmonic effects created by Ag clusters inside Ag-$BiVO_4$ nanocomposites are expected to enhance the photocatalytic activity as it was demonstrated on 3 at.% doped Ag-$BiVO_4$ composites.

References:

[1] L. Kranz, C. Gretener, J. Perrenoud, R. Schmitt, F. Pianezzi, F. La Mattina, et al., Doping of polycrystalline CdTe for high-efficiency solar cells on flexible metal foil, Nat. Commun. 4 (2013).

[2] A. Walsh, Y. Yan, M.N. Huda, M.M. Al-Jassim, S.H. Wei, Band edge electronic structure of $BiVO_4$: Elucidating the role of the Bi s and V d orbitals, Chem. Mater. 21 (2009) 547–551.

[3] M.G. Sorolla, M.L. Dalida, P. Khemthong, N. Grisdanurak, Photocatalytic degradation of paraquat using nano-sized Cu-TiO_2/SBA-15 under UV and visible light, J. Environ. Sci. 24 (2012) 1125–1132.

[4] B.B. Srivastava, S. Jana, N. Pradhan, Doping Cu in Semiconductor Nanocrystals: Some Old and Some New Physical Insights, J. Am. Chem. Soc. 133 (2011) 1007–1015.

[5] H. Xu, H. Li, C. Wu, J. Chu, Y. Yan, H. Shu, Preparation, characterization and photocatalytic activity of transition metal-loaded $BiVO_4$, Mater. Sci. Eng. B Solid-State Mater. Adv. Technol. 147 (2008) 52–56.

[6] Y. Wang, W. Duan, B. Liu, X. Chen, F. Yang, J. Guo, The Effects of Doping Copper and Mesoporous Structure on Photocatalytic Properties of TiO_2, J. Nanomater. 2014 (2014) 1–7.

[7] R. Venkatesan, S. Velumani, a. Kassiba, Mechanochemical synthesis of nanostructured $BiVO_4$ and investigations of related features, Mater. Chem. Phys. 135 (2012) 842–848.

[8] Z. Zhao, Z. Li, Z. Zou, Electronic structure and optical properties of monoclinic clinobisvanite $BiVO_4$., Phys. Chem. Chem. Phys. 13 (2011) 4746–4753.

[9] H.S. Park, K.E. Kweon, H. Ye, E. Paek, G.S. Hwang, A.J. Bard, Factors in the metal doping of $BiVO_4$ for improved photoelectrocatalytic activity as studied by scanning electrochemical microscopy and first-principles density-functional calculation, J. Phys. Chem. C. 115 (2011) 17870–17879.

[10] F.D. Hardcastle, I.E. Wachs, Determination of vanadium-oxygen bond distances and bond orders by Raman spectroscopy, J. Phys. Chem. 95 (1991) 5031–5041.

[11] L. Sandhya Kumari, P. Prabhakar Rao, a. Narayana Pillai Radhakrishnan, V. James, S. Sameera, P. Koshy, Brilliant yellow color and enhanced NIR reflectance of monoclinic

BiVO4 through distortion in VO_4^{3-} tetrahedra, Sol. Energy Mater. Sol. Cells. 112 (2013) 134–143.

[12] J. Yu, A. Kudo, Effects of structural variation on the photocatalytic performance of hydrothermally synthesized $BiVO_4$, Adv. Funct. Mater. 16 (2006) 2163–2169.

[13] M. Wang, Q. Liu, Y. Che, L. Zhang, D. Zhang, Characterization and photocatalytic properties of N-doped BiVO4 synthesized via a sol-gel method, J. Alloys Compd. 548 (2013) 70–76.

[14] H. JIANG, H. DAI, X. MENG, L. ZHANG, J. DENG, K. JI, Morphology-Dependent Photocatalytic Performance of Monoclinic $BiVO_4$ for Methyl Orange Degradation under Visible-Light Irradiation, Chinese J. Catal. 32 (2011) 939–949.

[15] R. Venkatesan, S. Velumani, M. Tabellout, N. Errien, A. Kassiba, Dielectric behavior, conduction and EPR active centres in $BiVO_4$ nanoparticles, J. Phys. Chem. Solids. 74 (2013) 1695–1702.

[16] A. Kudo, R. Niishiro, A. Iwase, H. Kato, Effects of doping of metal cations on morphology, activity, and visible light response of photocatalysts, Chem. Phys. 339 (2007) 104–110.

[17] A.P.Z. and J.Z. Zhang, Syntheses and activities of visible-light-driven Cu/$BiVO_4$ composite photocatalysts, Wuli Huaxue Xuebao,. (2010) 1337–1342.

[18] H. Xu, H. Li, C. Wu, J. Chu, Y. Yan, H. Shu, et al., Preparation, characterization and photocatalytic properties of Cu-loaded $BiVO_4$., J. Hazard. Mater. 153 (2008) 877–84.

[19] K. Ding, B. Chen, Z. Fang, Y. Zhang, Z. Chen, Why the photocatalytic activity of Mo-doped $BiVO_4$ is enhanced: a comprehensive density functional study., Phys. Chem. Chem. Phys. 16 (2014) 13465–76.

[20] C. Stampfl, C.G. Van de Walle, Density-functional calculations for III-V nitrides using the local-density approximation and the generalized gradient approximation, Phys. Rev. B. 59 (1999) 5521–5535.

[21] W. Yao, H. Iwai, J. Ye, Effects of molybdenum substitution on the photocatalytic behavior of $BiVO_4$., Dalton Trans. (2008) 1426–30.

[22] S.P. Berglund, A.J.E. Rettie, S. Hoang, C.B. Mullins, Incorporation of Mo and W into nanostructured $BiVO_4$ films for efficient photoelectrochemical water oxidation, Phys.

Chem. Chem. Phys. 14 (2012) 7065.

[23] Z. Zhao, W. Luo, Z. Li, Z. Zou, Density functional theory study of doping effects in monoclinic clinobisvanite $BiVO_4$, Phys. Lett. A. 374 (2010) 4919–4927.

[24] M. Wang, Y. Che, C. Niu, M. Dang, D. Dong, Effective visible light-active boron and europium co-doped $BiVO_4$ synthesized by sol-gel method for photodegradion of methyl orange., Elsevier B.V., 2013.

[25] W.-J. Shin, J.-Y. Lee, J.C. Kim, T.-H. Yoon, T.-S. Kim, O.-K. Song, Bulk and interface properties of molybdenum trioxide-doped hole transporting layer in organic light-emitting diodes, Org. Electron. 9 (2008) 333–338.

[26] G. Xie, Y. Meng, F. Wu, C. Tao, D. Zhang, M. Liu, et al., Appl. Phys. Lett. 92 (2008) 093305.

[27] S. Linic, P. Christopher, D.B. Ingram, Plasmonic-metal nanostructures for efficient conversion of solar to chemical energy, Nat. Mater. 10 (2011) 911–921.

[28] P. Christopher, D.B. Ingram, S. Linic, Enhancing photochemical activity of semiconductor nanoparticles with optically active Ag nanostructures: Photochemistry mediated by Ag surface plasmons, J. Phys. Chem. C. 114 (2010) 9173–9177.

[29] Z. Zheng, B. Huang, X. Qin, X. Zhang, Y. Dai, M.-H. Whangbo, Facile in situ synthesis of visible-light plasmonic photocatalysts $M@TiO_2$ (M = Au, Pt, Ag) and evaluation of their photocatalytic oxidation of benzene to phenol, J. Mater. Chem. 21 (2011) 9079.

[30] G. Thennarasu, A. Sivasamy, Metal ion doped semiconductor metal oxide nanosphere particles prepared by soft chemical method and its visible light photocatalytic activity in degradation of phenol, Powder Technol. 250 (2013) 1–12.

[31] M. Rycenga, C.M. Cobley, J. Zeng, W. Li, C.H. Moran, Q. Zhang, et al., Controlling the synthesis and assembly of silver nanostructures for plasmonic applications, Chem. Rev. 111 (2011) 3669–3712.

[32] P. V. Kamat, Photophysical, photochemical and photocatalytic aspects of metal nanoparticles, J. Phys. Chem. B. 106 (2002) 7729–7744.

[33] I. Ilisz, A. Dombi, Investigation of the photodecomposition of phenol in near-UV-irradiated aqueous TiO_2 suspensions. II. Effect of charge-trapping species on product distribution, Appl. Catal. A Gen. 180 (1999) 35–45.

[34] E. Stathatos, T. Petrova, P. Lianos, Study of the Efficiency of Visible-Light Photocatalytic Degradation of Basic Blue Adsorbed on Pure and Doped Mesoporous Titania Films, (2001) 5025–5030.

[35] S. Kuriakose, V. Choudhary, B. Satpati, S. Mohapatra, Enhanced photocatalytic activity of Ag-ZnO hybrid plasmonic nanostructures prepared by a facile wet chemical method., Beilstein J. Nanotechnol. 5 (2014) 639–50.

[36] X. Chen, Z. Zheng, X. Ke, E. Jaatinen, T. Xie, D. Wang, et al., Supported silver nanoparticles as photocatalysts under ultraviolet and visible light irradiation, Green Chem. 12 (2010) 414.

[37] M.K. Seery, R. George, P. Floris, S.C. Pillai, Silver doped titanium dioxide nanomaterials for enhanced visible light photocatalysis, J. Photochem. Photobiol. A Chem. 189 (2007) 258–263.

[38] B. Xin, L. Jing, Z. Ren, B. Wang, H. Fu, Effects of simultaneously doped and deposited Ag on the photocatalytic activity and surface states of TiO_2, J. Phys. Chem. B. 109 (2005) 2805–2809.

[39] A. Zhang, J. Zhang, Synthesis and characterization of Ag/$BiVO_4$ composite photocatalyst, Appl. Surf. Sci. 256 (2010) 3224–3227.

[40] S.M. Thalluri, C. Martinez Suarez, M. Hussain, S. Hernandez, A. Virga, G. Saracco, et al., Evaluation of the Parameters Affecting the Visible-Light-Induced Photocatalytic Activity of Monoclinic $BiVO_4$ for Water Oxidation, Ind. Eng. Chem. Res. 52 (2013) 17414–17418.

[41] J. Yu, A. Kudo, Effects of Structural Variation on the Photocatalytic Performance of Hydrothermally Synthesized $BiVO_4$, Adv. Funct. Mater. 16 (2006) 2163–2169.

[42] H. Zhang, G. Wang, D. Chen, X. Lv, J. Li, Tuning Photoelectrochemical Performances of Ag - TiO_2 Nanocomposites via Reduction / Oxidation of Ag, (2008) 6543–6549.

[43] A.Y. Booshehri, S. Chun-Kiat Goh, J. Hong, R. Jiang, R. Xu, Effect of depositing silver nanoparticles on $BiVO_4$ in enhancing visible light photocatalytic inactivation of bacteria in water, J. Mater. Chem. A. 2 (2014) 6209.

[44] S. Havriliak, S. Negami, J. Polym. Symp. 14 (1966).

Chapter-4

Synthesis and characterization of M doped $BiVO_4$ (M - Mo, Cu and Ag) nanoparticles via sol-gel method

In this chapter, we study the structural, optical and morphological properties of metal ion doped $BiVO_4$ obtained by sol-gel technique. The challenge of this synthesis approach lies in the possibility to realize substitutional doping of $BiVO_4$ by metallic ions within crystalline sites of monoclinic scheelite phase. Sol-gel synthesis was used for $BiVO_4$ nanoparticles doped with several metal ions such as Molybdenum (Mo), Copper (Cu) and Silver (Ag) with 2at% (atomic percentage). The choice of doping elements is based on the expected change in the electronic band structure of $BiVO_4$ leading to the improvement of photo-induced charge transfer required in photocatalytic reactions. The characterization methods ensure relevant features for the application of heterogeneous photocatalysis by degradation of organic dyes in solution. The sol–gel process is one of the most widely used methods because of

- Simple and easy synthesis technique.
- It can obtain very fine and nanoscale particles with high homogeneity.
- Low processing temperatures.
- Good control of the composition and better homogeneity of the final products.

4.1. Results and Discussion

4.1.1. X-ray powder diffraction analysis

M-$BiVO_4$ (M- Mo, Cu and Ag) powders were synthesized by sol-gel technique as explained in Chapter 2.section 2. All samples were investigated by X-ray powder diffraction technique and the crystalline phase indicate the occurrence of pure monoclinic scheelite corresponding to JCPDS data no: 083-1699 shown in Fig. 4.1(A). The characteristic diffraction peak at $2\theta = 28.97$ corresponds to (hkl) plane (112) with a slightly higher 2θ shift for doped $BiVO_4$ in comparison with pure $BiVO_4$. All the doped samples have shown good crystalline quality, by observing the doublet peaks (2θ) at 18.67°, 18.97° and 34.4°, 35. 2° as shown in Fig. 4.1(B) with higher angles of 2θ shift for Mo, Cu doped $BiVO_4$ samples. This shift indicates the occurrence of compressive strain induced in clinobisvanite structure with variation in the lattice dimensions [1] (further justified by Raman analysis in the Fig.4.2) by the incorporation

of copper / molybdenum in place of vanadium in monoclinic structure of $BiVO_4$. This substitution occurred, since the ionic radii of V^{5+} (0.050 nm) is close to Mo^{6+} (0.055 nm) and Cu^{2+} (0.071 nm) in the same tetrahedral arrangement [2]. For Ag doped $BiVO_4$ sample, good crystalline phase is obtained with well-defined characteristic peaks at 2θ= 28.59°, 28.80° and 28.95°. Only slight shift in 2θ towards higher angle is noticed due to uniform strain without significant lattice deformation. It is well known that doping process induces lattice distortions for substitutional elements into the crystal host sites. Lattice parameters and atomic position were calculated for Cu, Mo and Ag doped $BiVO_4$ and for pure $BiVO_4$ by Rietveld method using MAUD *v*2.33 software. Refined parameters are summarized in tables 4.2a, b respectively. The compressed unit cell of M-$BiVO_4$ is due to the substitution of Cu / Mo in few sites of V as reflected from the positional change of V, O1 and O2, while Bi didn't show departure from positions in pristine sample. These data have confirmed the substitution of tetrahedral coordinated V by Mo and Cu ions in the crystal lattice due to their close ionic radii values. Crystal domain sizes were estimated for Cu, Mo and Ag-$BiVO_4$ and undoped $BiVO_4$ from the diffraction peak widths (FWHM) using Scherrer's formula. The calculated values are tabulated in Table 4.1 and is found in good agreement with refined pattern crystal size data. The line broadening was measured by using a standard diffraction pattern of LaB_6 (Lanthanum Hexaboride powder). Instrumental broadening was measured as 0.046 degrees in 2θ and was subtracted from the FWHM observed in diffracted patterns of Mo, Cu and Ag doped $BiVO_4$ powders.

Table 4.1. Crystallite size and crystallographic data of undoped and 2 at.% M doped -$BiVO_4$ (M - Mo, Cu and Ag) 2at.% doping content.

samples	FWHM	2θ position (-121)	Crystallite size(nm)	Band gap E_g(eV)
$BiVO_4$	0.228	28.91	44.75	2.54
2at.% Mo-$BiVO_4$	0.245	29.02	36.6	2.52
2at.% Cu-$BiVO_4$	0.255	28.96	39.2	2.49
2at.% Ag-$BiVO_4$	0.227	28.95	50.3	2.52

Table 4.2(A) Lattice parameters for monoclinic scheelite phase of undoped and M doped $BiVO_4$ (M – Mo, Cu and Ag) 2at.% doping content.

	Crystal lattice parameters				
Sample name	Crystal size(nm)	a(Å)	b(Å)	c(Å)	γ(°)
$BiVO_4$	124.3	5.165 ($\pm 2.7e^{-4}$)	5.101 ($2.7e^{-4}$)	11.657 ($5.5e^{-4}$)	90.33
2at.%Mo-$BiVO_4$	106.5	5.173 ($\pm 2.3e^{-4}$)	5.087 ($\pm 2.6e^{-4}$)	11.661 ($7.1e^{-4}$)	90.3
2at.%Cu-$BiVO_4$	97.01	5.166 ($\pm 2.2e^{-4}$)	5.100 ($2.3e^{-4}$)	11.68 ($5.0e^{-4}$)	90.04
2at.%Ag-$BiVO_4$	180.2	5.183 ($\pm 4.5e^{-4}$)	5.089 ($4.3e^{-4}$)	11.681 ($9.1e^{-4}$)	90.33

Table 4.2(B) Atomic positions in undoped and M doped $BiVO_4$ (M- Mo, Cu and Ag) 2at% doping content. Refined by Rietveld method.

Sample name	**Bi**			**V**			**O_1**			**O_2**		
$BiVO_4$	0	0.249	0.6306	0	0.25	0.138	0.144	0.531	0.189	0.35	0.360	0.435
	(±0.001-0.002)			(±0.002-0.003)			(±0.002-0.003)			(±0.002-0.003)		
2at%Mo-$BiVO_4$	0	0.25	0.6275	0.005	0.255	0.104	0.121	0.483	0.184	0.35	0.414	0.45
	(±0.001-0.002)			(±0.002-0.003)			(±0.002-0.003)			(±0.002-0.003)		
2at%Cu-$BiVO_4$	4.0e-4	0.25	0.623	1.7e-4	0.25	0.109	0.141	0.56	0.215	0.38	0.359	0.43
	(±0.0007-0.001)			(±0.002-0.003)			(±0.002-0.003)			(±0.002-0.003)		
2at%Ag-$BiVO_4$	1.1e-4	0.249	0.6305	0	0.25	0.136	0.160	0.516	0.191	0.355	0.353	0.437
	(±0.002-0.003)			(±0.002-0.003)			(±0.002-0.003)			(±0.002-0.003)		

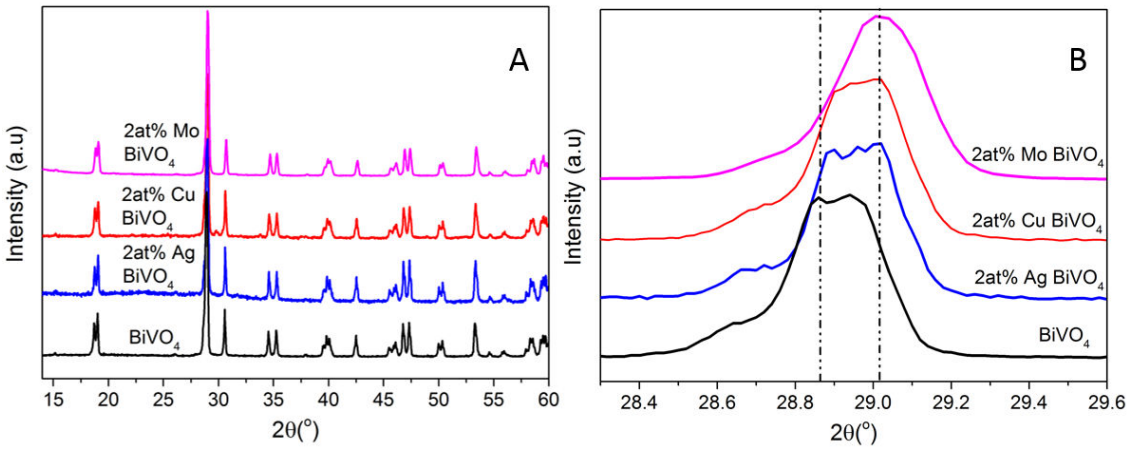

Fig.4.1. (A) XRD pattern of pristine and M-$BiVO_4$ (M - Mo, Cu and Ag) synthesized by sol-gel method in comparison with diffraction pattern of JCPDS No-14-0688. (B) The characteristic peak shift to higher 2θ angle.

4.1.2. Raman investigations

The normalized Raman spectra (Fig. 4.2) has shown similar features for pristine and 2at.% M-doped $BiVO_4$ (M - Mo, Cu and Ag) powders obtained by sol-gel technique. Monoclinic scheelite structure gives rise to five noticeable Raman bands which are related to VO_4 tetrahedron structure. The dominant Raman band near ca. 827 cm^{-1} is assigned to υ_s(V-O), with a weak shoulder at ca.710 cm^{-1} which is assigned to υ_{as}(V-O). The $\delta_a(VO_4^{-3})$ and $\delta_{as}(VO_4^{-3})$ modes are around ca. 327 and 367 cm^{-1}. External (rotational/translational) modes are near ca. 213 cm^{-1} [3]. All the Raman mode positions of M-$BiVO_4$ (M - Mo, Cu and Ag) were tabulated in Table 4.3. For Cu and Mo-$BiVO_4$, the V-O stretching mode is shifted to a lower wavenumber (817 $cm^{-1}$for Mo and 819 cm^{-1} for Cu) as compared to 827 cm^{-1} for $BiVO_4$ (denoted by '★'). This reveals that changes occur in the molecular bonds within VO_4 tetrahedron, which is in agreement with increase in V-O bond length due to the substitution of V by Cu and Mo in respective samples [157,162]. This is also confirmed by the presence of Mo-O-Mo stretching mode at ca.871cm^{-1}. For Ag doped $BiVO_4$ sample, there is no much noticeable change as compared to undoped $BiVO_4$ sample. Since Ag particles were segregated on the surface of $BiVO_4$ as shown in HRTEM images in Fig.4.7 (A, B).

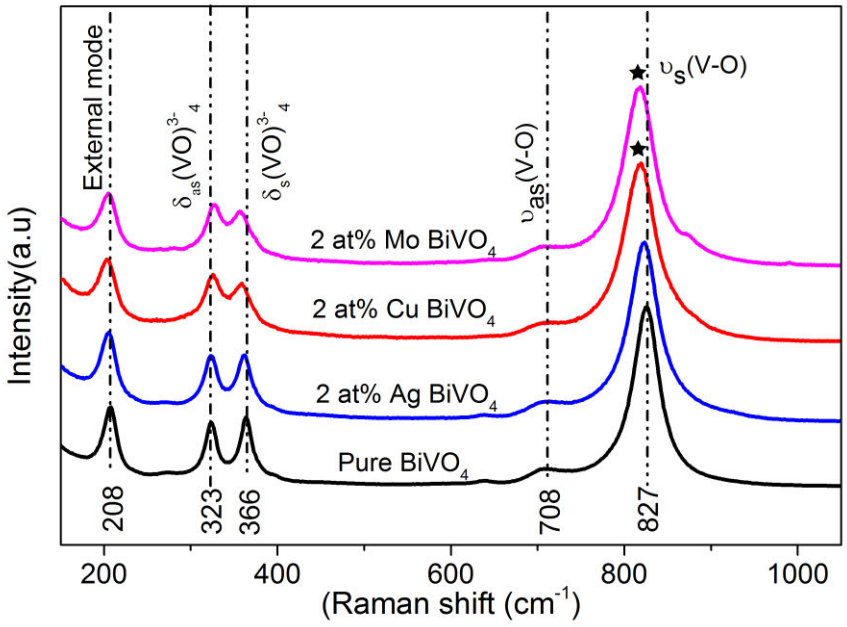

Fig.4.2. Normalized Raman spectra of 2at.% M-$BiVO_4$ (Mo, Cu and Ag) compared to undoped $BiVO_4$.

Table 4.3. Raman stretching and bending modes with respective notations υ_s symmetric stretching mode, υ_{ass}: asymmetric stretching mode, δ_s: symmetric deformation mode, δ_{ass}: asymmetric deformation mode, w: weak; m: medium; vs: very strong.

Tentative assignments	$BiVO_4$	Mo-$BiVO_4$	Cu-$BiVO_4$	Ag-$BiVO_4$
ν_s(V–O)(vs)	826.3	818.1	819.3	823.3
ν_{ass}(V–O)(w)	708.2	703	707.2	705.2
$\delta_s(VO_4^{3-})$(m)	364.1	357.7	358.7	361.9
$\delta_{ass}(VO_4^{3-})$(m)	322.9	326.1	325.2	322.9
External mode(m)	207.8	205.6	203.4	205.6

4.1.3. EPR probing of metal ions in $BiVO_4$

EPR spectroscopy is a sensitive tool to probe the doping process and/or surface effects where the oxidation state of particular ion leads to electronic configurations with unpaired spins. The fundamental electronic configuration of molybdenum is [Kr] $4d^5$ $5s^1$. The paramagnetic ions Mo^{3+} ($4d^3$), and Mo^{5+} ($4d^1$) give rise to EPR signals with quite different features since these ions are characterized by effective spins S=1/2, 3/2 respectively. For copper doping of $BiVO_4$, the fundamental electronic configuration of copper is [Ar] $3d^{10}$ $4d^1$. Oxygen

environment stabilizes the oxidation state Cu^{2+} with an electronic configuration [Ar]($3d^9$) giving rise to EPR signal with an electronic spin S=1/2. EPR spectra of metal ion doped $BiVO_4$ are summarized in Fig.4.3. In the perfect crystalline structure, vanadium ions possess the valence state V^{5+} leading to spinless ions. However, due to oxygen vacancies induced notably in nanosized particles with highly specific surfaces, the departure of vanadium from its normal valence state leads to reduced species as V^{4+} which are paramagnetic ions. The electronic configuration of V^{4+} ($3d^1$) possesses an effective electronic spin (S=1/2) giving rise to an EPR signal. As the valance state of V ions is '+5', this should be the expected valence for substitutional Mo ions in the host crystal sites of $BiVO_4$. This situation is indeed involved in Mo-doped $BiVO_4$ and the experimental EPR spectrum (Fig.4.3) is well accounted by an effective spin S=1/2 as for Mo^{5+}. The experimental EPR spectra were adjusted by using Bruker-Winsinfonia software and the procedure of fitting determines the magnetic fields (B_{ir}) related to both electronic and nuclear spin states. By using derivative of Lorentzian lines centred at different B_{ir} and using suitable line width we can reproduce precisely all features of the experimental spectra. This allows extracting g_x, g_y, g_z components and the other parameters. EPR parameter for Mo-$BiVO_4$ samples are g_x=1.94, g_y=1.91, g_z=1.99 and the hyperfine parameters are A_x=30 Gauss, A_y=40 Gauss, A_z=120 Gauss. The anisotropy of the spectral parameters underlines the location of Mo^{5+} in crystal sites with orthorhombic local symmetry. This result is consistent with the Raman investigations, which have shown that distortion of the tetrahedrons (VO_4) is due to Mo substitution. The EPR signal associated to Cu^{2+} ions is accounted by unresolved hyperfine structures, for both ions are accounted by dipolar or exchange interactions between copper and vanadium ions situated at relatively short distances. Thus, Raman and EPR experiments support the achievement of Mo and Cu substitution inside the crystal sites of $BiVO_4$. These changes will be exhibited on the electronic and optical features of respective dopant of $BiVO_4$.

Similarly, the fundamental electronic configuration of Silver is [Kr] $4d^{10}$ $5s^1$. The oxidation state of Ag can be stabilized as Ag^0, Ag^{1+}, Ag^{2+}, $Ag^{3+}$and Ag^{4+}. However, some valence states as Ag^{1+} and Ag^{3+} are EPR silent species and cannot be identified because they are spin-less ions. Naturally silver is available in two isotopes ^{107}Ag and ^{109}Ag with almost equal abundance of 51 and 49 %. The paramagnetic ions Ag^0 ($5s^1$) and Ag^{2+} ($4d^9$) give rise to EPR signals with nuclear spin I=1/2 having tetragonal geometry. They possess quite different features since these ions are characterized by effective spins S=1/2, 3/2 respectively which are associated to nuclear spin I=1/2 [163,164]. From the Fig.4.3, EPR spectra of Ag-$BiVO_4$ doesn't

have any resolved hyperfine splitting peaks, and are almost similar to pristine form of $BiVO_4$ prepared by sol-gel method. Thus, major amount of silver must be present in diamagnetic form such as Ag nano clusters (further justified by HR-TEM images as shown in Fig.4.7) [8].

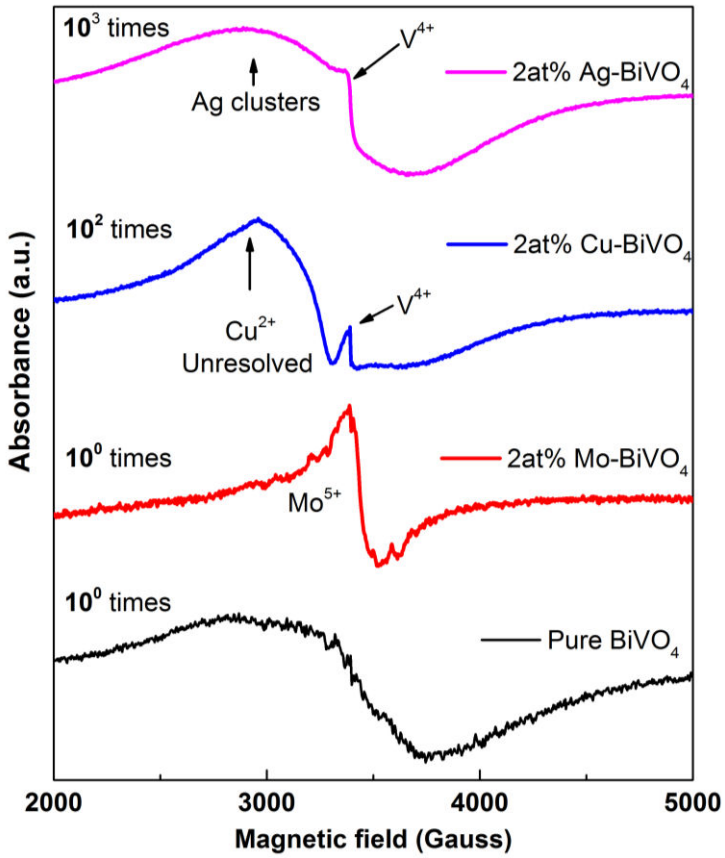

Fig.4.3. Electron paramagnetic resonance spectra of Mo^{5+}, Cu^{2+}, Ag^{1+} ions for 2 at% M-$BiVO_4$ powders (M - Mo, Cu and Ag).

4.1.4. Morphological studies

FESEM micrographs of pristine and M-$BiVO_4$ (M-Cu Mo and Ag) doped $BiVO_4$ samples prepared by sol-gel are shown in Fig.4.4. The particle agglomeration presented in all the samples is due to sintering at 450°C. However, pristine and Ag doped $BiVO_4$ particles have similar behavior, such as they exhibit weak coalescence of spherical shaped particles with size range from 400 - 500 nm. For molybdenum and copper doped $BiVO_4$, grain particles were smaller in size, ranging from 50 to 150 nm having weak agglomerations. The reduction in particle size can be seen clearly for Mo and Cu doped $BiVO_4$ powders as compared to others. It seems that the inhibition of particle growth occurs from the metal ion incorporated into the lattice of $BiVO_4$, without distortions in monoclinic phase. Moreover M. Wang has observed similar effect for Eu doped $BiVO_4$ [9] which inhibits the $BiVO_4$ particle growth. The grains of

Ag doped $BiVO_4$ shows similar behavior as pristine which confirms incorporation of Ag superficially. The elemental composition analysis was performed by EDAX for undoped, as well asMo, Ag and Cu doped-$BiVO_4$ nanoparticles and their measured at. % values are summarized in Table 4.4.

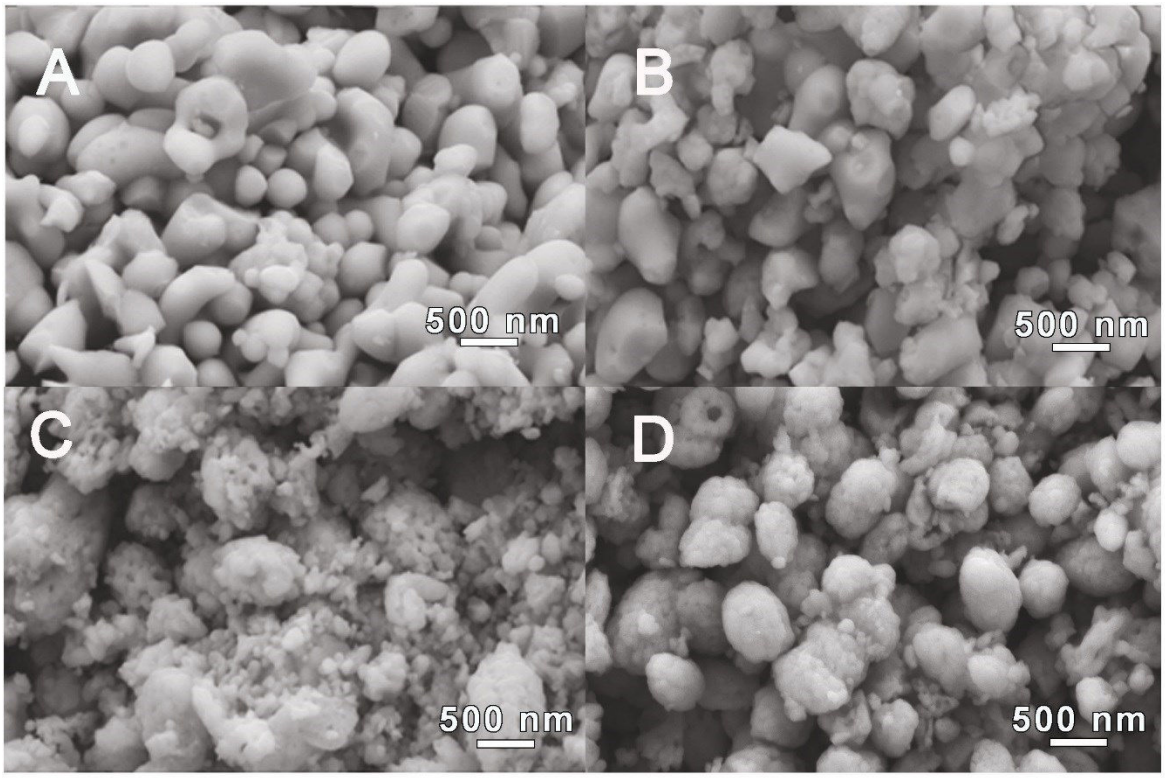

Fig.4.1. SEM images of undoped $BiVO_4$ and M-$BiVO_4$ (Mo, Cu and Ag), where A - Pure $BiVO_4$, B - Ag doped, C - Cu doped and D -Mo doped $BiVO_4$ powders.

Table 4.4. Elemental composition of $BiVO_4$ and 2at% M-doped $BiVO_4$ (M - Mo, Cu and Ag) powder samples from EDAX.

Samples	Bi	V	O	dopant
$BiVO_4$	20.48	23.79	55.73	-
2at% Mo-$BiVO_4$	24.20	18.51	56.23	1.06
2at% Ag-$BiVO_4$	15.36	14.04	69.42	1.19
2at% Cu-$BiVO_4$	21.11	21.03	56.25	1.61

4.1.5. Elemental analysis

The presence of Cu, Mo in doped samples is well ensured in agreement with the above structural and electronic characterizations. However elemental analysis was made by scanning transmission electron microscopy (STEM) to probe the distribution of chemical constituents in M-$BiVO_4$ doped samples. The STEM analysis of Mo doped $BiVO_4$ is shown in Fig.4.5.

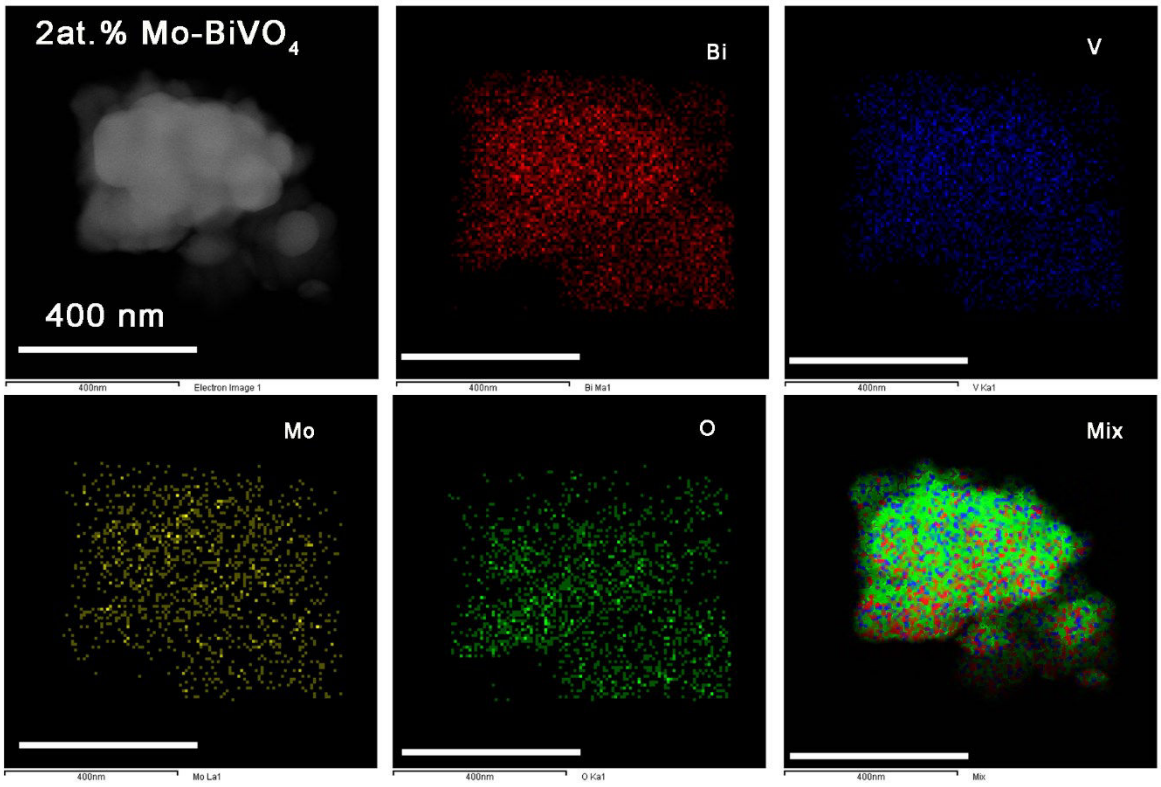

Fig. 4.5. Elemental distribution probed by STEM analysis of 2at.% Mo doped $BiVO_4$ samples.

STEM analysis was carried out for Cu doped $BiVO_4$ but we could not get the proper statistical analysis since the Cu grid was used. So, EDAX analysis was performed from the FESEM to further confirm the chemical constituents as shown in below Fig. 4.6.

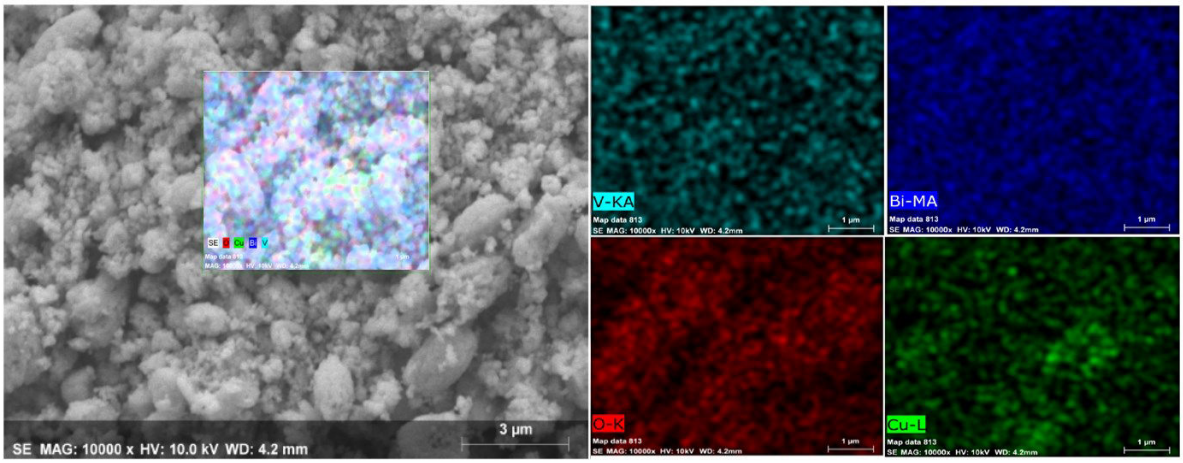

Fig.4.6. EDAX chemical composition of 2at.% Cu doped $BiVO_4$ nanoparticles with individual elemental mappings.

For Ag loaded sample, we could clearly observe Ag nanoparticles on the surface of $BiVO_4$ particles showing difference in the contrast at Fig. 4.7(A, B) different locations. STEM analysis further confirmed that Ag is segregated on the surface at random places as shown in Fig.4.7(C, D).

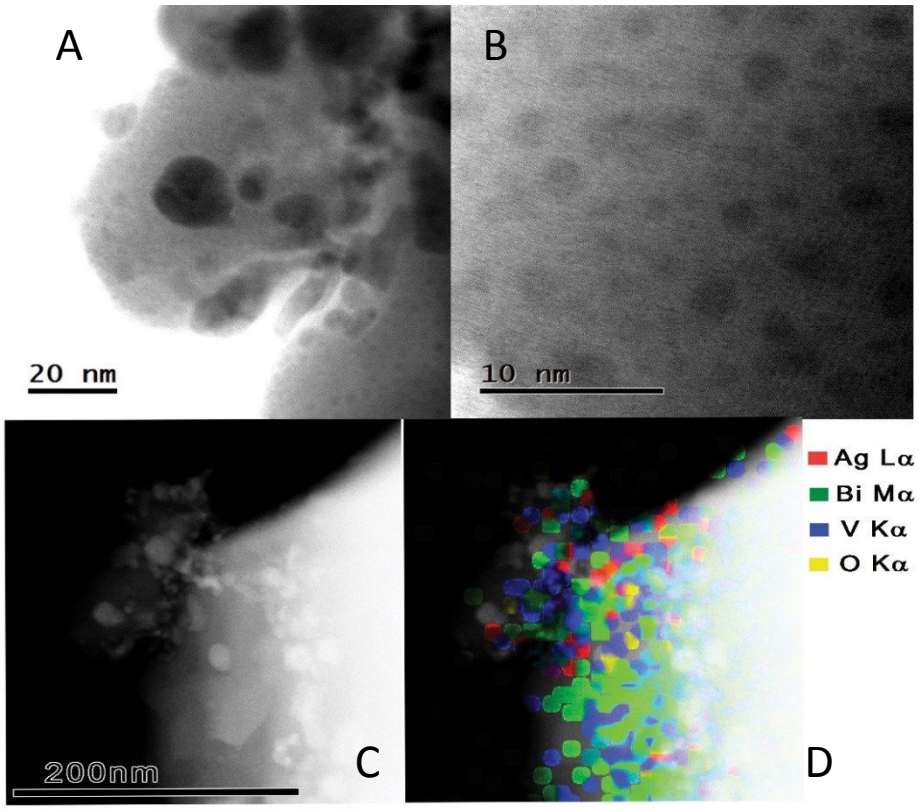

Fig.4.7. HRTEM images of 2at.% Ag doped $BiVO_4$ nanoparticles with two different locations (A) and (B). Where (C) and (D) are elemental distribution probed by STEM analysis.

4.1.6. Optical features

Diffuse reflectance spectra of pristine and M-$BiVO_4$ powder samples are shown in Fig.4.8. M-$BiVO_4$ induces strong absorption in visible region (500-850 nm) with slight red shift of absorption threshold edges as compared to pristine $BiVO_4$. From the diffuse reflectance spectra, the optical band gap measurements were determined by using approximate formula derived from Kubelka-Munk model (eq.4.1):

$$F(R) = \frac{(1-R)^2}{2R} = \frac{k}{s} = \frac{Ac}{s} \qquad (4.1)$$

Where R is the absolute reflectance of the sample, k- molar absorption coefficient, s-scattering coefficient, c-concentration of the absorbing species and A-absorbance. For Mo doped $BiVO_4$ has shown broad absorption in the range of 500-850 nm. The threshold appears at 520 nm for Ag doped $BiVO_4$ that can be attributed to the surface plasma resonance (SPR) effect of Ag (0) [10]. Cu doped $BiVO_4$ powders have shown broad absorption in the range of 500-850 nm with slight reduction in bandgap that is evident in the Tauc plot (Fig. 4.8(B)). The calculated energy band gaps are 2.54 eV and 2.52, 2.52 and 2.49 eV for pristine, 2at.% Mo, 2at.% Ag and 2at.% Cu doped $BiVO_4$ respectively. The substituted Cu in $BiVO_4$ lattice is expected to form impurity energy levels by hybridization of 3d orbitals of Cu and 2p orbital of oxygen between the VB and CB. Shallow Cu doping allow the formation of acceptor energy levels just above VBM. This is due to Cu 3d energy states hybridized with O 2p states, which reduces bandgap of $BiVO_4$. It is expected that such reduction in the band would be accompanied by an increase in the hole carrier density, lighten their effective mass, as well as increase their diffusion lengths. Similarly, for Mo-$BiVO_4$ lattice,there is a formation of impurity energy levels by hybridization of 4d orbitals of Mo and the 2p orbital of oxygen between the VB and CB. As a result, changes in the optical absorption are expected from the band edge states induced by bonding and antibonding molecular Mo-O orbitals [2]. Consequently, there is an increment in the optical absorption due to Mo doping, but the shift in the band gap is negligible, probably due to low doping rates. On the other hand, surface location of Ag onto $BiVO_4$ particles should enhance photocatalytic performance due to plasmonic enhanced photocatalytic system. Moreover, metallic clusters associated to semiconductor structures are far more efficient in electron trapping but obviously it could not alter the band gap of $BiVO_4$ as shown in the optical absorption changes.

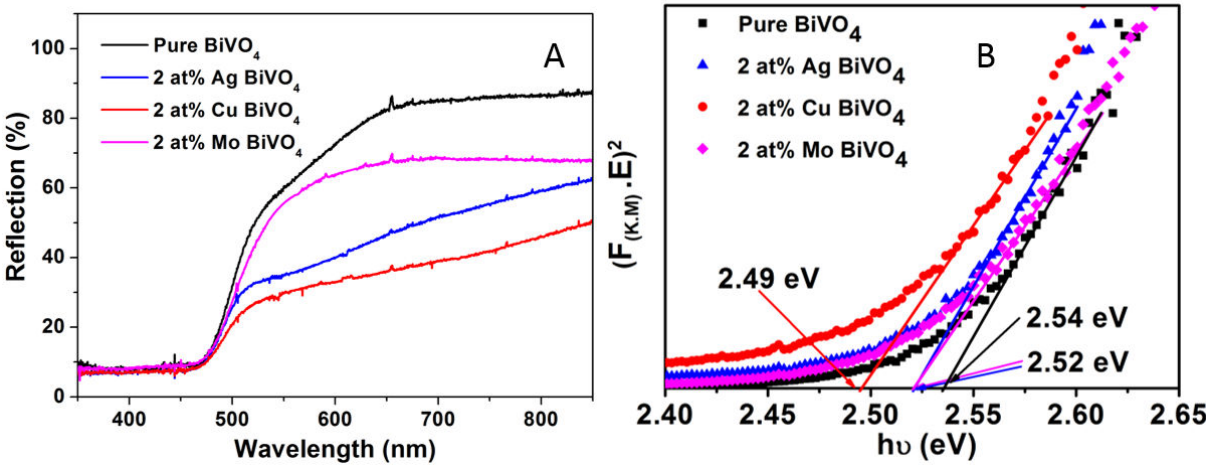

Fig.4.8. (A) Diffuse reflectance spectra for undoped and M-doped $BiVO_4$ (M - Mo, Cu and Ag), (B) Kubelka-Munk model for evaluation of their respective energy band gaps.

4.2. Photocatalytic studies

The photocatalytic activity of pristine and M-$BiVO_4$ (M-Cu Mo and Ag) samples synthesized by sol-gel route was tested for the degradation of AB 113 dye (double azo group) in aqueous solution method. Initially, solutions with powder catalysts were stirred under dark for 20 mins for absorption/ desorption equilibrium. Later in the presence of light, metal ion doped $BiVO_4$ powders exhibit the most efficient photocatalytic process illustrated by the rapid decrease in intensity of the absorption band at 566 nm, thus suggesting a rapid degradation of the azo groups. The photocatalytic activity is compared between different dopant metal ions (Fig.4.9 (A)) and indicates that the Cu doped $BiVO_4$ sample exhibits the best efficiency to degrade AB113 groups, later followed by Ag, pure and Mo doped $BiVO_4$ samples. Several reasons may be invoked to explain such difference in photocatalytic efficiency. From FESEM and EDAX, Cu has incorporated little higher percentage and possess smaller particle size as compared to other dopants. XRD, Raman and EPR reveals that Cu and Mo has substituted in the lattice of $BiVO_4$ in tetrahedral environments. The electronic configurations of ions suggest that Cu^{2+} induces higher hole density in contrast toMo^{6+} inducing higher electron density. As a consequence, Cu contributes efficiently to the formation of hydroxyl radicals (OH*) whereas Mo doped samples possess higher photo-induced charge recombination. The photocatalytic relationship between degradation efficiency and the irradiation time is illustrated in Fig.4.9 (B).

$$DE\ (\%) = \frac{[Abs]_t - [Abs]_0}{[Abs]_0} \times 100 \qquad \rightarrow (4.2)$$

Where, $[Abs]_o$ - initial absorbance of AB 113 dye in solution(10^{-5}M) and $[Abs]_t$ –absorbance of dye solution at measured with respect to irradiation time 't'.

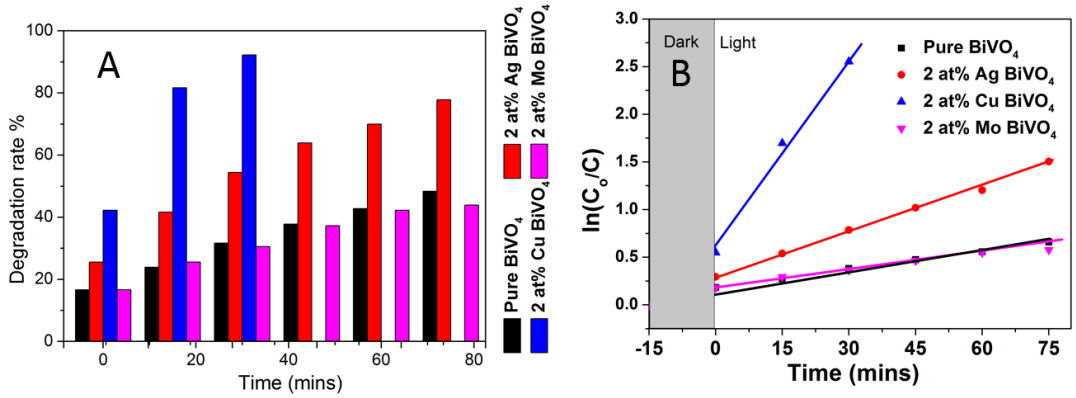

Fig.4.9. (A) Degradation rate of AB 113 dye measured by absorbance at 566 nm at room temperature with respect to 2at% metal ions doped $BiVO_4$ (Cu, Mo and Ag). (B) Shows the pseudo-first-order kinetics of degradation of AB 113 diazo in solution at absorbance peak 556 nm.

From Fig.4.9(B), the plot of ln (C_0/C) versus irradiation time shows that the photocatalytic degradation of AB113 is a pseudo-first-order reaction and varies as

$$[C]_t = [C]_0\, e^{-tk} \qquad \rightarrow (4.3)$$

Where, $[C]_0$ – initial concentration, $[C]_t$- measured concentration with irradiation time, t- irradiation time, k representes degradation rate constant or pseudo-first-order rate constant. The confirmation of the first-order rate kinetics was derived from the linearity of the plot. The rate constant for the degradation of azo groups in AB113 was estimated to 6.6×10^{-2} min^{-1} for 2at% Cu / $BiVO_4$. The degradation rate constant values are tabulated below after 30 min of irradiation time (Table 4.5).

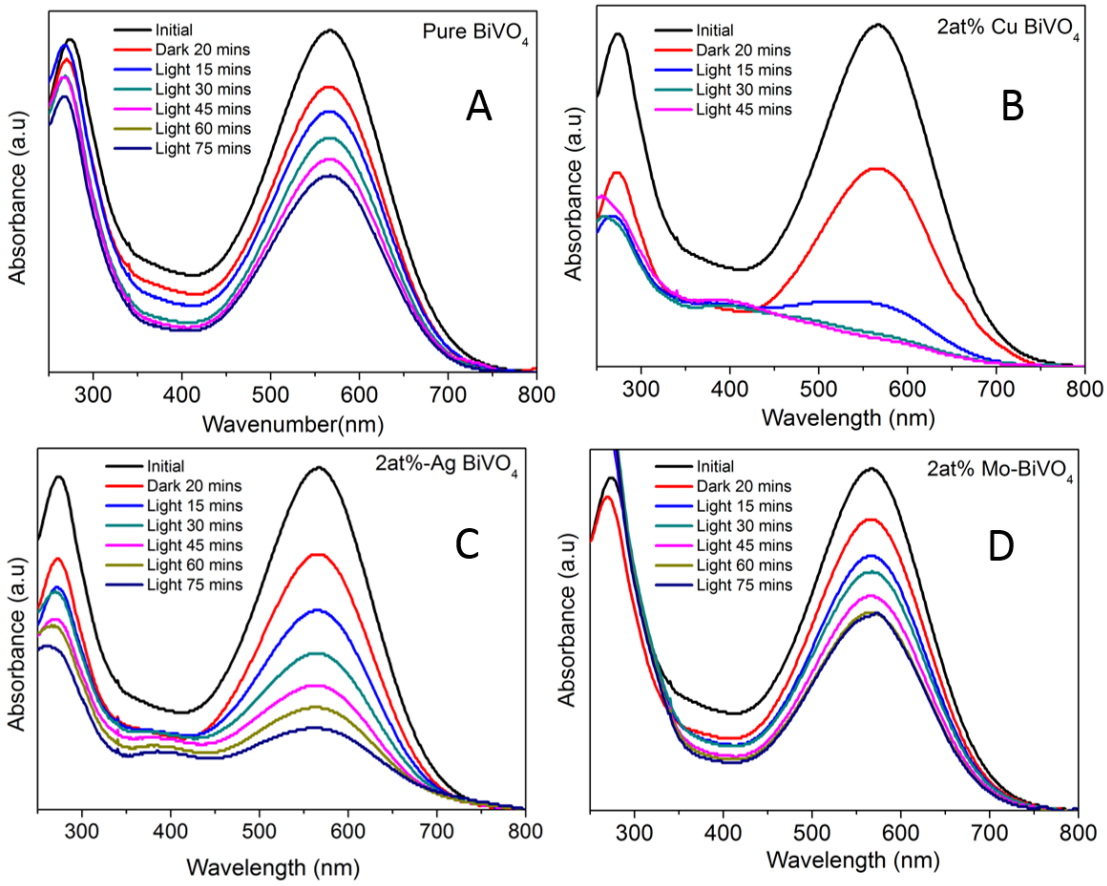

Fig.4.10. Evaluation of absorbance of AB 113 dye measured at 566 nm at room temperature with respect to undoped and 2at% metal ions doped $BiVO_4$ (Cu, Mo and Ag) powder samples.

Table 4.5. Pseudo first-order degradation rate constant of AB113 dye in the presence of M-/$BiVO_4$ powder prepared by solgel with 2at.% loading concentration.

Sample name	Degradation rate constant, k ±(error) after radiation for 30 min (%)	Remnant percent of AB113 after radiation for 30 min (%)
Pure $BiVO_4$	0.0066 ±3.29e-4	68.4
2at.%Ag-$BiVO_4$	0.0173±5.66e-4	45.6
2at.%Cu-$BiVO_4$	0.0668±5.54e-3	7.7
2at.%Mo-$BiVO_4$	0.0060±8.36e-4	69.5

4.3. Conclusions

$BiVO_4$ powder samples such as pristine and metal ions (Mo, Cu and Ag) doping were successfully synthesized by sol-gel technique. The role of doping on the structural, vibrational, morphological, electronic and optical features were investigated by XRD, micro-Raman, FESEM, HR-STEM, EPR and DRS spectroscopies. Irrespective to the doping elements, all the metal doped $BiVO_4$ samples have shown monoclinic scheelite phase exhibiting only moderate structural distortions inferred from XRD and Raman studies for Mo and Cu doped samples. EPR analysis has shown the substitutional location of Cu and Mo in the crystal sites of $BiVO_4$. Cu doping improves the photo-generated charge density, high specific surfaces of the doped powders due to lower particle sizes, higher optical absorption in a board spectral range while only a slight change is observed on the band gap values i.e. 2.45, 2.52, 2.52 eV for Cu, Mo and Ag respectively. The photocatalytic activity of doped powders were tested on the degradation of Acid blue 113 dyes in solution. In this process, Cu doped samples have shown better degradation rates compared to Ag and Mo doped powders. The different behaviour was discussed taking into account the optical absorbance, the higher photogenerated hole density and the smaller particles with higher surface area involved in Cu doped samples.

References:

[1] Y. Yang, Q. Zhang, B. Zhang, W.B. Mi, L. Chen, L. Li, et al., The influence of metal interlayers on the structural and optical properties of nano-crystalline TiO_2 films, Appl. Surf. Sci. 258 (2012) 4532–4537.

[2] K. Ding, B. Chen, Z. Fang, Y. Zhang, Z. Chen, Why the photocatalytic activity of Mo-doped $BiVO_4$ is enhanced: a comprehensive density functional study., Phys. Chem. Chem. Phys. 16 (2014) 13465–76.

[3] L. Sandhya Kumari, P. Prabhakar Rao, a. Narayana Pillai Radhakrishnan, V. James, S. Sameera, P. Koshy, Brilliant yellow color and enhanced NIR reflectance of monoclinic $BiVO_4$ through distortion in VO_4^{3-} tetrahedra, Sol. Energy Mater. Sol. Cells. 112 (2013) 134–143.

[4] J. Yu, A. Kudo, Effects of Structural Variation on the Photocatalytic Performance of Hydrothermally Synthesized $BiVO_4$, Adv. Funct. Mater. 16 (2006) 2163–2169.

[5] S.M. Thalluri, C. Martinez Suarez, M. Hussain, S. Hernandez, A. Virga, G. Saracco, et al., Evaluation of the Parameters Affecting the Visible-Light-Induced Photocatalytic Activity of Monoclinic $BiVO_4$ for Water Oxidation, Ind. Eng. Chem. Res. 52 (2013) 17414–17418.

[6] Z. Rong, R. Min-Zhi, Z. Ming-Qiu, Z. Han-Min, Studies on the Surface Interaction and Dispersity of Silver Nanoparticles in Organic Solvents, Chinese Phys. Lett. 17 (2000) 697–699.

[7] J.A. Howard, M. Tomietto, D.A. Wilkinson, Electron paramagnetic resonance study of the reaction of silver atoms with C60 in cyclohexane on a rotating cryostat, J. Am. Chem. Soc. 113 (1991) 7870–7872.

[8] A. Baldansuren, E. Roduner, EPR experiments of Ag species supported on NaA, Chem. Phys. Lett. 473 (2009) 135–137.

[9] M. Wang, Y. Che, C. Niu, M. Dang, D. Dong, Effective visible light-active boron and europium co-doped $BiVO_4$ synthesized by sol-gel method for photodegradion of methyl orange., Elsevier B.V., 2013.

[10] H. Zhang, G. Wang, D. Chen, X. Lv, J. Li, Tuning Photoelectrochemical Performances of Ag - TiO_2 Nanocomposites via Reduction / Oxidation of Ag, (2008) 6543–6549.

Chapter 5

RF sputtered deposition of Cu, Mo doped $BiVO_4$ nanostructured thin films for photocatalytic applications

Nanostructured materials have attracted considerable attention for photocatalytic applications, due to their high surface-to-volume ratios and size dependent properties [1]. Investigations of one dimensional (1D) and two dimensional (2D) photocatalysts were performed, that possesses very high specific surface. Thus, an efficient photocatalytic system needs to be developed notably for water splitting or purification and air cleaning etc. Though powder photocatalysts are easy to implement in heterogeneous catalysis system, the only difficulty is to separate the involved particles from the solution. This drawback limits the use of photocatalysts in the form of powders in such processes. Even for water splitting applications, the unavoidable mixing of O_2 and H_2 in a single volume is an important practical disadvantage. However, this problem can be avoided by using the photocatalyst in the form of thin films deposited on different types of substrates [2]. With respect to industrial technology applications, the realization of thin films is worthy of interest. So far, $BiVO_4$ thin films are prepared by various methods, such as dip coating [3] or spin coating by sol-gel processes [4], metal-organic decomposition [5, 6, 7, 8], reactive sputtering [9,10] and chemical vapour deposition [11] have different morphologies and mixed polymorphs that is strongly dependent on the preparation conditions. Among thin film preparation methods, RF magnetron sputtering is one of the most important technique due to its industrial implementation. This technique is suitable for optical coatings due to the high density, high adhesion, high hardness, and good control over thickness and uniformity of the deposited layer over a large area.

In this chapter, we report pristine, Cu and Mo doped $BiVO_4$ thin films deposited by rf sputtering technique with various surface states leading to nanostructured morphologies. Since Mo and Cu have shown lattice incorporation, whereas Ag segregated onto the surface, we are interested to perform thin films for Mo and Cu dopants. PLASSYS MP 300 rf sputtering system was used under defined conditions to able to modulate the surface features of deposited thin films. The structural, optical and morphological properties were analysed and discussed as a function of the deposition conditions. Photocatalytic reactions were studied by the

degradation of organic dyes as methyl orange charged in solutions with defined pH. The reaction rate constants were estimated as a function of the structural and surface morphology features of the film as well as the role of doping such structures.

5.1. Case Study 1(CS 1): Synthesis under argon partial pressures of metal doped $BiVO_4$ thin films

5.1.1. X-ray diffraction and Raman analysis

The deposition conditions of doped films on pre-cleaned Si substrates (2cm x 2cm) are given in Chapter 2.3. XRD investigations are recorded at room temperature for (Fig.5.1A) pristine, Cu and Mo doped $BiVO_4$ thin films deposited under CS 1 conditions. All the X-ray diffraction patterns corresponds to pure monoclinic scheelite phase of $BiVO_4$ (JPCDS 14-0688). A preferential orientation was inferred from XRD patterns and associated to (110) crystal plane (Fig.5.2.A).

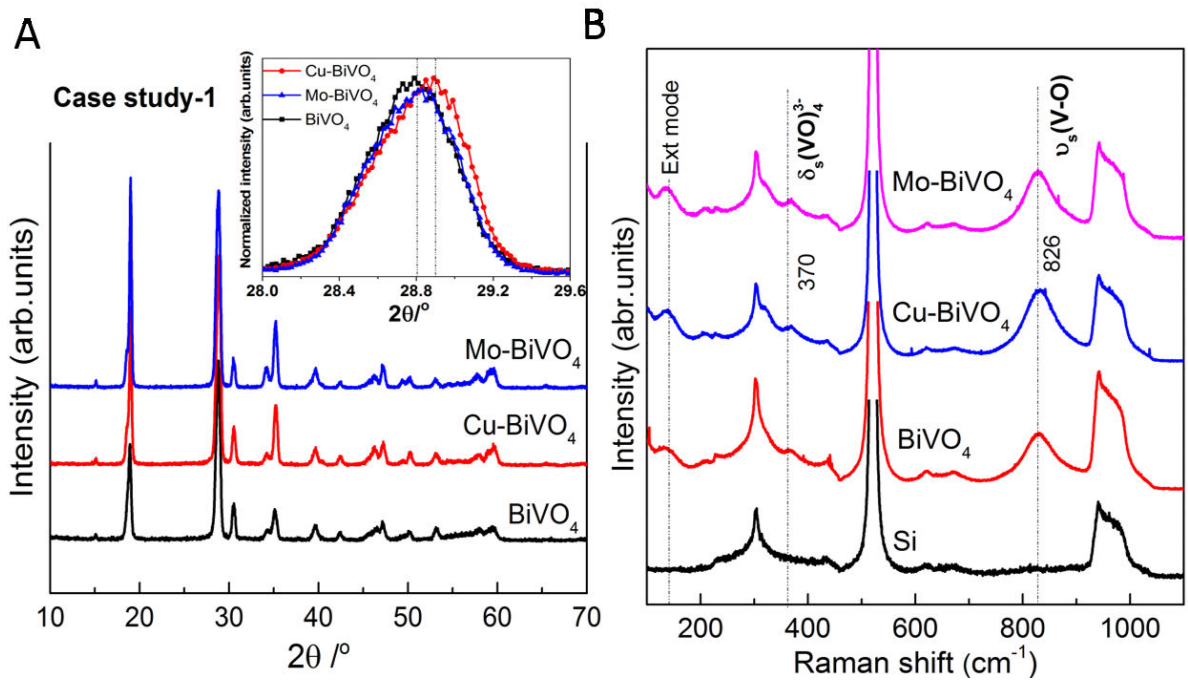

Fig. 5.1. (A) XRD pattern of the pristine, Cu and Mo doped $BiVO_4$ films on Si substrate; (B) Raman spectrum of pristine, Cu and Mo doped $BiVO_4$ films on Si substrates. Raman vibrational mode of Si substrate as shown at the bottom.

Similarly, structural properties were further analysed by using micro-Raman. The most prominent Raman mode related to monoclinic $BiVO_4$ is associated to the band centred at around 826 cm^{-1}. It corresponds to the symmetric stretching V-O mode of the VO_4 tetrahedron.

Weak Raman bands were observed around 211 and 130 cm^{-1} and assigned to external modes of the monoclinic structure [12]. The other Raman active modes expected at 326 and 367 cm^{-1} were not observed for CS 1 experimental conditions which is probably due to the low thickness of films (around 200 nm) (Fig.5.4).

5.1.2. SEM and profilometry analysis

SEM images of pristine, Cu and Mo doped $BiVO_4$ thin films from CS1 conditions are shown in Fig.5.2 with the same magnification. All the thin films are highly uniform in texture with smooth and flat surface with distinctive nano-sized grains on the surface. Low surface roughness was measured by using AFM analysis depicted in Fig.5.5. The chemical composition of these films were probed by using EDAX, which revealed the presence of Cu, Mo incorporated in the $BiVO_4$ host thin films (Table 5.1). As illustrated in Fig.5.3, EDAX chemical mapping shows homogeneous distributions of doping elements in the host material $BiVO_4$. The thickness of the deposited thin films was measured by using FE-SEM cross section analysis (Fig.5.2B). Average thickness values for pristine, Cu and Mo doped $BiVO_4$ thin films were around 180, 260 and 130 nm respectively, which is in agreement with stylus profilometer (KLA Tencor alpha-step 200) measurements (Fig.5.4). For profilometry thickness measurements, proper step was created by immersing a portion of thin film into diluted HCl solution for few seconds and later washed with ethanol and water. Stylus profilometer thickness measurements for pristine, Cu and Mo doped thin films were estimated as 150, 312 and 176 nm respectively.

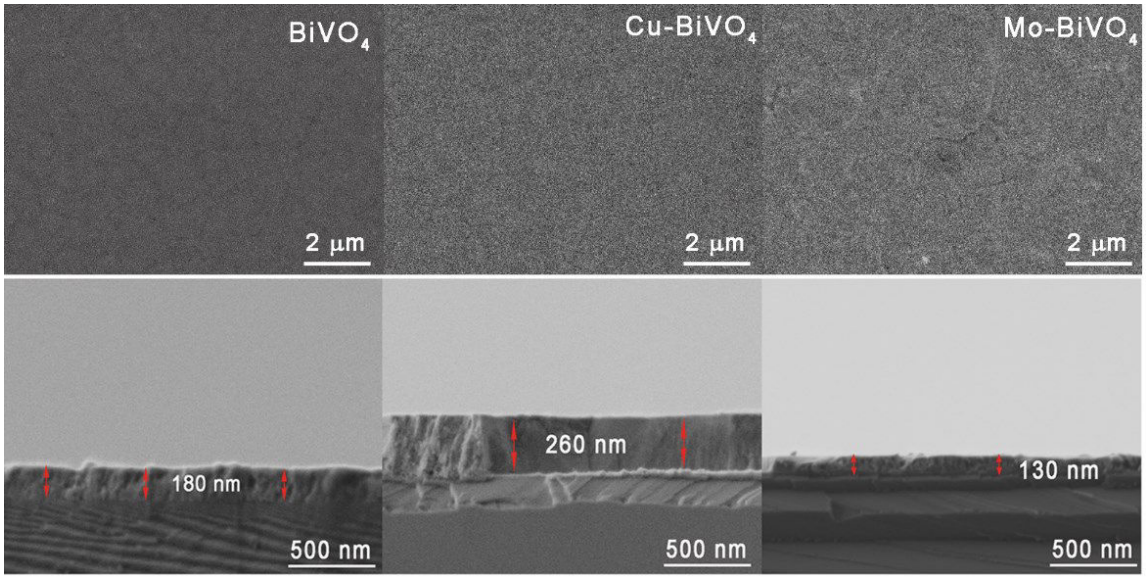

Fig. 5.2**.** SEM images of undoped, Cu and Mo doped $BiVO_4$ thin films deposited by rf sputtering with case study 1 conditions. Thin film cross section image recorded by FE-SEM for respective films.

Table 5.1. EDAX analysis with area mapping for undoped, Cu and Mo doped $BiVO_4$ thin films deposited by rf sputtering with case study 1 conditions.

Sample name	Bi (at.%)	V (at.%)	O (at.%)	Dopant (at.%)
$BiVO_4$	24.91	16.48	58.61	-
Cu-$BiVO_4$	25.68	17.09	56.30	0.92
Mo-$BiVO_4$	24.01	17.77	57.42	0.80

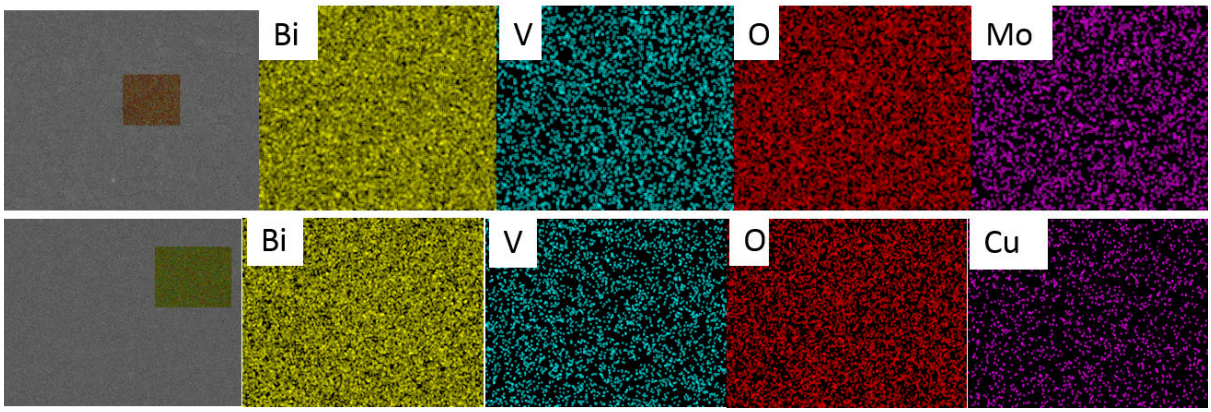

Fig. 5.3. EDAX analysis with area mapping for Cu and Mo doped $BiVO_4$ thin films deposited by rf sputtering under case study 1 conditions.

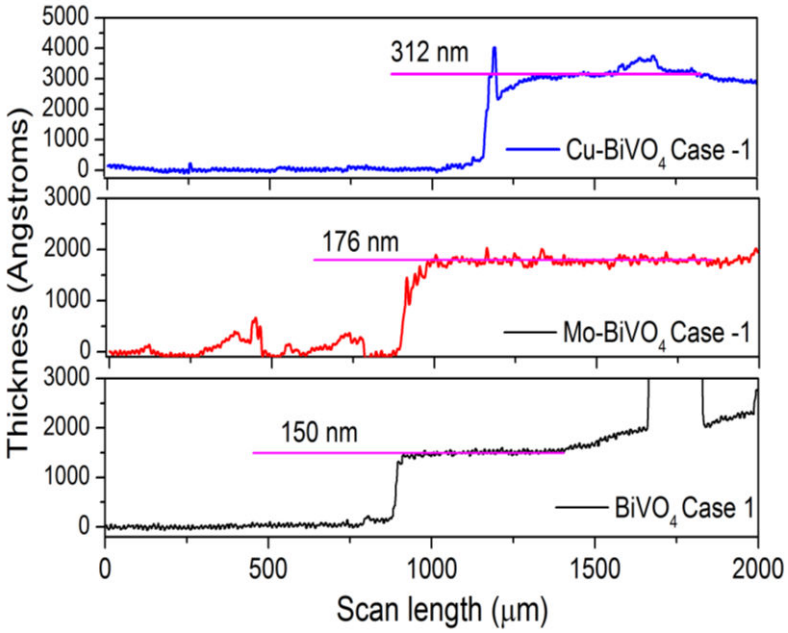

Fig. 5.4. Step profile thickness measurements by using stylus profilometer.

5.1.3 AFM topography analysis

Surface topography analysis was investigated by using Atomic Force Microscopy (AFM). AFM images exposed a high uniformity of thin films with the presence of nano-islands on the surface under CS1 deposition conditions. The surface roughness (RMS) of pristine, Cu and Mo doped $BiVO_4$ thin films were evaluated respectively at 2.85 nm, 4.93 nm and 5.08 nm as shown in Fig.5.5.

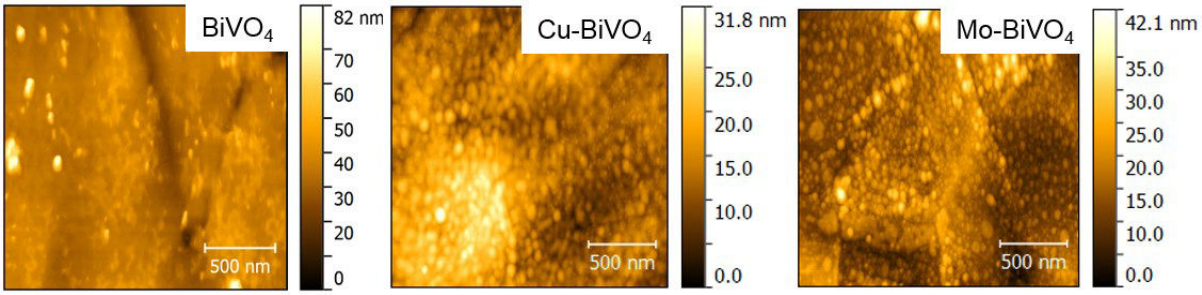

Fig.5.5. AFM topographical images (2 µm × 2 µm area) of pristine, Cu and Mo doped $BiVO_4$ thin films deposited by rf sputtering with case study 1 conditions.

5.1.4. XPS analysis

XPS technique was used to probe the chemical bonding information in the pristine, Cu and Mo doped $BiVO_4$ thin films deposited at CS1 conditions (Fig.5.6). XPS spectra are consistent with the binding energies related to Bi 4f, V 2p, O 1s for pristine films. The doping ions were also identified from characteristic peaks related to Mo 3d and Cu 2p core states for Mo and Cu doped $BiVO_4$ thin films respectively (Fig.5.6). The XPS spectra related to Bi – 4f, possess two intense peaks at E_b = 159.8 and 165.1 eV that corresponds to Bi - $4f_{7/2}$ and Bi - $4f_{5/2}$ terms respectively. The XPS spectrum of V $2p_{3/2}$ depicts a peak at E_b = 516.4 eV, which is attributed to the surface V^{5+} species. V 2p and Bi 4f have shown no change for Cu and slightly shifted to lower binding energies for Mo doped $BiVO_4$ films. XPS spectra of O1s has asymmetric peaks centred at 530.3 and 532.5 eV that is associated to lattice oxygen O^{-2} species (O_{latt}) and adsorbed oxygen or disassociated (O_{ads}) species, respectively. However, the intensity of O_{abs} peak decreases for Cu and Mo doped $BiVO_4$ samples as compared to pristine, which might confirm that the doping elements Cu, Mo are bonded in oxygen environment. The binding energies of Cu species, at E_b = 933 eV were assigned to the spectroscopic terms Cu-$2p_{3/2}$ (Fig.5.6). The XPS spectra of Mo-3d core-levels have two components suggesting that Mo is present in one oxidation state (Mo^{6+}). The binding energies at 233.2 and 236.4 eV correspond to the Mo $3d_{5/2}$ and Mo $3d_{3/2}$ components.

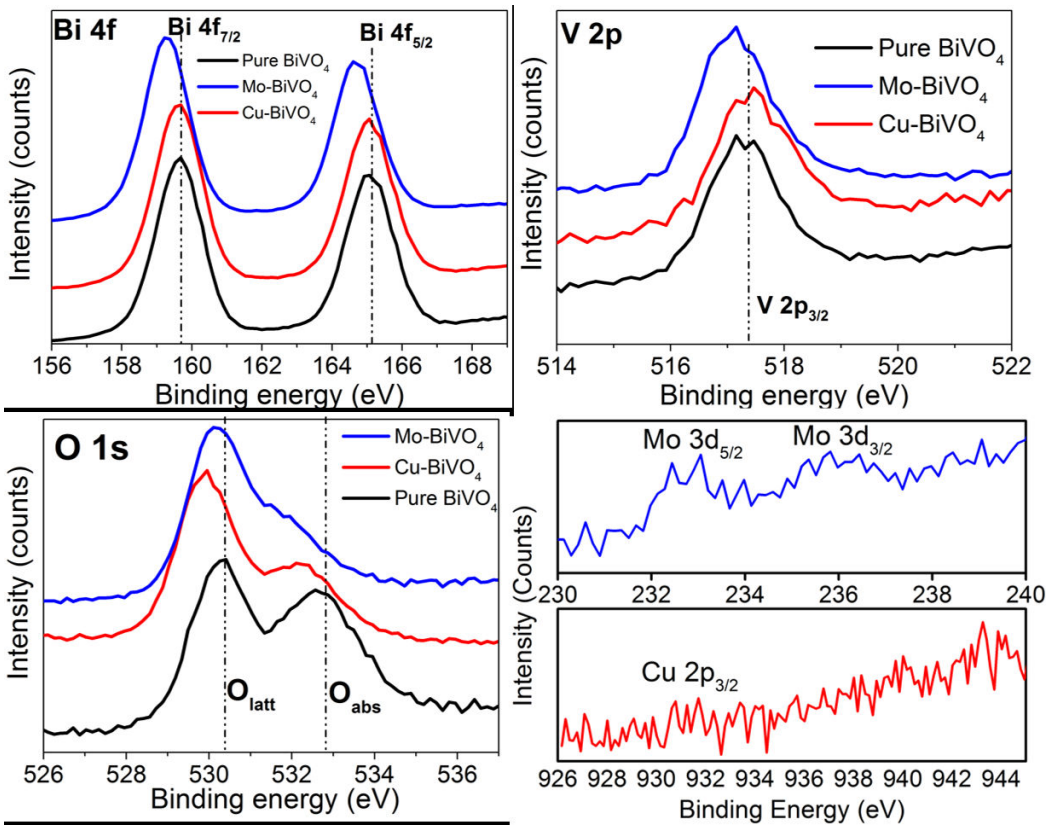

Fig.5.6. XPS spectra of Bi 4f, V 2p, O 1s in pure $BiVO_4$ and the doping elements Cu-2p and Mo-3d for Cu and Mo doped $BiVO_4$ thin films.

5.1.5. Optical analysis

The electronic structure of semiconductors can be revealed by the interaction of light under defined wavelengths. By studying the crystalline structure, morphology and doping by suitable elements, the electronic and optical features can be fine-tuned to harvest defined spectral range of light [13]. The UV-Vis absorption spectra for the pristine Cu, and Mo doped $BiVO_4$ thin films deposited on boro-float glass substrate with CS1 conditions and annealed at 400 °C for 2 hours, is shown in Fig.5.7. In order to evaluate the optical band gap, the optical absorption near the band edge can be described by equation (5.1)

$$\alpha h\upsilon = A(h\nu - E_g)^m \qquad \rightarrow(5.1)$$

Where α represents the absorption coefficient, $h\upsilon$ is the photon energy, A is a constant, E_g is the optical band gap of the semiconductor, and m depends on the type of transition: m = 1/2 for a direct band gap parameter, and m = 2 for an indirect band gap. The bandgap energy was

calculated from the Tauc's plots (inset of Fig.5.7) for pristine, Cu and Mo doped $BiVO_4$ samples which are estimated around 2.52, 2.6 and 2.55 eV respectively. No substantial change is noticed in the band gap probably due to the low doping rate. However, doping may contribute extensively to increase the charge carriers under light irradiation as it will be discussed based on the photocatalytic experiments reported below.

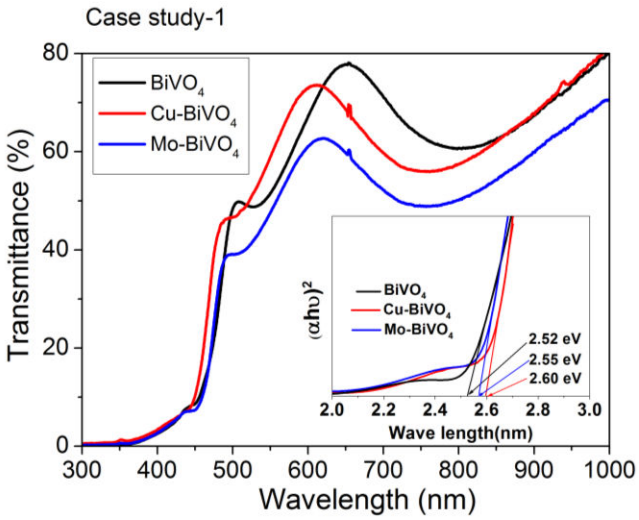

Fig.5.7. UV-Vis absorption spectra of pristine, Cu, Mo doped $BiVO_4$ films on boro-float glass substrate at CS 1 deposition condition, with the inset showing the energy band gap values extrapolation for these films.

5.1.6. Photocatalytic studies

Photocatalytic tests for pristine, Cu and Mo doped $BiVO_4$ thin films were carried out for the degradation of MO dyes in aqueous solution with a typical concentration of about $4x10^{-5}$ M. The UV–Visible absorption spectra for MO charged solution at pH 3 shows a major absorption peak at 485 nm. The photocatalytic activity is compared between the different doped films and is evaluated by the degradation rate constant 'k' related to the degradation of MO groups under visible light irradiation. Thus, Mo doped $BiVO_4$ has shown better degradation rate kinetics, which may due to higher electron density (replacement of V^{5+} sites with versatile valences $Mo^{6,5,4,3+}$) as well as low thickness of the films inducing rapid and easy carrier transportation to the electrolyte. Indeed, the film thickness is expected to play crucial role in the photocatalysis process because the light intensity usually attenuates as it penetrates into the solid photocatalyst film [14]. When the film thickness is larger than the light penetration depth, the overall photocatalyst will not be irradiated, thus inhibiting the photogenerated charge carriers [15]. It was reported that electron-hole pairs in $BiVO_4$ are mostly generated within the

penetration length of light (α^{-1}) which is about ~100 nm for pristine $BiVO_4$ [16]. The photo induced electrons need to travel across the entire thickness of the film to the $BiVO_4$/silicon interface while the resultant holes needs to travel through $BiVO_4$ to MO dye electrolyte solution for degradation process as shown in schematic representation (Fig.5.8). Since Mo doped thin films have low thickness, they promote photo-induced charge carriers faster to electrolyte as compared to Cu and pristine. Similarly, Cu dopant would increase the hole density which directly enhances the degradation efficiency as compared to pristine $BiVO_4$.

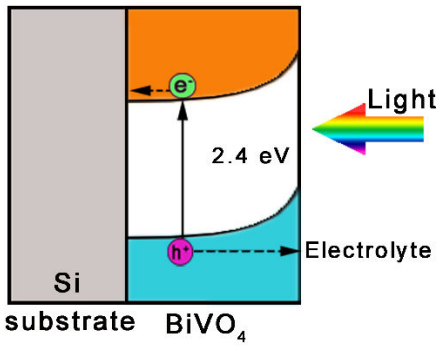

Fig.5.8. Schematic representation of photo-induced carrier flow in undoped and doped $BiVO_4$ thin films grown on Si substrate.

The evolution of MO dye degradation process follows pseudo first order rate kinetics model. The effective first order rate constants have been determined and tabulated below.

Table 5.2. Photodegradation rate constant (k) of MO dyes by pure and Mo, Cu doped $BiVO_4$ thin films with the corresponding kinetic degradation reaction rates.

150 W Oriel Xenon lamp with 11.5 W/cm^2		Degradation rate constant, k (min^{-1}) ± error for Methyl Orange (4x10^{-5} M) at pH-3
Case 1 (Ar-72 sccm-RT Anneal 400^{o}C)	Pure $BiVO_4$	0.022±0.002
	Cu-$BiVO_4$	0.028±0.002
	Mo-$BiVO_4$	0.031±0.002

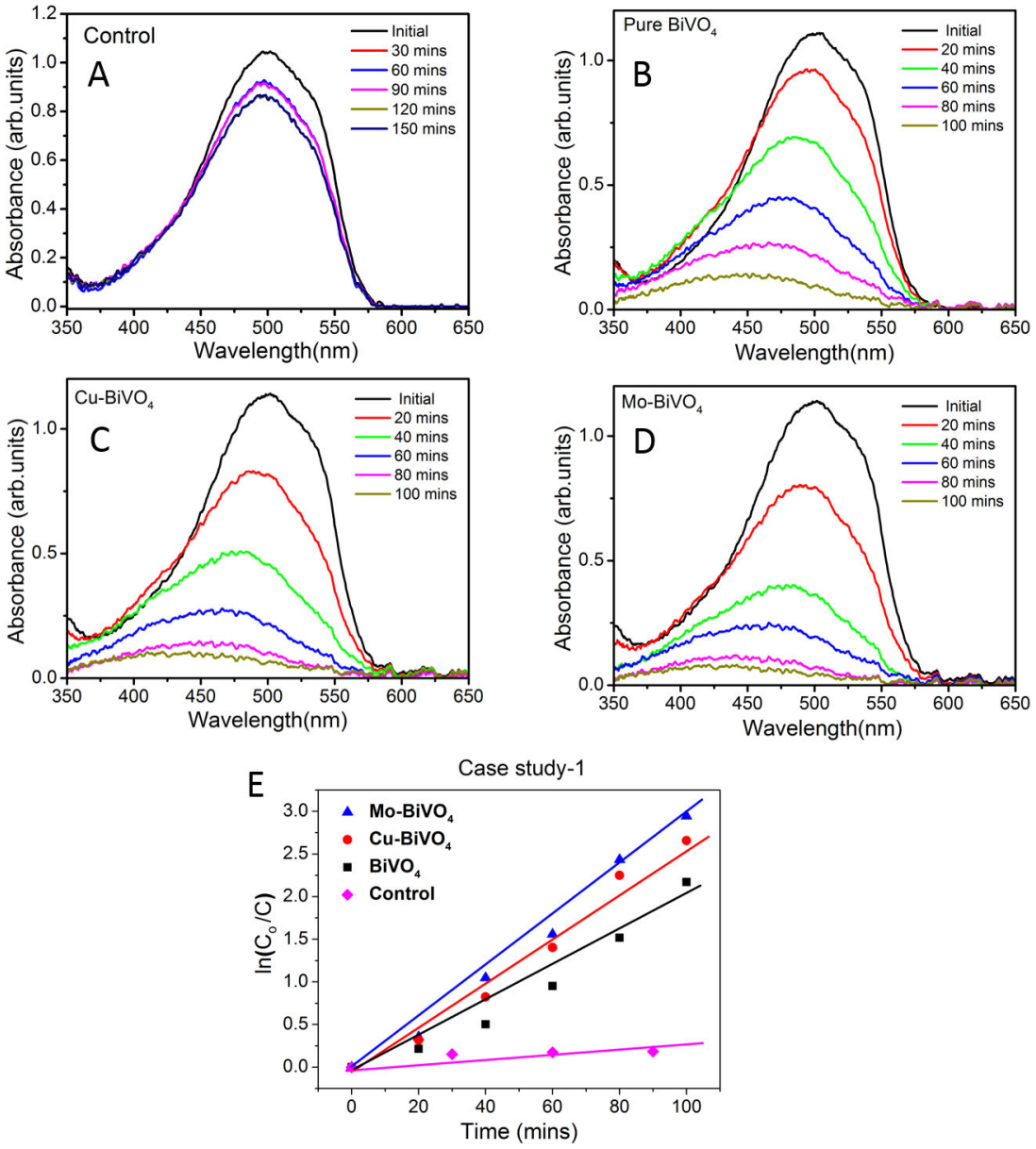

Fig.5.9. Evaluation of degradation of MO dye solution without sample (control), undoped, Cu and Mo doped $BiVO_4$ thin films (A, B, C and D) deposited with the case study 1 parameters. (E). Shows the pseudo-first-order kinetics of degradation of Mo dyes in solution.

5.1.7. Summarizing features of CS 1 deposited thin films

Pristine, Cu and Mo doped $BiVO_4$ thin films were synthesized by rf-sputtering method under Ar partial pressures (CS1 parameters). Monoclinic polymorph phase with (110) preferential plane orientation growth on Si substrate was observed. Low surface roughness with homogenous and flat morphologies of nanosized grains on the surface was exposed from AFM and SEM analysis. Due to a high adhesion of the film on Si substrate, photocatalyst degradation

of MO dye were compared through their degradation reaction constants. Thus, Mo doped $BiVO_4$ has shown highest degradation rates as compared to Cu doped and pristine samples. Small thickness (~150 nm) of thin films favoured a better light penetration depth and higher electron density from possible multi-valance states of $Mo^{6,5,4,3+}$ substituted in crystalline sites of V^{5+}. Similarly, Cu doping induces higher hole density which contributes directly to enhance the photocatalytic efficiency as compared to pristine $BiVO_4$.

5.2. Case Study 2 (CS 2): Deposition of doped $BiVO_4$ thin films under argon and oxygen partial pressures

5.2.1. X-ray diffraction and Raman analysis

XRD patterns (Fig.5.10A) were recorded for pristine, Cu and Mo doped $BiVO_4$ thin films deposited under CS 2 parameters. Monoclinic scheelite phase of $BiVO_4$ (JPCDS 14-0688) was confirmed for all the samples.

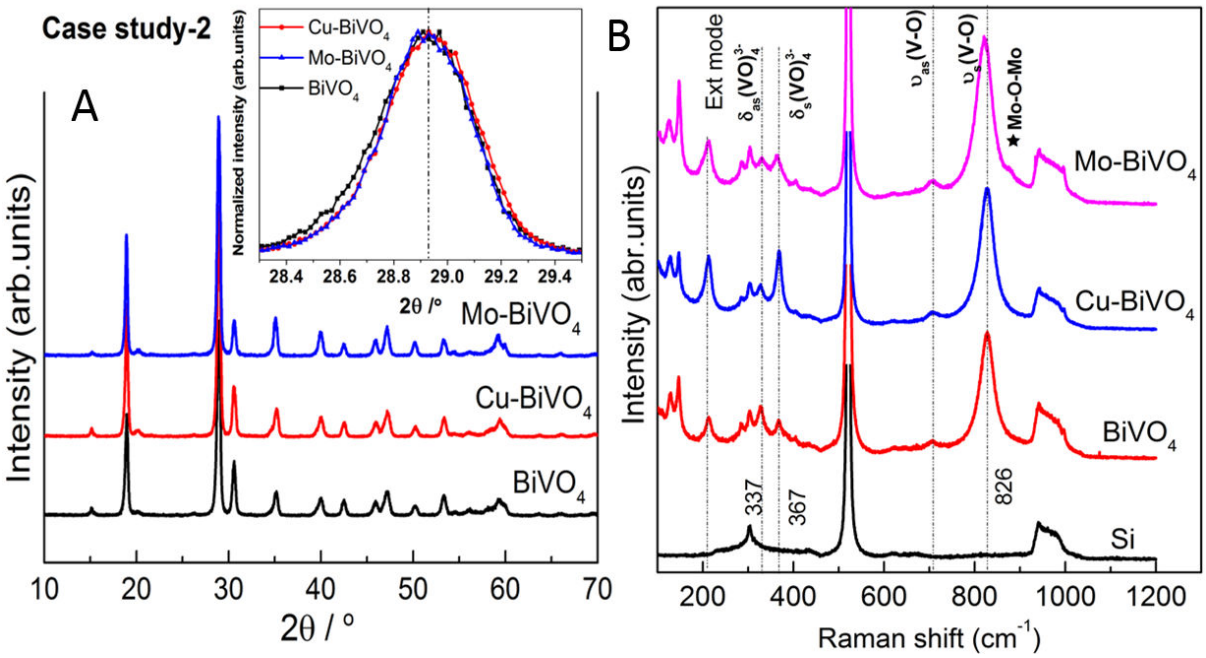

Fig.5.10. (A) XRD patterns of the Cu, Mo doped and pristine $BiVO_4$ films deposited on Si substrate at ambient temperature under partial pressures of Ar and O_2; (B) Raman spectra of $BiVO_4$ Cu, Mo doped and pristine $BiVO_4$ films on Si substrates. Raman vibrational mode of Si substrate are reported on the spectrum at the bottom of B graph.

Similarly, structural properties were further investigated by using micro-Raman analysis with the major active mode of monoclinic $BiVO_4$ centred at around 826 cm^{-1}. This Raman band corresponds to symmetric stretching V-O modes of the VO_4 tetrahedra. Low intense vibrational

bands were also observed around 211 and 130 cm^{-1} corresponding to crystal lattice vibrations (external modes) [12]. The doublet peaks located at 326 and 367 cm^{-1} are attributed to bending modes of VO_4 tetrahedra. Compared to the CS1 conditions, the obtained films under CS2 have shown the presence of weak fraction of vanadium oxide (V_2O_5) giving rise to weak characteristic bands. Such vibrational bands are located at 300 cm^{-1} assigned to V–O stretching modes while 404 and 995 cm^{-1} bands are inferred from V-O-O bending modes of V_2O_5 structure. From the doping element as Mo substituted to vanadium, an additional vibrational shoulder around 871 cm^{-1} can be attributed to Mo-O-Mo bonds within MoO_4 groups.

5.2.2. SEM and profilometry analysis

SEM micrographs with the same magnification are shown in Fig.5.11A and reveal the morphology of pristine, Cu and Mo doped $BiVO_4$ thin films deposited under CS2 conditions. The obtained films showed smooth and distinctive nanosized grains on the surface with more uniform grains compared to CS1 conditions. AFM analysis exposed a higher growth rate of the film under O_2 partial pressures with low surface roughness as illustrated in Fig.5.14. Thin film thickness were measured by FESEM cross-section analysis as well as stylus profilometer. The average estimated thickness were around 350, 520 and 340 nm from FESEM analysis whereas 323, 684 and 231nm with profilometer for pristine , Cu and Mo doped $BiVO_4$ thin films respectively (Fig.5.13). These films were grown on Si substrate with continuous nanosized pores in the order of 20-30 nm (Fig.5.11C(i) and (ii)). The formation of pores in the deposited thin films were explained by a mechanism analogous to the Kirkendall effect [17]. The pore formation during the growth of metal oxide films can be explained by the fast outward diffusion of cations through the oxide layer accompanied by an inward flow of vacancies to the metal–oxide interfaces [18]. In the present work under CS2 deposition conditions, the pore formation is clearly seen in Cu and Mo doped $BiVO_4$ thin films compared to pristine.

Chemical composition of these film were analysed by using EDAX, which revealed the presence of Cu, Mo incorporated in the $BiVO_4$ host thin films (Table 5.3). EDAX chemical elemental mapping from Fig.5.12 depicts the homogeneous distribution of doping elements in the host material $BiVO_4$.

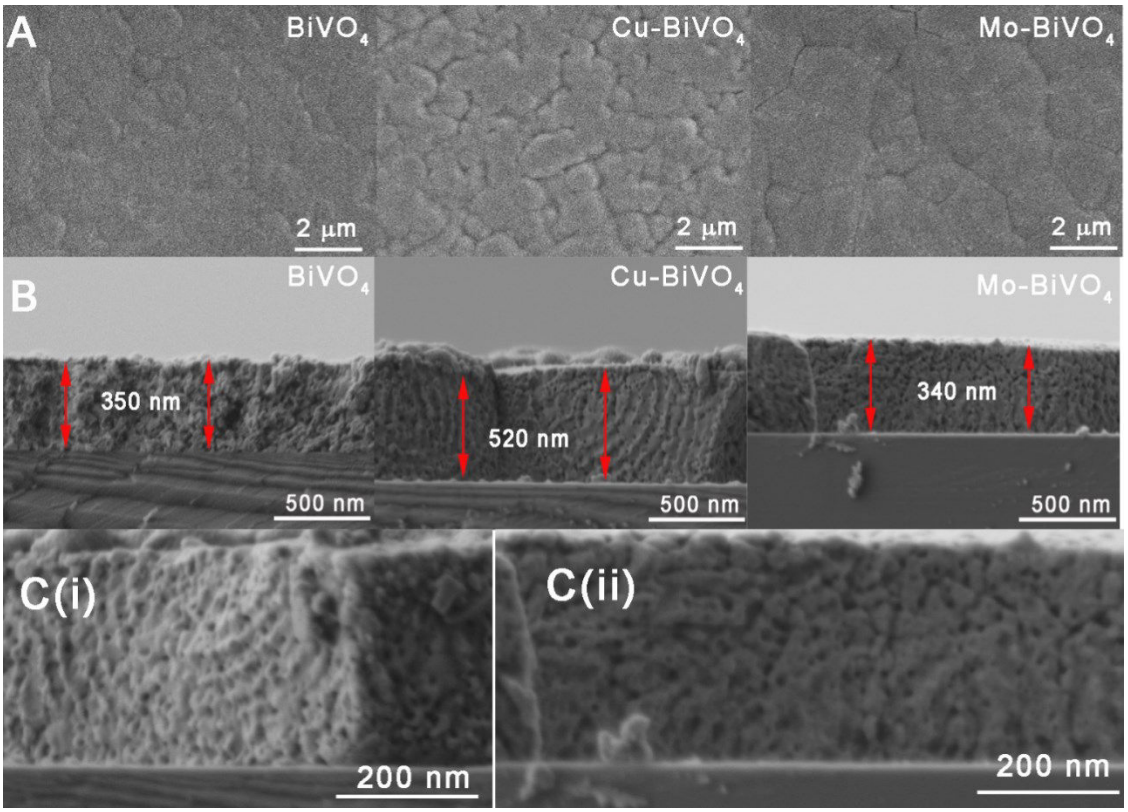

Fig.5.11. SEM images of pristine, Cu and Mo doped $BiVO_4$ thin films deposited by rf sputtering with case study 2 (CS2) conditions. Thin film cross section image recorded by FE-SEM for respective films. A and B shows nanosized porous across the film growth.

Table 5.3. EDAX analysis with area mapping for pristine, Cu and Mo doped $BiVO_4$ thin films deposited by rf sputtering with CS2 conditions.

Samples	Bi (at.%)	V (at.%)	O (at.%)	Dopant (at.%)
$BiVO_4$	20.48	23.79	55.73	-
Cu-$BiVO_4$	20.11	26.20	52.50	1.19
Mo-$BiVO_4$	18.97	24.60	55.63	0.81

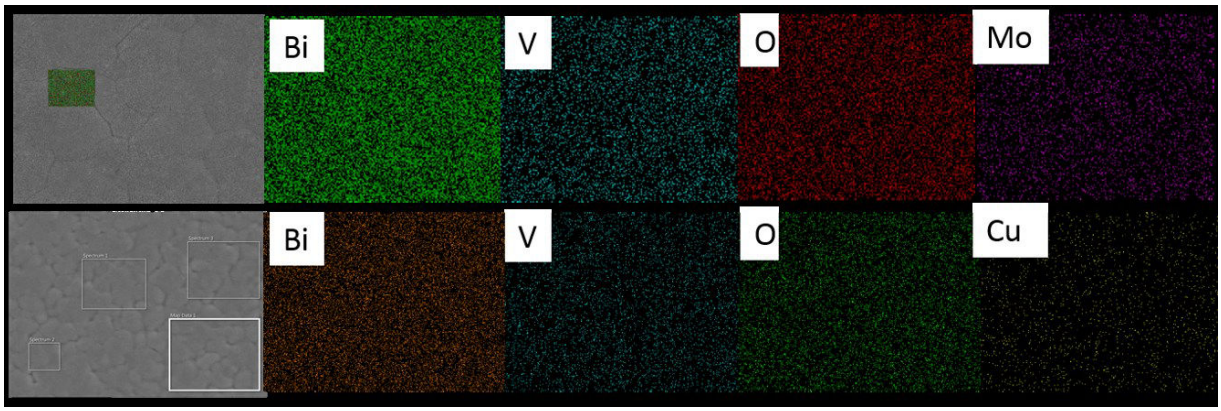

Fig.5.12. EDAX analysis with area mapping for Cu and Mo doped $BiVO_4$ thin films deposited by rf sputtering under CS2 conditions.

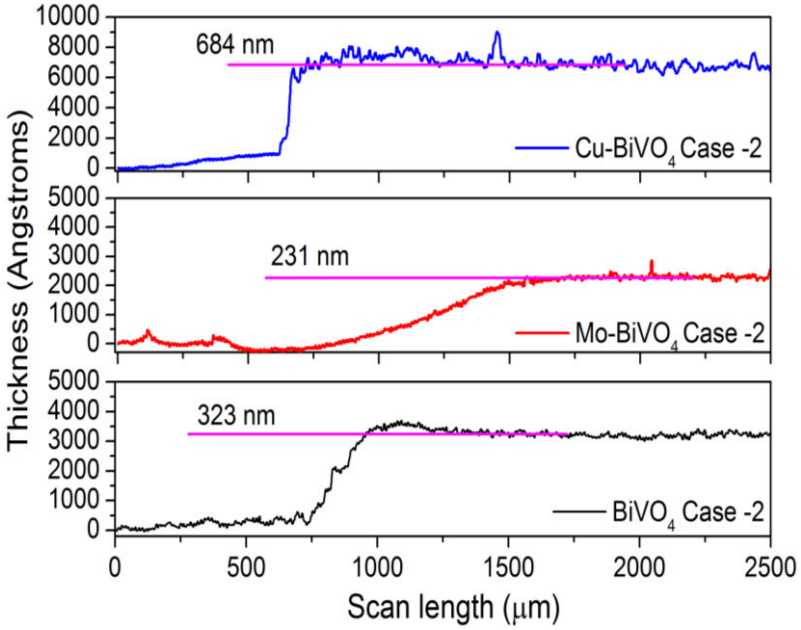

Fig. 5.13. Step profile thickness measurements by using stylus profilometer.

5.2.3. AFM topographical analysis

Topographical analysis was studied by using AFM technique for undoped, Cu and Mo doped $BiVO_4$ thin films for case 2 deposition conditions. All thin films presented low surface roughness with homogeneous nanosized grains on the surface. The surface roughness (RMS) values are 7.68, 9.18 and 9.63 nm for pristine, Cu and Mo $BiVO_4$ thin films respectively (Fig.5.14).

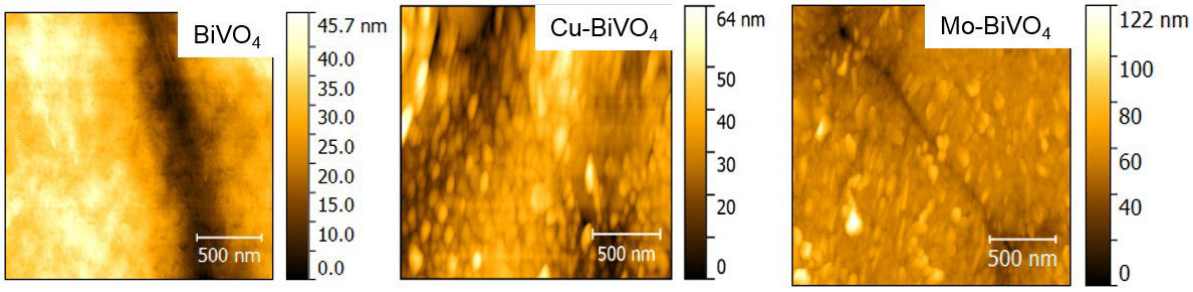

Fig.5.14. AFM topographical images (2 µm × 2 µm) of pristine, Cu and Mo doped $BiVO_4$ thin films deposited by rf sputtering with CS2 conditions.

5.2.4. XPS analysis

X-ray photoelectron spectra for the pristine, Cu and Mo doped $BiVO_4$ thin films deposited under CS2 parameters are reported in Fig.5.15. XPS spectra reveal the binding energy levels of Bi 4f, V 2p, O 1s along with the doping elements Mo 3d and Cu 2p (Fig.5.15). Cu 2p core levels were not found for Cu doped $BiVO_4$ suggesting that Cu doping was not homogenous all over the films. The XPS spectra related to Bi – 4f doublets were found in their trivalent oxidation state. Similarly, XPS spectra of V $2p_{3/2}$ with the peak at E_b = 516.4 eV is attributed to the surface V^{5+} species. V 2p and Bi 4f didn't show any change for Cu but slightly lower shift in binding energies for Mo doped $BiVO_4$ films. XPS spectra of O1s with lattice oxygen O^{-2} species (O_{latt}) and adsorbed oxygen or disassociated (O_{ads}) species were revealed with relatively quite low O_{abs}/O_{latt} molar ratios for Cu. For Mo doping, the associated XPS bands confirm the bonding with oxygen elements. Compared to CS1 case, the XPS spectra of Mo 3d doublet agreed with the involved oxidation state (Mo^{6+}), as identified by the binding energies at 233.2 and 236.4 eV for the Mo $3d_{5/2}$ and Mo $3d_{3/2}$ components. We have further justified the presence of Mo-O-Mo vibrational bond at 871 cm^{-1} from the micro-Raman analysis (Fig.5.10B).

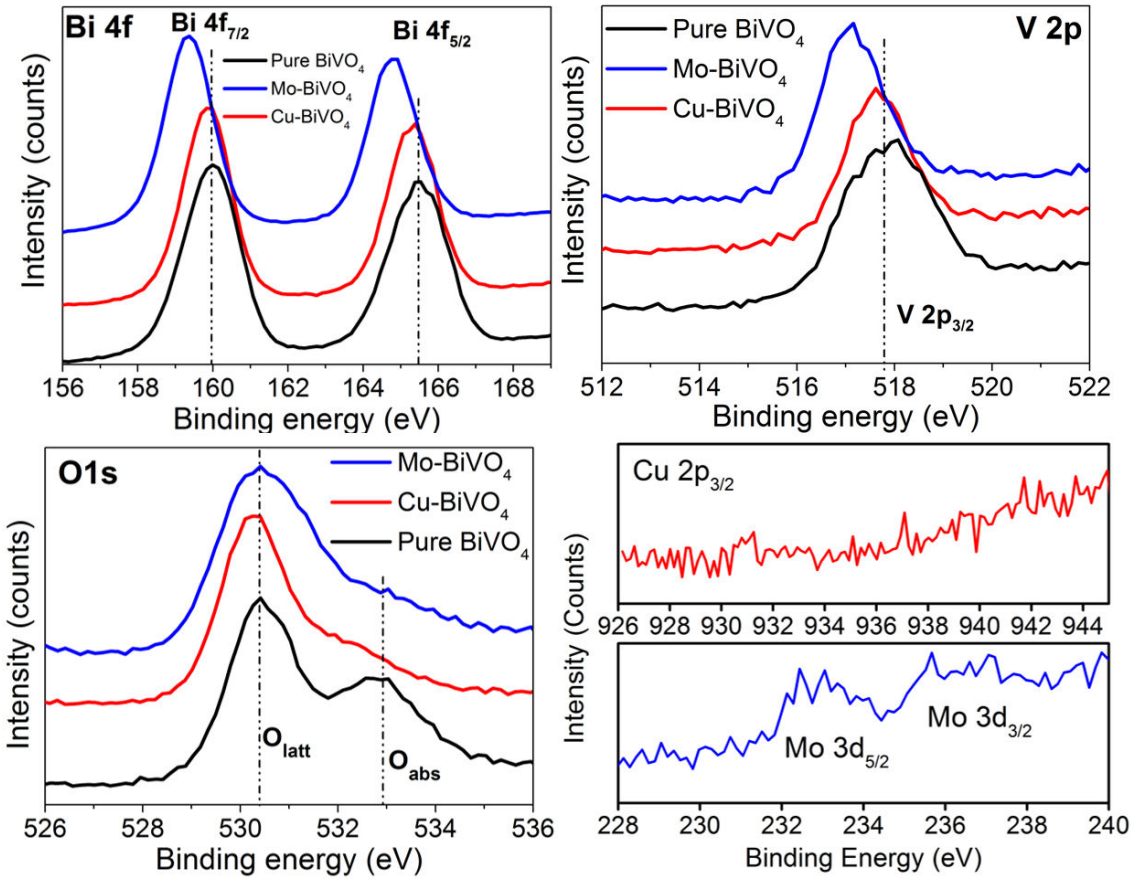

Fig. 5.15. XPS spectra of Bi 4f, V 2p, O 1s for pristine $BiVO_4$ and along with that doping elements with electronic configurations Cu 2p, Mo 3d chemical states for Cu and Mo doped $BiVO_4$ thin films.

5.2.5. Optical studies

The optical absorption of a photocatalyst is a key parameter which determines its efficiency in harvesting light for photocatalytic reactions [13] The UV-Vis absorption spectra of the pristine and doped $BiVO_4$ thin films deposited on boro-float glass substrate is shown in Fig.5.16. These films obtained from CS2 deposition conditions were annealed at 400°C for 2 hours in order to improve their crystalline features. The energy band gaps were calculated from Tauc's plots (inset Fig.5.16) and estimated as 2.52, 2.6 and 2.56 eV for pristine, Cu and Mo doped $BiVO_4$ films respectively. The shift in optical absorption for metal doped $BiVO_4$ thin films might be due to the creation of inter-band states of doping elements.

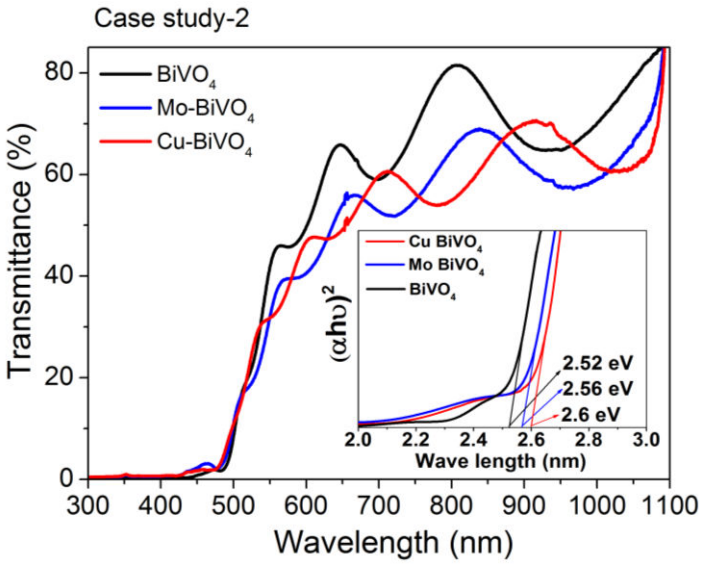

Fig. 5.16. UV-vis absorption spectra of pristine, Cu, and Mo doped $BiVO_4$ films on boro-float glass substrates with CS2 deposition condition. The inset shows the band gap associated to the different investigated films.

5.3.6. Photocatalytic studies

The photocatalytic activity of pristine, Cu and Mo doped thin films deposited under CS 2 conditions are compared (Fig.5.17), whereas these films have shown low efficiency in the degradation of organic dyes as compared to CS1.Among doped $BiVO_4$ thin films, Mo has shown better degradation rate compared to Cu doping. Such behavior is probably connected to higher electron density and mobility favored by the versatile valence states of Mo ions. The role of the porous structure of the doped films on the photocatalytic efficiency can be also qualitatively addressed. Indeed, it is proved that photocatalysis depends highly on the interface states. The photogenerated electrons and holes in the present samples can either recombine in the bulk structure or migrate to the surface to initiate various redox reactions. So the charge carrier transport through the nano-porous thin films is relatively dispersive which is similar to amorphous films. It shows that transport through the grains is fairly efficient, whereas limitation of charge transportation occurs due to charge traps in porous as well as near grain boundaries [19,20]. This leads to poor carrier transportation in these films deposited under oxygen partial pressures. If pores are filled with electrolyte, recombination and charge trapping can be reduced, which seems to be realized in the above case.

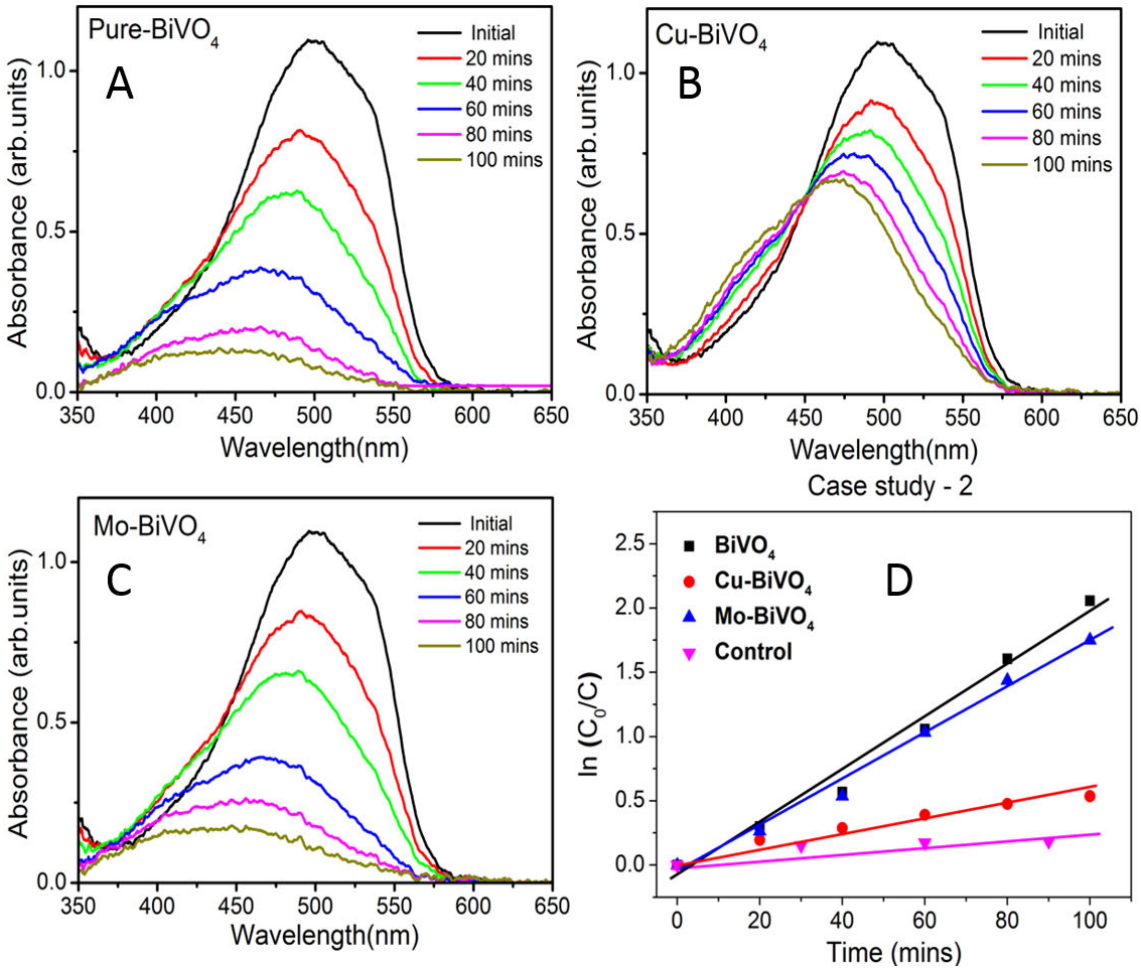

Fig. 5.17. (A, B and C) Evaluation of degradation of MO dyes for pristine, Cu and Mo doped $BiVO_4$ thin films deposited under CS2 parameters. D. shows the pseudo-first-order kinetics of degradation of Mo dyes in solution.

The degradation reaction kinetics follows a pseudo first order behaviour with the degradation rate constant evaluated from the slopes of ln (C_o/C) with respect to time as tabulated below.

Table 5.4. Photodegradation rate (%) of MO dyes by pure and Mo, Cu doped $BiVO_4$ thin films with the corresponding kinetic degradation reaction rates.

150 W Oriel Xenon lamp with 11.5 W/cm^2		Degradation rate constant, k (min^{-1}) ± error for Methyl Orange (4x10^{-5} M) at pH-3
Case 2 (Ar-O_2-60-12 sccm-RT Anneal 400^{o}C)	Pure $BiVO_4$	0.021±0.001
	Cu-$BiVO_4$	0.005±5e-4
	Mo-$BiVO_4$	0.019±9e-4

5.3.7 Summarizing the features of CS2 deposited thin films

Pristine, Cu and Mo doped $BiVO_4$ thin films were deposited at ambient temperatures under partial pressures of Ar and O_2 with 60:12 sccm ratio (CS2). Monoclinic polymorph phase was obtained for all the deposited films. Low surface roughness with homogenous and smooth surface morphologies were revealed by FE-SEM and AFM techniques. FESEM probed the nanosized porous morphology involved on the surface as well as in the cross section of the thin film. Under oxygen partial pressures, the excess of oxygen contributes to oxidize all the metal cations and favors porous formation after annealing at 400 ^oC. Nano-sized pores in the bulk or at the surface are expected limit the photo-generated carriers transportation due to the occurrence of charge traps at porous and near grain boundaries. This situation is more pronounced for Cu doped thin films as compared to Mo doped ones due to the higher film thickness (~600 nm) for Cu case. For the photocatalysis efficiency, Mo-$BiVO_4$ films have shown higher degradation constant rates which is due to versatile valance states of Mo ions may contribute higher electron density and lower film thickness preventing photogenerated electron-hole recombination. Micro Raman analysis has confirmed the formation of secondary phase of V_2O_5. Such compositions associated with the nano-sized porosity of the films are plausibly behind the low efficiency of photocatalysis of CS2 deposited films as compared to the films deposited under CS1 conditions.

5.3. Case Study 3 (CS 3): Deposition of doped $BiVO_4$ thin films under argon and oxygen environment at 450°C for the substrate temperature

5.3.1. X-ray diffraction and Raman analysis

XRD patterns for pristine, Cu and Mo doped $BiVO_4$ thin films deposited with CS 3 conditions (Table 2.1, Chapter-2) are shown in Fig.5.18A and accounted by monoclinic scheelite phase of $BiVO_4$ (JPCDS - 14-0688). Moreover, structural properties were further analysed by using micro-Raman in order to evaluate the doping effects on the vibration frequency of Raman active modes. The most prominent Raman band involved for monoclinic $BiVO_4$ is centred around 826 cm^{-1} and assigned to the antisymmetric stretching V-O modes of the VO_4 tetrahedron. In parallel, the doublet peaks observed at 326 and 367 cm^{-1} depicts the bending modes of V-O present in VO_4 tetrahedron. The Raman active modes at 211 and 130 cm^{-1} are related to external modes generally involved at low frequencies and related to vibrations of bismuth and VO_4 tetrahedron groups [12]. In the case of Mo doping, the involved

shoulder on the Raman band at 871 cm^{-1} could be attributed to Mo-O-Mo bonds which might be occurred due to Mo replace the crystal sites of vanadium.

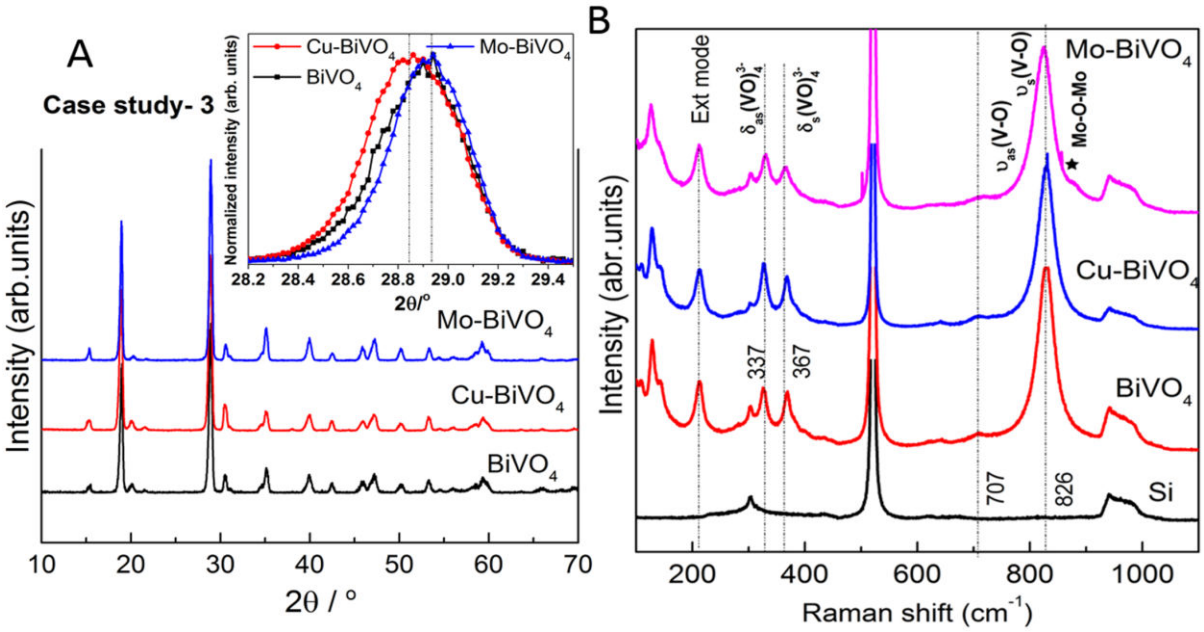

Fig. 5.18. (A) XRD patterns (B) Raman spectra of the Cu, Mo doped and pristine $BiVO_4$ thin films deposited on Si substrate at 450°C under partial pressures of Ar and O_2 Raman vibrational modes of Si substrate are shown at the bottom of B graph.

5.3.2. SEM and profilometry investigations

SEM images of pristine and doped $BiVO_4$ thin films synthesized under the CS3 condition (Fig.5.19) exhibits nanofibres on their outermost surfaces. The excess of oxygen partial pressures as well as high temperatures would create lower energy for the unidirectional growth of nano fibres. Measurements of the film thickness were realized by using SEM cross-section as illustrated in Fig.5.19 and the average thickness estimated for pure, Cu and Mo doped $BiVO_4$ thin films are 410, 550 and 490 nm respectively. Similarly, the thickness of these films were evaluated by using profilometry where the values in the order of 356, 507. 720 nm respectively(Fig.5.21).

EDAX chemical composition of these respective films are tabulated in Table 5.5 where Cu and Mo are indeed incorporated in the $BiVO_4$ matrices. EDAX chemical elemental mapping of Fig.5.20 reveals the homogeneous distribution of doping elements inside the host structure of $BiVO_4$.

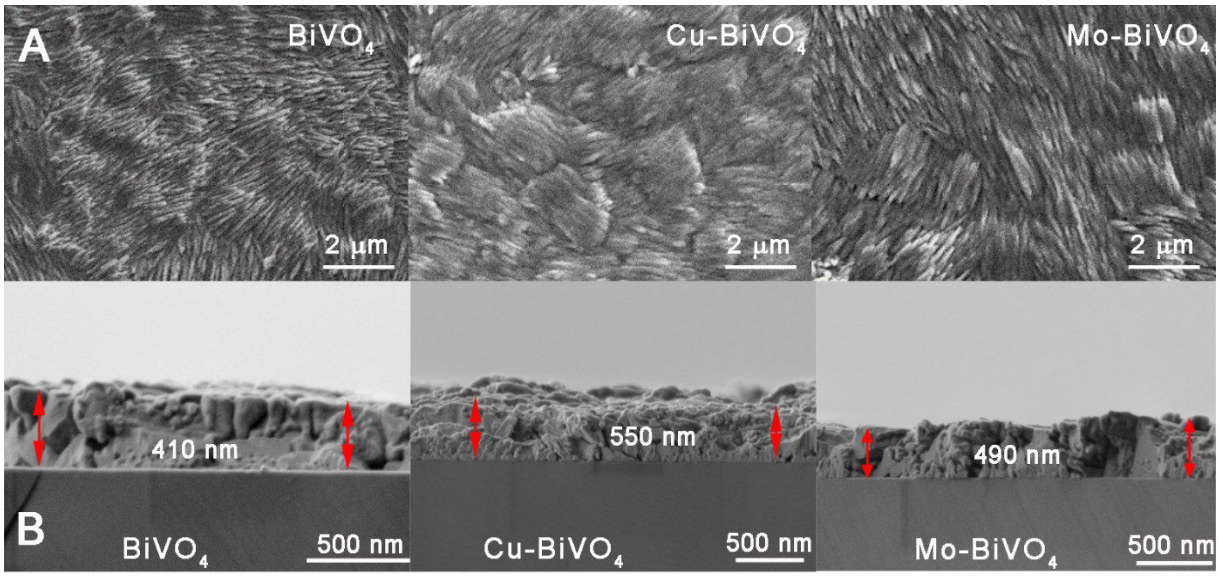

Fig. 5.19. SEM images of undoped, Cu and Mo doped $BiVO_4$ thin films deposited by rf sputtering with CS 3 conditions. The cross section images were recorded by FE-SEM for evaluation of the respective films thickness.

Table 5.5. EDAX analysis with area mapping for undoped, Cu and Mo doped $BiVO_4$ thin films deposited by rf sputtering under CS 3 conditions.

Samples	Bi (at.%)	V (at.%)	O (at.%)	Dopant (at.%)
$BiVO_4$	20.53	25.72	53.75	-
Cu-$BiVO_4$	19.54	24.18	55.47	0.81
Mo-$BiVO_4$	18.88	24.10	55.66	1.36

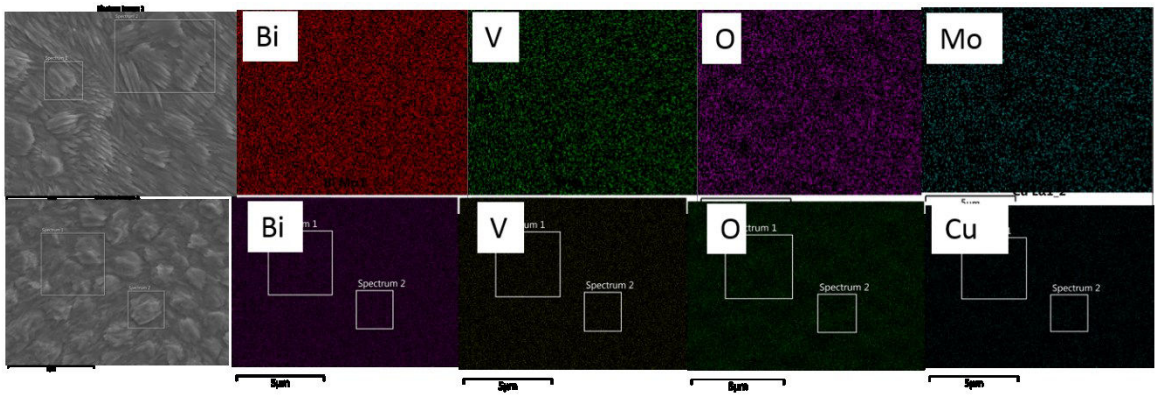

Fig.5.20. EDAX analysis with area mapping for Cu and Mo doped $BiVO_4$ thin films deposited by rf sputtering under CS 3 conditions.

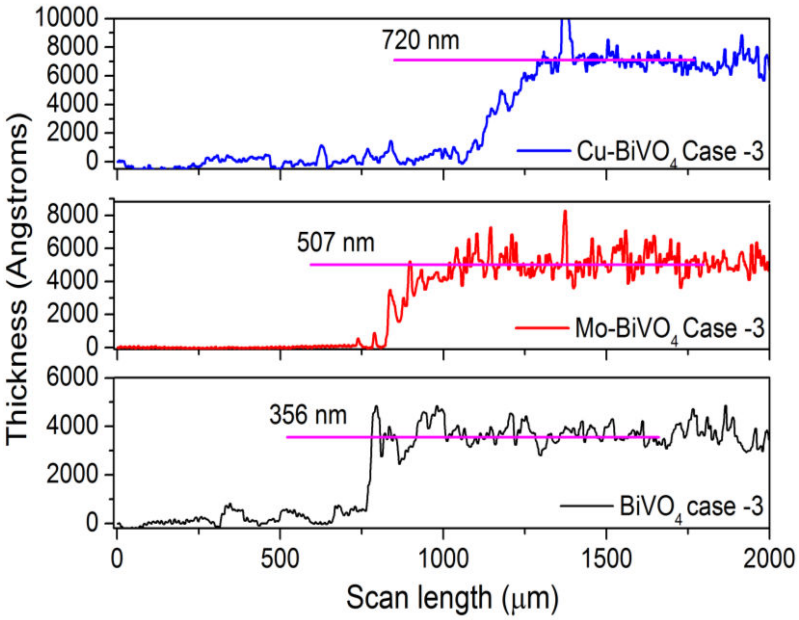

Fig.5.21. Step profile thickness measurements by using stylus profilometer for thin films deposited under CS3 conditions.

5.3.3. XPS analysis

The XPS spectra of pristine, Cu and Mo doped $BiVO_4$ thin films deposited at CS 3 parameters (Fig.5.22),reveal the binding energy levels of Bi 4f, V 2p, O 1s along with Mo 3d and Cu 2p doping elements. In the case study 2, Cu 2p core levels were not seen in the films which might be due to non- homogenous distribution of Cu doping all over the films. The XPS spectra related to Bi – 4f doublets were found in their trivalent oxidation state. Similarly, the XPS band of V $2p_{3/2}$ is well resolved at E_b = 516.4 eV and account also for surface V^{5+} species. On the other hand, XPS bands related to V 2p and Bi 4f didn't show any changes for Cu or Mo doping $BiVO_4$ films. It is probably due to no bonding between such elements and the doping ions. As observed in CS 2 deposited films, the XPS spectra of O1s which may occur from lattice oxygen O^{2-} species (O_{latt}) and adsorbed oxygen or disassociated (O_{ads}) species have also shown similar behavior here as well. Particularly, O_{abs}/O_{latt} molar ratios are relatively low for Cu and Mo doped $BiVO_4$ samples indicating that Cu, Mo elements are bound with only few sites of oxygen atoms. In similar situation as for films obtained by CS1 conditions, the XPS spectra of Mo-3d doublet suggest that the molybdenum is present and strongly seen with Mo^{6+} oxidation state. We have further justified the presence of Mo-O-Mo vibrational bond at 871 cm^{-1} from the micro Raman analysis in Fig.5.18B.

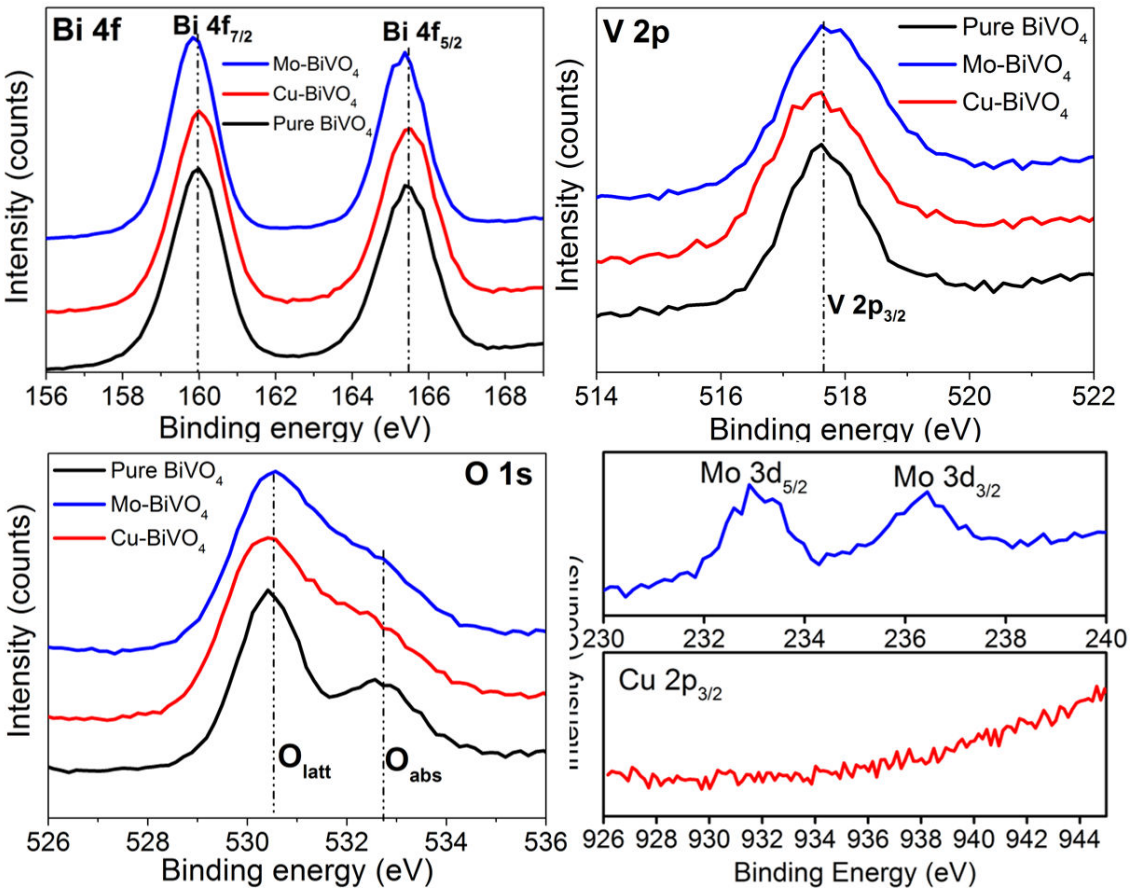

Fig.5.22. XPS spectra of Bi4f, V2p, O1s and doping elements Cu 2p, Mo 3d chemical states for pristine, Cu and Mo doped $BiVO_4$ thin films.

5.3.4. Optical features

UV-Vis spectra for the pristine and doped $BiVO_4$ thin films deposited under CS 3 conditions and annealed at 400°C for 2 hours are shown in Fig.5.23. The band gap energies were calculated from the Tauc's plots (inset Fig.5.4.4) and estimated as 2.5, 2.42 and 2.5 eV for pristine, Cu and Mo doped $BiVO_4$ films respectively. Within the measurement uncertainty, no substantial change occurs on the energy band gap of doped samples. However, as clearly seen on the UV-Vis absorption spectrum of Cu-$BiVO_4$, a shoulder extends toward the red range of the visible range. This behavior is probably due to Cu doping ions which may induce allowed states within the band gap. Mo doped and pristine $BiVO_4$ thin films have shown similar band gaps and spectra shapes. The interferences fringes observed in the spectrum shapes indicate similar thickness for pure and Mo-doped films as compared to thick films obtained with Cu doping (Fig.5.23). Indeed, Cu doped $BiVO_4$ thin films have shown reduction in the energy band gap with more number of optical fringes which are due to high crystalline quality, thick

films and better growth rate compared to the other films such as pristine and Mo doped $BiVO_4$ thin films.

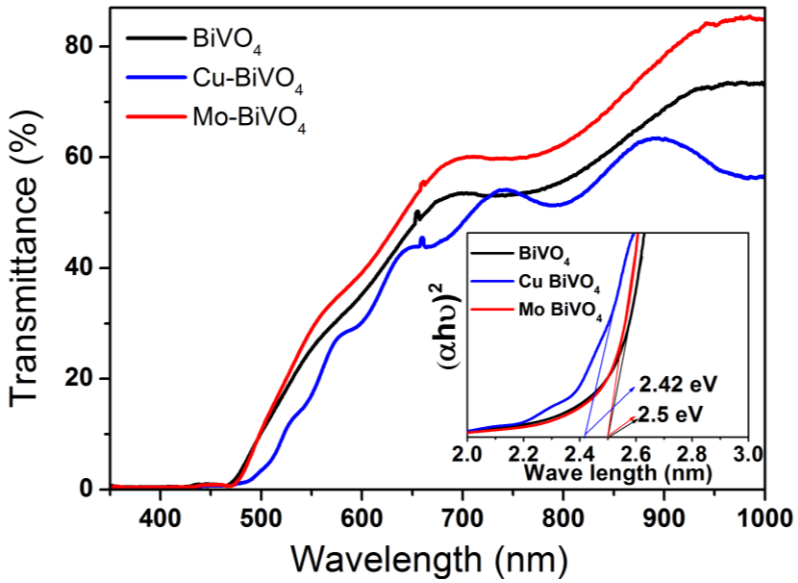

Fig.5.23. UV-vis absorption spectra of pristine, Cu and Mo doped $BiVO_4$ films on boro-float glass substrate at CS 3 deposition condition, with the inset shows the band gap extrapolation for these films.

5.3.5. Photocatalytic studies

Photocatalytic studies were carried out in a similar manner as previous cases (CS1 and CS2) for the CS 3 deposited thin films for the degradation of MO dye of $4x10^{-5}$ M concentration under visible light irradiation. The photocatalytic activity for pristine, Cu and Mo doped thin film were analysed by comparing their degradation rates. In this study, Mo and Cu doped $BiVO_4$ samples exhibited better efficiencies in the degradation of MO dye groups as compared to pristine. However, Mo doped $BiVO_4$ films are more efficient probably due to higher electron density and low film thickness which allow easy transportation of photogenerated charge carriers by avoiding their recombination. Since electron-hole pairs in $BiVO_4$ are mostly generated within the penetration length of the light (~100 nm), the electrons need to travel across the entire thickness of the film (~500 nm) to the $BiVO_4$ and silicon interface. Similarly on the other hand, the associated holes need to travel through $BiVO_4$ to the MO dyes in solution for the degradation process.

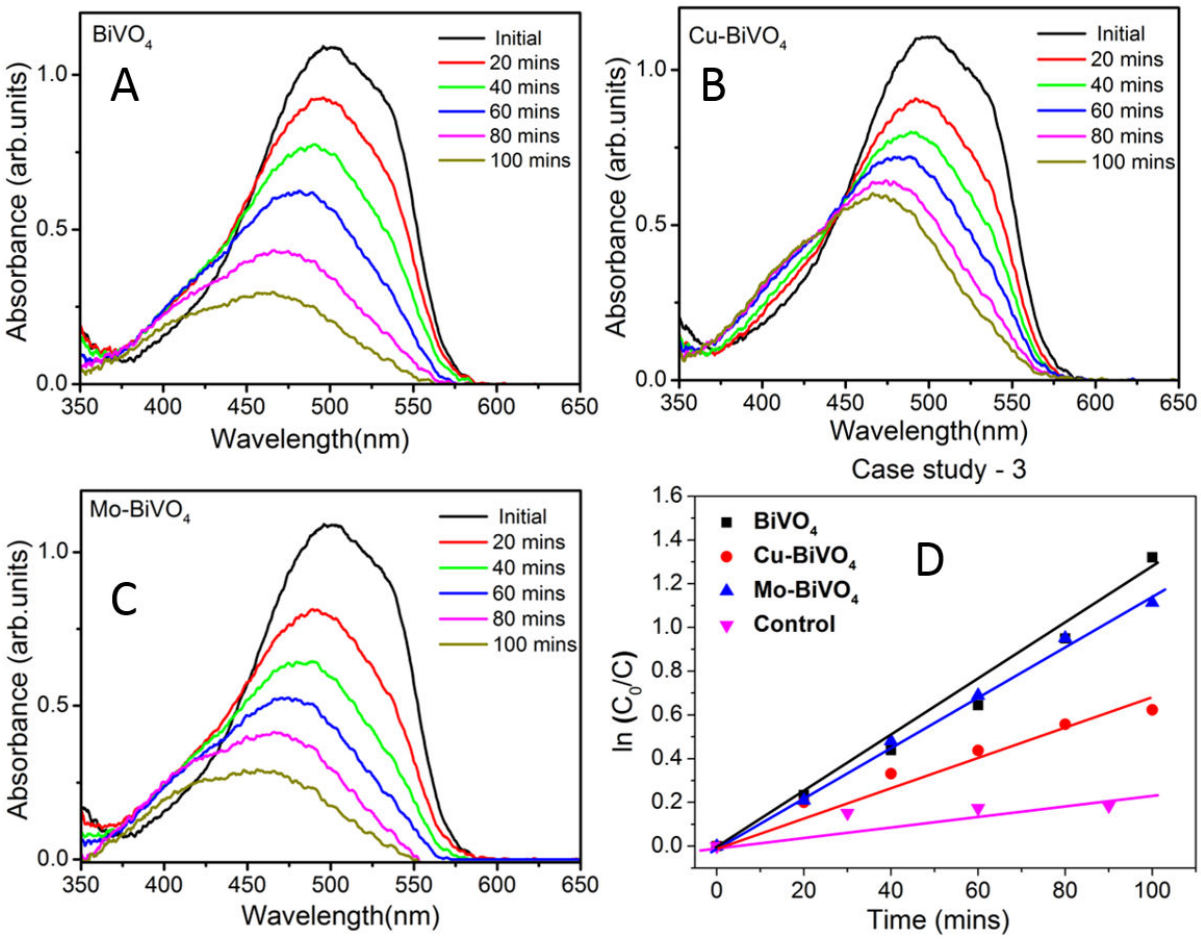

Fig.5.24. (A, B and C) Evaluation of degradation of MO dyes in solution for pristine Cu and Mo doped $BiVO_4$ thin films deposited at case study 3 parameters. D. shows the pseudo-first-order kinetics of degradation of Mo dyes in solution.

The degradation reactions versus time follows a first order kinetics. The reaction constant rates are determined from the slopes of ln (C_o/C) with respect to time and summarized below in table 5.6.

Table 5.6. Photodegradation rate (%) of MO dyes for pristine and Mo, Cu doped $BiVO_4$ thin films under visible light irradiation.

150 W Oriel Xenon lamp with 11.5 W/cm^2		Degradation rate constant, k (min^{-1}) ± error for Methyl Orange (4x10^{-5} M) at pH-3
Case 3 (Ar-O_2-60-12 sccm-450^{o}C)	Pure $BiVO_4$	0.0128±8e-4
	Cu-$BiVO_4$	0.0061±5e-4
	Mo-$BiVO_4$	0.0114±4e-4

5.3.6. Summary of the CS3 conditions

Pristine, Cu and Mo doped $BiVO_4$ thin films were deposited under partial pressures of Ar and O_2 with 60:12 sccm ratio at substrate temperature 450^oC. Monoclinic polymorph phase was obtained for all the deposited films. Nano fibres morphology with thickness ~200 nm with higher surface roughness were probed by FESEM and AFM analysis. Micro-Raman analysis has confirmed the formation of secondary phase V_2O_5 for the films deposited under Ar/O_2 partial pressures (CS2 and CS3). The formation of V_2O_5 secondary phases are the reason for poor photocatalytic efficiencies as compared to films obtained by CS1 conditions. The low PC performance is noticed for Cu doped thin films as compared to Mo doped films which lead to better degradation rates. The possible reasons might be due to higher electron density and lower film thickness (~500 nm).

5.4. Conclusions of the study

Pristine, Mo and Cu doped $BiVO_4$ thin films are synthesized by using R.F sputtering technique. These films have been deposited on Si substrate under three different case studies (CS 1, 2 & 3) as aforementioned. Under CS1 conditions, pristine and Mo and Cu doped $BiVO_4$ thin films were grown with preferential orientation (110), without any defects such as grain boundaries and porous structure. Topography and morphological analysis have shown highly uniform smooth surface exhibiting nano-sized islands. These features enhanced the performance of photocatalytic degradation for MO dyes in solution. Especially, Mo ions substituted to vanadium sites seems to induce higher charge carrier density that enhances photodegradation of MO dyes in solution as compared to Cu and Pristine.

In the case of CS2 and CS3 deposition conditions with major effects on doped $BiVO_4$ thin films deposited under Ar and O_2 60:12 sccm partial pressures at ambient (CS2) and at 450^oC substrate temperatures (CS3) respectively. The observed morphologies were nanosized islands on the surface but nanosized porous cavities were implemented on the cross section of films deposited with CS2 conditions. Different morphologies were realized as nano-fibers with typical sizes around 200 nm and segregated on the outermost surfaces of the films obtained by using CS 3 conditions. However, Cu and Mo doped $BiVO_4$ films have shown poor photocatalytic degradation of MO dyes in solutions as compared to pristine or to samples synthesized by CS1 conditions. The reasons are due to the limited charge carrier mobility

induced by a weak fraction of secondary phase as V_2O_5 associated with nanosized porous structure. All these features may act as barriers on the conduction channels and then limits the effects from photogenerated charge carriers in samples synthesized with an excess of oxygen.

References:

[1] G. Hodes, When Small Is Different: Some Recent Advances in Concepts and Applications of Nanoscale Phenomena, Adv. Mater. 19 (2007) 639–655.

[2] R.. Sonawane, S.. Hegde, M.. Dongare, Preparation of titanium(IV) oxide thin film photocatalyst by sol–gel dip coating, Mater. Chem. Phys. 77 (2003) 744–750.

[3] M.R. da Silva, L.H. Dall'Antonia, L.V.A. Scalvi, D.I. dos Santos, L.O. Ruggiero, A. Urbano, Deposition and characterization of $BiVO_4$ thin films and evaluation as photoanodes for methylene blue degradation, J. Solid State Electrochem. 16 (2012) 3267–3274.

[4] H. Luo, A.H. Mueller, T.M. McCleskey, A.K. Burrell, E. Bauer, Q.X. Jia, Structural and Photoelectrochemical Properties of $BiVO_4$ Thin Films, J. Phys. Chem. C. 112 (2008) 6099–6102.

[5] A. Galembeck, O.L. Alves, $BiVO_4$ thin film preparation by metalorganic decomposition, Thin Solid Films. 365 (2000) 90–93.

[6] K. Sayama, A. Nomura, Z. Zou, R. Abe, Y. Abe, H. Arakawa, Photoelectrochemical decomposition of water on nanocrystalline $BiVO_4$ film electrodes under visible light, Chem. Commun. (2003) 2908.

[7] K. Sayama, A. Nomura, T. Arai, T. Sugita, R. Abe, M. Yanagida, et al., Photoelectrochemical decomposition of water into H_2 and O_2 on porous $BiVO_4$ thin-film electrodes under visible light and significant effect of Ag ion treatment., J. Phys. Chem. B. 110 (2006) 11352–60.

[8] X. Zhang, Y. Zhang, X. Quan, S. Chen, Preparation of Ag doped $BiVO_4$ film and its enhanced photoelectrocatalytic (PEC) ability of phenol degradation under visible light., J. Hazard. Mater. 167 (2009) 911–4.

[9] L. Chen, E. Alarcón-Lladó, M. Hettick, I.D. Sharp, Y. Lin, A. Javey, et al., Reactive Sputtering of Bismuth Vanadate Photoanodes for Solar Water Splitting, J. Phys. Chem. C. 117 (2013) 21635–21642.

[10] L. Chen, F.M. Toma, J.K. Cooper, A. Lyon, Y. Lin, I.D. Sharp, et al., Mo-Doped $BiVO_4$ Photoanodes Synthesized by Reactive Sputtering, ChemSusChem. 8 (2015) 1066–1071.

[11] E. Alarcón-Lladó, L. Chen, M. Hettick, N. Mashouf, Y. Lin, A. Javey, et al., $BiVO_4$

thin film photoanodes grown by chemical vapor deposition., Phys. Chem. Chem. Phys. 16 (2014) 1651–7.

[12] Y. Liang, T. Tsubota, L.P.A. Mooij, R. van de Krol, Highly Improved Quantum Efficiencies for Thin Film $BiVO_4$ Photoanodes, J. Phys. Chem. C. 115 (2011) 17594–17598.

[13] M. Oshikiri, M. Boero, J. Ye, Z. Zou, G. Kido, Electronic structures of promising photocatalysts $InMO_4$ (M=V, Nb, Ta) and $BiVO_4$ for water decomposition in the visible wavelength region, J. Chem. Phys. 117 (2002) 7313.

[14] H. Chang, A kinetic model for photocatalytic degradation of organic contaminants in a thin-film TiO_2 catalyst, Water Res. 34 (2000) 407–416.

[15] T. Huo, X. Zhang, X. Dong, X. Zhang, C. Ma, G. Wang, et al., Photonic crystal coupled porous $BiVO_4$ hybrid for efficient photocatalysis under visible light irradiation, J. Mater. Chem. A. 2 (2014) 17366–17370.

[16] L. Zhang, E. Reisner, J.J. Baumberg, Al-doped ZnO inverse opal networks as efficient electron collectors in $BiVO_4$ photoanodes for solar water oxidation, Energy Environ. Sci. 7 (2014) 1402.

[17] L. Zhang, J.C. Yu, Z. Zheng, C.W. Leung, Fabrication of hierarchical porous iron oxide films utilizing the Kirkendall effect, Chem. Commun. (2005) 2683.

[18] Y. Wang, H. Xu, X. Wang, X. Zhang, H. Jia, L. Zhang, et al., A General Approach to Porous Crystalline TiO_2 , $SrTiO_3$, and $BaTiO_3$ Spheres, J. Phys. Chem. B. 110 (2006) 13835–13840.

[19] R. Könenkamp, Carrier transport in nanoporous TiO_2 films. *Phys. Rev. B* **61,** (2000) 11057–11064.

[20] F.F. Abdi, T.J. Savenije, M.M. May, B. Dam, R. van de Krol, The Origin of Slow Carrier Transport in $BiVO_4$ Thin Film Photoanodes: A Time-Resolved Microwave Conductivity Study, J. Phys. Chem. Lett. 4 (2013) 2752–2757.

Chapter 6

Conclusions

This thesis is an ardent effort towards the synthesis of photoactive semiconducting oxides based on metal doped bismuth vanadate (Mo, Cu, Ag) - $BiVO_4$ materials and investigations of their related physical features with the aim of photocatalytic applications. The synthesis of the samples was achieved by using high energy ball milling technique to obtain metal doped $BiVO_4$ (Cu, Mo and Ag) powders with nano-sized crystalline domains. Doped $BiVO_4$ thin films were also realized by using RF sputtering technique with Mo or Cu dopants through ball mill prepared targets. All the deposited thin film possessed unique crystalline phase as monoclinic polymorph with nanostructured surfaces exhibiting nano-islands with high specific surfaces. Investigations of their structural, electronic, morphological and optical features were realized using complementary techniques. Representative samples were tested for heterogeneous photocatalysis devoted to the degradation of organic dyes in solutions. The photocatalytic efficiencies were estimated and compared as function of the organisation of the samples as nanostructured powders or thin films with defined surface states.

One of the prime objectives of thesis are successfully achieved by synthesis of high energy ball milled Cu, Mo and Ag doped $BiVO_4$ nanoparticles with defined doping rates. Their investigations were conducted by using XRD, micro-Raman, FESEM, HRTEM and EPR in order to probe their structural, morphological and doping features. The structural properties were characterized by quantitative estimation of the lattice parameters and the lattice compressions as function of the metal ion nature and doping rates. Monoclinic scheelite structure was obtained for all the metal doped $BiVO_4$ samples irrespective of doping ratios. The substitutional doping (Cu, Mo) justified by EPR analysis, acts on the sample morphologies and electronic features through the particle size reduction and the slight lowering of electronic band gap leading to red shifted absorption thresholds. The photocatalytic studies showed an enhancement of the related efficiency with an increase in the Cu doping rates. This effect is also correlated with the reduction of oxygen vacancies by Cu doping which contributes to increase the photogenerated charge densities and their lifetimes. For Mo doped $BiVO_4$ samples, there was a good relationship between doping rate, particle size and crystalline quality which seems to be achieved for the 2 at.% Mo doped $BiVO_4$, inducing higher efficiency as compared

to the pristine structure. For Ag doped $BiVO_4$ samples, careful analysis of the grain morphology notably by HRTEM observations and electron diffraction evidenced that Ag clusters were associated with $BiVO_4$ particles leading to the formation of Ag-$BiVO_4$ nanocomposites. Electronic, dielectric and optical behaviours were investigated which points out the interfacial polarization and dynamic charge transfer mechanism induced Ag loading. Surface plasmonic effects occur from Ag nanoclusters and enhance the photocatalytic activity demonstrated for 3 at.% doped Ag-$BiVO_4$ composites.

In sol-gel route, metal doped $BiVO_4$ (Cu, Mo and Ag) powders were successfully prepared and their relevant physical features were investigated. The doped samples with the same doing rate show monoclinic polymorph, moderate structural distortions were observed for Mo and Cu doped samples except Ag doping. EPR analysis has evidenced the achievement of Cu and Mo doping through its substitution in the crystal sites of vanadium in $BiVO_4$ host. Cu doping induces better degradation compared to Ag and Mo association in the photocatalytic activity. Thus, higher optical absorbance and smaller particle size are the key factors of Cu doping, which show an improvement in photocatalytic efficiency.

The other important objective of this work is dedicated towards pure and metal doped thin films grown by R.F sputtering technique. The selection of Mo/Cu are due to substitutional doping behaviour in sites of V in $BiVO_4$. Thus, Pristine, Mo and Cu doped $BiVO_4$ thin films were deposited on Si substrate under different conditions such as substrate temperatures and the partial pressures of pure Ar or a mixture of Ar/O_2. Depending on the chosen experimental configuration, the topography and morphology of Mo and Cu doped films have shown highly uniform smooth surface with nano-sized islands that can be relevant for the photocatalytic activity. In the other experimental configuration, the film deposition were performed under Ar/O_2 partial pressures. The topography can be as smooth surface with nano sized pores inside the films as shown on their cross sections or alternatively as nano-fibers agglomerated on the outermost film surfaces. Comparative photocatalytic reactions were performed for representative samples and their efficiencies were analysed in correlation with the structure, composition and surface topography features. Particularly, when the organisation of the films leads to the formation of nano-sized pores, limitation of the mean free path of the photogenerated charge carriers overcame the photocatalytic activity.

Particular conclusion:

The present work realizes all the specific objectives of the thesis,

- All physical features related to metal doped $BiVO_4$ (Cu, Mo and Ag) nanostructured powders prepared by mechano-chemical (HEM) synthesis technique. Cu / Mo are substituted in the sites of V in $BiVO_4$, whereas Ag segregated on the surface of $BiVO_4$. Cu as substitutional dopant and Ag as plasmonic catalyst showed improved features for efficient photocatalysis.
- Doped $BiVO_4$ nanostructures with Cu, Ag, and Mo were achieved by Sol-gel technique, Cu doped $BiVO_4$ has shown better efficiency, due to smaller particle size with effective doping as comparative Mo and Ag.
- The three versatile conditions are used for the deposition of Mo and Cu doped $BiVO_4$ thin films by rf sputtering technique. It has given a wide spectrum of grain morphologies and surface states associated with the modulation of the electronic and optical properties. Comparative photocatalytic investigations were carried out for the degradation of organic dyes. CS1 condition, i.e., deposition under Ar partial pressures showed thin films of thickness<200 nm with nano-sized island morphologies having more active sites. Among Mo and Cu doping elements, Mo has shown better efficiency due to its versatile valence states $Mo^{3,4,5,6+}$ especially its homogeneous doping with higher electron density improve the photocatalytic reactions.

Thus, metal doped $BiVO_4$ (Cu, Mo and Ag) nanostructured material has shown enhancements in photocatalytic reactions in several aspects and pave the way for promising photocatalytic applications required for the environment preservation.

Future potential directions

The present thesis work is devoted towards the synthesis and characterization of metal doped bismuth vanadate (Mo, Cu, Ag) - $BiVO_4$ materials and investigations of their related physical features with the aim of photocatalytic applications. There are some possible future work aspects and potential directions towards enhancement of photocatalytic efficiencies.

1. One of the main objectives of this thesis work is focused on mechano-chemical synthesis of metal doped $BiVO_4$ (Cu, Mo and Ag) with defined doping rates under dry air milling conditions. So it would be interesting to observe/investigate the doping mechanism under wet milling process for similar metal doped $BiVO_4$ (Cu, Mo and Ag) nanoparticles. This may be benefit towards the synthesis of different morphologies. The alcohol atmosphere could be ethanol, methanol or isopropanol or ethylene glycol etc
2. Synthesis of plasmonic Ag/$BiVO_4$ nanocomposites are very attractive work from this thesis, where synthesis of such materials can be achieved in short times as compared to other chemical routes such as Sol-gel / hydrothermal etc. It would be interesting to check and compare all the physico-chemical properties as well as photocatalytic studies for other noble metals (Au, Pt, Pd etc.) with $BiVO_4$ as nanocomposites under same milling conditions.
3. The investigation on metal doped $BiVO_4$ (Cu and Mo) thin films obtained by rf sputtering technique at condition CS 3 led to nano-fibre growth under argon and oxygen partial pressures. It would be interesting to check the nano fibre growth under only argon partial pressures at 450°C substrate temperature.
4. The investigation on the photocatalytic ability of metal doped $BiVO_4$ (Cu and Mo) thin films obtained by rf sputtering technique are tested for degradation of organic pollutants, It would be interesting to study on water splitting applications.
5. It was proposed that metal doped $BiVO_4$ nanoparticles are efficient for degradation of organic pollutants, it is also possible to use simultaneously for water splitting (hydrogen production) application under same setup.
6. Monoclinic phase $BiVO_4$ as visible light driven photocatalyst with energy bandgap nearly 2.4 eV, could be possibly used to form heterejuction structures with large bandgaps such as TiO_2,WO_3, ZnO etc. or lower bandgaps such as Fe_2O_3, CuO, AgO, Si etc, to enhance the utilization of solar spectrum for efficient photocatalytic performances as Z-scheme method.

Publications and communications:

Publications in peer-reviewed journals

1. V.I. Merupo, S. Velumani, K. Ordon, N. Errien, J. Szade, A. Kassiba, "Structural and optical characterization of ball-milled copper-doped bismuth vanadium oxide ($BiVO_4$)", CrystEngComm, 2015, 17, 3366-3375.

2. V.I. Merupo, S. Velumani, Goldie Oza, M.Makowska-Janusik, A. Kassiba, "Structural, electronic and optical features of molybdenum doped bisumth vanadium oxide", Materials Science in Semiconductor Processing 31 (2015) 618–623.

Publications as Conference Proceedings:

1. V.I. Merupo, S. Velumani, M. A. García-Sánchez and A. Kassiba "Structural and Optical properties of Molybdenum doped Bismuth vanadate powders"
IEEE, DOI: 10.1109/ICEEE.2014.6978299.

2. V.I. Merupo, S. Velumani, M.Bizzaro and A. Kassiba "Structural, morphological and Optical properties of sol-gel prepared Cu doped $BiVO_4$ powders" Accepted for IEEE Conference publication-2015. DOI: 10.1109/ICEEE.2015.7357978

Article in preparation

1. V.I. Merupo, S. Velumani, G. Oza, M.Tabellout, M. Bizarro, C. Sandrine and A. Kassiba "High energy ball milled Ag/$BiVO_4$ plasmonic photocatalysts" communicated in Wiley-chemistry Select journal- under review.